

**Developing highly efficient and durable
electrocatalysts for water splitting over a wide pH
range**

by

Suchada Sirisomboonchai

**A Dissertation Presented to
the Graduate School of Science and Technology of the
Hirosaki University in partial fulfillment of the requirement
for the degree of Philosophy in Energy Engineering**

Hirosaki University

2020

ABSTRACT

Water splitting is a promising process to convert water to hydrogen energy and other chemicals via renewable energy, in which two half-cell reactions, i.e., oxygen evolution reactions (OER) and hydrogen evolution reactions (HER), occur simultaneously. Comparing with the two-electron transfer reaction of HER, the OER is a four-electron transfer reaction, which is more kinetically sluggish. Therefore, the OER always governs the overall electrochemical water splitting efficiency. To date, Iridium dioxide (IrO_2) and ruthenium dioxide (RuO_2) is state-of-the-art OER electrocatalysts with low overpotential and Tafel slope while platinum (Pt) and Pt-based alloys are the state-of-the-art HER electrocatalysts. However, their scarcity and high price limit their industrial applications. This study focuses on developing earth-abundant and low-cost transition metal-based nanostructured electrocatalysts for highly efficient and durable water splitting over a wide pH range.

Firstly, Ni-Fe layer double hydroxide (LDH) based OER electrocatalysts were developed. To improve the OER performance, NiO@NiFe-LDH electrocatalysts with a core@shell structure were decorated on a three-dimensional (3D) mesoporous nickel foam (NF) by a two-step hydrothermal synthesis process followed by and a calcination step. Due to the 3D rational configuration with highly active sites, the obtained composite electrode showed high performance for OER, which needed a low apparent overpotential of 265 mV to afford the standard current density of 10 mA cm^{-2} . In addition, the NiO@NiFe-LDH coated electrode was further treated in an organic solution via ultrasound for *in situ* intercalations of the NiFe-LDH to provide larger channels for ion transportation and gas diffusion. As a result, the charge transition resistance was obviously reduced and the apparent activity, as well as the long-term stability, were improved. The optimized NiO@NiFe-LDH composite exhibited excellent long-term stability in 50 h even at high current densities of 50 and 100 mA cm^{-2} , and meanwhile, the required apparent overpotential of OER for sustaining the standard current density (10 mA cm^{-2}) was reduced from 265 to 210 mV.

Secondly, to develop HER electrocatalysts with high efficiency, long-term stability, and low-cost for the large-scale and effective application of renewable energy, a binder-free NiCoP-carbon nanocomposite (denoted as NiCoP-C(TPA)) film with unique

nanostructure was successfully coated on the electrode for the first time by deposition of a terephthalic acid-induced NiCo bimetallic compound precursor film on the NF with a hydrothermal synthesis method followed by a calcination process in Ar atmosphere and continuous phosphorization treatment with NaH_2PO_2 . In the obtained NiCoP-C(TPA) electrocatalyst, bimetallic phosphide nanoparticles were well combined with graphite carbon. It is found that the bimetallic NiCo alloy was also formed in the carbonization process, which affected the performance of the final catalyst. As a result, the NiCoP-C(TPA) electrocatalyst had much higher activity than the monometallic phosphides of NiP-C(TPA)/NF and CoP-C(TPA)/NF, and the NiCoP-C(TPA)/NF electrode exhibited an overpotential as low as 78 mV at the standard current density of 10 mA cm^{-2} with a small Tafel slope of 73.4 mV dec^{-1} , a faradic efficiency of $\sim 94\%$ and long-term stability at high current density in the alkaline electrolyte. Meanwhile, the NiCoP-C(TPA)/NF electrode also exhibited superior HER performance in the acidic electrolyte with an overpotential of $94 \text{ mV}@10 \text{ mA cm}^{-2}$, a Tafel slope of 81.1 mV dec^{-1} , and long-term stability although a relatively high overpotential of $248 \text{ mV}@10 \text{ mA cm}^{-2}$ with a high Tafel slope of $112.5 \text{ mV dec}^{-1}$ was obtained in the neutral electrolyte. It is expected to provide a novel synthesis method by using organic solid acid to derive high-performance bimetallic phosphide-based electrocatalysts with special nanostructure for HER in the water-splitting process.

Lastly, the bifunctional electrocatalysts for the overall water splitting were developed, in which combining oxides with bimetallic elements was considered as an efficient route to modify the electronic distribution for improving the intrinsic activity of electrocatalysts, and further engineering the defect structure and adjusting the valence state could provide more adsorption sites as well as active sites for the decomposition of the reactants and/or intermediates. NiMnO_x nanosheets with rich defects were electrochemically deposited on the surface of $\text{Cu}(\text{OH})_2$ nanowires followed by a thermal treatment process to form a CuO_x nanowires @ NiMnO_x nanosheets (CuO_x NWs@ NiMnO_x NSs) electrocatalyst with core-shell configuration. Structure characterizations indicated that NiMnO_x nanosheet had numerous vacancies with scattered defects and dislocations with partial cracking of the inert basal planes, resulting in extra active edge sites and coordination-unsaturated spinel crystal. As such, the valence states of Ni and Mn elements became unstable in the defect-modified NiMnO_x materials

under the applied potential. Comparing with the initial NiMnO_x, more Ni³⁺ and Mn⁴⁺ were formed during the oxygen evolution reaction (OER) whereas they were converted to Ni²⁺ and Mn³⁺ during the hydrogen evolution reaction (HER). These controllable valence state changes of metal elements endowed the NiMnO_x to have a high ability for catalyzing overall water electrolysis. As a result, the CuO_x NWs@NiMnO_x NSs bifunctional electrocatalysts exhibited high performances in both HER and OER in alkaline electrolytes. Meanwhile, by using the same electrocatalysts in the neutral electrolyte, the overpotentials@10 mA cm⁻² was also as low as 80.7 and 390 mV with Tafel slopes of 77.6 and 101.6 mV dce⁻¹ for HER and OER, respectively. A two-electrode overall water electrolysis system using this bifunctional electrocatalyst exhibited low cell voltages of 1.62 and 1.75V in the alkaline and neutral electrolytes respectively at the standard current density of 10 mA cm⁻² with long-term stability, indicating that this CuO_x NWs@NiMnO_x NSs core@shell-type material should be an effective bifunctional electrocatalyst in both alkaline and neutral pH media.

ACKNOWLEDGMENTS

First of all, I would like to appreciate my profound and respectable academic advisor, Professor Dr. Guoqing Guan, for his valuable instruction, suggestion, and encouragement, supportive and guidelines for my experiments, manuscripts, patents, dissertation during my Ph.D. program and my stay in Japan.

I would like to thank Professor Abuliti Abudula and Associate Professor Dr. Akihiro Yoshida for their kind supports and suggestions on my research.

I would like to thank Associate Professor Dr. Chanatip Samart, Department of Chemistry, Science and Technology, Thammasat University, for introducing me to the applied MEXT scholarship and recommending me towards a Ph.D. degree in this laboratory.

I would like to thank all professors and staff at the Institute of Regional Innovation (IRI) and Graduated School of Science and Technology, Hirosaki University, for all kinds of helpful supports of my study.

I would like to thank all members of our research group for their helpful supports and for exchanging their good experiences and good friendships.

I would like to thank my family, all of my friends for their encouragement, love and always supporting me during my stay in Japan.

Finally, I would like to deeply acknowledge the scholarship from the Ministry of Education, Culture, Sports, Science, and Technology (MEXT) of Japan for full supports along with my Ph.D. study at Graduate School of Science and Technology, Hirosaki University.

Thank you all very much!

Suchada Sirisomboonchai

TABLE OF CONTENTS

ABSTRACT	i
ACKNOWLEDGMENTS	iv
TABLE OF CONTENTS.....	v
LIST OF TABLES	viii
LIST OF FIGURES	ix
CHAPTER 1 INTRODUCTION.....	1
1.1 THEORETICAL OF HYDROGEN EVOLUTION	2
1.2 THEORETICAL OF OXYGEN EVOLUTION	3
1.3 THEORETICAL OF OVERALL WATER SPLITTING	5
1.4 ELECTROCATALYSTS FOR WATER SPLITTING	6
1.4.1 Electrocatalysts for hydrogen evolution	6
1.4.2 Electrocatalysts for oxygen evolution	11
1.4.3 Electrocatalysts for bifunctional overall water splitting.....	14
1.5 SUBSTRATE FOR SUPPORT ELECTROCATALYSTS WATER SPLITTING	20
1.6 THE ACTIVITY PARAMETER	21
1.6.1 Overpotential	21
1.6.2 Tafel slope and exchange current density	23
1.6.3 Electrochemical active surface area	24
1.6.4 Faradaic efficiency	24
1.6.5 Stability test	25
1.7 OBJECTIVE OF THIS STUDY	25
1.8 SCOPE OF THIS DISSERTATION	26
REFERENCE	29

CHAPTER 2 Fabrication of NiO microflake@NiFe-LDH nanosheet heterostructure electrocatalysts for oxygen evolution reaction	42
2.1 INTRODUCTION	42
2.2 EXPERIMENT	44
2.2.1 Chemicals and Materials	44
2.2.2 Synthesis of NiO/NF electrode.....	44
2.2.3 Synthesis of NiO@NiFe-LDH/NF electrode	44
2.2.4 Structural characterization.....	45
2.2.5 Electrochemical measurements	45
2.3 RESULTS AND DISCUSSION.....	46
2.3.1 Morphology structure and composition characterization.	46
2.3.2 Influence condition on performance of NiO@NiFe-LDH/NF-US electrode.	51
2.3.3 Catalytic activity, conductivity and stability analysis of electrodes.	52
2.4 CONCLUSION	61
REFERENCE	61
CHAPTER 3 Terephthalic Acid Induced Binder-free NiCoP-carbon Nanocomposite for Highly Efficient Electrocatalysis of Hydrogen Evolution Reaction	67
3.1 INTRODUCTION	67
3.2 EXPERIMENT	69
3.2.1 Chemicals and materials.....	69
3.2.2 Synthesis of organic acid derived NiCo bimetallic compound film on NF...	69
3.2.3 Phosphorization for the preparation of NiCoP-C(TPA)/NF electrode	70
3.2.4 Characterizations	71
3.2.5 Electrochemical measurements	71
3.3 RESULTS AND DISCUSSION	72
3.3.1 Influence of preparation parameters on HER catalytic performance	72

3.3.2 Microstructure and composition analysis of NiCoP-C(TPA)/NF catalyst. ...	75
3.3.3 Catalytic activity, conductivity and stability analysis of electrodes.	81
3.3.4 Catalytic activity, conductivity and stability analysis of electrodes compare wide pH range electrolyte.	89
3.4 CONCLUSION	92
REFERENCES	92
CHAPTER 4 Fabrication of CuO _x nanowires@NiMnO _x nanosheets core@shell-type electrocatalysts: crucial roles of defect modification and valence state for overall water electrolysis	98
4.1 INTRODUCTION	98
4.2 EXPERIMENTAL	102
4.2.1 Chemicals and Materials	102
4.3 RESULTS AND DISCUSSION	104
4.3.1 Microstructure and composition analysis of CuO _x NWs@NiMnO _x /CF catalyst.	104
4.3.2 HER and OER in alkaline medium.	113
4.3.3 HER and OER in neutral pH medium.	122
4.3.4 Overall-Water Splitting in alkaline and neutral solution.	128
4.4 CONCLUSIONS	130
REFERENCES	131
CHAPTER 5	146
5.1 Conclusions	146
5.2 Prospects	147
CURRICULUM VITAE	149
List of Publications and Presentations	150
List of Patents	153

LIST OF TABLES

Table 1.1 Summary of HER activity of Ni-based electrocatalysts in wide pH range. ..	17
Table 1.2 Summary of OER activity of Ni-based electrocatalysts in wide pH range. ..	18
Table 1.3 Summary of bifunctional overall water splitting activity of Ni-based electrocatalysts in wide pH range.	19
Table 2.1 The molar ratios of Ni/Fe on the surfaces of composites by EDS analysis... 48	48
Table 2.2 The molar ratios of Ni/Fe on the surfaces of composites by XPS analysis... 50	50
Table 2.3 Comparison of this work with the recently reported Ni-based electrodes for OER in alkaline solution.	60
Table 3.1 Summary of the overpotentials @ 10 mA cm ⁻² current density and the corresponding Tafel slope of the three organic acid derived NiCo(organic compound) films on nickel foam electrodes in Figure 6.	74
Table 3.2 Summary of the overpotentials @ 10 mA cm ⁻² current density and the corresponding Tafel slopes of NiCo-C(TPA)/NF electrodes with different Ni/Co molar ratios in Figure S2.	74
Table 3.3 Comparison Tafel slopes from two different techniques-based Figure 3.10. 83	83
Table 3.4 Calculated ECSA and roughness of surface (R _f) of the samples in Figure S8.	86
Table 3.5 Comparison of this work with other related electrocatalysts working in alkaline electrolyte in the literatures.	91
Table 4.1 Element valence states of Ni, Mn and Cu species in the CuOx NWs@NiMnOx NSs and their relative percentage ratio based on the deconvolution of peak areas.....	126
Table 4.2 Element valence states of Ni, Mn and Cu species in the CuOx NWs@NiMnOx NSs and their relative percentage ratio based on the deconvolution of peak areas.....	127

LIST OF FIGURES

Figure 1.1 (A) OER mechanism for alkaline (red line) and acidic (green line) conditions. The black line indicates that the OER involves the formation of a peroxide (M–OH) intermediate, while the light blue line indicates the direct reaction of two adjacent oxo (M–O intermediates to produce oxygen.[17] (B) Plot of Gibbs free energy of reactive species and intermediates (horizontal lines) of the oxygen evolution reaction (OER) versus the reaction coordinate.[18].....	5
Figure 1.2 Schematic illustration of alkaline HER on Ni-based catalyst.[29].....	7
Figure 1.3 The NiCoP facets: (A) (111); (B) (100); (C) (001)- NiP-t; and (D) (001)-CoPt.[41]	11
Figure 1.4 (A) Bode’s diagram for Ni(OH) ₂ –NiOOH redox transformations.[46] (B) Sabatier-type volcano plots for Ni-based oxyhydroxide sites doped with transition metals.[47] (C) Scheme of LDH structure.[48] (D) Intercalation/exfoliation LDH.[49]	12
Figure 1.5 Schematic illustration of bifunctional electrocatalyst overall water splitting.	15
Figure 1.6 schematic polarization curve for HER and OER.	22
Figure 2.1 Schematic diagram of fabrication NiO@NiFe-LDH/NF-US.....	45
Figure 2.2(a,b) Surface morphologies of (a) NiO/NF (b) NiO@NiFe-LDH/NF by SEM; (c,d) TEM images of NiO@NiFe-LDH/NF in different magnifications.....	47
Figure 2.3 EDS spectra in NiO@NiFe/NF-US.....	48
Figure 2.4 (a) XRD patterns of nickel foam (NF), NiO/NF, NiFe-LDH/NF, NiO@NiFe-LDH/NF and NiO@NiFe-LDH/NF-US, (b) XRD patterns of NiO@NiFe-LDH/NF before and after ultrasound treatment in the range of 10-30 degree represent the diffraction peak corresponding to (003) is shifted from 12.2° to a lower value of 11.8° after ultrasound treatment in formamide solution.....	49
Figure 2.5 (a) XPS survey spectra of NiO, NiO@NiFe-LDH, and NiO@NiFe-LDH-US catalysts. (b) XPS O 1s spectra; (c) Ni 2p spectra; and (d) Fe 2p spectra of NiO, NiO@NiFe-LDH, and NiO@NiFe-LDH-US catalysts.....	50
Figure 2.6 LSV curves of NiO@NiFe-LDH/NF-US for OER with a scan rate of 5 mV s ⁻¹ in 1.0 M KOH solution, where various mole ratios of Ni/Fe (1:1, 4:1, 9:1, 1:4) in initial	

solution for the synthesis of NiFe-LDH on the NF were used with scan rate 5 mV s ⁻¹ in 1 M KOH.....	52
Figure 2.7 (a) LSV curves of NiO/NF, NiFe-LDH/NF, NiO@NiFe-LDH/NF and NiO@NiFe-LDH/NF-US with a scan rate of 5 mV/s; (b) Tafel plots of NiO/NF, NiFe-LDH/NF, NiO@NiFe-LDH/NF and NiO@NiFe-LDH/NF-US collected in 1.0 M KOH electrolyte; (c) Chronopotentiometry lines of NiO/NF, NiFe-LDH/NF, NiO@NiFe-LDH/NF and NiO@NiFe-LDH/NF-US at 10 mA cm ⁻² current density with a duration of 1000 sec; (d) EIS spectra of NiFe-LDH@NiO/NF and NiFe-LDH@NiO/NF-US electrodes at an overpotential of 340 mV.	54
Figure 2.8 CV curves for determining electrochemical activity surface areas (ECSAs) of (a) nickel foam (NF) substrate, (b) NiO/NF, (c) NiFe-LDH/NF, (d) NiFe-LDH@NiO/NF and (e) NiFe-LDH@NiO/NF-US collected between potential range 1.024-1.124 V (vs RHE) with scan rate 5, 10, 20, 50, 70 and 100 mV/s respectively in 1M KOH solution.	56
Figure 2.9 OER polarization curves of NF, NiO/NF, NiFe-LDH/NF, NiO@NiFe-LDH/NF and NiO@NiFe-LDH/NF-US normalized based on ESCA.....	56
Figure 2.10 (a) Capacitive current vs scan rate at a potential range from 1.02 to 1.12 V (vs RHE) with different scan rates in the range of 5-100 mV/s; (b) Multi-current process of NiO@NiFe-LDH/NF-US electrode in 1.0 M KOH electrolyte (The current density started from 20 mA/cm ² and ended at 200 mA/cm ² with an increment of 20 mA/cm ² during 500 sec; (c) Time-dependent chonopotentiometry curve of NiO@NiFe-LDH/NF-US at fixed current densities of 50 and 100 mA cm ⁻² with a total duration time of 50 h.	57
Figure 2.11 SEM images of NiO@NiFe-LDH /NF-US with different magnifications after 50 h long-term stability test.....	58
Figure 2.12 XRD patterns of NiO@NiFe-LDH/NF-US before and after 50 h long-term stability test.....	58
Figure 2.13 evolution amounts based on the theoretical calculation and experimental results over NiO@NiFe-LDH/NF-US coated electrode.....	59
Figure 3.1 Schematic illustration of NiCoP-C(TPA)/NF electrode fabrication.....	71
Figure 3.2 Electrochemical evaluation of three organic acid derived NiCo(organic compound) films on nickel foam electrode before calcination: (A) LSV polarization	

curves for HER; (B) Tafel slopes in 1.0 M KOH electrolyte at a scan rate of 1 mV s⁻¹. 73

Figure 3.3 Electrochemical evaluation of NiCo-C(TPA)/NF electrodes with different mole ratios of Ni/Co: (A) LSV polarization curves for HER; (B) Tafel slopes in 1.0 M KOH electrolyte at a scan rate of 1 mV s⁻¹..... 73

Figure 3.4 (A and B) SEM image of NiCo-(TPA) film after the hydrothermal synthesis but without calcination process at (A) 5μm and (B) 2μm. (c) Raman spectra of NiCo(TPA) before calcination. (D) FT-IR spectra of pure terephthalic acid (TPA), NiCo(TPA) before calcination, NiCo-C(TPA) and NiCoP-C(TPA)..... 77

Figure 3.5 SEM images of (A) NiP-C(TPA) (B) CoP-C(TPA). TEM images of (A', A'') NiP-C(TPA) and (B', B'') CoP-C(TPA). 78

Figure 3.6 (A, B) SEM images of (A) NiCo-C(TPA)/NF and (B) NiCoP-C(TPA)/NF; (C) EDS mapping of NiCoP-C(TPA)/NF; (D) TEM and HRTEM images of NiCoP-C(TPA)/NF; (E) Raman spectra of NiCo-C(TPA)/NF and NiCoP-C(TPA)/NF..... 78

Figure 3.7 (A) XRD patterns of Co-C(TPA), Ni-C(TPA), NiCo-C(TPA) and NiCoP-C(TPA). (B) The corresponding magnification region with 2θ ranging from 42° to 48°. 80

Figure 3.8 (A) XRD pattern of NiCoP-C(TPA); (B) Survey XPS spectra of NiCo-C(TPA) and NiCoP-C(TPA); and the related XPS spectra of (C) Ni 2p, (D) Co 2p, (E) P 2p in NiCoP-C(TPA). 80

Figure 3.9 Electrocatalytic performances of various samples in HER. (A) LSV polarization curves at a scan rate of 1 mV s⁻¹ collected in 1 M KOH electrolyte. (B) Corresponding Tafel plots derived from the LSV curves in (A). (C) EIS Nyquist plots of various electrodes at an overpotential of 200 mV in 1 M KOH electrolyte. (D) Enlarged Nyquist plots of CoP-C(TPA)/NF, NiP-C(TPA)/NF, NiCo-C(TPA)/NF and NiCoP-C(TPA)/NF in (C). 82

Figure 3.10 (A) Tafel curves converted from voltammogram. (B) Tafel curves obtained by direct measuring the Tafel characteristics using the electrochemical workstation. (C) Estimated Tafel data for evaluation of the reaction rate determining step (selection of NiCoP-(TPA)/NF and 20%wt Pt/C coated NF as the examples). 82

Figure 3.11 Cyclic voltammograms of (A) nickel foam (NF), (B) NiCo-C(TPA)/NF, (C) NiCoP-C(TPA)/NF collected between a potential range of 0.1-0.3V (vs RHE) with scan rates of 5, 10, 20, 40, 60, 80, 100 mV/s, respectively in 1 M KOH electrolyte. (D)

Dependence of current on the scan rate at different double layer capacitances for the estimation of the electrochemical surface area. (E) LSV polarization curve normalized based on ECSA.....	85
Figure 3.12 (A) HER multi-step chronopotentiometric curve of NiCoP-(TPA)/NF electrode with the current density started started at current density -20 mA cm^{-2} and ended at -200 mA cm^{-2} with an increment of 20 mA cm^{-2} every 500s. (B) Chronopotentiometry curves of NiCoP-(TPA)/NF electrode at current density of 100 mA cm^{-2} (red line) and at the constant overpotential of 78 mV (Blue line) collected at a duration time of 20 h in 1 M KOH electrolyte (Inset figure: LSV curves before and after 1000 cycles). (C) Faradaic efficiency of H_2 production for NiCoP-C(TPA)/NF at a current density of -10 mA cm^{-2}	87
Figure 3.13 SEM image of NiCoP-C(TPA)/NF (A) fresh catalyst (B) after stability test 20h EDS mapping of NiCoP-C(TPA)/NF (A') before test and (B') after test stability test in 1M KOH electrolyte.	88
Figure 3.14 High-resolution XPS spectra of NiCoP-C(TPA) of (A-D) before HER test and (E-H) after HER test in the alkaline media solution.	88
Figure 3.15 HER performances of NiCoP-C(TPA)/NF in acidic, neutral and alkaline electrolytes. (A) LSV curves. (B) Tafel plots. (C) Nyquist plots at an overpotential of 200 mV and (D) Multi-current step started at a current density of -20 mA cm^{-2} and ended at -200 mA cm^{-2} with an increment of 20 mA cm^{-2} every 500 sec. (E,F) Chronopotentiometry of NiCoP-C(TPA)/NF at a current density of -100 mA cm^{-2} duration a period of 20 h in (E) 0.5 M H_2SO_4 (pH=0). (F) 1M PBS (pH=7).....	90
Figure 4.1 Schematic illustration for the fabrication of CuOx NWs @NiMnOx NSs/CF electrode.....	105
Figure 4.2 SEM images of the obtained $\text{Cu}(\text{OH})_2$ NWs (A), CuOx NWs@MnOx (B), CuOx NWs@NiO (C) and CuOx NWs@NiMnOx NSs (D) on CF; elemental distributions on CuOx NWs@NiMnOx NSs/CF electrode (inset: enlarged SEM image at scales of 500 nm and 200 nm) (E); and TEM image of CuOx NWs@NiMnOx NSs (F). TEM image with an enlargement scale of 2 nm for MnO_2 crystal in CuOx NWs@MnOx (G), NiO of CuOx@NiO (H) and defect structure of NiMn_2O_4 in the obtained CuOx NWs@NiMnOx NSs.	106
Figure 4.3 TEM images of (A, A') MnOx, (B, B') NiO, and (C, C') NiMnOx NSs. ...	107

Figure 4.4 TEM images of the obtained Ni(OH) ₂ /Mn(OH) ₂ NSs (A, B); TEM images of the obtained CuOx NWs@NiMnOx NSs (D) on CF; and corresponding partial enlarged views (D, E, F); Schematic diagram of edge dislocation (G), screw dislocation (H), lattice distortion and additional active edge sites (I).....	109
Figure 4.5 (A) XRD patterns of Mn(OH) ₂ /CP, Ni(OH) ₂ /CP and Mn(OH) ₂ /Ni(OH) ₂ /CP composite.....	110
Figure 4.6 (A) XRD patterns of CuOx NWs@MnOx/CF, CuOx NWs@NiO/CF, CuOx NWs@NiMnOx NSs/CF. (B-D) XRD pattern of catalysts deposited on carbon paper (CP) substrate (D) NiO/CP (C) MnOx/CP (D) NiMnOx NSs/CP.....	111
Figure 4.7 High-resolution XPS spectra of CuOx NWs@NiMnOx NSs: (A) survey peak, (B) Cu 2p, (C) O 1s, (D) Ni 2p, and (E) Mn 2p spectra.	112
Figure 4.8 High-resolution XPS spectra of (A-C) CuOx NWs@NiO: (A) Cu 2p, (B) O 1s, (C) Ni 2p, and (D-F) CuOx NWs@MnOx: (D) Cu 2p, (E) O 1s, (F) Mn 2p.	113
Figure 4.9 SEM images of CuOx NWs@NiMnOx NSs prepared with different ratios of Ni:Mn in the initial presursors: (A) 4:1 (B) 1:1 (C) 1:4.	114
Figure 4.10 LSV polarization curves in 1.0 M KOH solution for HER over CuOx NWs@NiMnOx NSs/CF electrodes prepared at different Ni/Mn ratios (4:1, 1:1 and 1:4) in the initial presursors (A) and related Tafel plots (B).	114
Figure 4.11 SEM images of CuOx NWs@NiMnOx NSs prepared with different UPED deposition cycles: (A) 500 cycles (B) 1000 cycles (C) 1500 cycles and (D) 2000 cycles.	115
Figure 4.12 LSV polarization curves in the 1.0 M KOH solution for HER over CuOx NWs@NiMnOx NSs/CF electrodes prepared with different UPED deposition cycles (500, 1000, 1500 and 2000 cycles) (A) and the related Nyquist plots at a potential of 0.2 V (B).	115
Figure 4.13 (A) LSV polarization curves for HER over various prepared electrodes at a scan rate of 2 mV/s; (B) Tafel plots; (C) Nyquist plots of various electrodes at an overpotential of 200 mV. (D) Multi-current step test for the CuOx NWs@NiMnOx NSs/CF electrode started from the current density of 10 until 300 mA cm ⁻² with an increment of 50 mA cm ⁻² every 500 s and returned back to 10 mA cm ⁻² after tested at 300 mA cm ⁻² ; (E) Chronopotentiometric curve obtained with the CuOx NWs@NiMnOx NSs/CF electrode in 1.0 M KOH solution with the standard current density of 10 mA cm ⁻²	

² for continuous 60 h test (inset: HER polarization curves before and after the 1000 cycles). (F) Comparison with the reported results on the Ni- and Mn-based electrodes at the standard current density 10 mA cm⁻² in the alkaline media: 20wt%Pt/C (this work), Mn-CoP [3], Mn-NiP₂/CC [10], Mn-Co-P/Ti [21], NiP₂ NS/CC [27], Ni₂P/Ni/NF [39], Ni-P/film [43], CoFe@CoNi [46], Ni₂P nanoparticles [48], NiS₂ NA/CC [41], Ni-Mn₃O₄/NF [31] and Mo-Ni₂P/NF [65]. (CC: carbon cloth; NF: nickel foam).....117

Figure 4.14 Water electrolysis performance of MnOx/CF, NiO/CF, CuOx NWs@MnOx/CF, CuOx NWs@NiO/CF, NiMnOx/CF and CuOx NWs@NiMnOx NSs/CF electrodes (A-B) LSV polarization curves at a scan rate of 2 mV/s in 1.0 M KOH solution: (A) HER and (B) OER. (C-D) Tafel plots (C) HER and (D) OER.118

Figure 4.15 Cyclic voltammetry curves of (A) bare CF (CF), (B) CuOx NWs/CF, (C) CuOx NWs@MnOx/CF, (D) CuOx NWs@NiO/CF, (E) CuOx NWs@NiMnOx NSs/CF collected between a potential range of 0.1-0.3 V (vs RHE) with scan rates of 5, 10, 15, 20, 25, 30 mV/s, respectively, in 1.0 M KOH solution. (F) Dependence of current on the scan rate at different double layer capacitances for the estimation of the electrochemical active surface area.119

Figure 4.16 (A) LSV polarization curves for OER over various prepared electrodes at a scan rate of 2 mV/s; (B) Tafel plots; (C) Nyquist plots of various electrodes at an overpotential of 200 mV. (D) Multi-current step test for the CuOx NWs@NiMnOx NSs/CF electrode started from the current density of 10 until 300 mA cm⁻² with an increment of 50 mA cm⁻² every 500 s and returned back to 10 mA cm⁻² after tested at 300 mA cm⁻²; (E) Chronopotentiometric curve obtained with the CuOx NWs@NiMnOx NSs/CF electrode in 1.0 M KOH solution with the standard current density of 10 mA cm⁻² for continuous 60 h test (inset: OER polarization curves before and after the 1000 cycles). (F) Comparison with the reported results on the Ni- and Mn-based electrodes at the standard current density 10 mA cm⁻² in the alkaline media: NiFe-LDH-US [4], Ni₃FeN-NPs [9], Co²⁺/MnO₂ [20], Ni_{2.0}Mo_{0.26}@NC [26], , Mn₃O₄@NF [40], NiFe@NiO/NF [44], NiO/Ni [44], NS-MnO₂ [49], NiMn LDH/ NiCo₂O₄ [52], selenide-NiMn LDH/GC [63], NiMn LDH/RGO/NF [68], NiMn-LDH/GC [68], Ni₅Mn-LDH/MWCNT [71] (US: ultrasonic treatment; NPs: nanoparticles; NC: nitrogen-doped carbon; NF: nickel foam; LDH: layer double hydroxide; RGO:reduce graphene oxide; GC: glassy carbon; MWCNT: Multi-walled carbon nanotubes)...... 121

Figure 4.17 LSV polarization curves for HER and OER over the CuOx NWs@NiMnOx NSs/CF electrode at a scan rate of 2 mV/s and compared with the noble-metal-based catalysts of Pt/C and RuO₂ in the neutral pH media; (B) Tafel plots corresponding to Fig. 6 (A); (C) Multi-current step test for the CuOx NWs@NiMnOx NSs/CF electrode started from the current density of 10 until 300 mA cm⁻² with an increment of 50 mA cm⁻² every 500 s and returned back to 10 mA cm⁻² after tested at 300 mA cm⁻². (D) Chronopotentiometric curves obtained with the CuOx NWs@NiMnOx NSs/CF electrode in 1.0 M PB solution with the standard current density of 10 mA cm⁻² for continuous 40 h HER and OER tests; (E) Comparison with the reported results on the Ni- and Mn-based electrodes at the standard current density 10 mA cm⁻² for HER in the neutral pH solution: MnMoO₄ NSA/NF [2], Mn-NiO-Ni/Ni-F [8], CoNiP/NF [17], NiP₂/CC [10], Mo-Ni₂P/NF [41], Mn-Ni₂P/CC [10], Ni-Mo-S [47], NiS₂/MoS₂ [51], Mn-Co-P/Ti [21]. (Herein, NF: nickel foam; Ni-F: nickel foam; CC: carbon cloth) (F) Comparison with the reported results on the Ni- and Mn-based electrodes at the standard current density 10 mA cm⁻² for OER in neutral pH solutions: CoP NA/CC [64], Co₂S₄ ultrathin nanosheet [69], Co-Bi NS/G [70], np-Co₉S₄P₄ [67], a-Co₂P [77], Ni(S_{0.5}Se_{0.5}) [79], CuCo₂O₂/NrGO [80], NiCo₂Te₄/PTCDA [72]. (Herein, CC: carbon cloth; G: graphene; PTCDA: perylene-3, 4, 9, 10-tetracarboxylic dianhydride). 123

Figure 4.18 XRD pattern of CuOx NWs@ NiMnOx NSs/CF after HER and OER stability test in alkaline and neutral media solution. 124

Figure 4.19 High-resolution XPS spectra of the CuOx NWs@NiMnOx NSs after the stability test in the alkaline pH solutions for HER and OER: (A) Ni 2p, (B) Mn 2p and (C) Cu 2p. 126

Figure 4.20 High-resolution XPS spectra of the CuOx NWs@NiMnOx NSs after the stability test in the neutral pH solution for HER and OER: (A) Ni 2p, (B) Mn 2p and (C) Cu 2p. 127

Figure 4.21 SEM images of CuOx NWs@NiMnOx NSs catalysts: (A) before test; (B) after HER stability test in 1.0 M KOH solution; (C) after HER stability test in neutral PB solution; (D) after OER stability test in 1.0 M KOH solutions; and (E) after OER stability test in in neutral PB solution. 128

Figure 4.22 Overall water electrolysis in neutral and alkaline solutions. (A) LSV curves obtained during the overall water electrolysis in the two-electrode cell consisting of CuOx

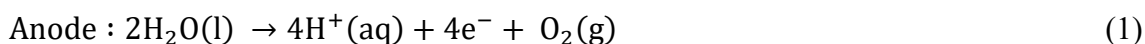
NWs@NiMnOx NSs/CF || CuOx NWs@NiMnOx NSs/CF (-/+) and compared with the Pt/C||RuO₂ (-/+) cell; (B) Chronopotentiometric curves at current density of 10 mA cm⁻² for 40 h continuous test in the alkaline solution (inset: Comparison with the recent reported ones: Ni@NC [1], CoMnCH [7], Ni₅P₄ [13], NiCo₂S₅ [22], Ni₃S₂/NF [38], NiFe LDH/NF [42] and NiCo₂O₄/NF [45]. Herein, NC: nitrogen-doped carbon, CH: carbonate hydroxide, NF: nickel foam). (C) Chronopotentiometric curve at the current density of 10 mA cm⁻² for 24 h continuous test in neutral pH solution (inset: Comparison with the recent reported ones: Ni(S_{0.5}Se_{0.5}) [11], Ni_{0.5}Co_{0.5}P [45], S-NiFe₂O₄ [62], np-Co₃S₄P [67], NiCo₂Te₄/PTCDA [72], and CoO/CoSe₂-Ti [75]. Herein, PTCDA: perylene-3, 4, 9, 10-tetracarboxylic dianhydride)..... 129

Figure 4.23 Theoretical hydrogen and oxygen evolution amounts vs. measured gas evolutions in 1.0 M KOH and 1.0 M PB solutions during the course of electrolysis using CuOx NWs@NiMnOx NSs/CF electrodes in the two-electrode system for overall water electrolysis. 130

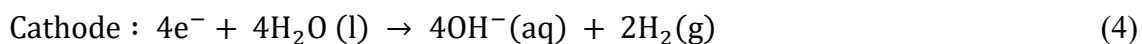
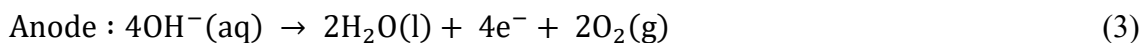
CHAPTER 1 Introduction

Nowadays, electrochemical water splitting is an attractive and environmentally friendly way for pure hydrogen production. It is also a good way for renewable energy storage by converting unstable renewable energy such as solar, wind, and tidal energy to stable hydrogen energy. Many researchers have tried to improve the performance of water electrolyzer and develop novel electrochemical water splitting methods. Electrocatalysts always exhibit high activity in either strong acid solutions or alkaline solutions but low activity in neutral solutions due to high resistance[1, 2]. For different electrolytes, different electrode reactions occur:

In acid solution:



In alkaline and neutral:



Moreover, the factors to affect the performances of electrode materials for water electrolysis include activation energy, gas bubble generation, and diffusion, ion diffusion in the electrolyte, electrolyte concentration, electrolyte/electrode interface resistance and internal resistance, and so on. The overpotential (η) at the standard current density of 10 mA cm^{-2} is generally used to evaluate the performance of electrocatalysts. The lower overpotential means lower energy loss during the water splitting. Moreover, it should be considered the anode and cathode performances together for a water electrolyzer. Thus, a combination of hydrogen evolution reaction (HER) and oxygen evolution reaction (OER) activity is important for the device design[3]. In addition, recent research also focuses on the development of electrocatalysts which can work in a wide pH range to reduce the effect of corrosion in the strong acid and alkaline solutions[4, 5]. However, some of the non-noble metal electrocatalysts are highly active in strong acid, but inactive in the alkaline electrolytes. It is still an important issue to develop high-performance

electrocatalysts for such a purpose. Recently, the fabrication of bifunctional (HER and OER) electrocatalysts for the overall water splitting becomes one of the hot topics since using a single bifunctional HER–OER electrocatalysts can simplify the overall system design and lower the cost[6].

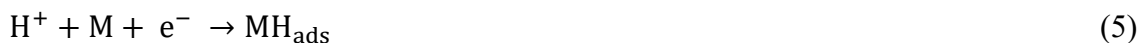
To date, the benchmark electrocatalysts are still the Pt-based material for HER and Ir/Ru-based materials for OER[2, 7]. Recently, various non-precious but highly efficient catalysts such as transition metal carbides, sulfides, and phosphides (for HER), and transition metal oxide and hydroxide (for OER) have been developed as alternatives for the precious metal-based catalysts. Ideally, water splitting electrocatalysts should be set for both HER and OER reactions in the same pH condition[8]. However, since many electrocatalysts have high activity in the acid electrolyte but low activity or instability in the alkaline electrolyte and especially in the neutral electrolyte, or can work for the HER but are not good for the OER, it is a challenge to develop bifunctional electrocatalysts working at a wide pH range and even in seawater [8,9]. Thus, it is important to understand the catalysis mechanisms in various conditions for the development of such almighty catalysts.

1.1 THEORETICAL OF HYDROGEN EVOLUTION

The cathodic reaction in the electrochemical water splitting via two-electron transfer reaction is HER. The HER can be performed in different pH electrolytes based on either the Volmer–Heyrovsky or Volmer–Tafel mechanisms[10, 11]:

Volmer reaction is the combination of proton and surface of catalysts via electrochemical hydrogen atom adsorption.

In acidic electrolyte:



In alkaline electrolyte:



Heyrovsky reaction is electrochemical desorption between hydrogen atom with proton and electron.

In acidic electrolyte:



In alkaline electrolyte:



Tafel reaction is a chemical of hydrogen desorption to produce a hydrogen molecule.



Ideally, the Tafel slope is used to describe the rate-limiting step of HER as follows: Heyrovsky reaction $\sim 40 \text{ mVdec}^{-1}$, Tafel reaction $\sim 30 \text{ mV dce}^{-1}$, and Volmer reaction $\sim 120 \text{ mV dce}^{-1}$. Herein, the structure of electrocatalysts, the applied potential, and the mass transfer could affect the Tafel slope [12, 13].

1.2 THEORETICAL OF OXYGEN EVOLUTION

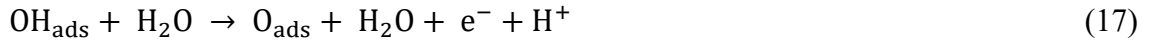
The anodic reaction in electrochemical water splitting is OER. The thermodynamic potential for OER (under the standard condition) is 1.23 V (E^0). The reaction of OER can be determined by the adsorption of OH^- and O species on the surface of catalysts in the alkaline electrolyte[14-17], which include the following steps:



where the active site of catalyst is “*” and “ads” is adsorption on the surface of catalyst. The O_2 production occurs by two pathways. One is directly from the reaction (12). The other follows by the reaction of O_{ads} with OH^- (eq. 13) with the subsequent combining with OH^- (eq. 14). In addition, a neutral pH electrolyte is obtained by:



Herein, the adsorption of O_{ads} , OH_{ads} and OOH_{ads} depends on the Gibbs free energies. The free energy of proton can be calculated by Nernst equation: $\Delta G_{\text{H}} + (\text{pH}) = -k_{\text{B}} - T \ln(10) \times \text{pH}$. In the acidic electrolyte, the OER can occur as follows:



Although the OER mechanisms are differently demonstrated in alkaline and acid electrolytes, OH_{ads} and O_{ads} intermediates always involve in the OER process so that $\Delta G_{\text{O}^-} - \Delta G_{\text{OH}}$ can be used as the descriptor for OER electrocatalysts. To date, the electrocatalysts for OER are generally metal oxides, and the volcano plots for it have been also constructed by $\Delta G_{\text{O}^-} - \Delta G_{\text{OH}}$ for a wide variety of metal oxide surfaces including rutile, perovskite, spinel, rock salt, and bixbyite oxides. From Figure 1.1B on the plot of Gibbs free energy of reactive species and intermediates of the OER versus the reaction coordinate. The blue lines and red lines indicate the energetics of a real catalyst and an ideal catalyst, respectively, at three different electrode potentials. Dashed lines indicate energetics at the electrode potential where all thermochemical barriers disappear (denote as “thermochemical overpotential”); ΔG is the free reaction energy of the two elementary reaction steps[18]. The red ideal case corresponds to a catalyst with the overpotential. Herein, the overpotential is restrictive by the maximum charge of Gibbs-free chemical adsorbed energy. In addition, the theoretical overpotential of OER can be described by the following equation[19]:

$$\eta = \max [\Delta G_1, \Delta G_2, \Delta G_3, \Delta G_4] / e - 1.23[\text{V}] \quad (20)$$

One can see that the experimental overpotentials at 1 mA cm^{-2} for some electrocatalysts are agreement well to the theoretical overpotential volcano when plotted against this simple descriptor.

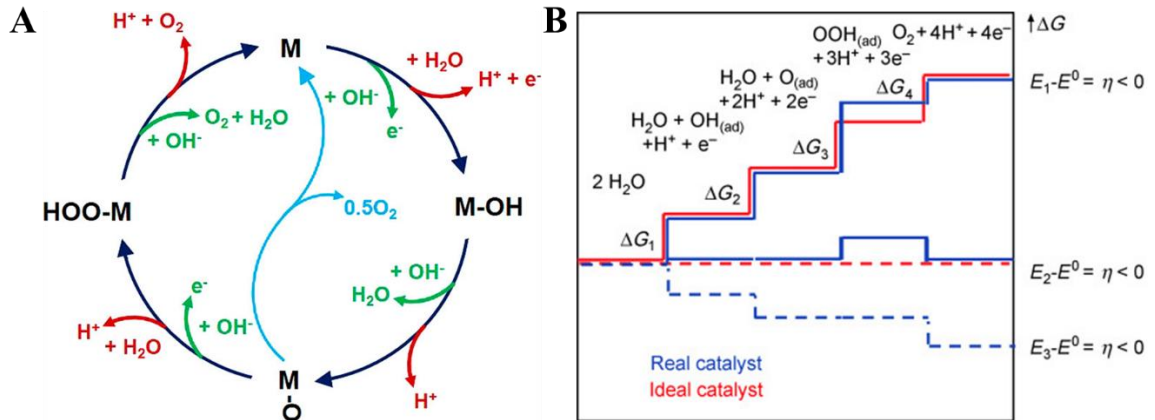
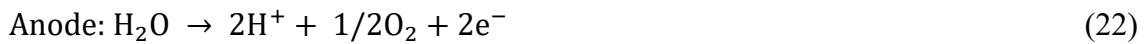
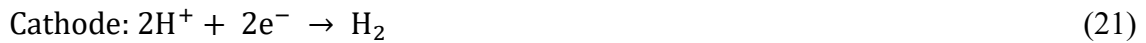


Figure 1.1 (A) OER mechanism for alkaline (red line) and acidic (green line) conditions. The black line indicates that the OER involves the formation of a peroxide (M–OH) intermediate, while the light blue line indicates the direct reaction of two adjacent oxo (M–O) intermediates to produce oxygen[17]. (B) The plot of Gibbs free energy of reactive species and intermediates (horizontal lines) of the oxygen evolution reaction (OER) versus the reaction coordinate[18].

1.3 THEORETICAL OF OVERALL WATER SPLITTING

Bifunctional electrocatalysts can catalyze both HER and OER for the overall water splitting in the same electrolyte solution. By using efficient bifunctional earth-abundant electrocatalysts could reduce the economic problem to some extent. Theoretically, the thermodynamic voltage of water splitting is 1.23 V at 25°C and 1 atm[20, 21]. The reactions in the acidic electrolytes are also different from those in the neutral and alkaline electrolytes.

In the acidic electrolyte,



In the neutral and alkaline electrolytes,



However, total reaction in any electrolytes should be the same:



The overpotential is related to the performance's cathode, anode, and the resistance between the electrodes. The reaction of water splitting is dependent on the cathodic (η_c) and anodic(η_a) overpotentials at the steady-state current density. Additionally, the resistance (η_{other}) is also related to the design of the electrolysis cell. The practical operational voltage (E_{op}) for the overall water splitting can be represented by the following equation:

$$E_{\text{op}} = 1.23 + \eta_a + \eta_c + \eta_{\text{other}} \quad (26)$$

Tafel slope (b) can be used to explain the mechanism of electrode reaction, which can be determined via the overpotential (η) and logarithmically of the current density (j) as indicated by the following Tafel equation ($\eta > 0.05\text{V}$):

$$\eta = a + b \log(j) \quad (27)$$

Herein, when $\eta = 0$, the obtained current density is called exchange current density (j_0), which represents the intrinsic activity of the electrode material under the equilibrium state. High j_0 with a small Tafel slope indicates high activity. In addition, the overpotential record at the standard current density of 10 mA cm^{-2} (the efficiency of solar water splitting device is $\sim 12.3\%$ at 10 mA cm^{-2}) is generally used to evaluate the performance of the electrodes.

1.4 ELECTROCATALYSTS FOR WATER SPLITTING

1.4.1 Electrocatalysts for HER

Noble metal catalysts, especially platinum group metals (PGMs) such as Pt, Ru, Ir, Rh, and Pd are highly active for HER. Among them, Pt is one of the most active catalysts for HER in both acidic and alkaline electrolytes. Since the high cost of Pt needs to be considered, many efforts have been carried out for the development of nanostructured PGMs with controllable sizes and shapes to improve their electrocatalytic performance[22]. It is reported that the surface [1 1 0] of Pt crystal has higher activity than the surfaces of [1 1 1] and [1 0 0] [23]. Therefore, it is important to create more

active surfaces of the Pt crystal could enhance the catalytic activity. Meanwhile, alloying PGMs with other metals can also increase site-specific activity. Moreover, the advantages of alloying of PGMs with other metals could: (i) reduce the cost of catalysts and (ii) increase the activity. However, to decrease the cost of PGMs, as summarized in the following, many alternative non-noble catalysts such as transition metal oxides, transition metal carbides, metal sulfides, selenides, phosphide and metal free catalysts have been developed [24-26].

1.4.1.1 Transition metal Ni-based catalysts

To date, earth-abundant transition metals (TMs) such as Ni, Co, Fe, Mo, W, and Cu have been widely tested as electrocatalysts for HER. Ni-based catalysts are the most widely used ones due to their high conductivity, chemical stability, and low cost. The pristine Ni atom is active in the form of oxidation states like NiO, which showed superior HER performance[27], and the Ni/NiO catalysts (Fig. 1.2) have been considered for HER in the industrial-scale alkaline water splitting device[28]. Moreover, as the Ni is combined with other metals such as Cu and Mo, the obtained Ni-Cu alloys and Ni-Mo alloys exhibited the promoted HER kinetics in the alkaline electrolyte. Ni can be also combined with other noble and non-noble metals

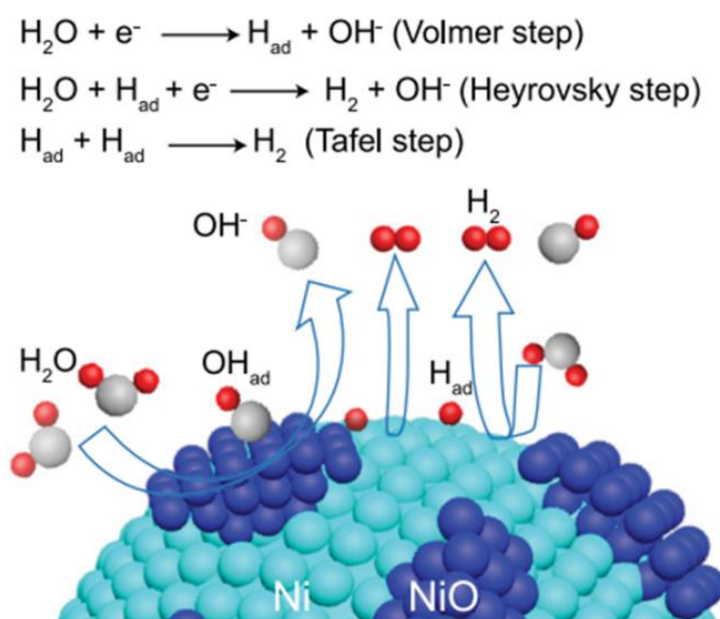


Figure 1.2 Schematic illustration of alkaline HER on Ni-based catalyst.[29]

Nickel-Platinum alloys catalyst: Pt always shows outstanding efficiency for hydrogen generation via the chemisorption on the surface. However, it is expensive and rare. Combining Pt with Ni to fabricate Pt-Ni-based catalyst is an alternative to solve this issue. For example, to enhance the surface activity of Ni-based electrocatalysts, Pt particles were deposited on three-dimensional (3D) porous nickel by an electrodeposition method, which showed a high exchange current density of 9.47 mA cm^{-2} , a low overpotential of 45 mV, and a small impedance resistance[30]. Meanwhile, a Ni-Pt thin film was fabricated via an electrodeposition way with a micelle-assistance process. As a result, the Ni-Pt thin film with 5 at% Pt showed good performance for HER. However, the leaching occurred after the stability test due to corrosion[31]. Moreover, it is found that the fabrication of oxides-hydroxides on the Pt-Ni-based catalysts can assist to break the HO-H bond and promote the desorbing of OH⁻ groups[32]. Chen *et al.* designed nano-sized Pt/NiO@Ni/NF electrocatalysts, in which a NiO layer was combined. The obtained electrocatalysts coated electrode with a low Pt loading (0.1 mg cm^{-2}) required ultra-low overpotential of 34 mV at the standard current density of 10 mA cm^{-2} and a low Tafel slope of 39 mV dec^{-1} , which is even lower than that of the commercial Pt/C coated one. Herein, because of the effect of active sites for the H₂ desorption, the combination of Pt nanocluster and NiO layer greatly promoted the utilization efficiency of Pt, providing more active sites definitely reachable to the reactants[33]. Feng *et al.* [34] synthesized Pt/NiS@Al₂O₃ electrode via a four-step preparation process. Firstly, fabrication of a flower-like Ni₂Al(CO₃)₂(OH)₃ nanosheets with a hetero-nanostructure by a hydrothermal method. Then, a sulfurization under H₂ atmosphere was performed to obtain a NiS@Al₂O₃ electrode, in which the NiS nanoparticles were covered on the Al₂O₃ nanosheets with a hetero-interface. Thereafter, the electrode was soaked in an acidic solution to produce the porous γ -Al₂O₃ nanosheets, and finally, Pt was doped to improve electrocatalytic activity and atomic efficiency. As a result, the obtained Pt/NiS@Al₂O₃ catalyst showed a very low overpotential of 34 mV@ 10 mA cm^{-2} with a small Tafel slope of 35 mV dec^{-1} . Herein, it is found that the loading of Pt led to a low onset overpotential via a high redox reaction. Moreover, the layer of the well-dispersed γ -Al₂O₃ nanosheets also improved HER performance and increased the specific surface area[34]. Guan *et al.* fabricated Pt atom doped Ganoderma-like MoS₂/NiS₂ with a heterostructure. Herein, the strong interaction between NiS₂ and MoS₂ resulted in a high conductivity while the

surface area activity was greatly increased by the doping of Pt atoms. The nanostructured Pt@MoS₂/NiS₂ electrocatalyst with 1.8 at% Pt exhibited ultralow overpotential of 34 mV with a Tafel slope of 40 mV dec⁻¹. In addition, a long-term duration stability (< 5% drop of performance) was also achieved[35].

Nickel-based bi/tri-metal alloys catalysts: Transition metal oxides (TMOs) such as NiO, CoO_x, and MnO₂ have low toxicity, low cost, and high catalytic performance. Xing *et al.* [36] fabricated nickel hydroxide@nickel film on the carbon cloth (CC) substrate (Ni(OH)₂@Ni/CC) via a two-step electrodeposition method. Due to the synergistic effect of Ni(OH)₂ nanosheets and Ni nanoparticles, a cell voltage of 1.58 V@10 mA cm⁻² with excellent long-term stability for overall water splitting was achieved. Zhao *et al.*[29] designed bi-component nanocrystal of Ni/NiO on the electrode with a hetero-surface structure, which showed high efficient and stable activity toward HER in the alkaline solution. Based on the DFT calculations, it is found that NiO had an outstanding low energy barrier for the decomposition of H₂O into H_{ad} and OH_{ads} while H₂ molecule can be generated on the Ni surface. Bimetal alloys based on Ni metal incorporating with other metals (Ni-M (M is Fe, Co, Mn, or Mo)) also exhibited outstanding high performance for HER. For example, Chen *et al.*[37] successfully obtained a self-templated MoNi₄ nanocrystal and MoO_{3-x} coated Ni foam via a one-step solvothermal method, in which Ni²⁺ was generated on Ni foam by mild acid solution treatment and then combined with Mo to grow the MoNi₄/MoO_{3-x} on the Ni foam. The optimum catalysts exhibited an ultralow overpotential of 17 mV@10 mA cm⁻² and a low overpotential 114 mV at the extremely high current density of 500 mA cm⁻². Moreover, the MoNi₄/MoO_{3-x} electrode can serve as the bifunctional electrocatalysts with a cell voltage 1.6 V at 30 mA cm⁻² for overall water splitting. The Mn species has various forms of oxidation state. It is reported that the Mn₃O₄ can provide highly active sites for the splitting of H₂O molecules [38]. Li *et al.*[38] coated Ni-Mn₃O₄ nanocomposites on Ni foam substrate via a hydrothermal process, which exhibited high electrocatalytic performance for the generation of H₂ at a low overpotential of 91 mV@10 mA cm⁻² in the alkaline condition with long-term stability. The NiCo mixed oxide is another good electrocatalysts with high electroconductivity and redox properties. Wei and coworker [39] fabricated the oxygen-deficient NiCo₂O₄ on the carbon paper (CP) via a hydrothermal process followed by the calcination in Ar atmosphere. The morphology of NiCo₂O₄ showed well-defined

nanowire arrays with full covering on the CP substrate. The NiCo₂O₄ electrocatalyst exhibited highly electrocatalytic activity with a low overpotential, long duration stability and 99% of Faradaic efficiency due to the reducing adsorption of H₂O molecules by the oxygen vacancies.

Nickel-based Phosphide catalysts: Metal phosphide is another type of electrocatalysts with high performance for HER with low overpotential. Ni-based phosphides have been widely investigated and metal mixed phosphides always exhibited higher activity than single metal phosphides. Moreover, the different facets could show different surface energies, thereby exhibiting different performances. For example, for the NiCo mixed phosphides (NiCoP), the durability of HER activity based on the surface energy followed the order of NiCoP (111) > NiCoP (001)-CoP-t > NiCoP (100) > NiCoP (001)-NiP-t based on the ΔG^{ad} (NiCoP facets are shown in Figure 1.3). The NiCoP (111) facet exhibited the highest activity for HER at 1 atm[40]. Thus, the NiCoP electrocatalyst with different morphologies showed different HER activities[41]. Liu *et al.*[42] fabricated oxygen doped porous NiCoP nanowires on Ni foam, and found that the H-NiCoP NWAs/NF had a high activity for HER with fast charge transfer and long-term stability in the neutral and alkaline solutions. Especially, it exhibited an overpotential as low as 51 mV@10 mA cm⁻² with a Tafel slope of 79.2 mV dec⁻¹ in the neutral electrolyte. Herein, the hydrogen atom binding energy on Co and P sites greatly enhanced HER activity. Ma and coworker[43] reported nanocube-like 3D-NiCoP electrocatalysts prepared by a hydrothermal method followed with a phosphorization process, which displayed high performance with a low overpotential as well as low Tafel slope and good stability in the acidic and alkaline solutions. Cai *et al.*[44] also synthesized NiCoP/NF electrocatalyst for HER by a three-step process, which showed a whisker nanowire structure on the nanosheet with high surface area activity. Zhang *et al.*[45] constructed a hallow-on-hallow NiCoP nanostructure (HiHo-NiCoP) using a MOF template, in which the synthesis started by using ZIF-67 nanopolyhedrons to induce the formation of layer double hydroxide (LDH), leading to a yolk-shell structure (ZIF-67@NiCo-LDH nanopolyhedrons), and then carbonization of organic ligands of ZIF-67 was performed to form carbon species in it and finally the HiHo-NiCoP electrode was obtained by a phosphorization process. This catalyst exhibited high efficiency toward HER with increased surface activity and superior mechanical robustness to reduce the corrosion even in the strong pH electrolyte

solution.

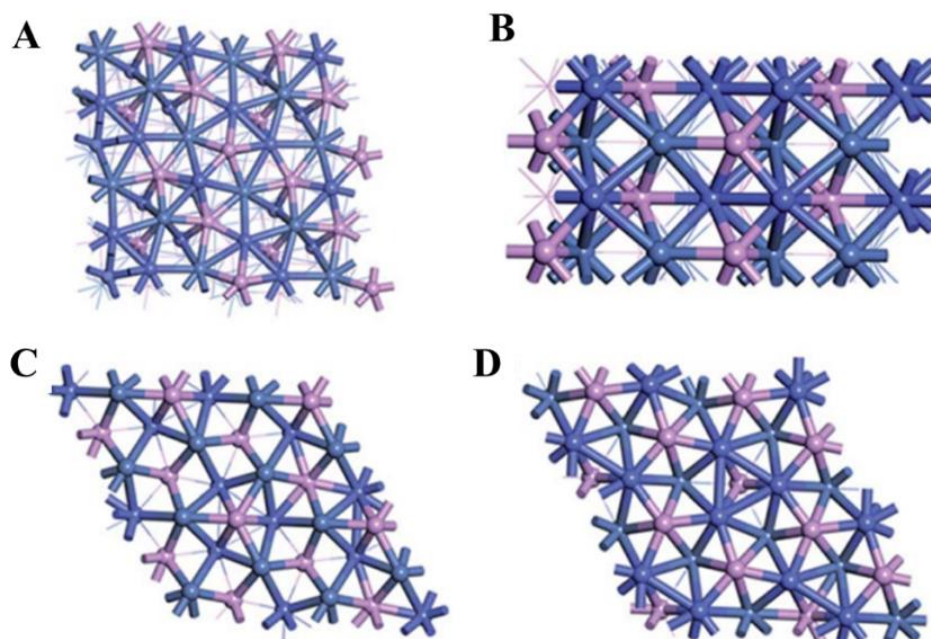


Figure 1.3 The NiCoP facets: (A) (111); (B) (100); (C) (001)- NiP-t; and (D) (001)-CoP-t.[41]

1.4.2 Electrocatalysts for oxygen evolution reaction

Oxygen evolution reaction (OER) is a complex four-electron oxidation process. The Ir and Ru-based catalysts are the benchmark ones for OER with an activity order of $\text{IrO}_2 \ll \text{RuO}_2 < \text{Ir} \ll \text{Ru}$. Due to their high-cost and rareness, transition metal-based catalysts Ni, Co, and Mn-based ones are now widely investigated as alternatives. Tuning the catalyst nanostructure for the improvement of the catalysis performance has become the main way for such OER catalysts area[21].

1.4.2.1 Transition metal-based catalysts for OER

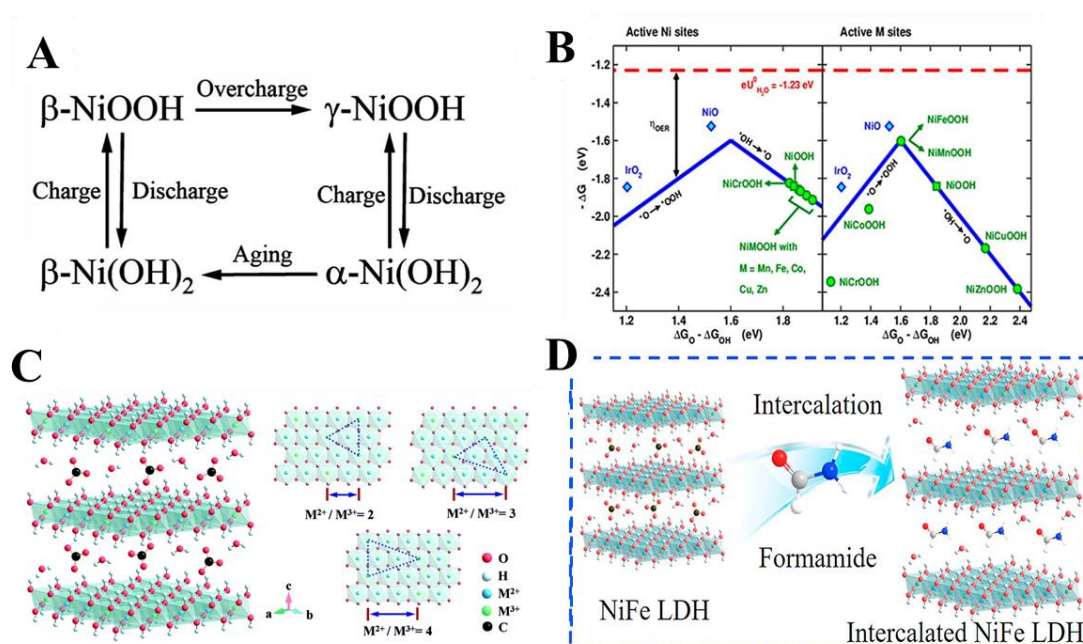


Figure 1.4 (A) Bode's diagram for Ni(OH)₂-NiOOH redox transformations.[46] (B) Sabatier-type volcano plots for Ni-based oxyhydroxide sites doped with transition metals.[47] (C) Scheme of LDH structure.[48] (D) Intercalation/exfoliation LDH.[49]

Ni-based catalysts: Nickel-oxides and Ni-(oxy) hydroxides (e.g., NiOx, Ni(OH)₂, and NiOOH) have been widely used for OER. Bode's diagram (Figure 1.4A) is generally adopted to illustrate the Ni-based redox transformations, in which γ -NiOOH can be changed to β -NiOOH and β -NiOOH could be more active for OER. To enhance the OER catalytic activity, design unique morphology with a special nanostructure is important for the increase of surface area activity, and shortens the pathway for mass diffusion and charge transfer. Babar and coworkers[50] fabricated a self-supported 3D NiO on NF via a thermal oxidation method, which exhibited an overpotential of 310 mV@10 mA cm⁻² with a Tafel slope of 54 mV dec⁻¹ and excellent long-term stability for OER. Jin and coworkers [51] illustrated the synergistic function of Mo- and Fe- modified Ni(OH)₂/NiOOH catalyst. The modified catalysts outperformed low overpotential and long-term stability even at high current density. Based on the DFT calculations, it is found that the modified NiOOH had increased adsorption ability and enhanced interaction strength with O_{ad} for OER. Besides, the combination of Ni with other metals such as Fe

also resulted in superior OER activity (Figure 1.4B). Li *et al.*[52] established NiFe oxide on the Ni foam substrate by a hydrothermal method. The optimum NiFe oxide electrode of Ni_{0.77}Fe_{0.23} had a flower-like nanosheet structure, which exhibited the lowest overpotential of 225 mV in an alkaline electrolyte with enhanced kinetic activity. Recently, the Ni-Mn based bimetallic oxides were also investigated for OER. Mn species have various oxidation states such as Mn²⁺, Mn³⁺, and Mn⁴⁺, in which the Mn³⁺ has a higher activity for OER. He *et al.*[53] reported Ni and Mn oxide-based bifunctional electrocatalysts for OER and ORR, and found that NiMnO₃/NiMn₂O₄ hybrid oxides showed the lowest overpotential of 380 mV with a smallest Tafel slope, which was much better than the single oxides since more active sites were generated in the mixed oxide-based in the turn over frequency (TOF) analyses. Qin *et al.*[54] coupled Ni-NiMn₂O₄ with N-dope carbon nanotube (NCNT/Ni-NiMn₂O₄/Ni foam) on the electrode by a hydrothermal treatment under Ar/NH₃ atmosphere, which exhibited a low overpotential of 300 mV in 1 M KOH solution with long-term stability.

Layered double hydroxide-based catalysts for OER: In the crystal structure of layered double hydroxide (LDH), the transition metal species situated in the center of the layered-stacking octahedron crystal structure with the oxygen as MO₆. The two-dimensional octahedron crystal structure of LDHs can be expressed as a chemical formula of [M_{1-x}²⁺M_x³⁺(OH)₂]^{x+}[A_{x/n}]_n·mH₂O, where metal divalent cations (M²⁺ as Co²⁺, Ni²⁺, Mn²⁺, Fe²⁺) and metal trivalent cations (M³⁺ as Fe³⁺, Mn³⁺) are compensated by the solvate anions of Aⁿ⁻. In general, the bonding of MO₆ in the bulk LDHs with low electron transfer ability could interrupt the OH⁻ anion to adsorb O atom of surface for the formation of -OOH species (Figure 1.4C)[48, 55]. The bulk LDH catalysts always have low conductivity as well as ion transmission rate to limit OER activity. To solve these issues, the interlayer spacing and crystal size can be tuned. It is found that the binary transition metal NiFe-LDH exhibited higher activity than NiCo and CoCo LDHs[56]. Lu *et al.*[57] prepared NiFe-LDH nanoplates on the skeleton of Ni foam (NiFe-LDH NPs/NF), in which the Ni(OH)₂-NiOOH redox couple has cooperated with the Fe(III) ions. It exhibited an overpotential as low as 230 mV. Li *et al.*[49] *in-situ* intercalated NiFe LDH based electrocatalysts on the electrode(Figure 1.4D) by an ultrasonic method so that the overpotential decreased up to 210 mV. Lu and coworkers[58] synthesized ternary NiFeMn-LDHs with a flower-like structure uniformly coated on the carbon paper

substrate. Herein, Mn^{4+} doping on NiFe LDH increased the electrochemical double-layer capacitance (C_{dl}), which is related to the electrochemical surface area active (ECSA). Moreover, the extraordinary structure and the synergistic effect of three metal species promoted catalytic activity, conductivity, and charge transfer. Meanwhile, Sasaki group [59] studied the synergistic function of Ni and Mn species in the NiMn LDH nanoplatelets supported on graphene oxide (GO/rGO), in which the interlayer space of LDH was expanded by chloride anions (Cl^-). This catalyst exhibited high activity with a low overpotential of 260 mV and increased electro-conductivity. Jia *et al.*[60] also fabricated binary Ni_5Mn LDH/MWCNT hybrid electrode by a chemical bath deposition method, in which Ni_5Mn LDH covered MWCNT very well. They considered that the binary metal hydroxide coupling with carbon-based materials can result in outstanding catalytic activity ($\eta_{10} = 350$ mV) due to the fast electron transfer to the substrate.

1.4.3 Bifunctional electrocatalysts for overall water splitting

1.4.3.1 Transition metal Ni-based compounds

Ni-based electrodes with various Ni compound forms such as oxide, hydroxide, phosphide, sulfide, and carbide have been found to have either high HER or OER performances. Thus, they can be used as the bifunctional electrodes for the overall water splitting.

Ni-oxide based catalysts: Hybridizing of nickel-oxide and nickel hydroxide materials could assist the ion transfer balance between them. Zhang *et al.*[61] designed a bifunctional Ni-based electrocatalyst by loading Ni_5Fe LDH on Ni foam, and found that an ultrathin layer of Ni_5Fe LDH with large space can enhance the electron transfer, and when it was applied in a two-electrode system with alkaline electrolyte, a cell voltage of $1.59\text{V}@10$ mA/cm² was achieved for the water electrolysis.

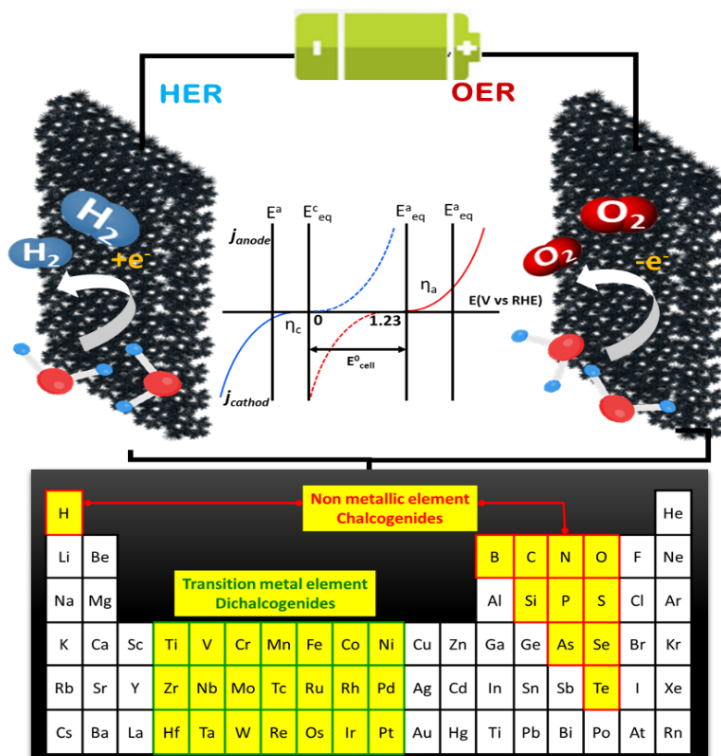


Figure 1.5 Schematic illustration of bifunctional electrocatalyst for overall water splitting.

Bifunctional ternary metal composite electrocatalysts were also synthesized for the overall water splitting. Qin *et al.* [62] synthesized NiFeMo trimetallic thin film on Ni foam via a hydrothermal process followed by annealing, which showed high activities in either HER ($\eta_{10} = 45$ mV) or OER ($\eta_{10} = 238$ mV). When it was applied in a two-electrode system NiFeMo(-)||NiFeMo(+) with an alkaline solution, a low cell voltage of $1.45\text{V}@10$ mA/cm² was achieved. Meanwhile, combining two or more composites could also improve the performance of electrodes for overall water splitting. Wang *et al.*[63] grew NiFe LDH ultrathin sheets on the NiCo₂O₄ nanowires by a two-step hydrothermal synthesis process, which displayed excellent catalytic activities for HER and OER, and a cell voltage of $1.6\text{ V}@10$ mA/cm² was obtained when it was used on a two-electrode water electrolyzer. Gong *et al.*[64] prepared grass mat-like NiCo₂O₄ nanowires@CoMoO₄ nanosheets on Ni foam substrate by a hydrothermal method with a further annealing process, which presented overpotentials of 121 mV for HER and 265 mV for OER in the alkaline condition and resulted in a cell voltage of $1.55\text{V}@10$ mA/cm² when it was used on a two-electrode water electrolyzer.

Recently, the researches on the bifunctional electrocatalysts working in neutral pH

media conditions are increasing. Liu *et al.*[65] fabricated sulfur-incorporated nickel ferrite ultra-small nanoparticle built nanosheets vertically grown on Ni foam (S-NiFe₂O₄/NF) by co-deposition of Ni²⁺ and Fe³⁺ ions followed the annealing under Ar atmosphere, in which the sulfur doping increased the conductivity and the nanosheet structure provided more active sites for HER and OER. This bifunctional electrocatalyst showed high activity in a wide pH range with cell voltages of 1.65 and 1.95V@10 mA/cm² in the alkaline and neutral electrolytes, respectively. Tao *et al.*[66] designed a new bifunctional electrocatalyst by combining nickel cobaltite telluride (NiCo₂Te₄) nanoclusters with perylene-3,4,9,10-tetracarboxylic dianhydride (PTCDA). The obtained NiCo₂Te₄/PTCDA electrocatalysts exhibited extremely high efficiency for HER and OER with overpotentials of 60 and 120 mV at the standard current density of 10 mA cm⁻², respectively. Herein, the PTCDA effective had a perylene core (O=C-O-C=O) and two anhydrides with excellent chemical stability, which can promote electron carrier mobility. When it was used for overall water spitting in near-neutral pH electrolyte (1M PBS), a cell voltage of 1.55V@10 mA/cm² was achieved. Liu et al. [67] synthesized Co₂P NPs@NiCo₂O₄ spheres growing on FTO. The hybrid catalysts delivered the bifunctional electrocatalysts for overall water splitting.

Table 1.1 Summary of HER activities of Ni-based electrocatalysts in a wide pH range.

Catalyst	Electrolyte	Mass loading	$\eta @ j$ mA cm ⁻² (mV)	Tafel slope (mV dec ⁻¹)	Stability	Substrate	Ref.
Ni-Pt	0.5 H ₂ SO ₄	N/A	90@10	41	N/A	Si substrate	[31]
3D-NiCoP	0.5 H ₂ SO ₄	N/A	80@10	37	16h	Nickel foam (NF)	[43]
	1M KOH		107@10	79	16h		
NiCo ₂ P _x nanowires	0.5 H ₂ SO ₄	5.9 mg cm ⁻²	50@10	59.6	30h	Carbon felt (CF)	[68]
	1M KOH		58@10	34.3	30h		
	1MPBS		63@10	63.3	30h		
Pt/NiO@Ni/NF	1M KOH	~2.0 mg cm ⁻²	34@10	39	24h	Nickel foam (NF)	[33]
Ni(OH) ₂ @Ni/CC	1M KOH	2.8 mg cm ⁻²	68@10	97	40h	Carbon cloth (CC)	[36]
MoNi ₄ /MoO _{3-x}	1M KOH	N/A	17@10 52@100	36	20h	Nickel foam (NF)	[69]
Ni-Mn ₃ O ₄ /NF	1M KOH	N/A	91@10	110	20h	Nickel foam (NF)	[70]
Ar-NiCo ₂ O ₄	1M KOH	N/A	104@10	112	24h	Carbon paper (CP)	[39]
H-NiCoP NWAs/NF	1M KOH	10 mg cm ⁻²	44@10	38.6	30h	Nickel foam (NF)	[71]
	1M PBS		51@10	79.2	30h		
Nest-like NiCoP/CC	1M KOH	2 mg cm ⁻²	62@10	38.5	15h	Carbon cloth (CC)	[72]
Ni/NiP	1M KOH	~10.58 mg cm ⁻²	130@10	106	24h	Nickel foam (NF)	[73]
NiFeO _x /CFP	1M KOH	1.6 mg cm ⁻²	79@10	51	100h	Carbon paper (CP)	[74]
Ni ₂ P/NF	1M KOH	N/A	98@10	72	20h	Nickel foam (NF)	[75]
Mn-NiP ₂ /CC	0.5M H ₂ SO ₄	4.4 mg cm ⁻²	69@10	45	20h	Carbon cloth (CC)	[76]
	1M KOH		97@10	61	24h		
	1M PBS		107@10	91	24h		
NiP ₂ NS/CC	0.5M H ₂ SO ₄	4.3 mg cm ⁻²	75@10	51	57h	Carbon cloth (CC)	[77]
	1M KOH		102@10	65	57h		
CoFe@CoNi	1M KOH	~2.15 mg cm ⁻²	82@10	96	60h	Nickel foam (NF)	[78]
Mo-Ni ₂ P/NF	0.5M H ₂ SO ₄	1.13 mg cm ⁻²	67@10	77	2500	Nickel foam (NF)	[79]
	1M KOH		78@10	109	cycles		
	1M PBS		84@10	85	2500cycles		
					2500cycles		
NiCoP/rGO	1M PBS	0.15 mg cm ⁻²	124@10	91	18h	Carbon fiber paper	[80]
NiCo ₂ P _x /CF	1M PBS	5.9 mg cm ⁻²	63@10	63.3	30h	Cu foam (CF)	[81]
Ni _{0.89} Co _{0.1} Se ₂ MNSN/NF	1M PBS	2.62 mg cm ⁻²	82@10	78	30h	Nickel foam (NF)	[82]
NiCoP-C(TPA)/NF	0.5M H ₂ SO ₄	~20.13 mg cm ⁻²	94@10	81.1	20h	Nickel foam (NF)	[83]
	1M KOH		78@10	73.4	20h		
	1MPBS		248@10	112.5	20h		
CuO _x NWs@NiMnO _x	1M KOH	N/A	71.6@10	62.7	60h	Cu foam (CF)	[84]
NSs	1M PB		80.7@10	67.9	40h		
MnMoO ₄ NSA/NF	0.5 H ₂ SO ₄	1.17 mg cm ⁻²	89@10	61	1000cycles	Nickel foam (NF)	[85]
	1M KOH		105@10	113	1000cycles		
	1M PBS		161@10	151	1000cycles		
Mn-NiO-Ni/Ni-F	1M PB	0.25 mg cm ⁻²	107@10	121	~50h	Nickel foam (NF)	[86]
	Seawater (pH~8.3)		140@10	N/A	14h		
CoNiP/NF	0.5M H ₂ SO ₄	N/A	60@10	39	24h	Nickel foam (NF)	[87]
	1M KOH		155@10	115	24h		
	1M KPi		120@10	103	24h		

Table 1.2 Summary of OER activities of Ni-based electrocatalysts in a wide pH range.

Catalyst	Electrolyte	Mass loading	$\eta @ j$ mA cm ⁻² (mV)	Tafel slope (mV dec ⁻¹)	Stability	Substrate	Ref.
Ni(OH) ₂ @Ni/CC	1M KOH	2.8 mg cm ⁻²	460@10	168	20h	Carbon cloth (CC)	[36]
NiO/NF	1M KOH	N/A	310@10	54	24h	Nickel foam (NF)	[50]
NiFe-LDH	0.1M KOH	N/A	230#10	50	10h	Nickel foam (NF)	[57]
NiFe LDH	1M KOH	N/A	265@10	50	16h	Carbon rod (CR)	[49]
NiFe LDH-US	1M KOH	N/A	203@10	42	16h	Carbon rod (CR)	[49]
NiO@NiFe LDH-US	1M KOH	N/A	210@10	72	50h	Nickel foam (NF)	[88]
NiFeMn LDH	1M KOH	0.2 mg cm ⁻²	262@10	47	15h	Carbo fiber paper (CFP)	[58]
NiMn LDH/rGO	1M KOH	N/A	260@10	46	N/A	Glassy carbon (GC)	[59]
Ni ₅ Mn LDH/MWCNT	1M KOH	0.283 mg cm ⁻²	350@10	83.5	30000s	Rotating disk (RDE)	[60]
NiMn LDH/NiCo ₂ O ₄	1M KOH	5.4 mg cm ⁻²	310@10	99	8h	Nickel foam (NF)	[89]
Ni _{2.0} Mo _{0.26} @NC	1M KOH	5 mg cm ⁻²	310@10	62.7	10h	Rotating disk (RDE)	[90]
MoFe:NiOOH/Ni(OH) ₂	1M KOH	N/A	~280@10	47	50h	Nickel foam (NF)	[51]
Ni _{0.77} Fe _{0.23} oxide	1M KOH	N/A	225@10	55	12h	Nickel foam (NF)	[52]
NiMnO ₃ /NiMn ₂ O ₄	1M KOH	2.5 mg cm ⁻²	~380@10	73.3	24h	Glassy carbon disk (GCE)	[53]
NCNT/Ni-NiFe ₂ O ₄	1M KOH	0.21 mg cm ⁻²	140@10	85	20000s	Nickel foam (NF)	[54]
NCNT/Ni-NiMn ₂ O ₄	1M KOH	0.21 mg cm ⁻²	188@10	76	20000s	Nickel foam (NF)	[54]
CuO _x NWs@NiMnO _x NSs	1M KOH	N/A	225@10	80	60h	Cu foam (CF)	[84]
	1M PBS		390@10	101.3	40h		
Ni ₃ N NA/CC	1M KHCO ₃	1.8 mg cm ⁻²	540@20	162	12h	Carbon cloth (CC)	[91]
Ni ₃ N@Ni-Ci NA/CC	1M KHCO ₃	1.8 mg cm ⁻²	400@20	143	12h	Carbon cloth (CC)	[91]
NiCo ₂ O ₄ /CC	1M KHCO ₃	1.7 mg cm ⁻²	339@10	91	20h	Carbon cloth (CC)	[92]
NiCo ₂ O ₄ @Ni-Co-Ci/CC	1M KHCO ₃	N/A	309@10	156	N/A	Carbon cloth (CC)	[92]
Ni-Bi/CC	0.1M K-Bi	N/A	470@10	107	25h	Carbon cloth (CC)	[93]
NiO _x -Cat/GC	0.2M K-Ci	N/A	~600@1.15	N/A	60000s	Glassy carbon	[94]

Table 1.3 Summary of bifunctional activities of Ni-based electrocatalysts for overall water splitting in a wide pH range.

Catalyst	Electrolyte	Mass loading	Cell voltage@ j mA cm ⁻² (V)	Stability	Substrate	Ref.
NiCoFeB nanochain	~0.5 H ₂ SO ₄	0.5 mg cm ⁻²	1.6@32.8	20h	Carbon fiber paper (CFP)	[95]
	1M KOH		1.81@10	20h		
CoNi/CoFe ₂ O ₄ /NF	1MKOH	~2 mg cm ⁻²	1.57@10	48h	Nickel foam (NF)	[78]
NiO-Ni ₃ S ₂	1M KOH	N/A	1.57@10	20h	Nickel foam (NF)	[96]
Ni(OH) ₂ /Ni ₃ S ₂	1M KOH	4.8 mg cm ⁻²	1.64@10	120h	Nickel foam (NF)	[97]
Mo/Mn-Ni _x S _y /NF	1M KOH	7.67 mg cm ⁻²	1.45@10	24h	Nickel foam (NF)	[98]
Ni-Fe-P/NF	1M KOH	N/A	1.58@10	24h	Nickel foam (NF)	[99]
NP-NiCo ₂ O ₄	1M KOH	~1.2 mg cm ⁻²	1.63@10	5h	Nickel foam (NF)	[100]
NiFeMo	1M KOH	1.6 mg cm ⁻²	1.45@10	50h	Nickel foam (NF)	[62]
NiFe LDH/NiCo ₂ O ₄	1M KOH	4.9 mg cm ⁻²	1.60@10	12h	Nickel foam (NF)	[63]
NiCo ₂ O ₄ @CoMoO ₄ /NF	1M KOH	N/A	1.55@10	12h	Nickel foam (NF)	[64]
NiFe/NiCo ₂ O ₄	1M KOH	1 mg cm ⁻²	1.67@10	10h	Nickel foam (NF)	[101]
Ni ₅ P ₄	1M KOH	13.9 mg cm ⁻²	1.7@10	20h	Ni foil	[102]
NiMo HNEs/TiM	1M KOH	N/A	1.64@10	10h	Ti mesh	[103]
NiCo-NiCo ₂ O ₄ @NC	1M KOH	3 mg cm ⁻²	1.44@20	50h	Glassy carbon (GC)	[104]
Ni _x Co _{3-x} S ₄ /Ni ₃ S ₂ /NF	1M KOH	N/A	1.53@10	200h	Nickel foam (NF)	[105]
S-NiFe ₂ O ₄ /NF	1M KOH	N/A	1.65@10	24h	Nickel foam (NF)	[65]
	1M PBS		1.95@10	24h		
NiCo ₂ Te ₄ /PTCDA	1M PBS	N/A	1.55@10	30h	Rotating ring disk electrode (RRDE)	[66]
CuO _x NWs@NiMnO _x NSs	1M KOH	N/A	1.62@10	40h	Cu foam (CF)	[84]
	1M PBS		1.75@10	24h		
Ni(S _{0.5} Se _{0.9}) ₉	1M PBS	0.75 mg cm ⁻²	1.87@10	12h	Nickel foam (NF)	[106]
Ni _{0.1} Co _{0.9} P	1M PBS	0.58 mg cm ⁻²	1.89@10	20h	Carbon paper (CP)	[107]
NiP ₂ /CC	1M PBS	3.8 mg cm ⁻²	1.65@10	14h	Carbon cloth	[108]

1.5 SUBSTRATES FOR SUPPORT ELECTROCATALYSTS FOR WATER SPLITTING

The electrocatalysts are always supported on conductive substrates such as Ni foam (NF), carbon cloth (CC), carbon paper (CP), copper foam (CF), glassy carbon disc (GC), FTO, and stainless-steel for water electrolysis. There are two main ways to support electrocatalysts. One is to coat the slurry composed of electrocatalyst powders and binder additive on the substrate. However, the performance of the electrocatalysts could drop to some extent since the binder could block some active sites. Moreover, the coated electrocatalysts could be peeled off from the substrate surface after a long-term test since the generated gas bubble could reduce the adhesion strength in the strong pH solutions. The other one is to prepare electrocatalysts on the conductive substrates. In this case, the contact between catalyst and substrate should be much stronger so that the peeling-off problems of electrocatalysts can be solved. Thus, many pieces of research are focusing on the development of 3D porous nanostructured electrocatalysts with a high surface area on the substrate[109-111].

Ni foam (NF) support is widely used for the support of various electrocatalysts. The hydrothermal method is generally used for the synthesis of nanostructured active electrocatalysts directly on the NF by the control of chemical compositions in the precursors. However, before use, NF should be pretreated with hydrochloric acid (HCl) solution to remove the surface oxide layer. To date, various electrocatalysts have been successfully grown on the NF. For example, Li. *et al.*[112] fabricated NiCo precursor on the NF substrate via a hydrothermal synthesis process, and then performed a phosphorization process to achieve a NiCoP nanosheet array structure on the NF substrate. Han *et al.*[87] directly synthesized CoNiP with nanosheet structure uniformly on NF (CoNiP@NF) by a hydrothermal method. Li and coworkers [78] obtained CoNi/CoFe₂O₄/NF electrode with a flower-like unique structure using a three-step synthesis method, in which CoFe(OH)_x was grown on NF by a hydrothermal method at first and then, it was changed to oxide form (CoFe₂O₄) by calcination, and finally a bimetal CoNi layer was coated on the CoFe₂O₄/NF via an electrodeposition method. These catalysts with the unique structure exhibited high activities for both HER and OER. When it was used as the bifunctional electrocatalysts, a cell voltage of 1.57 V@10 mA/cm² was obtained with high-performance stability.

Cu foam (CF) substrate is another widely used electrocatalyst supporter, on which Cu nanowires can be easily generated to provide any additional supporting area or serve as the electrocatalysts directly. For example, Lu *et al.*[113] fabricated Cu nanowires on CF directly (CuO nanowires/CF), which exhibited a low overpotential of 430 mV at 100 mA/cm² current density for OER. Moreover, the CuO nanowires/CF can be phosphorized to Cu₃P/CF for HER. These two CuO/CF and Cu₃P/CF electrodes can be applied to the two sides of the water electrolyzer for the overall water splitting in alkaline electrolytes. Zhou *et al.*[114] fabricated CuO nanowires on CF at first and then covered Co₃O₄ nanorods (NRs) on them to obtain CuO_x@ Co₃O₄ NRs core@shell 3D structure electrocatalysts, which showed large electrochemical surface area activity and synergistic effect with low overpotentials and low Tafel slopes for either HER or OER and can be used as the bifunctional catalyst toward overall water splitting in the alkaline electrolyte. Rong *et al.*[115] fabricated Co-doped Cu₃P on Cu foam using a self-supporting method, which also exhibited excellent performance and long duration stability for either HER or OER and a low cell voltage of 1.55 V @10 mA/cm² in a two-electrode water electrolyzer.

1.6 PARAMETERS to evaluate the catalysis performance

Overpotential at the standard current density, Tafel slope and exchange current density (j_0), double layer capacitance (C_{dl}) and electrochemically active surface area (ECSA), long-term stability test, and Faradaic efficiency (FE) are the basic parameters to evaluate the electrocatalysis performance.

1.6.1 Overpotential

Overpotential is an activity parameter at a defined current density, but the iR compensated overpotential ($\eta_{iR \text{ free}}$) is generally used to explain the real overpotential at first.

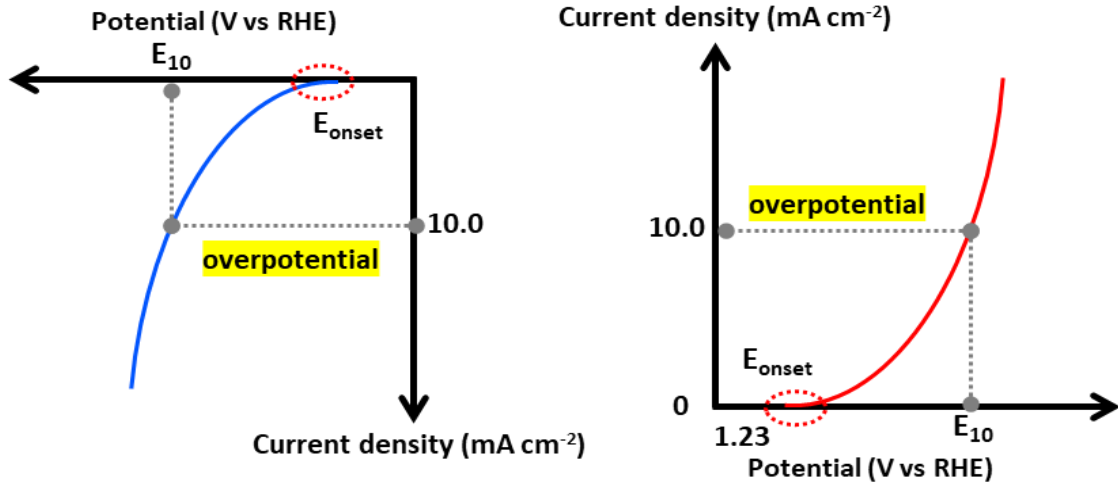


Figure 1.6 Schematic polarization curves for HER and OER.

Theoretically, the reversible potentials for HER and OER are 0 and 1.23 V vs. standard hydrogen electrode (SHE), respectively. The Nernst equation is related to the pH of electrolyte under standard condition 25°C at 1 atm. The calculated overpotentials at the desired current density without iR compensation for the HER and OER are based on the following equations[21]:

For HER:

$$E_{HER} = E_{(H_2/H^+)}^0 - \frac{RT}{F} \times \ln \left(\frac{a_{H^+}}{P_{H_2}^{1/2}} \right) \quad (28)$$

$$E_{HER} = -0.059 \times pH \text{ V vs. NHE} = 0V \text{ vs. RHE} \quad (29)$$

For OER:

$$E_{OER} = E_{(O_2/H_2O)}^0 - \frac{RT}{4F} \times \ln \left(\frac{a_{H^+}^4 P(O_2)/P^0}{a_{H_2O}^2} \right) \quad (30)$$

$$E_{OER} = 1.23 - 0.059 \times pH \text{ (V vs. NHE)} \quad (31)$$

Meanwhile, the following equations are used to calculate the iR drop compensated overpotentials for an electrocatalyst in OER and HER processes, respectively[116]:

$$iR \text{ drop free } (\eta_{HER}) = E_{RHE} - 0V - E_{iR} \quad (32)$$

$$iR \text{ drop free } (\eta_{OER}) = E_{RHE} - 1.23V - E_{iR} \quad (33)$$

Moreover, the current density of 10 mA cm^{-2} has been accepted as the standard one to compare and characterize various electrocatalytic materials for either HER or OER in all mediums. Sometimes, the overpotentials at 50 mA and/or 100 mA cm^{-2} current densities are also applied for the evaluation of electrocatalyst performances.

1.6.2 Tafel slope and exchange current density

The kinetic performance of electrocatalyst is usually determined from Tafel analysis of HER and OER processes. Tafel slope equation can be derived from the nature of kinetics of the electrocatalytic reaction at the catalytic interface. The relationship between current and overpotential at an electrical interface is given by the well-known Butler–Volmer equation as follows [117]:

$$I = I_0 \left[\exp \left(\frac{\alpha_A n F}{RT \times \eta} \right) - \exp \left(\frac{-\alpha_C n F}{RT \times \eta} \right) \right] \quad (34)$$

where I is current, I_0 is the exchange current (current at equilibrium potential), α_A and α_C are the charge transfer coefficients for anodic and cathodic reactions respectively, n is the number of electrons transferred, F is the Faraday constant (96485 C), R is the ideal gas constant, T is the absolute temperature in K and η is the overpotential. The exchange current density is obtained by linear of the Tafel plot and the logarithmical current density (j) as the Tafel equation:

$$\eta = a + b \log j \quad (35)$$

There is interception with the respective logarithmic current density at a reversible potential. The potentials of interceptions of 0 and 1.23 V (vs RHE) are used to calculate the current density exchanges of HER and OER, respectively. In addition, the inverse of the logarithmic current density of an electrocatalyst at the equilibrium potential of the electrocatalytic process under study is called exchange current density. Both Tafel slope and exchange current density of an electrocatalyst for a specific electrocatalytic study of interest have many insights on the kinetic behavior of the electrochemical process. Tafel slope for instance is usually used to semi-quantitatively predict how relatively faster the reaction is on an electrocatalytic interface. Three ways to extracting the Tafel slope using the electrochemical technique are voltammetry, chronoamperometry or chronopotentiometry, and EIS. The most widely-used technique to extract the Tafel slope

to explain Tafel equation mechanism is voltammetry (linear sweep voltammetry or segment of cyclic voltammetry). The basic of calculated Tafel slope is the iR drop compensated LSV or CV at a scan rate lower than 5 mV s^{-1} [1, 118].

1.6.3 Electrochemical active surface area

The electrochemically active surface area (ECSA) of an electrochemical material can be determined in more than five ways. As ECSA is believed to reflect the real surface active area of the material which is truly exposed to the electrolyte unlike the geometrical surface area, the activity normalized by the ECSA seems to be the more accurate one and in fact could provide a meaningful measure way in the evaluation of catalytic properties of different types of electrocatalysts that are distinguishable by size, shape, morphology, topography and porous nature. Though this method seems to be an interesting one to compare the activities of a set of similar materials and also to predict the reasons behind the activity trend, it has some serious disadvantages. The first one is that the relative ECSA determined by this method is purely based on the non-Faradaic ion adsorption and desorption processes whereas the gas evolution reactions are Faradaic processes. This means that correlating the ECSA derived from C_{dl} to the activity trends of electrocatalysts which purely Faradaic in nature makes it odd and strange. The resultant plot of scan rate against the difference of double layer charging current densities ($\Delta j (j_a - j_c)$) will yield a linear line, the slope of which is the double-layer capacitance of the material. It is found that this method in most cases is good agreement with the HER and OER activity trends of the catalytic materials with some exceptions[3, 119].

1.6.4 Faradaic efficiency

Faradaic efficiency is one of the three important indicators for any electrocatalyst, which is essential to show the selectivity of catalysts in the HER and OER electrocatalysis processes. There are two well-known and widely accepted methods to determine the FE of OER and HER. Both methods use a comparison between the experimentally measured quantity of evolved gas and the calculated amount of gas based on Faraday's laws of electrolysis. The first method is the conventional and reliable one where the evolved gas is collected in a graded cylindrical measuring jar via water-gas displacement. The volume of the collected gas is then converted into moles using Avogadro's principle and the number of moles of calculated gas molecules from the passed charge taking Faraday's

second law of electrolysis.[1] If the calculated volume and collected volume are in agreement with each other, the catalyst is then said to have 100% FE for the specific gas evolution reaction and shows that it is highly selective for that particular electrochemical reaction only. At this point, for the parameter of FE, it is concluded here that the FE of an electrocatalyst which is to be screened in water splitting electrocatalysis must be given along with other essential activity parameters as it reflects the selectivity of the catalyst. Moreover, the independence of FE from the size, shape, and morphology of the catalyst makes it free from experimental inaccuracy.

1.6.5 Stability test

The two methods to evaluate the long-term stability of the electrode are the chronopotentiometry-chronoamperometry curve and cyclic voltammetry (CV)/linear sweep voltammetry (LSV) curve. The chronopotentiometry/chronoamperometry test is always performed by setting up a constant current density/potential at a long-term duration (more than 12h is acceptable for the stability of scale up the same electrolyte condition)[78, 83], in which the current density could be decreased at a fixed potential or the overpotential is increased at a fixed current density (10 mA cm⁻² current density is a common fixed current density for the test and sometimes, a high current density of 100 mA cm⁻² is also used to evaluate the performance of the good electrocatalysts). The other method for the stability test is using the LSV curves converted from the CV test before and after at least 1000 cycles. In the CV test, long-term stability is determined by the shifts of the onset overpotential as well as the overpotential of the LSV curve after the test, and the smaller shift of curve means good stability.

1.7 OBJECTIVE OF THIS STUDY

From reviewed above, to improve the electrocatalytic performances for HER and OER, the design of suitable nanostructured electrocatalysts is very important since the conductivity, active surface area and synergistic effect could be enhanced by nanostructure design. The objective of this research is to fabricate nanostructured electrocatalysts with higher efficiency for either OER or HER. This study focuses on developing earth-abundant and low-cost transition metal-based nanostructured electrocatalysts for highly efficient and durable water splitting over a wide pH range.

Various novel electrocatalysts with low overpotential, low Tafel slope, high conductivity, fast electron transfer, long-term stability, and close to 100% Faradic efficiency were developed for the water splitting in various electrolytes. Some novel electrocatalysts synthesis methods were proposed and the reaction mechanisms were discussed. It is expected to provide some new routes for the development of electrocatalysts for overall water splitting in various environments.

1.8 SCOPE OF THIS DISSERTATION

Chapter 1 reviewed various electrocatalysts developed for the HER, OER, and especially the bifunctional electrocatalysts for the overall water splitting in a wide pH range electrolyte. The methods for the evaluation of various electrocatalysts were introduced. The issues on the electrocatalysts were discussed. Finally, the objective of this study was given.

In **Chapter 2**, the study on a novel OER electrocatalyst was introduced at first. Hierarchical NiO microflake@NiFe-LDH nanosheet core-shell arrays on nickel foam were fabricated by combining a two-step hydrothermal synthesis and a calcination process. The obtained electrodes were characterized using a scanning electron microscope (SEM) with an energy dispersive X-ray detector, Transmission electron microscope (TEM), X-ray photoelectron spectroscopy (XPS), and X-ray diffraction (XRD). Meanwhile, the OER activity was evaluated by using linear sweep voltammetry (LSV), and the long-term stability was tested at high current densities of 50 and 100 mA cm⁻². Due to the 3D rational configuration with highly active sites, the obtained composite electrode showed high performance for OER, which needed a low apparent overpotential of 265 mV to afford the standard current density of 10 mA cm⁻². In addition, the NiO@NiFe-LDH coated electrode was further treated in an organic solution via ultrasound for *in situ* intercalations of the NiFe-LDH to provide larger channels for ion transportation and gas diffusion. As a result, the charge transition resistance was obviously reduced and the apparent activity, as well as the long-term stability, were improved. The optimized NiO@NiFe-LDH composite exhibited excellent long-term stability in 50 h even at high current densities of 50 and 100 mA cm⁻², and meanwhile, the required apparent overpotential of OER for sustaining the standard current density (10

mA cm⁻²) was reduced from 265 to 210 mV. It is expected to provide a facile way to obtain low-cost nickel-based electrocatalysts with high activity and stability for OER in water-splitting process.

In **Chapter 3**, to develop HER electrocatalysts with high efficiency, long-term stability, and low-cost for the large-scale and effective application of renewable energy, a binder-free NiCoP-carbon nanocomposite (denoted as NiCoP-C(TPA)) film with unique nanostructure was successfully coated on the electrode for the first time by deposition of a terephthalic acid-induced NiCo bimetallic compound precursor film on the NF with a hydrothermal synthesis method followed by a calcination process in Ar atmosphere and continuous phosphorization treatment with NaH₂PO₂. In the obtained NiCoP-C(TPA) electrocatalyst, bimetallic phosphide nanoparticles were well combined with graphite carbon. It is found that the bimetallic NiCo alloy was also formed in the carbonization process, which affected the performance of the final catalyst. As a result, the NiCoP-C(TPA) electrocatalyst had much higher activity than the monometallic phosphides of NiP-C(TPA)/NF and CoP-C(TPA)/NF, and the NiCoP-C(TPA)/NF electrode exhibited an overpotential as low as 78 mV at the standard current density of 10 mA cm⁻² with a small Tafel slope of 73.4 mV dec⁻¹, a faradic efficiency of ~ 94% and long-term stability at high current density in the alkaline electrolyte. Meanwhile, the NiCoP-C(TPA)/NF electrode also exhibited superior HER performance in the acidic electrolyte with an overpotential of 94 mV@10 mA cm⁻², a Tafel slope of 81.1 mV dec⁻¹, and long-term stability although a relatively high overpotential of 248 mV@10 mA cm⁻² with a high Tafel slope of 112.5 mV dec⁻¹ was obtained in the neutral electrolyte. It is expected to provide a novel synthesis method by using organic solid acid to derive high-performance bimetallic phosphide based electrocatalysts with special nanostructure for HER in the water-splitting process

In **Chapter 4**, the bifunctional electrocatalysts for the overall water splitting were developed, in which combining oxides with bimetallic elements was considered as an efficient route to modify the electronic distribution for improving the intrinsic activity of electrocatalysts, and further engineering the defect structure and adjusting the valence state could provide more adsorption sites as well as active sites for the decomposition of

the reactants and/or intermediates. NiMnO_x nanosheets with rich defects were electrochemically deposited on the surface of Cu(OH)₂ nanowires followed by a thermal treatment process to form a CuO_x nanowires @NiMnO_x nanosheets (CuO_x NWs@NiMnO_x NSs) electrocatalyst with core-shell configuration. Structure characterizations indicated that NiMnO_x nanosheet had numerous vacancies with scattered defects and dislocations with partial cracking of the inert basal planes, resulting in extra active edge sites and coordination-unsaturated spinel crystal. As such, the valence states of Ni and Mn elements became unstable in the defect-modified NiMnO_x materials under the applied potential. Comparing with the initial NiMnO_x, more Ni³⁺ and Mn⁴⁺ were formed during the oxygen evolution reaction (OER) whereas they were converted to Ni²⁺ and Mn³⁺ during the hydrogen evolution reaction (HER). These controllable valence state changes of metal elements endowed the NiMnO_x to have a high ability for catalyzing overall water electrolysis. As a result, the CuO_x NWs@NiMnO_x NSs bifunctional electrocatalysts exhibited high performances in both HER and OER in alkaline electrolytes. Meanwhile, by using the same electrocatalysts in the neutral electrolyte, the overpotentials@10 mA cm⁻² was also as low as 80.7 and 390 mV with Tafel slopes of 77.6 and 101.6 mV dce⁻¹ for HER and OER, respectively. A two-electrode overall water electrolysis system using this bifunctional electrocatalyst exhibited low cell voltages of 1.62 and 1.75V in the alkaline and neutral electrolytes respectively at the standard current density of 10 mA cm⁻² with long-term stability, indicating that this CuO_x NWs@NiMnO_x NSs core@shell-type material should be an effective bifunctional electrocatalyst in both alkaline and neutral pH media.

Chapter 5 summarized the main results of this study, and an outlook for future work in this field was given.

REFERENCES

- [1] S. Anantharaj, S. R. Ede, K. Sakthikumar, K. Karthick, S. Mishra and S. Kundu, Recent Trends and Perspectives in Electrochemical Water Splitting with an Emphasis on Sulfide, Selenide, and Phosphide Catalysts of Fe, Co, and Ni: A Review. *ACS Catalysis*, 2016, 6(12), 8069-8097.
- [2] E. Fabbri, A. Haberer, K. Waltar, R. Kötz and T. J. Schmidt, Developments and perspectives of oxide-based catalysts for the oxygen evolution reaction. *Catalysis Science & Technology*, 2014, 4(11), 3800-3821.
- [3] Y. Jiao, Y. Zheng, M. Jaroniec and S. Z. Qiao, Design of electrocatalysts for oxygen- and hydrogen-involving energy conversion reactions. *Chemical Society Reviews*, 2015, 44(8), 2060-2086.
- [4] T. Shinagawa and K. Takanebe, Electrocatalytic Hydrogen Evolution under Densely Buffered Neutral pH Conditions. *The Journal of Physical Chemistry C*, 2015, 119(35), 20453-20458.
- [5] J. Wu, D. Wang, S. Wan, H. Liu, C. Wang and X. Wang, An Efficient Cobalt Phosphide Electrocatalyst Derived from Cobalt Phosphonate Complex for All-pH Hydrogen Evolution Reaction and Overall Water Splitting in Alkaline Solution. *Small*, 2020, 16(15), 1900550.
- [6] M. I. Jamesh, Recent progress on earth abundant hydrogen evolution reaction and oxygen evolution reaction bifunctional electrocatalyst for overall water splitting in alkaline media. *Journal of Power Sources*, 2016, 333, 213-236.
- [7] J. Chen, B. Lim, E. P. Lee and Y. Xia, Shape-controlled synthesis of platinum nanocrystals for catalytic and electrocatalytic applications. *Nano Today*, 2009, 4(1), 81-95.
- [8] Y. Yan, B. Y. Xia, B. Zhao and X. Wang, A review on noble-metal-free bifunctional heterogeneous catalysts for overall electrochemical water splitting. *Journal of Materials Chemistry A*, 2016, 4(45), 17587-17603.
- [9] Y. Kuang, M. J. Kenney, Y. Meng, W.-H. Hung, Y. Liu, J. E. Huang, R. Prasanna, P. Li, Y. Li, L. Wang, M.-C. Lin, M. D. McGehee, X. Sun and H. Dai, Solar-driven, highly sustained splitting of seawater into hydrogen and oxygen fuels. *Proceedings of the National Academy of Sciences*, 2019, 116(14), 6624.

- [10] Y. Li, J. Wang, X. Tian, L. Ma, C. Dai, C. Yang and Z. Zhou, Carbon doped molybdenum disulfide nanosheets stabilized on graphene for the hydrogen evolution reaction with high electrocatalytic ability. *Nanoscale*, 2016, 8(3), 1676-1683.
- [11] Q. Lu, G. S. Hutchings, W. Yu, Y. Zhou, R. V. Forest, R. Tao, J. Rosen, B. T. Yonemoto, Z. Cao, H. Zheng, J. Q. Xiao, F. Jiao and J. G. Chen, Highly porous non-precious bimetallic electrocatalysts for efficient hydrogen evolution. *Nature Communications*, 2015, 6(1), 6567.
- [12] J. K. Das, A. K. Samantara, S. Satyarthi, C. S. Rout and J. N. Behera, Three-dimensional NiCoP hollow spheres: an efficient electrode material for hydrogen evolution reaction and supercapacitor applications. *RSC Advances*, 2020, 10(8), 4650-4656.
- [13] C. Hu, L. Zhang and J. Gong, Recent progress made in the mechanism comprehension and design of electrocatalysts for alkaline water splitting. *Energy & Environmental Science*, 2019, 12(9), 2620-2645.
- [14] P. Li, X. Duan, Y. Kuang, Y. Li, G. Zhang, W. Liu and X. Sun, Tuning Electronic Structure of NiFe Layered Double Hydroxides with Vanadium Doping toward High Efficient Electrocatalytic Water Oxidation. *Advanced Energy Materials*, 2018, 8(15), 1703341.
- [15] D. Zhou, Z. Cai, Y. Bi, W. Tian, M. Luo, Q. Zhang, Q. Zhang, Q. Xie, J. Wang, Y. Li, Y. Kuang, X. Duan, M. Bajdich, S. Siahrostami and X. Sun, Effects of redox-active interlayer anions on the oxygen evolution reactivity of NiFe-layered double hydroxide nanosheets. *Nano Research*, 2018, 11(3), 1358-1368.
- [16] W. Zhu, Z. Yue, W. Zhang, N. Hu, Z. Luo, M. Ren, Z. Xu, Z. Wei, Y. Suo and J. Wang, Wet-chemistry topotactic synthesis of bimetallic iron–nickel sulfide nanoarrays: an advanced and versatile catalyst for energy efficient overall water and urea electrolysis. *Journal of Materials Chemistry A*, 2018, 6(10), 4346-4353.
- [17] H. Jin, C. Guo, X. Liu, J. Liu, A. Vasileff, Y. Jiao, Y. Zheng and S.-Z. Qiao, Emerging Two-Dimensional Nanomaterials for Electrocatalysis. *Chemical Reviews*, 2018, 118(13), 6337-6408.
- [18] H. Dau, C. Limberg, T. Reier, M. Risch, S. Roggan and P. Strasser, The Mechanism of Water Oxidation: From Electrolysis via Homogeneous to Biological Catalysis. *ChemCatChem*, 2010, 2(7), 724-761.

- [19] M. T. M. Koper, Thermodynamic theory of multi-electron transfer reactions: Implications for electrocatalysis. *Journal of Electroanalytical Chemistry*, 2011, 660(2), 254-260.
- [20] J. Wang, X. Yue, Y. Yang, S. Sirisomboonchai, P. Wang, X. Ma, A. Abudula and G. Guan, Earth-abundant transition-metal-based bifunctional catalysts for overall electrochemical water splitting: A review. *Journal of Alloys and Compounds*, 2020, 819, 153346.
- [21] X. Li, X. Hao, A. Abudula and G. Guan, Nanostructured catalysts for electrochemical water splitting: current state and prospects. *Journal of Materials Chemistry A*, 2016, 4(31), 11973-12000.
- [22] Z. Chen, X. Duan, W. Wei, S. Wang and B.-J. Ni, Recent advances in transition metal-based electrocatalysts for alkaline hydrogen evolution. *Journal of Materials Chemistry A*, 2019, 7(25), 14971-15005.
- [23] B. E. Conway and B. V. Tilak, Interfacial processes involving electrocatalytic evolution and oxidation of H₂, and the role of chemisorbed H. *Electrochimica Acta*, 2002, 47(22), 3571-3594.
- [24] B. Hinnemann, P. G. Moses, J. Bonde, K. P. Jørgensen, J. H. Nielsen, S. Horch, I. Chorkendorff and J. K. Nørskov, Biomimetic Hydrogen Evolution: MoS₂ Nanoparticles as Catalyst for Hydrogen Evolution. *Journal of the American Chemical Society*, 2005, 127(15), 5308-5309.
- [25] H. Vrubel and X. Hu, Molybdenum Boride and Carbide Catalyze Hydrogen Evolution in both Acidic and Basic Solutions. *Angewandte Chemie International Edition*, 2012, 51(51), 12703-12706.
- [26] D. Kong, H. Wang, Z. Lu and Y. Cui, CoSe₂ Nanoparticles Grown on Carbon Fiber Paper: An Efficient and Stable Electrocatalyst for Hydrogen Evolution Reaction. *Journal of the American Chemical Society*, 2014, 136(13), 4897-4900.
- [27] Y. Dong, J. Dang, W. Wang, S. Yin and Y. Wang, First-Principles Determination of Active Sites of Ni Metal-Based Electrocatalysts for Hydrogen Evolution Reaction. *ACS Applied Materials & Interfaces*, 2018, 10(46), 39624-39630.
- [28] J. Wang, S. Mao, Z. Liu, Z. Wei, H. Wang, Y. Chen and Y. Wang, Dominating Role of Ni⁰ on the Interface of Ni/NiO for Enhanced Hydrogen Evolution Reaction. *ACS Applied Materials & Interfaces*, 2017, 9(8), 7139-7147.

- [29] L. Zhao, Y. Zhang, Z. Zhao, Q.-H. Zhang, L.-B. Huang, L. Gu, G. Lu, J.-S. Hu and L.-J. Wan, Steering elementary steps towards efficient alkaline hydrogen evolution via size-dependent Ni/NiO nanoscale heterosurfaces. *National Science Review*, 2019, 7(1), 27-36.
- [30] X. Qian, T. Hang, S. Shanmugam and M. Li, Decoration of Micro-/Nanoscale Noble Metal Particles on 3D Porous Nickel Using Electrodeposition Technique as Electrocatalyst for Hydrogen Evolution Reaction in Alkaline Electrolyte. *ACS Applied Materials & Interfaces*, 2015, 7(29), 15716-15725.
- [31] K. Eiler, S. Suriñach, J. Sort and E. Pellicer, Mesoporous Ni-rich Ni–Pt thin films: Electrodeposition, characterization and performance toward hydrogen evolution reaction in acidic media. *Applied Catalysis B: Environmental*, 2020, 265, 118597.
- [32] V. Vij, S. Sultan, A. M. Harzandi, A. Meena, J. N. Tiwari, W.-G. Lee, T. Yoon and K. S. Kim, Nickel-Based Electrocatalysts for Energy-Related Applications: Oxygen Reduction, Oxygen Evolution, and Hydrogen Evolution Reactions. *ACS Catalysis*, 2017, 7(10), 7196-7225.
- [33] Z.-J. Chen, G.-X. Cao, L.-Y. Gan, H. Dai, N. Xu, M.-J. Zang, H.-B. Dai, H. Wu and P. Wang, Highly Dispersed Platinum on Honeycomb-like NiO@Ni Film as a Synergistic Electrocatalyst for the Hydrogen Evolution Reaction. *ACS Catalysis*, 2018, 8(9), 8866-8872.
- [34] Y. Feng, Y. Guan, H. Zhang, Z. Huang, J. Li, Z. Jiang, X. Gu and Y. Wang, Selectively anchoring Pt single atoms at hetero-interfaces of γ -Al₂O₃/NiS to promote the hydrogen evolution reaction. *Journal of Materials Chemistry A*, 2018, 6(25), 11783-11789.
- [35] Y. Guan, Y. Feng, J. Wan, X. Yang, L. Fang, X. Gu, R. Liu, Z. Huang, J. Li, J. Luo, C. Li and Y. Wang, Ganoderma-Like MoS₂/NiS₂ with Single Platinum Atoms Doping as an Efficient and Stable Hydrogen Evolution Reaction Catalyst. *Small*, 2018, 14(27), 1800697.
- [36] Z. Xing, L. Gan, J. Wang and X. Yang, Experimental and theoretical insights into sustained water splitting with an electrodeposited nanoporous nickel hydroxide@nickel film as an electrocatalyst. *Journal of Materials Chemistry A*, 2017, 5(17), 7744-7748.
- [37] Y.-Y. Chen, Y. Zhang, X. Zhang, T. Tang, H. Luo, S. Niu, Z.-H. Dai, L.-J. Wan and

- J.-S. Hu, Self-Templated Fabrication of MoNi₄/MoO_{3-x} Nanorod Arrays with Dual Active Components for Highly Efficient Hydrogen Evolution. *Advanced Materials*, 2017, 29(39), 1703311.
- [38] N. Danilovic, R. Subbaraman, D. Strmcnik, K.-C. Chang, A. P. Paulikas, V. R. Stamenkovic and N. M. Markovic, Enhancing the Alkaline Hydrogen Evolution Reaction Activity through the Bifunctionality of Ni(OH)₂/Metal Catalysts. *Angewandte Chemie International Edition*, 2012, 51(50), 12495-12498.
- [39] B. Wei, J. Wu, G. Mei, Z. Qi, W. Hu and Z. Wang, NiCo₂O₄ nanowire arrays rich in oxygen deficiencies for hydrogen evolution reaction. *International Journal of Hydrogen Energy*, 2019, 44(13), 6612-6617.
- [40] L. Song and S. Zhang, A novel cocatalyst of NiCoP significantly enhances visible-light photocatalytic hydrogen evolution over cadmium sulfide. *Journal of Industrial and Engineering Chemistry*, 2018, 61, 197-205.
- [41] J. Mou, Y. Gao, J. Wang, J. Ma and H. Ren, Hydrogen evolution reaction activity related to the facet-dependent electrocatalytic performance of NiCoP from first principles. *RSC Advances*, 2019, 9(21), 11755-11761.
- [42] C. Liu, G. Zhang, L. Yu, J. Qu and H. Liu, Oxygen Doping to Optimize Atomic Hydrogen Binding Energy on NiCoP for Highly Efficient Hydrogen Evolution. *Small*, 2018, 14(22), 1800421.
- [43] B. Ma, Z. Yang, Y. Chen and Z. Yuan, Nickel cobalt phosphide with three-dimensional nanostructure as a highly efficient electrocatalyst for hydrogen evolution reaction in both acidic and alkaline electrolytes. *Nano Research*, 2019, 12(2), 375-380.
- [44] Z. Cai, A. Wu, H. Yan, Y. Xiao, C. Chen, C. Tian, L. Wang, R. Wang and H. Fu, Hierarchical whisker-on-sheet NiCoP with adjustable surface structure for efficient hydrogen evolution reaction. *Nanoscale*, 2018, 10(16), 7619-7629.
- [45] J. Zhang, L. Zhang, X. Wang, W. Zhu and Z. Zhuang, A hierarchical hollow-on-hollow NiCoP electrocatalyst for efficient hydrogen evolution reaction. *Chemical Communications*, 2020, 56(1), 90-93.
- [46] Y. Chen, K. Rui, J. Zhu, S. X. Dou and W. Sun, Recent Progress on Nickel-Based Oxide/(Oxy)Hydroxide Electrocatalysts for the Oxygen Evolution Reaction. *Chemistry – A European Journal*, 2019, 25(3), 703-713.

- [47] O. Diaz-Morales, I. Ledezma-Yanez, M. T. M. Koper and F. Calle-Vallejo, Guidelines for the Rational Design of Ni-Based Double Hydroxide Electrocatalysts for the Oxygen Evolution Reaction. *ACS Catalysis*, 2015, 5(9), 5380-5387.
- [48] G. Fan, F. Li, D. G. Evans and X. Duan, Catalytic applications of layered double hydroxides: recent advances and perspectives. *Chemical Society Reviews*, 2014, 43(20), 7040-7066.
- [49] X. Li, X. Hao, Z. Wang, A. Abudula and G. Guan, In-situ intercalation of NiFe LDH materials: An efficient approach to improve electrocatalytic activity and stability for water splitting. *Journal of Power Sources*, 2017, 347, 193-200.
- [50] P. T. Babar, A. C. Lokhande, M. G. Gang, B. S. Pawar, S. M. Pawar and J. H. Kim, Thermally oxidized porous NiO as an efficient oxygen evolution reaction (OER) electrocatalyst for electrochemical water splitting application. *Journal of Industrial and Engineering Chemistry*, 2018, 60, 493-497.
- [51] Y. Jin, S. Huang, X. Yue, H. Du and P. K. Shen, Mo- and Fe-Modified Ni(OH)₂/NiOOH Nanosheets as Highly Active and Stable Electrocatalysts for Oxygen Evolution Reaction. *ACS Catalysis*, 2018, 8(3), 2359-2363.
- [52] Q. F. Bo Li, Feng Jiang, Lizhi Peng, Tianfu Liu, Flower-like NiFe Oxide Nanosheets on Ni Foam as Efficient Bifunctional Electrocatalysts for the Overall Water Splitting. *International journal of electrochemical science*, 2019, 14, 4878-4890.
- [53] X. He, F. Yin, Y. Li, H. Wang, J. Chen, Y. Wang and B. Chen, NiMnO₃/NiMn₂O₄ Oxides Synthesized via the Aid of Pollen: Ilmenite/Spinel Hybrid Nanoparticles for Highly Efficient Bifunctional Oxygen Electrocatalysis. *ACS Applied Materials & Interfaces*, 2016, 8(40), 26740-26757.
- [54] Q. Qin, L. Chen, T. Wei, Y. Wang and X. Liu, Ni/NiM₂O₄ (M = Mn or Fe) supported on N-doped carbon nanotubes as trifunctional electrocatalysts for ORR, OER and HER. *Catalysis Science & Technology*, 2019, 9(7), 1595-1601.
- [55] Z. Cai, X. Bu, P. Wang, J. C. Ho, J. Yang and X. Wang, Recent advances in layered double hydroxide electrocatalysts for the oxygen evolution reaction. *Journal of Materials Chemistry A*, 2019, 7(10), 5069-5089.
- [56] F. Song and X. Hu, Exfoliation of layered double hydroxides for enhanced oxygen evolution catalysis. *Nature Communications*, 2014, 5(1), 4477.
- [57] Z. Lu, W. Xu, W. Zhu, Q. Yang, X. Lei, J. Liu, Y. Li, X. Sun and X. Duan, Three-

- dimensional NiFe layered double hydroxide film for high-efficiency oxygen evolution reaction. *Chemical Communications*, 2014, 50(49), 6479-6482.
- [58] Z. Lu, L. Qian, Y. Tian, Y. Li, X. Sun and X. Duan, Ternary NiFeMn layered double hydroxides as highly-efficient oxygen evolution catalysts. *Chemical Communications*, 2016, 52(5), 908-911.
- [59] W. Ma, R. Ma, J. Wu, P. Sun, X. Liu, K. Zhou and T. Sasaki, Development of efficient electrocatalysts via molecular hybridization of NiMn layered double hydroxide nanosheets and graphene. *Nanoscale*, 2016, 8(19), 10425-10432.
- [60] G. Jia, Y. Hu, Q. Qian, Y. Yao, S. Zhang, Z. Li and Z. Zou, Formation of Hierarchical Structure Composed of (Co/Ni)Mn-LDH Nanosheets on MWCNT Backbones for Efficient Electrocatalytic Water Oxidation. *ACS Applied Materials & Interfaces*, 2016, 8(23), 14527-14534.
- [61] Y. Zhang, Q. Shao, Y. Pi, J. Guo and X. Huang, A Cost-Efficient Bifunctional Ultrathin Nanosheets Array for Electrochemical Overall Water Splitting. *Small*, 2017, 13(27), 1700355.
- [62] F. Qin, Z. Zhao, M. K. Alam, Y. Ni, F. Robles-Hernandez, L. Yu, S. Chen, Z. Ren, Z. Wang and J. Bao, Trimetallic NiFeMo for Overall Electrochemical Water Splitting with a Low Cell Voltage. *ACS Energy Letters*, 2018, 3(3), 546-554.
- [63] Z. Wang, S. Zeng, W. Liu, X. Wang, Q. Li, Z. Zhao and F. Geng, Coupling Molecularly Ultrathin Sheets of NiFe-Layered Double Hydroxide on NiCo₂O₄ Nanowire Arrays for Highly Efficient Overall Water-Splitting Activity. *ACS Applied Materials & Interfaces*, 2017, 9(2), 1488-1495.
- [64] Y. Gong, Z. Yang, Y. Lin, J. Wang, H. Pan and Z. Xu, Hierarchical heterostructure NiCo₂O₄@CoMoO₄/NF as an efficient bifunctional electrocatalyst for overall water splitting. *Journal of Materials Chemistry A*, 2018, 6(35), 16950-16958.
- [65] J. Liu, D. Zhu, T. Ling, A. Vasileff and S.-Z. Qiao, S-NiFe₂O₄ ultra-small nanoparticle built nanosheets for efficient water splitting in alkaline and neutral pH. *Nano Energy*, 2017, 40, 264-273.
- [66] L. Tao, M. Huang, S. Guo, Q. Wang, M. Li, X. Xiao, G. Cao, Y. Shao, Y. Shen, Y. Fu and M. Wang, Surface modification of NiCo₂Te₄ nanoclusters: a highly efficient electrocatalyst for overall water-splitting in neutral solution. *Applied Catalysis B: Environmental*, 2019, 254, 424-431.

- [67] Y. Liu, F. Yang, W. Qin and G. Yang, Co₂P@NiCo₂O₄ bi-functional electrocatalyst with low overpotential for water splitting in wide range pH electrolytes. *Journal of Colloid and Interface Science*, 2019, 534(15), 55-63.
- [68] R. Zhang, X. Wang, S. Yu, T. Wen, X. Zhu, F. Yang, X. Sun, X. Wang and W. Hu, Ternary NiCo(2) P(x) Nanowires as pH-Universal Electrocatalysts for Highly Efficient Hydrogen Evolution Reaction. *Adv Mater*, 2017, 29(9).
- [69] Y.-Y. Chen, Y. Zhang, X. Zhang, T. Tang, H. Luo, S. Niu, Z.-H. Dai, L.-J. Wan and J.-S. Hu, Self-Templated Fabrication of MoNi₄/MoO_{3-x} Nanorod Arrays with Dual Active Components for Highly Efficient Hydrogen Evolution. 2017, 29(39), 1703311.
- [70] X. Li, P. F. Liu, L. Zhang, M. Y. Zu, Y. X. Yang and H. G. Yang, Enhancing alkaline hydrogen evolution reaction activity through Ni–Mn₃O₄ nanocomposites. *Chemical Communications*, 2016, 52(69), 10566-10569.
- [71] C. Liu, G. Zhang, L. Yu, J. Qu and H. Liu, Oxygen Doping to Optimize Atomic Hydrogen Binding Energy on NiCoP for Highly Efficient Hydrogen Evolution. 2018, 14(22), 1800421.
- [72] C. Du, L. Yang, F. Yang, G. Cheng and W. Luo, Nest-like NiCoP for Highly Efficient Overall Water Splitting. *ACS Catalysis*, 2017, 7(6), 4131-4137.
- [73] G.-F. Chen, T. Y. Ma, Z.-Q. Liu, N. Li, Y.-Z. Su, K. Davey and S.-Z. Qiao, Efficient and Stable Bifunctional Electrocatalysts Ni/Ni_xM_y (M = P, S) for Overall Water Splitting. *Adv. Funct. Mater.*, 2016, 26(19), 3314-3323.
- [74] H. Wang, H.-W. Lee, Y. Deng, Z. Lu, P.-C. Hsu, Y. Liu, D. Lin and Y. Cui, Bifunctional non-noble metal oxide nanoparticle electrocatalysts through lithium-induced conversion for overall water splitting. *Nature Communications*, 2015, 6(1), 7261.
- [75] B. You, N. Jiang, M. Sheng, M. W. Bhushan and Y. Sun, Hierarchically Porous Urchin-Like Ni₂P Superstructures Supported on Nickel Foam as Efficient Bifunctional Electrocatalysts for Overall Water Splitting. *ACS Catalysis*, 2016, 6(2), 714-721.
- [76] X. Wang, H. Zhou, D. Zhang, M. Pi, J. Feng and S. Chen, Mn-doped NiP₂ nanosheets as an efficient electrocatalyst for enhanced hydrogen evolution reaction at all pH values. *Journal of Power Sources*, 2018, 387, 1-8.

- [77] P. Jiang, Q. Liu and X. Sun, NiP₂ nanosheet arrays supported on carbon cloth: an efficient 3D hydrogen evolution cathode in both acidic and alkaline solutions. *Nanoscale*, 2014, 6(22), 13440-13445.
- [78] S. Li, S. Sirisomboonchai, A. Yoshida, X. An, X. Hao, A. Abudula and G. Guan, Bifunctional CoNi/CoFe₂O₄ /Ni foam electrodes for efficient overall water splitting at a high current density. *Journal of Materials Chemistry A*, 2018, 6(39), 19221-19230.
- [79] Y. Sun, L. Hang, Q. Shen, T. Zhang, H. Li, X. Zhang, X. Lyu and Y. Li, Mo doped Ni₂P nanowire arrays: an efficient electrocatalyst for the hydrogen evolution reaction with enhanced activity at all pH values. *Nanoscale*, 2017, 9(43), 16674-16679.
- [80] J. Li, M. Yan, X. Zhou, Z.-Q. Huang, Z. Xia, C.-R. Chang, Y. Ma and Y. Qu, Mechanistic Insights on Ternary Ni_{2-x}Co_xP for Hydrogen Evolution and Their Hybrids with Graphene as Highly Efficient and Robust Catalysts for Overall Water Splitting. 2016, 26(37), 6785-6796.
- [81] R. Zhang, X. Wang, S. Yu, T. Wen, X. Zhu, F. Yang, X. Sun, X. Wang and W. Hu, Ternary NiCo₂P_x Nanowires as pH-Universal Electrocatalysts for Highly Efficient Hydrogen Evolution Reaction. 2017, 29(9), 1605502.
- [82] B. Liu, Y.-F. Zhao, H.-Q. Peng, Z.-Y. Zhang, C.-K. Sit, M.-F. Yuen, T.-R. Zhang, C.-S. Lee and W.-J. Zhang, Nickel–Cobalt Diselenide 3D Mesoporous Nanosheet Networks Supported on Ni Foam: An All-pH Highly Efficient Integrated Electrocatalyst for Hydrogen Evolution. 2017, 29(19), 1606521.
- [83] S. Sirisomboonchai, S. Li, A. Yoshida, S. Kongparakul, C. Samart, Y. Kansha, X. Hao, A. Abudula and G. Guan, Terephthalic acid induced binder-free NiCoP–carbon nanocomposite for highly efficient electrocatalysis of hydrogen evolution reaction. *Catalysis Science & Technology*, 2019, 9(17), 4651-4658.
- [84] S. Sirisomboonchai, X. Li, N. Kitiphapiboon, R. Channoo, S. Li, Y. Ma, S. Kongparakul, C. Samart, A. Abudula and G. Guan, Fabrication of CuOx nanowires@NiMnOx nanosheets core@shell-type electrocatalysts: crucial roles of defect modification and valence states for overall water electrolysis. *Journal of Materials Chemistry A*, 2020, 8(32), 16463-16476.
- [85] L. Wen, Y. Sun, T. Zhang, Y. Bai, X. Li, X. Lyu, W. Cai and Y. Li, MnMoO₄ nanosheet array: an efficient electrocatalyst for hydrogen evolution reaction with enhanced

- activity over a wide pH range. *Nanotechnology*, 2018, 29(33), 335403.
- [86] X. Lu, J. Pan, E. Lovell, T. H. Tan, Y. H. Ng and R. Amal, A sea-change: manganese doped nickel/nickel oxide electrocatalysts for hydrogen generation from seawater. *Energy & Environmental Science*, 2018, 11(7), 1898-1910.
- [87] A. Han, H. Chen, H. Zhang, Z. Sun and P. Du, Ternary metal phosphide nanosheets as a highly efficient electrocatalyst for water reduction to hydrogen over a wide pH range from 0 to 14. *Journal of Materials Chemistry A*, 2016, 4(26), 10195-10202.
- [88] S. Sirisomboonchai, S. Li, A. Yoshida, X. Li, C. Samart, A. Abudula and G. Guan, Fabrication of NiO Microflake@NiFe-LDH Nanosheet Heterostructure Electrocatalysts for Oxygen Evolution Reaction. *ACS Sustainable Chemistry & Engineering*, 2019, 7(2), 2327-2334.
- [89] L. Yang, L. Chen, D. Yang, X. Yu, H. Xue and L. Feng, NiMn layered double hydroxide nanosheets/NiCo₂O₄ nanowires with surface rich high valence state metal oxide as an efficient electrocatalyst for oxygen evolution reaction. *Journal of Power Sources*, 2018, 392, 23-32.
- [90] X. Zhang, L. Huang, Y. Han, M. Xu and S. Dong, Nitrogen-doped carbon encapsulating γ -MoC/Ni heterostructures for efficient oxygen evolution electrocatalysts. *Nanoscale*, 2017, 9(17), 5583-5588.
- [91] F. Xie, H. Wu, J. Mou, D. Lin, C. Xu, C. Wu and X. Sun, Ni₃N@Ni-Ci nanoarray as a highly active and durable non-noble-metal electrocatalyst for water oxidation at near-neutral pH. *Journal of Catalysis*, 2017, 356, 165-172.
- [92] R. Ge, M. Ma, X. Ren, F. Qu, Z. Liu, G. Du, A. M. Asiri, L. Chen, B. Zheng and X. Sun, A NiCo₂O₄@Ni-Co-Ci core-shell nanowire array as an efficient electrocatalyst for water oxidation at near-neutral pH. *Chemical Communications*, 2017, 53(55), 7812-7815.
- [93] X. Ji, L. Cui, D. Liu, S. Hao, J. Liu, F. Qu, Y. Ma, G. Du, A. M. Asiri and X. Sun, A nickel-borate nanoarray: a highly active 3D oxygen-evolving catalyst electrode operating in near-neutral water. *Chemical Communications*, 2017, 53(21), 3070-3073.
- [94] K. S. Joya, Y. F. Joya and H. J. M. de Groot, Ni-Based Electrocatalyst for Water Oxidation Developed In-Situ in a HCO₃⁻/CO₂ System at Near-Neutral pH. 2014, 4(9), 1301929.

- [95] Y. Li, B. Huang, Y. Sun, M. Luo, Y. Yang, Y. Qin, L. Wang, C. Li, F. Lv, W. Zhang and S. Guo, Multimetal Borides Nanochains as Efficient Electrocatalysts for Overall Water Splitting. 2019, 15(1), 1804212.
- [96] L. Peng, J. Shen, X. Zheng, R. Xiang, M. Deng, Z. Mao, Z. Feng, L. Zhang, L. Li and Z. Wei, Rationally design of monometallic NiO-Ni₃S₂/NF heteronanosheets as bifunctional electrocatalysts for overall water splitting. Journal of Catalysis, 2019, 369, 345-351.
- [97] Q. Xu, H. Jiang, H. Zhang, Y. Hu and C. Li, Heterogeneous interface engineered atomic configuration on ultrathin Ni(OH)₂/Ni₃S₂ nanoforests for efficient water splitting. Applied Catalysis B: Environmental, 2019, 242, 60-66.
- [98] Y. Gong, Y. Zhi, Y. Lin, T. Zhou, J. Li, F. Jiao and W. Wang, Controlled synthesis of bifunctional particle-like Mo/Mn-Ni_xS_y/NF electrocatalyst for highly efficient overall water splitting. Dalton Transactions, 2019, 48(20), 6718-6729.
- [99] K. Wang, K. Sun, T. Yu, X. Liu, G. Wang, L. Jiang and G. Xie, Facile synthesis of nanoporous Ni-Fe-P bifunctional catalysts with high performance for overall water splitting. Journal of Materials Chemistry A, 2019, 7(6), 2518-2523.
- [100] R. Elakkiya, R. Ramkumar and G. Maduraiveeran, Flower-like nickel-cobalt oxide nanomaterials as bi-functional catalyst for electrochemical water splitting. Materials Research Bulletin, 2019, 116, 98-105.
- [101] C. Xiao, Y. Li, X. Lu and C. Zhao, Bifunctional Porous NiFe/NiCo₂O₄/Ni Foam Electrodes with Triple Hierarchy and Double Synergies for Efficient Whole Cell Water Splitting. 2016, 26(20), 3515-3523.
- [102] M. Ledendecker, S. Krick Calderón, C. Papp, H.-P. Steinrück, M. Antonietti and M. Shalom, The Synthesis of Nanostructured Ni₅P₄ Films and their Use as a Non-Noble Bifunctional Electrocatalyst for Full Water Splitting. 2015, 54(42), 12361-12365.
- [103] J. Tian, N. Cheng, Q. Liu, X. Sun, Y. He and A. M. Asiri, Self-supported NiMo hollow nanorod array: an efficient 3D bifunctional catalytic electrode for overall water splitting. Journal of Materials Chemistry A, 2015, 3(40), 20056-20059.
- [104] Y. Xiao, P. Zhang, X. Zhang, X. Dai, Y. Ma, Y. Wang, Y. Jiang, M. Liu and Y. Wang, Bimetallic thin film NiCo-NiCoO₂@NC as a superior bifunctional electrocatalyst for overall water splitting in alkaline media. Journal of Materials Chemistry A, 2017, 5(30), 15901-15912.

- [105] Y. Wu, Y. Liu, G.-D. Li, X. Zou, X. Lian, D. Wang, L. Sun, T. Asefa and X. Zou, Efficient electrocatalysis of overall water splitting by ultrasmall $\text{Ni}_x\text{Co}_{3-x}\text{S}_4$ coupled Ni_3S_2 nanosheet arrays. *Nano Energy*, 2017, 35, 161-170.
- [106] L. Zeng, K. Sun, Y. Chen, Z. Liu, Y. Chen, Y. Pan, R. Zhao, Y. Liu and C. Liu, Neutral-pH overall water splitting catalyzed efficiently by a hollow and porous structured ternary nickel sulfoselenide electrocatalyst. *Journal of Materials Chemistry A*, 2019, 7(28), 16793-16802.
- [107] R. Wu, B. Xiao, Q. Gao, Y. R. Zheng, X. S. Zheng, J. F. Zhu, M. R. Gao and S. H. Yu, A Janus Nickel Cobalt Phosphide Catalyst for High-Efficiency Neutral-pH Water Splitting. *Angew Chem Int Ed*, 2018, 57(47), 15445-15449.
- [108] Z. Pu, Y. Xue, W. Li, I. S. Amiin and S. Mu, Efficient water splitting catalyzed by flexible NiP_2 nanosheet array electrodes under both neutral and alkaline solutions. *New Journal of Chemistry*, 2017, 41(5), 2154-2159.
- [109] N. K. Chaudhari, H. Jin, B. Kim and K. Lee, Nanostructured materials on 3D nickel foam as electrocatalysts for water splitting. *Nanoscale*, 2017, 9(34), 12231-12247.
- [110] P. Li, Z. Jin, J. Yang, Y. Jin and D. Xiao, Highly Active 3D-Nanoarray-Supported Oxygen-Evolving Electrode Generated from Cobalt-Phytate Nanoplates. *Chemistry of Materials*, 2016, 28(1), 153-161.
- [111] X. Wang, W. Li, D. Xiong, D. Y. Petrovykh and L. Liu, Bifunctional Nickel Phosphide Nanocatalysts Supported on Carbon Fiber Paper for Highly Efficient and Stable Overall Water Splitting. *Advanced Functional Materials*, 2016, 26(23), 4067-4077.
- [112] Y. Li, H. Zhang, M. Jiang, Y. Kuang, X. Sun and X. Duan, Ternary NiCoP nanosheet arrays: An excellent bifunctional catalyst for alkaline overall water splitting. *Nano Research*, 2016, 9(8), 2251-2259.
- [113] C. Lu, J. Wang, S. Czoska, H. Dong and Z. Chen, Hierarchically Structured Cu-Based Electrocatalysts with Nanowires Array for Water Splitting. *The Journal of Physical Chemistry C*, 2017, 121(46), 25875-25881.
- [114] Q. Zhou, T.-T. Li, J. Qian, Y. Hu, F. Guo and Y.-Q. Zheng, Self-supported hierarchical $\text{CuOx}@ \text{Co}_3\text{O}_4$ heterostructures as efficient bifunctional electrocatalysts for water splitting. *Journal of Materials Chemistry A*, 2018, 6(29), 14431-14439.
- [115] Y. Rong, Y. Ma, F. Guo, J. Qian, H. Li, M. Zhou, Z. Xu, Y.-Q. Zheng and T.-T. Li,

- Paintbrush-like Co doped Cu₃P grown on Cu foam as an efficient janus electrode for overall water splitting. *International Journal of Hydrogen Energy*, 2019, 44(54), 28833-28840.
- [116] S. Anantharaj, S. R. Ede, K. Karthick, S. Sam Sankar, K. Sangeetha, P. E. Karthik and S. Kundu, Precision and correctness in the evaluation of electrocatalytic water splitting: revisiting activity parameters with a critical assessment. *Energy & Environmental Science*, 2018, 11(4), 744-771.
- [117] T. Shinagawa, A. T. Garcia-Esparza and K. Takanebe, Insight on Tafel slopes from a microkinetic analysis of aqueous electrocatalysis for energy conversion. *Scientific Reports*, 2015, 5(1), 13801.
- [118] Y. Shi and B. Zhang, Recent advances in transition metal phosphide nanomaterials: synthesis and applications in hydrogen evolution reaction. *Chemical Society Reviews*, 2016, 45(6), 1529-1541.
- [119] Y. Xu, L. Wang, X. Liu, S. Zhang, C. Liu, D. Yan, Y. Zeng, Y. Pei, Y. Liu and S. Luo, Monolayer MoS₂ with S vacancies from interlayer spacing expanded counterparts for highly efficient electrochemical hydrogen production. *Journal of Materials Chemistry A*, 2016, 4(42), 16524-16530.

CHAPTER 2 Fabrication of NiO microflake@NiFe-LDH nanosheet heterostructure electrocatalysts for oxygen evolution reaction

2.1 INTRODUCTION

Water electrolysis via renewable source derived electricity has been one of the most promising technologies of sustainable energy utilization. [1,2] In the water electrolysis process, oxygen evolution reaction (OER) on the anode side is a four electron-transfer coupled reaction which requires a higher overpotential to overcome the kinetic barrier than hydrogen evolution reaction (HER) on the cathode side. [3-6] Recently, numerous efforts have been devoted to developing highly efficient OER catalysts to improve the reaction kinetics and intrinsic catalytic activity. To date, noble metal-based electrocatalysts such as Ir, Ru, IrO₂, and RuO₂ are still considered the best ones for OER in an alkaline solution, but the high price and the scarcity restrict their large-scale applications. [7,8] Thusly, it is necessary to develop noble-metal-free catalysts with low-cost but excellent activity as well as stability. [9]

Nickel-based electrocatalysts have garnered enormously and are among the most efficient noble-metal-free OER catalysts due to their high catalytic activity and low-cost. [10] Although pure nickel oxide has high activity, the electrode based on it always exhibits high overpotential in the alkaline solution due to the poor electric conductivity. [11, 12] It is found that the overpotential can be reduced by designing nickel-based catalysts with optimum hierarchical hybrid heterostructure. Among them, the catalysts with core-shell nanostructures featuring metal-oxide@metal-oxide composition are particularly promising. As the core and shell are active materials, they can both contribute to the whole electrocatalytic activity, and meanwhile, the synergy among them could improve the catalytic performance. Especially, the shell growing on the core can greatly increase the surface area of the entire electrode, which would provide more active sites for electrochemical reactions. [13]

Layer double hydroxides (LDHs) have attracted considerable attention as electrocatalysts due to their large surface area, chemical versatility, and open structure. For OER, the metal atoms on the LDH sheets can provide abundant exposed active sites, and especially,

the special anion-exchange property and the ease of delamination of LDHs make the engineering nanostructured assembly of LDHs towards enhanced OER performance more easily. To improve the water oxidation activity, iron incorporation into nickel film with layered structure was found to be a very useful way. [14] Recently, NiFe-LDH with a two-dimension layer (2D) structure was found to have outstanding OER electrocatalytic activity and stability in the alkaline solution. [15-23] Furthermore, exfoliating or intercalation of NiFe-LDHs could further improve the catalytic performance since it can increase the active edge sites and surface area. For instance, NiFe-LDH can be exfoliated to obtain single-layer nanosheets without alternating their composition and structure, and the exfoliated NiFe-LDH single nanosheets delivered enhanced OER activity and generated larger current density than the bulk counterpart as well as commercial IrO₂. [24] However, when such exfoliated materials are used for fabrication of the electrode, the exfoliated materials have to be grafted onto the preselected substrate by using a polymer binder. [25] In our group, an in-situ intercalation method was performed to expand the inter-layer spacing of electrodeposited NiFe-LDH electrode. [25] It is found that the inter-layer distance of NiFe-LDH material on the electrode can be increased by immersing it in formamide at 80 °C, and the required apparent overpotential of OER for sustaining 10 mA cm⁻² current density was reduced from 256 to 210 mV. Moreover, with the assistance of ultrasound treatment, the required intercalation time is reduced drastically and the apparent overpotential@10 mA cm⁻² current density is further decreased to 203 mV. [26]

Herein, to reduce the apparent overpotential and improve the long-term stability at a high current density of Nickel-based electrocatalysts coated electrode for OER at the alkaline environment, hierarchical NiO microflake@NiFe-LDH nanosheet core-shell arrays on nickel foam were fabricated by combining a two-step hydrothermal synthesis and a calcination process. To improve the catalytic activity and stability, ultrasonic was used for in-situ intercalation of inter-layer distance of NiFe-LDH. The obtained electrodes were characterized using a scanning electron microscope (SEM) with an energy dispersive X-ray detector, Transmission electron microscope (TEM), X-ray photoelectron spectroscopy (XPS), and X-ray diffraction (XRD). Meanwhile, the OER activity was evaluated by using linear sweep voltammetry (LSV), and the long-term stability was tested at high current densities of 50 and 100 mA cm⁻². It is expected to provide a facile

way to obtain low-cost Nickel-based electrocatalysts with high activity and stability for OER in water splitting process.

2.2 EXPERIMENT

2.2.1 Chemicals and Materials

Nickel (II) nitrate hexahydrate, Iron (III) nitrate nonahydrate, Ammonium fluoride, and Urea (Wako, Japan) with analytical grade were used for preparing NiO and NiFe-LDH. Potassium hydroxide (Wako, Japan) with analytical grade was employed to prepare an electrolyte solution for water splitting. Nickel foam (NF, thickness: 1.5 mm, bulk density: 0.23 g/cm³; a number of pores per inch: 110) was provided by MTI, Japan. Prior to use, the NF was cleaned with 1.0 M hydrochloric acid solution and washed with ethanol and distilled water successively.

2.2.2 Synthesis of NiO/NF electrode

Firstly, 2 mmol Ni(NO₃)₂·6H₂O, 4 mmol NH₄F, and 5 mmol CO(NH₂)₂ were dissolved in 20 ml distilled water with stirring for 15 min. Then, the obtained solution was transferred into a Teflon-lined autoclave with a piece of cleaned Ni foam (size: 1 x 1 cm²), subsequently heated at 100 °C for 12 h. As such, Ni(OH)₂/NF electrode was obtained, which was further calcined at 450 °C for 2 h in air with a heat rate of 5 °C/min to get the final NiO/NF electrode.

2.2.3 Synthesis of NiO@NiFe-LDH/NF electrode

For the preparation of NiO@NiFe-LDH/NF electrode, a set of preliminary experiments were performed (Figure 2.6), in which various initial molar ratios (1:1, 4:1, 9:1 and 1:4) of Ni(NO₃)₂·6H₂O: Fe(NO₃)₃·9H₂O with a total amount of 1 mmol were dissolved in 20 ml distilled water with 4 mmol NH₄F and 5 mmol CO(NH₂)₂ at first and then, transferred into a Teflon line autoclave with the above-obtained NiO/NF electrode, which was heated at 140 °C for 6 h and as such, NiO@NiFe-LDH/NF electrodes were formed. Thereafter, the electrodes were rinsed with distilled water and dried in a vacuum oven at 60 °C for 2 h. In addition, since some unstable NiFe-LDH particles were found to be formed on the surface of NiO/NF electrode, the obtained NiO@NiFe-LDH/NF electrodes were ultrasonically treated in distilled water for 5 min to move out these unstable particles. In this study, as shown in Figure. 2.6, the highest activity was achieved by using the Ni/Fe initial molar ratio of 4:1. Therefore, in the following study, NiO@NiFe-LDH/NF

electrode was prepared by using this Ni/Fe initial molar ratio. For comparison, NiFe-LDH using the optimum Ni/Fe initial molar ratio was also solely coated on NF to obtain a NiFe-LDH/NF electrode.

The in-situ intercalation of NiO@NiFe-LDH/NF on the electrode was performed in an ultrasonic cleaner, where NiO@NiFe-LDH/NF electrode was immersed into 20 ml formamide solution at 30 °C for 5 min under ultrasonic condition. Finally, the obtained electrode (NiO@NiFe-LDH/NF-US) was washed with distilled water and dried at 60 °C for 12 h. Here, the selected ultrasonic condition was based on preliminary experiments.

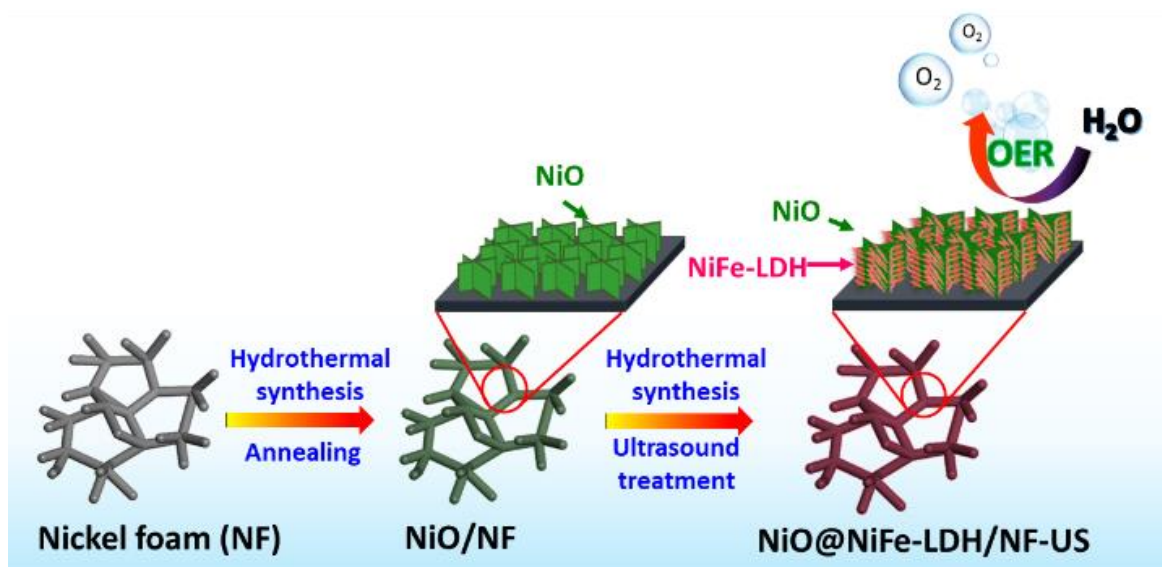


Figure 2.1 Schematic diagram of fabrication NiO@NiFe-LDH/NF-US.

2.2.4 Structural characterization

The morphology of electrode was characterized by SEM (SU8010, Hitachi, Japan) with an EDS (Horiba Scientific, Japan) as well as TEM (JEM-2100F, JEOL, Japan) at an acceleration voltage of 200 kV. The chemical states of the sample were determined by XPS in a Thermo VG Scientific ESCALab250i-XL unit. The crystalline structure and composition of the sample were analyzed by XRD (Rigaku Smartlab, Japan) with Cu-K α radiation ($\lambda=0.15418$ nm) in a range of 20°-80°.

2.2.5 Electrochemical measurements

Electrochemical measurements were conducted on an electrochemical workstation (Potentiostat) with a three electrodes system in a 1.0 M KOH solution (pH=14) at room temperature. Pt wire, Ag/AgCl in saturated 3.0 M KCl, and the above-obtained

electrocatalyst coated NF electrode were used as a counter electrode, reference electrode, and working electrode respectively. Herein, Ag/AgCl reference electrode was used in alkaline solution instead of Hg/HgO one because no obviously different experimental results between them were observed even in a long-term stability test. The OER activity was measured by using linear sweep voltammetry (LSV) with a scan rate of 5 mV s^{-1} at a potential range of 1.2-1.8 V (vs. reversible hydrogen electrode, RHE). All potentials reported in this study were calibrated to the values based on the reversible hydrogen electrode (RHE) using equation $E_{\text{RHE}} = E_{\text{Ag/AgCl}} + 0.059 \text{ pH} + 0.198 \text{ (V)}$, where $E(\text{RHE})$ is the potential referred to RHE and $E(\text{Ag/AgCl})$ is the measured potential against Ag/AgCl (saturated 3.0 M KCl) reference electrode. Electrochemical impedance spectroscopy (EIS) measurement was carried out in a range of 105-0.01 Hz at an overpotential of 340 mV. Electrochemical active surface area (ECSA) of electrocatalyst at the non-faradaic overpotential was measured by cyclic voltammetry (CV) at a potential range of 1.02-1.12 V vs. RHE. The C_{dl} was estimated by plotting current density at different scan rate ($\Delta J = J_a - J_c$) with a potential of 1.07 V. The stability test was performed by chronopotentiometry measurement at high current densities of 50 mA cm^{-2} and 100 mA cm^{-2} for 25 h, respectively, where the fresh alkaline solution was continuously pumped into the test cell.

2.3 RESULTS AND DISCUSSION

2.3.1 Morphology structure and composition characterization.

The surface morphologies of NiO/NF and NiO@NiFe-LDH/NF electrodes were examined using SEM. As shown in Figure. 2.2(a), NiO microflakes cover uniformly on the NF after the hydrothermal synthesis followed by the calcination process. The formation of such macroflake film could be based on heterogeneous nucleation and growth due to the lower interfacial nucleation energy on the NF surface. In particular, it should be noted that the thickness of NiO microflake is less than 100 nm, which could provide enough active sites for the electrochemical reaction. As illustrated in Figure 2.2(b), numerous NiFe-LDH ultrathin nanosheets are well grown on the surfaces of NiO microflakes to form a highly porous core-shell structure. Such a special structure should be a benefit to the full utilization of the active materials. Besides, the voids among the nanosheets on the microflakes should act as effective transportation channels for the

electrolytes and generated gas during the water-splitting process. The NiO@NiFe-LDH catalyst was scratched down from NF, and the structure was observed by using TEM (Figure. 2.2 (c) and (d)). THE high-resolution TEM (HRTEM) image shown in Figure 2.2 (d) reveals that the shell has two visible lattice fringes with interplanar spacings of 0.228 nm and 0.7429 nm, corresponding well to the (015) and (003) planes of NiFe-LDH. Meanwhile, the core has a distinct set of visible lattice fringes with an interplanar spacing of 0.142 nm, corresponds well to the (220) plane of NiO.

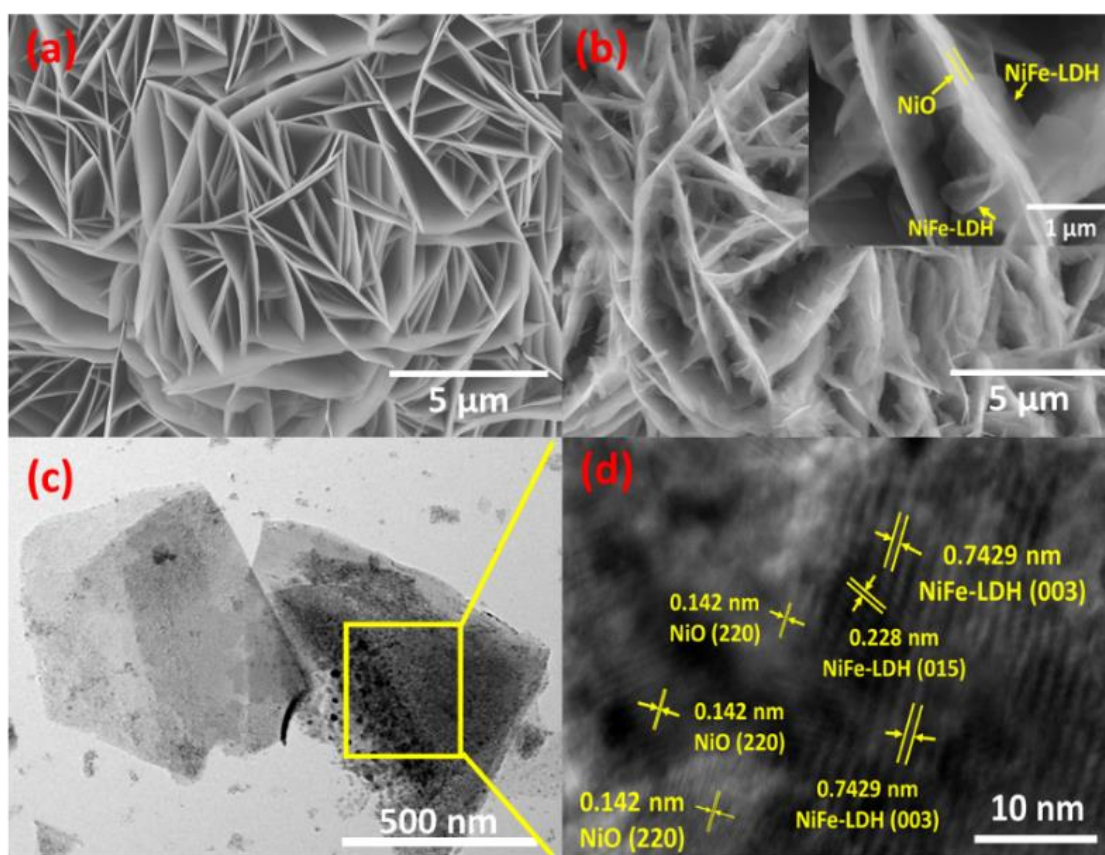


Figure 2.2 (a,b) Surface morphologies of (a) NiO/NF (b) NiO@NiFe-LDH/NF by SEM; (c,d) TEM images of NiO@NiFe-LDH/NF in different magnifications.

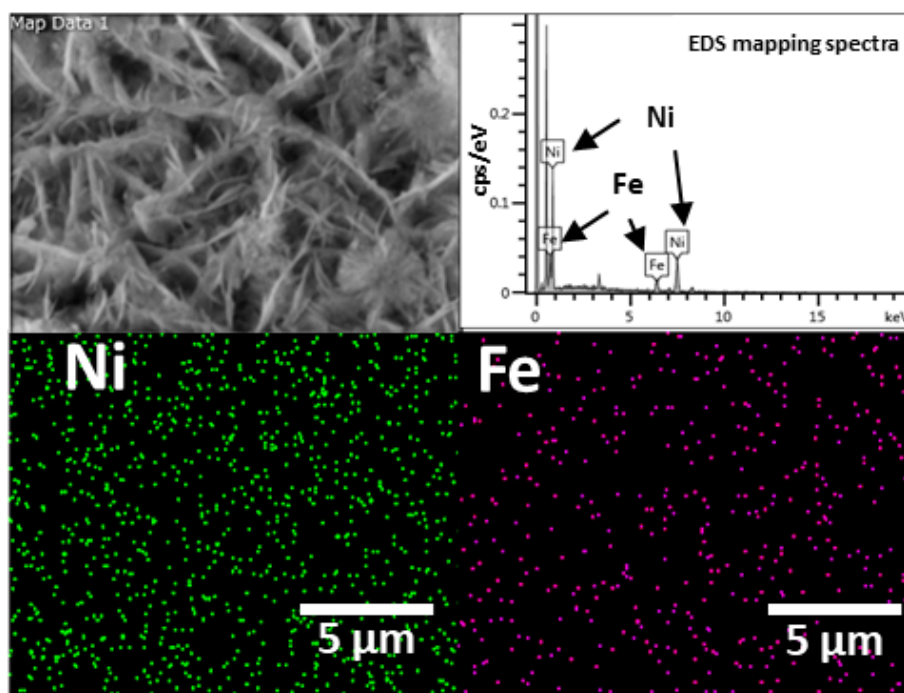


Figure 2.3 EDS spectra in NiO@NiFe/NF-US.

Table 2.1 The molar ratios of Ni/Fe on the surfaces of composites by EDS analysis.

Materials	Ni (wt%)	Fe (wt%)	Molar ratio of Ni:Fe
NiFe-LDH	80.54	19.46	4:1
NiO@NiFe-LDH	95.34	4.66	20:1
NiO@NiFe-LDH-US	95.82	4.18	23:1

In addition, as shown in Figure 2.3, Ni and Fe elements were obviously existed on the electrode, indicating that Fe was combined with Ni in the electrode. The molar ratios of Ni/Fe on the surfaces of electrocatalysts by EDS analysis are shown in Table 2.1. It is found that the molar ratio of Ni/Fe in NiFe-LDH is reasonable. Figure 2.4 shows XRD patterns of NF, NiO/NF, NiFe-LDH/NF, and NiFe-LDH/NF-US. The characteristic peaks at 37.47° , 43.47° , and 62.76° in the XRD pattern of NiO/NF electrode correspond well to the (111), (200) and (220) crystalline facets of NiO (diffraction standard pattern of JPCDC no.47-1049). The characteristic peaks corresponding to (003), (006), (012), (015), (018),

(110), and (113) facets of NiFe-LDH (diffraction standard JPDC no. 40-0215) should be located at 12.29, 23.38, 33.96, 39.3, 46.49, 60.13, 61.33° in the XRD patterns of NiFe-LDH/NF and NiFe-LDH/NF-US. However, due to the strong characteristic peaks of NF, the peaks corresponding to the main (003), (006), and (015) facets of NiFe-LDH are not so obvious in the presence of NiO. Although it can indicate the existence of NiFe-LDH on the electrode, it is difficult to characterize the exact intercalation results for NiFe-LDH/NF-US by using XRD analysis. However, as shown in Figure 2.4(b), the diffraction peak corresponding to (003) facet is shifted from 12.2° to a lower value of 11.8° after the ultrasound treatment in the formamide solution, indicating that inter-layer distance of NiFe LDH is increased to some extent.

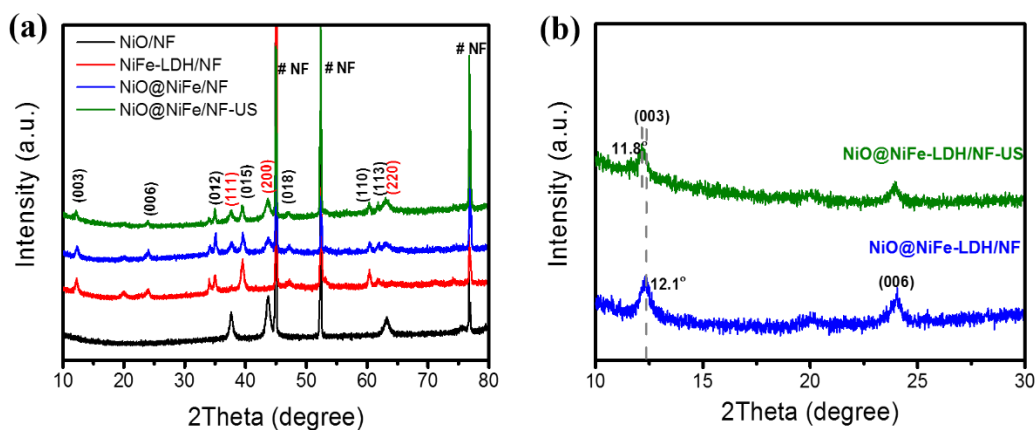


Figure 2.4 (a) XRD patterns of nickel foam (NF), NiO/NF, NiFe-LDH/NF, NiO@NiFe-LDH/NF and NiO@NiFe-LDH/NF-US, (b) XRD patterns of NiO@NiFe-LDH/NF before and after ultrasound treatment in the range of 10-30 degree represent the diffraction peak corresponding to (003) is shifted from 12.2° to a lower value of 11.8° after ultrasound treatment in formamide solution.

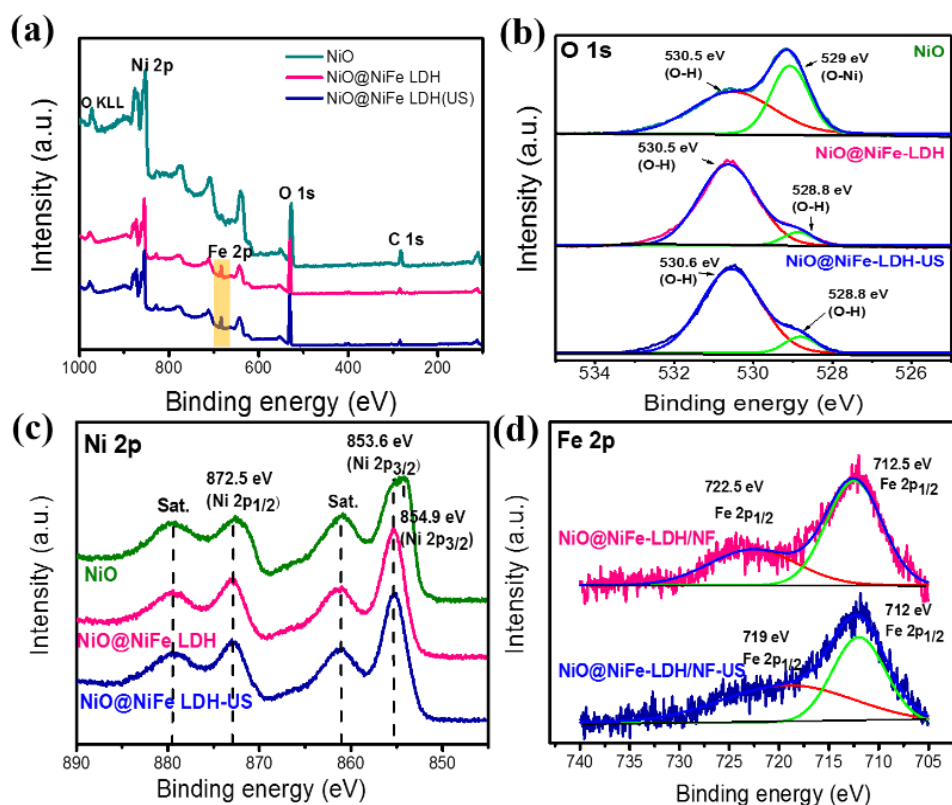


Figure 2.5 (a) XPS survey spectra of NiO, NiO@NiFe-LDH, and NiO@NiFe-LDH-US catalysts. (b) XPS O 1s spectra; (c) Ni 2p spectra; and (d) Fe 2p spectra of NiO, NiO@NiFe-LDH, and NiO@NiFe-LDH-US catalysts.

Table 2.2 The molar ratios of Ni/Fe on the surfaces of composites by XPS analysis.

Materials	Mass atomic %				wt%				Molar ratio of Ni : Fe
	O	C	Ni	Fe	O	C	Ni	Fe	
NiO@NiFe-LDH	52.01	14.17	32.13	1.64	27.9	5.7	63.3	3.1	20:1
NiO@NiFe-LDH-US	51.37	14.41	33.05	1.18	27.4	5.8	64.5	2.2	29:1

Note: To convert mass atomic % to wt% were calculated by the equation: Weight of element = (Mass atomic% x molecular weight)/Avogadro's constant and wt% = (weight of element x 100%)/(total weight of composites)

Herein, the $-\text{C}=\text{O}$ group of formamide (HCONH_2) can form strong hydrogen-bonding with hydroxyl slabs so that it is stable in LDH materials. To further confirm the chemical composition and the surface electronic states, XPS analyses of NiO, NiO@NiFe-LDH, and NiO@NiFe-LDH-US powders scratched down from NF were performed. As shown in Figure 2.5, all the Ni, Fe, and O elements can be defined. It should be noted that the XPS spectra have no obvious change for NiO@NiFe-LDH and NiO@NiFe-LDH-US powders since the intercalation could only expand the layer distance of NiFe-LDH but cannot change the surface electronic states. In the high-resolution XPS O 1s spectra of NiO (Figure 2.5(b)), two bonds are deconvoluted, involving Ni-O bond at 528.8 eV and surface hydroxyl groups or oxygen vacancies (H-O bonds) at 530.5 eV. After coated by NiFe-LDH, it is obvious that the peak intensity of O-H bonds increases, indicating the NiFe-LDH shell covers NiO core. Furthermore, in the high-resolution XPS Ni 2p spectra (Figure 2.5(c)), the peaks at 872.5 and 854.8 eV correspond to Ni-O bonds. Meanwhile, in the high-resolution XPS Fe 2p spectra (Figure 2.5(d)), the peaks at 722.5 and 712.5 eV are assigned to Fe-OH bonds. These results indicate that the oxidation states of Ni and Fe elements in NiO@NiFe-LDH should include 2+ and 3+, respectively [27, 28]. Table 2.2 shows the molar ratios of Ni/Fe on the surfaces of NiO@NiFe-LDH and NiO@NiFe-LDH-US based on XPS analysis, which is almost consistent with the EDS analysis results (Table 2.1). In addition, EDS analysis revealed that the molar ratio of Ni:Fe is about 4:1, which further confirms that the NiFe-LDH was successfully coated on NiO/NF electrode.

2.3.2 Influence condition on the performance of NiO@NiFe-LDH/NF-US electrode.

OER catalytic activities of the as-prepared electrocatalysts for OER were determined by measuring LSV curves in a 1.0 M KOH solution using a typical three-electrode system. The various NiO@NiFe-LDH/NF electrodes were prepared using different Ni/Fe initial molar ratios in the synthesis solutions to get the optimum Ni/Fe initial molar ratio at first. As shown in Figure 2.6, NiO@Ni₄Fe₁-LDH/NF shows the lowest apparent overpotential of 340 mV@50 mAcm⁻².

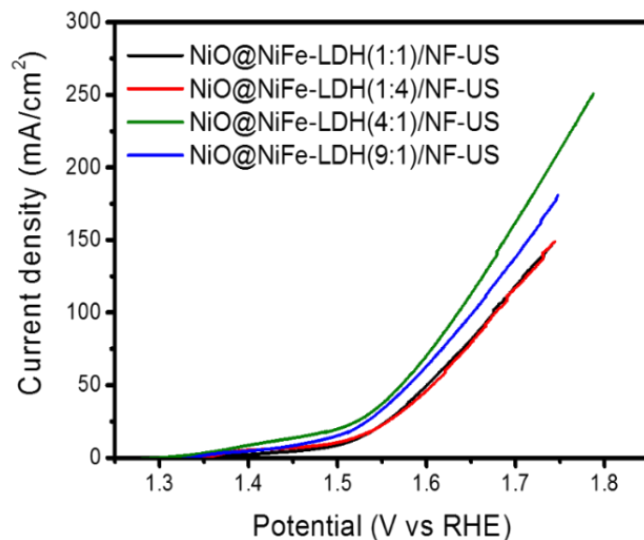


Figure 2.6 LSV curves of NiO@NiFe-LDH/NF-US for OER with a scan rate of 5 mV s^{-1} in 1.0 M KOH solution, where various mole ratios of Ni/Fe (1:1, 4:1, 9:1, 1:4) in initial solution for the synthesis of NiFe-LDH on the NF were used with scan rate 5 mV s^{-1} in 1 M KOH .

2.3.3 Catalytic activity, conductivity and stability analysis of electrodes.

Figure 2.7(a), NiFe-LDH/NF exhibits much higher response current density than NiO/NF at the same overpotential, indicating that NiFe-LDH has higher electrocatalytic activity than NiO. As NiFe-LDH nanosheets are coated on NiO microflakes, the obtained NiO@NiFe-LDH/NF core-shell electrode shows a higher electrocatalytic activity, confirming a synergic effect of these two catalysts. Furthermore, as NiO@NiFe-LDH/NF core-shell electrode is *in-situ* intercalated, the apparent activity of NiO@NiFe-LDH/NF-US is improved more and the apparent overpotentials as low as 210 and 325 mV at current densities of 10 and 40 mA cm^{-2} are achieved, respectively, which is even better than of benchmark catalyst IrO_2 ($225 \text{ mV}@10 \text{ mA cm}^{-2}$). [29] This result also confirms that the *in-situ* intercalation way is benefit to enhancing the performance of LDH materials coated electrode. [25] Table 2.3 compares the results on the apparent overpotential@ 10 mA cm^{-2} obtained in this study with other reported Ni-based electrodes for OER in an alkaline solution. One can see that the NiO@NiFe-LDH/NF-US exhibits a lower apparent overpotential@ 10 mA cm^{-2} than many other Ni-based electrocatalysts such as Ni(OH)_2 (595 mV) [30], NiO/Ni (300 mV) [31], NiFe-LDH (240 mV) [32], NiO/NiFe₂O₄ (302

mV) [33]. The notably improved electrocatalytic performance of NiO@NiFe-LDH/NF-US should arise from the special core-shell microstructure with numerous active sites for OER from NiO, NiFe-LDH and their defective interfaces for effective electrons transfer from NF as well as microchannels in the 3D structures for the diffusions of electrolyte and produced gas. To evaluate the kinetics for the OER, Tafel slopes of the as-prepared electrocatalysts were obtained from the polarization curves. As shown in Figure 2.7(b), the Tafel slopes of nickel foam (NF), NiO/NF, NiFe-LDH/NF, NiO@NiFe-LDH/NF, and NiO@NiFe-LDH/NF-US are 157.3, 155.8, 123, 80, and 72 mV dec⁻¹, respectively. It should be noted that the Tafel slopes of both NiO@NiFe-LDH/NF and NiO@NiFe-LDH/NF-US are lower than that of the benchmark electrocatalyst of IrO₂ (89.2 and 149 mV dec⁻¹), [29, 34] demonstrating the favorable OER reaction kinetics with efficient electron and mass transfers between materials and electrolyte media solution in the system. [35, 36] As stated above, it should be attributed to the special NiO microflake @ NiFe-LDH nanosheet core-shell structure, which could provide a large surface area for the fast ion diffusion and more active sites for OER, and simultaneously provide an efficient pathway of electron transfer from the inner NiO microflake layer to the outer NiFe-LDH nanosheets. Chronopotentiometry (CP) plots (Figure. 2.7(c)) were also employed to measure the apparent overpotential of various electrodes for supporting current density of 10 mA cm⁻² to avoid the influence of charging during LSV measurements. One can see that the NiO@NiFe-LDH/NF-US also shows the lowest apparent overpotential, indicating that NiFe-LDH coated on NiO microflakes enables an excellent electrical connection between them. In addition, as shown in Figure 2.7(d), the Nyquist plots by the electrochemical impedance spectra (EIS) analysis revealed that the NiO@NiFe-LDH/NF-US electrode (0.98 Ω) displays a smaller series resistance (R_s) than NiO@NiFe-LDH/NF one (1.26 Ω), indicating that the former catalyst has a better interface connection with the substrate. Thusly, the ultrathin NiFe-LDH nanosheets coated on NiO microflakes can effectively improve the whole electrical conductivity and such a unique heterostructure could provide an ideal pathway for electron transport without high kinetic limitation. [37]

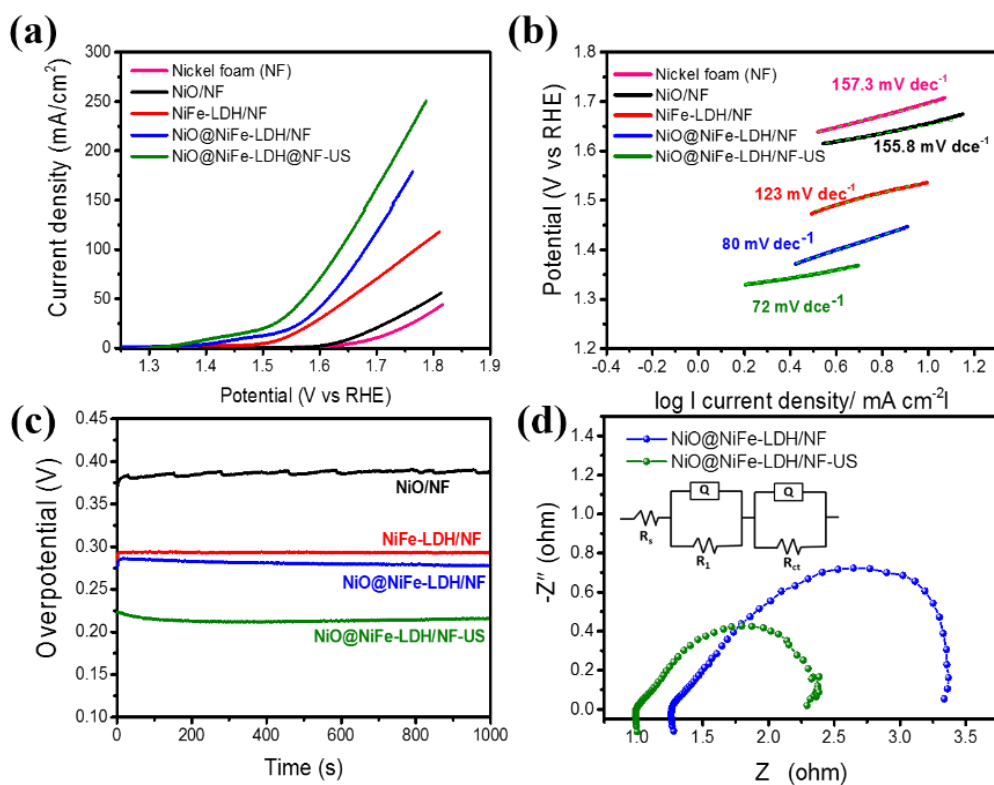


Figure 2.7 (a) LSV curves of NiO/NF, NiFe-LDH/NF, NiO@NiFe-LDH/NF and NiO@NiFe-LDH/NF-US with a scan rate of 5 mV/s; (b) Tafel plots of NiO/NF, NiFe-LDH/NF, NiO@NiFe-LDH/NF, and NiO@NiFe-LDH/NF-US collected in 1.0 M KOH electrolyte; (c) Chronopotentiometry lines of NiO/NF, NiFe-LDH/NF, NiO@NiFe-LDH/NF and NiO@NiFe-LDH/NF-US at 10 mA cm⁻² current density with a duration of 1000 sec; (d) EIS spectra of NiFe-LDH@NiO/NF and NiFe-LDH@NiO/NF-US electrodes at an overpotential of 340 mV.

To further understand the enhanced OER activity of NiO@NiFe-LDH/NF-US, electrochemical activity surface areas (ECSAs) of NF, NiO/NF, NiFe-LDH/NF, NiO@NiFe-LDH/NF, and NiO@NiFe-LDH/NF-US are calculated based on cyclic voltammetry (CV) test at various scan rates in the non-Faraday region (see Figure 2.8). The electrochemical double layer capacitance (C_{dl}) is estimated by plotting the $\Delta j = (j_a - j_c)$ at 1.07 V, where j_a and j_c are the anodic and cathodic current densities, respectively. The linear relationships of C_{dl} and scan rate (Figure 2.10a) represent that the slope of NiO@NiFe-LDH/NF-US core-shell electrode has higher capacitance (6.1 mF/cm²) than NiO@NiFe-LDH/NF (4.3 mF/cm²), NiFe-LDH/NF (3 mF/cm²), NiO/NF (2.2 mF/cm²)

or nickel foam (2.1 mF/cm^2). Such a high ESCA means that more active sites can be exposed to the OER, which should be attributed to the special core-shell hetero-architecture. As a result, it is favorable for water molecule adsorption and enhances the contact between the electrolyte and the active sites in the electrode. [38] The ECSA normalization electrocatalytic performance was evaluated by setting the ECSA of NF as 1, and as such, the ECSAs of NiO@NiFe-LDH/NF-US, NiO@NiFe-LDH/NF, NiFe-LDH/NF and NiO/NF are 3.05, 2.15, 1.5 and 1.1, respectively. The obtained OER polarization curves based on the normalized LSV current density of various electrodes based on the ESCA corresponding to Figure 2.10(a) are shown in Figure 2.9. Before ECSA normalization, the apparent overpotentials are $210 \text{ mV}@10 \text{ mA cm}^{-2}$ and $325 \text{ mV}@40 \text{ mA cm}^{-2}$ for NiO@NiFe-LDH/NF-US. However, after ECSA normalization, these values become to $299 \text{ mV}@10 \text{ mA cm}^{-2}$ and $420 \text{ mV}@40 \text{ mA cm}^{-2}$. Similarly, after the ECSA normalization, the overpotentials of NiO@NiFe-LDH/NF, NiFe-LDH/NF and NiO/NF change to 320, 330, and $430 \text{ mV}@10 \text{ mA cm}^{-2}$ from 265, 297, and $400 \text{ mV}@10 \text{ mA cm}^{-2}$, and 430, 444 and $549 \text{ mV}@40 \text{ mA cm}^{-2}$ from 367, 396 and $535 \text{ mV}@40 \text{ mA cm}^{-2}$, respectively. It should be noted that after the ECSA normalization, the real overpotential difference of NiO@NiFe-LDH/NF-US and NiO@NiFe-LDH/NF becomes narrow (from 55 to $21 \text{ mV}@10 \text{ mA cm}^{-2}$), indicating that ECSA of the coated electrocatalysts on the NF plays the main role on the performance. Although formamide intercalating changes the microstructure of NiFe-LDH to some extent and is benefit to the diffusion of reactants and generated gases, it does not change the real active sites greatly.

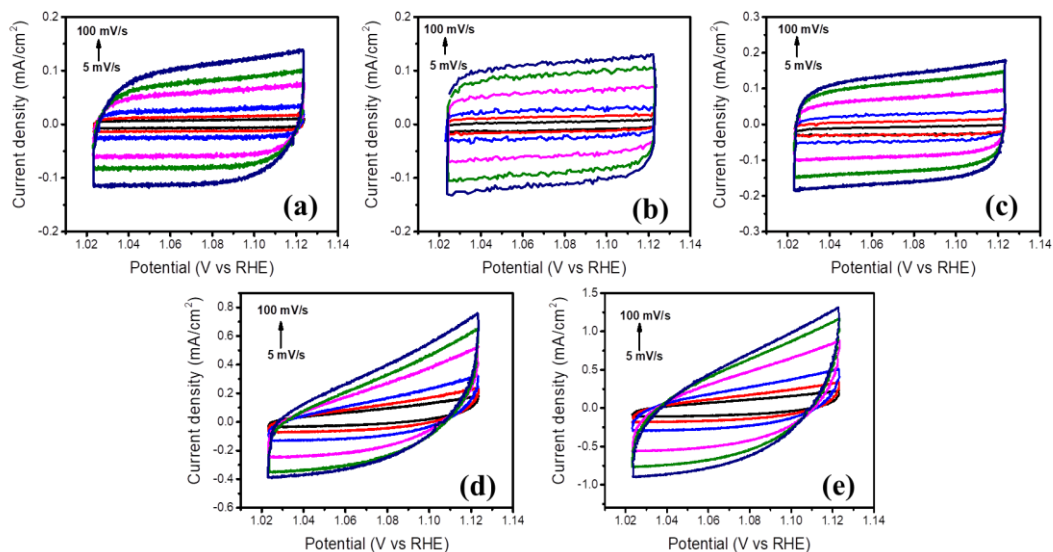


Figure 2.8 CV curves for determining electrochemical activity surface areas (ECSAs) of (a) nickel foam (NF) substrate, (b) NiO/NF, (c) NiFe-LDH/NF, (d) NiFe-LDH@NiO/NF and (e) NiFe-LDH@NiO/NF-US collected between potential range 1.024-1.124 V (vs RHE) with scan rate 5, 10, 20, 50, 70 and 100 mV/s respectively in 1M KOH solution.

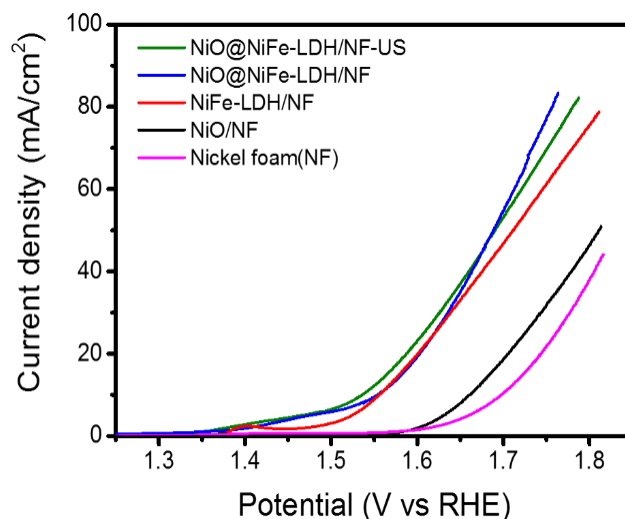


Figure 2.9 OER polarization curves of NF, NiO/NF, NiFe-LDH/NF, NiO@NiFe-LDH/NF and NiO@NiFe-LDH/NF-US normalized based on ECSA.

Figure 2.10(b) shows the multi-step chronopotentiometry curve of NiO@NiFe-LDH/NF-US, which was obtained by measuring it from the initial current density of 20 mA cm^{-2} and ended at 200 mA cm^{-2} with an increased step of 20 mA cm^{-2} interval during 500 s data collection. It can be seen that the potential instantaneously levels off at 1.55 V at 20 mA cm^{-2} and remains at a constant for the next 500 s, and other steps present similar results up to 200 mA cm^{-2} . It demonstrates that NiO@NiFe-LDH/NF-US electrode has outstanding mass transport property and mechanical robustness.^{39,40} O_2 evolution amounts based on the theoretical calculation and experimental results over NiO@NiFe-LDH/NF-US coated electrode were also investigated. As shown in Figure 2.13, the fitted curve of theoretical O_2 production amount is $y_1 = 0.00154X_1$ while the fitted curve of the measured O_2 production amount is $y_2 = 0.00151X_2$, Thusly, the faradic efficiency is $y_2/y_1 = 0.00151/0.00154 \sim 98.1\%$. The long-term durability of NiO@NiFe-LDH/NF-US for OER was assessed by a chronoamperometry measurement for 50 h, in which the electrode worked at a current density of 50 mA cm^{-2} for 25 h at first and then, the current density was increased to 100 mA cm^{-2} for the other 25 h to verify if it can be applied for a large scale commercial utilization at a high current density. As shown in Figure. 2.10(c), the overpotential of this electrode remained almost unchanged under two relatively high current densities, Furthermore, as shown in Figures 2.11 and 2.12, the morphology and XRD pattern also remain almost unchanged. It indicates excellent stability of the NiO@NiFe-LDH/NF-US towards the OER.

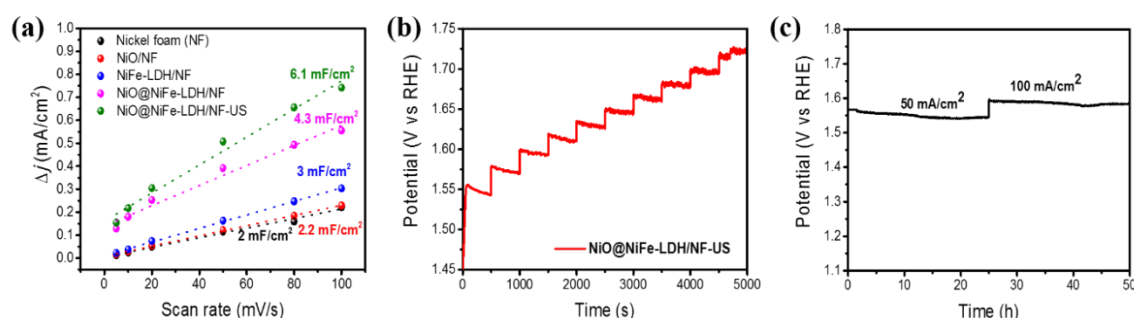


Figure 2.10 (a) Capacitive current vs scan rate at a potential range from 1.02 to 1.12 V (vs RHE) with different scan rates in the range of 5-100 mV/s; (b) Multi-current process of NiO@NiFe-LDH/NF-US electrode in 1.0 M KOH electrolyte (The current density started from 20 mA/cm^2 and ended at 200 mA/cm^2 with an increment of 20 mA/cm^2 during 500 sec; (c) Time-dependent chonopotentiometry curve of NiO@NiFe-LDH/NF-US

US at fixed current densities of 50 and 100 mA cm⁻² with a total duration time of 50 h.

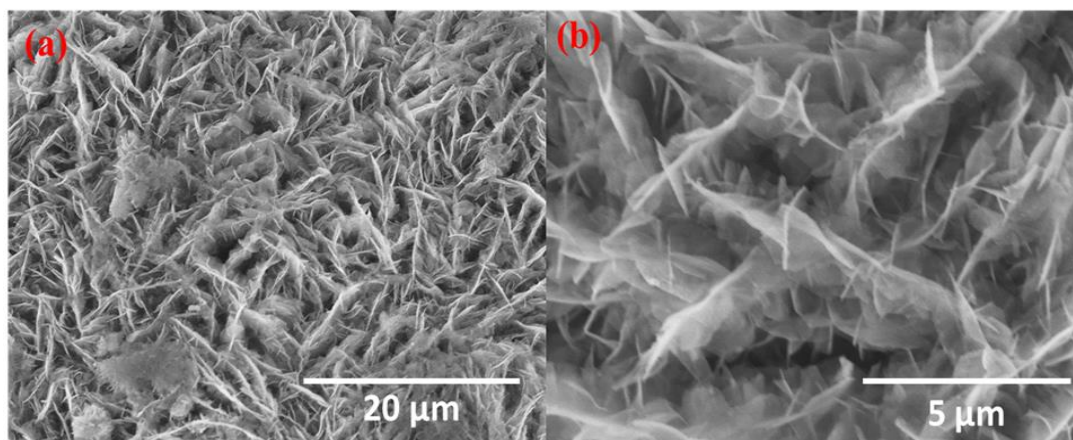


Figure 2.11 SEM images of NiO@NiFe-LDH/NF-US with different magnifications after 50 h long-term stability test.

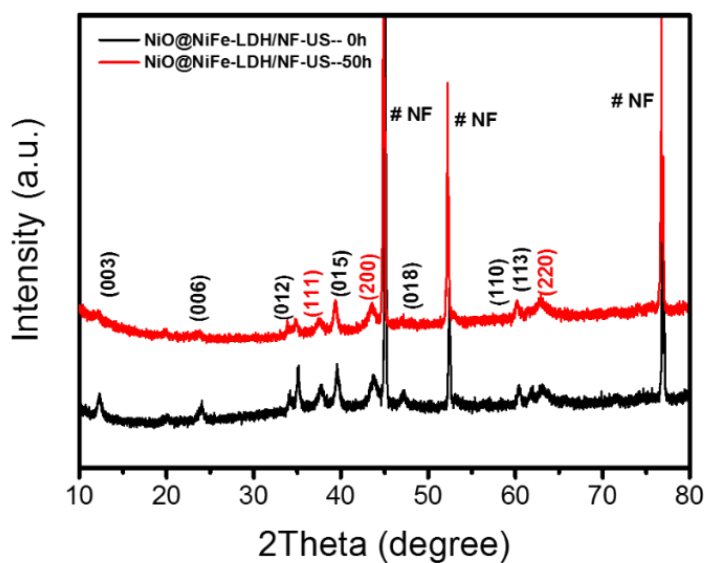


Figure 2.12 XRD patterns of NiO@NiFe-LDH/NF-US before and after 50 h long-term stability test.

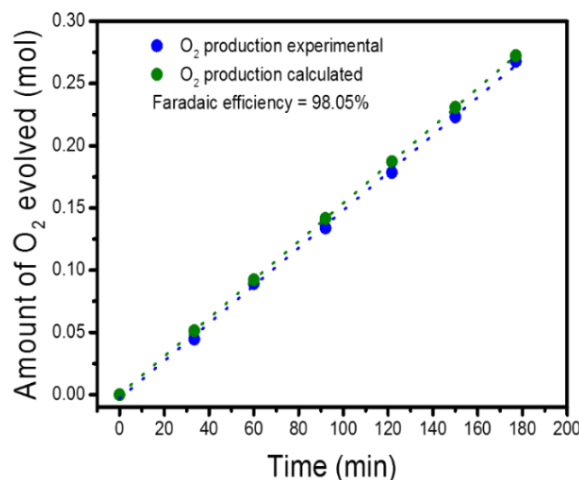


Figure 2.13 evolution amounts based on the theoretical calculation and experimental results over NiO@NiFe-LDH/NF-US coated electrode.

Summarily, the good performance of NiO@NiFe-LDH/NF-US based electrode should be attributed to a series of advantages of catalyst heterostructure and intercalation treatment. Firstly, in this study, it is believed that the NiO is effective for cleaving the HO–H bond in H₂O molecule, [41] which could be a benefit for the conversion of adsorbed -OH to O₂. Secondly, the interlayer distance of NiFe-LDH can be extended by formamide to expose more catalytic active sites and provide wider channels for the diffusions of electrolyte as well as generated gases. Thirdly, as revealed by the microstructure of composite, the good interface connection between them, facilitating electrons transferring from the catalyst array to the current collector during anodic polarization. Fourthly, the porous core/shell array configuration largely increases the amount of contact areas between the electrolyte and active sites, and simultaneously greatly facilitates ion and electron diffusions. Moreover, the inside NiO flakes not only serve as physical support for NiFe-LDH nanoarrays but also provide the channels for electron transport, and simultaneously, the highly porous NiFe-LDH nanosheets are well wrapped around the NiO flakes, which favors the exposure of more active sites and thus enhances the catalytic activity per geometric area. Fifthly, the open spaces between neighboring composite branches facilitate the diffusion of electrolytes and the generation of oxygen. Finally, the binder-free nature avoids the increase of various transfer resistances, the blockage of active sites, and the inhibition of diffusion.

Table 2.3 Comparison of this work with the recently reported Ni-based electrodes for OER in alkaline solution.

Catalysts	η_{10} (mV)	η_{50} (mV)	Tafel slope (mV/dec)	Electrolyte	Ref
NiFe@NiO/NF (This work)	210 (ECSA:299)	340 (ECSA η_{40} :420)	78	1M KOH	This work
Ni(OH) ₂	300	N/A	53	1M KOH	[11]
Ni(OH) ₂	595	N/A	N/A	1M KOH	[41]
NiOx	330	N/A	54	1M KOH	[11]
NiO/Ni	345	N/A	53	1M KOH	[31]
Fe dope NiO nanotube	418	N/A	56	1M KOH	[42]
Fe dope β -Ni(OH) ₂	260	N/A	32	1MKOH	[43]
NiO/NiFe ₂ O ₄	302	N/A	42	1M KOH	[33]
NiO-NiFe ₂ O ₄ /rGO	296	N/A	43	1M KOH	[44]
NiFe-LDH	224	N/A	52.8	1M KOH	[26]
NiFe-LDH-US	203	230	42	1M KOH	[26]
NiFe LDH	240	N/A	N/A	1M KOH	[32]
B-Ni(OH) ₂ nanoparticle	390	N/A	65	1M KOH	[45]
NiCo-LDH	420	N/A	113	1M KOH	[46]
NiCo ₂ O ₄	290	N/A	53	1M NaOH	[47]
Ni _{2.0} Mo _{0.26} @NC	310	N/A	62.7	1M KOH	[48]

2.4 CONCLUSION

NiO microflake@NiFe-LDH nanosheet heterostructure electrocatalysts for OER in electrochemical water splitting process were successfully fabricated by using a two-step hydrothermal synthesis followed by a calcination process. The obtained electrocatalysts with a 3D porous structure showed high-performance for OER with a low apparent overpotential of 265 mV@10 mA cm⁻². As the NiO@NiFe-LDH coated electrode was further treated in organic solution via ultrasound for in-situ intercalation, the charge transition resistance was obviously reduced and the required apparent overpotential@10 mA cm⁻² was reduced from 265 to 210 mV with a small Tafel slope 72 mV dec⁻¹ in alkaline media solution. Furthermore, the optimized NiO@NiFe-LDH composite exhibited excellent long-term stability in 50 h even at high current densities of 50 and 100 mA cm⁻². The synergistic interactions between NiO microflakes and NiFe-LDH nanosheets and the special 3D nanostructure are considered to contribute to the enhanced activity for OER. This study provided a facial way to fabricate low-cost electrocatalysts with high activity as well as stability.

REFERENCE

- [1] X. Li, X. Hao, A. Abudula, G. Guan, Nanostructured Catalysts for Electrochemical Water Splitting: Current State and Prospects. *J. Mater. Chem. A*, 2016, 4, 11973-12000.
- [2] X. Li, S. Li, A. Yoshida, S. Sirisomboonchai, K. Tang, Z. Zuo, X. Hao, A. Abudula, G. Guan, Mn Doped CoP Nanoparticle Clusters: An Efficient Electrocatalyst for Hydrogen Evolution Reaction, *Catal. Sci. Technol.*, 2018, 8, 4407-4412.
- [3] C. Tang, H. F. Wang, X. L. Zhu, B. Q. Li, Q. Zhang, Advances in Hybrid Electrocatalysts for Oxygen Evolution Reactions: Rational Integration of NiFe Layered Double Hydroxides and Nanocarbon, *Part. Syst. Charact.* 2016, 33, 473–486
- [4] R. Li, C. Li, Photocatalytic Water Splitting on Semiconductor-Based Photocatalysts, *Adv. Catal.*, 2017, 60, 1-57.
- [5] N. T. Suen, S. F. Hung, Q. Quan, N. Zhang, Y. J. Xu, H. M. Chen, Electrocatalysis for the Oxygen Evolution Reaction: Recent Development and Future Perspectives, *Chem. Soc. Rev.* 2017, 46, 337-365.

- [6] M. Carmo, D. L. Fritz, J. Merge, D. A. Stolten, Comprehensive Review on PEM Water Electrolysis, *Int. J. Hydrogen Energ.* 2013, 38 (12), 4901-4934.
- [7] R. Tobias, O. Mehtap, S. Peter, Electrocatalytic Oxygen Evolution Reaction (OER) on Ru, Ir, and Pt Catalysts: A Comparative Study of Nanoparticles and Bulk Materials, *ACS Catal.* 2012, 2 (8), 1766-1772.
- [8] G. Li, S. Li, J. Ge, C. Liu, W. Xing, Discontinuously Covered IrO₂-RuO₂@Ru Electrocatalysts for The Oxygen Evolution Reaction: How High Activity and Long-Term Durability can be Simultaneously Realized in The Synergistic and Hybrid Nano-Structure, *J. Mater. Chem. A.* 2017, 5, 17221-17229.
- [9] Y. Xue, S. Sun, Q. Wang, Z. Dong, Z. Liu, Transition Metal Oxide-Based Oxygen Reduction Reaction Electrocatalysts for Energy Conversion Systems with Aqueous Electrolytes, *J. Mater. Chem. A.* 2018, 6, 10595-10626.
- [10] V. Vij, S. Sultan, A. M. Harzandi, A. Meena, J. N. Tiwari, W. G. Lee, T. Yoon, K. S. Kim, Nickel-Based Electrocatalysts for Energy-Related Applications: Oxygen Reduction, Oxygen Evolution, and Hydrogen Evolution Reactions, *ACS Catal.* 2017, 7 (10), 7196-7225.
- [11] L. A. Stern, X. Hu, Enhanced Oxygen Evolution Activity by NiO_x and Ni(OH)₂ Nanoparticles, *Faraday Discuss.* 2014, 176, 363-379.
- [12] S. Klaus, Y. Cai, M. W. Louie, L. Trotochaud, A. T. Bell, Effects of Fe Electrolyte Impurities on Ni(OH)₂/NiOOH Structure and Oxygen Evolution Activity, *J. Phys. Chem. C.*, 2015, 119 (13), 7243-7254.
- [13] W. Zhou, D. Kong, X. Jia, C. Ding, C. Cheng, G. Wen, NiCo₂O₄ Nanosheet Supported Hierarchical Core-Shell Arrays for High-Performance Supercapacitors, *J. Mater. Chem. A.*, 2014, 2, 6310-6315
- [14] B. M. Hunter, H. B. Gray, A. M. Müller, Earth-Abundant Heterogeneous Water Oxidation Catalysts *Chem. Rev.*, 2016, 116 (22), 14120-14136.
- [15] H. Wang, T. Zhou, P. Li, Z. Cao, W. Xi, Y. Zhao, Y. Ding, Self-Supported Hierarchical Nanostructured NiFe-LDH and Cu₃P Weaving Mesh Electrodes for Efficient Water Splitting, *ACS Sustainable Chem. Eng.*, 2018, 6 (1), 380-388.
- [16] Z. Wu, Z. Zou, J. Huang, F. Gao, NiFe₂O₄ Nanoparticles/NiFe Layered Double-Hydroxide Nanosheet Heterostructure Array for Efficient Overall Water Splitting at large Current Densities, *ACS Appl. Mater. Interfaces*, 2018, 10 (31), 26283-26293

- [17] H. Liang, A. N. Gandi, C. Xia, M. N. Hedhili, D. H. Anjum, U. Schwingenschlogl, H. N. Alshareef, Amorphous NiFe-OH/NiFeP Electrocatalyst Fabricated at Low Temperatures for Water Oxidation Applications, *ACS Energy Lett.*, 2017, 2 (5), 1035-1042.
- [18] C. C. L. McCrory, S. Jung, J. C. Peters, T. F. Jaramillo, Benchmarking Heterogeneous Electrocatalysts for the Oxygen Evolution Reaction, *J. Am. Chem. Soc.*, 2013, 135 (45), 16977-16987.
- [19] G. Fan, F. Li, D. G. Evans, X. Duan, Catalytic Applications of Layered Double Hydroxides: Recent Advances and Perspectives, *Chem. Soc. Rev.* 2014, 43, 7040-7066.
- [20] J. Yu, Q. Wang, D. O'Hare, L. Sun, Preparation of Two Dimensional Layered Double Hydroxide Nanosheets and Their Applications, *Chem. Soc. Rev.*, 2017, 46, 5950-5974.
- [21] B. M. Hunter, W. Hieringer, J. R. Winkler, H. B. Gray, A. M. Müller, Effect of Interlayer Anions on [NiFe]-LDH Nanosheet Water Oxidation Activity, *Energy Environ. Sci.*, 2016, 9, 1734-1743.
- [22] M. Görlin, P. Chernev, J. F. De Araújo, T. Reier, S. Dresp, B. Dresp, R. D. H. Krähnert, P. Strasser, Oxygen Evolution Reaction Dynamics, Faradaic Charge Efficiency, and The Active Metal Redox States of Ni-Fe Oxide Water Splitting Electrocatalysts, *J. Am. Chem. Soc.*, 2016, 138 (17), 5603-5614.
- [23] J. Yu, F. Yang, G. Cheng, W. Luo, Construction of a Hierarchical NiFe Layered Double Hydroxide with A 3D Mesoporous Structure as an Advanced Electrocatalyst for Water Oxidation, *Inorg. Chem. Front.*, 2018, 5, 1795-1799.
- [24] F. Song, X. Hu, Exfoliation of layered double hydroxides for enhanced oxygen evolution catalysis, *Nat. Commun.*, 2014, 5, 4477.
- [25] G. Abellán, J. A. Carrasco, E. Coronado, J. Romero, M. Varela, Alkoxide-intercalated CoFe-layered double hydroxides as precursors of colloidal nanosheet suspensions: structural, magnetic and electrochemical properties, *J. Mater. Chem. C.* 2014, 2, 3723-3731.
- [26] X. Li, X. Hao, Z. Wang, A. Abudula, G. Guan, In-situ Intercalation of NiFe LDH Materials: An Efficient Approach to Improve Electrocatalytic Activity and Stability for Water Splitting, *J. Power Sources*, 2017, 347, 193-200.

- [27] J. Liu, Y. Zheng, Z. Wang, Z. Lu, A. Vasileff, S. Z. Qiao, Free-Standing Single-Crystalline NiFe-Hydroxide Nanoflake Arrays: A Self-Activated and Robust Electrocatalyst for Oxygen Evolution, *Chem. Commun.*, 2018, 54, 463-466.
- [28] H. Q. Wangac, X. P. Fana, X. H. Zhanga, Y. G. Huanga, Q. Wub, Q. C. Pana, Q. Y. Li, In Situ Growth of NiO Nanoparticles on Carbon Paper as A Cathode for Rechargeable Li–O₂ Batteries, *RSC Adv.*, 2017, 7, 23328-23333.
- [29] L. Yu, H. Zhou, J. Sun, I. K. Mishra, K. Ishwar, D. Luo, F. Yu, Y. Yu, S. Chen, Z. Ren, Amorphous NiFe Layered Double Hydroxide Nanosheets Decorated on 3D Nickel Phosphide Nanoarrays: A Hierarchical Core–Shell Electrocatalyst for Efficient Oxygen Evolution, *J. Mater. Chem. A.*, 2018, 6, 13619-13623.
- [30] X. Zhou, Z. Xia, Z. Zhang, Y. Ma, Y. Qu, One-Step Synthesis of Multi-Walled Carbon Nanotubes/Ultra-thin Ni(OH)₂ Nanoplate Composite as Efficient Catalysts for Water Oxidation, *J. Mater. Chem. A.*, 2014, 2, 11799-11806.
- [31] J. Liang, Y. Z. Wang, C. C. Wang, S. Y. Lu, In Situ Formation of NiO on Ni Foam Prepared with a Novel Leaven Dough Method as An Outstanding Electrocatalyst for Oxygen Evolution Reactions, *J. Mater. Chem. A.*, 2016, 4, 9797-9806.
- [32] J. Luo, J. H. Im, M. T. Mayer, M. Schreier, M. K. Nazeeruddin, N. G. Park, S. D. Tilley, H. J. Fan, M. Grätzel, Water Photolysis at 12.3% Efficiency via Perovskite Photovoltaics and Earth-Abundant Catalysts, *Science*, 2014, 345 (6204), 1593-1596.
- [33] G. Liu, X. Gao, K. Wang, D. He, J. Li, Uniformly Mesoporous NiO/NiFe₂O₄ Biphasic Nanorods as Efficient Oxygen Evolving Catalyst for Water Splitting, *Int. J. Hydrogen Energy*, 2016, 41 (40), 17976-17986.
- [34] L. Jiao, Y. X. Zhou, H. L. Jiang, Metal–Organic Framework-Based CoP/Reduced Graphene Oxide: High-Performance Bifunctional Electrocatalyst for Overall Water Splitting, *Chem. Sci.*, 2016, 7, 1690–1695.
- [35] E. G. L. Michael, L. D. Richard, Oxygen Evolution at Oxidised Iron Electrodes: A Tale of Two Slopes, *Int. J. Electrochem. Sci.*, 2012, 7 (10), 9488 – 9501.
- [36] S. Tatsuya, A. T. Garcia-Esparza, K. Takanabe, Insight on Tafel Slopes from a Microkinetic Analysis of Aqueous Electrocatalysis for Energy Conversion, *Scientific Reports*, 2015, 5, 13801.
- [37] D. A. García-Osorio, R. Jaimes, J. Vazquez-Arenas, R. H. Lara, J. Alvarez-Ramirez, The Kinetic Parameters of the Oxygen Evolution Reaction (OER) Calculated on

- Inactive Anodes via EIS Transfer Functions: OH Formation, *J. Electrochem. Soc.*, 2017, 164, 3321-3328.
- [38] L. Yu, H. Zhou, J. Sun, F. Qin, F. Yu, J. Bao, Y. Yu, S. Chen, Z. Ren, Cu Nanowires Shelled with NiFe Layered Double Hydroxide Nanosheets as Bifunctional Electrocatalysts for Overall Water Splitting, *Energy Environ. Sci.* 2017, 10, 1820-1827.
- [39] X. Lu and C. Zhao, Electrodeposition of Hierarchically Structured Three-Dimensional Nickel–Iron Electrodes for Efficient Oxygen Evolution at High Current Densities, *Nat. Commun.* 2015, 6, 6616/1-7.
- [40] J. Zhao J, X. Ren, H. Ma, X. Sun, Y. Zhang, T. Yan, Q. Wei, D. Wu, Synthesis of Self-Supported Amorphous CoMoO₄ Nanowire Array for Highly Efficient Hydrogen Evolution Reaction. *ACS Sustainable Chem. Eng.* 2017, 5 (11), 10093–10098.
- [41] X. Zhou, Z. Xia, Z. Zhang, Y. Ma, Y. Qu, One-step synthesis of multi-walled carbon nanotubes/ultra-thin Ni(OH)₂ nanoplate composite as efficient catalysts for water oxidation. *J. Mater. Chem. A.* 2014, 2, 11799-11806.
- [42] G. Wu, W. Chen, X. Zheng, D. He, Y. Luo, X. Wang, J. Yang, Y. Wu, W. Yan, Z. Zhuang, X. Hong, Y. Li, Hierarchical Fe-doped NiOx nanotubes assembled from ultrathin nanosheets containing trivalent nickel for oxygen evolution reaction. *Nano Energy* 2017, 38, 167-174.
- [43] K. Zhu, H. Liu, M. Li, X. Li, J. Wang, X. Zhu X, W. Yang, Atomic-scale topochemical preparation of crystalline Fe³⁺-doped β-Ni(OH)₂ for an ultrahigh-rate oxygen evolution reaction. *J. Mater. Chem. A.* 2017, 5, 7753-7758.
- [44] G. Zhang, Y. Li, Y. Zhou, F. Yang, NiFe Layered Double Hydroxide-Derived NiO-NiFe₂O₄/Reduced Graphene Oxide Architectures for Enhanced Electrocatalysis of Alkaline Water Splitting. *Chem. Electro. Chem.* 2016, 3, 1927-1936.
- [45] Z. Lu, W. Xu, W. Zhu, Q. Yang, X. Lei, J. Lui, Y. Li, X. Sun, X. Duan, Three-dimensional NiFe layered double hydroxide film for high-efficiency oxygen evolution reaction. *Chem. Commun. (Cambridge, U. K.)* 2014, 50, 6479-6482.
- [46] J. Jiang, A. Zhang, L. Li, L. Ai, Nickel–cobalt layered double hydroxide nanosheets as high-performance electrocatalyst for oxygen evolution reaction. *J. Power Sources* 2015, 278, 445-451.

- [47] X. Gao, H. Zhang, Q. Li, X. Yu, Z. Hong, X. Zhang, C. Liang, Z. Lin, Hierarchical NiCo₂O₄ Hollow Microcuboids as Bifunctional Electrocatalysts for Overall Water-Splitting. *Angew. Chem. Int. Ed.* 2016, 55, 6290-6294.
- [48] X. Zhang, L. Huang, Y. Han, M. Xu, S. Dong, Nitrogen-doped carbon encapsulating γ -MoC/Ni heterostructures for efficient oxygen evolution electrocatalysts. *Nanoscale* 2017, 9, 5583-5588.

CHAPTER 3 Terephthalic Acid Induced Binder-free NiCoP-carbon Nanocomposite for Highly Efficient Electrocatalysis of Hydrogen Evolution Reaction

3.1 INTRODUCTION

The large-scale use of fossil fuels in past years has caused serious environmental pollution and global warming. It is time to use renewable energy such as wind and solar energy to replace fossil energy. However, except the biomass energy, almost all other renewable energy is unstable and not so easy to be effectively used. One of the promising ways is to use the unstable electricity to split water for the production of hydrogen, an environmentally friendly fuel, which can be widely applied in a hydrogen society. Water electrolysis is a traditional and simple way to produce hydrogen, however, limited efficiency of electrolysis and usage of expensive electrodes hinder its wider implementation in society. In the water electrolysis process, two half-reactions, i.e., hydrogen evolution reaction (HER) and oxygen evolution reaction (OER) are included. [1] Both need electrocatalysts with high activity and stability. To date, Pt-based materials are still the most efficient catalysts with superior stability for HER. However, the high cost and scarcity of Pt hinder its large-scale application. [2, 3] As such, many researchers devote themselves to finding inexpensive but highly efficient electrocatalysts such as transition metal carbides, transition metal sulfides [4, 5], and transition metal phosphide for HER in a wide pH range. [6-8]

Transition metal phosphides (TMPs) are a family of earth-abundant materials with an outstanding excellent electrocatalytic performance for HER since their appropriate surface structure can provide rich proton acceptor sites for the moderately affinitive adsorption of the H atoms and the desorption of H₂ gas. Especially, the iron triad phosphides have been identified to have high electrocatalytic activity toward HER. [9, 10] TMPs mainly include iron, cobalt, and nickel phosphides and their binary or ternary mixtures with various morphologies such as nanorods, nanosheets, nanospheres, and so on. [11] Among them, nickel phosphide (Ni₂P) exhibited the highest activity in the acid electrolyte. [12] However, the strongly acidic environment usually results in the erosion of electrolysis devices, and simultaneously the acid vapor could contaminate the produced

H₂ gas during the electrolysis process. Thus, it has more advantages by designing novel electrocatalysts working in either the alkaline or even neutral electrolytes. Recently, it is found that the bimetal phosphides could show higher activity for HER than the single metal ones since the redistributions of the valence electrons among the binary transition metal atoms could generate more active sites, leading to the increase of the HER catalytic efficiency. [13, 14] Recently, it is found that the three-dimensional (3D)-NiCoP catalyst had an excellent activity in both acid and alkaline electrolytes. [15]

To stabilize the active sites and improve the conductivity of HER electrocatalysts, combining TMPs with conductive materials such as carbon-based materials is considered an effective way. Moreover, the synergic interaction between carbon and catalysts could decrease the adsorption energy of the active species and prevent the catalyst erosion during electrolysis, resulting in lower overpotential and higher stability for the electrocatalysis. For instance, by using glucose as the carbon resource, the obtained carbon-coated nickel phosphide nanosheet array electrode showed overpotentials of 144 mV@10 mA•cm⁻² in 1 M KOH solution and 110 mV@10 mA•cm⁻² in 0.5 M H₂SO₄ electrolyte. [16] Meanwhile, the cobalt phosphide (CoP) combined with carbon nanotube (CoP-CNT) exhibited an overpotential of 122 mV@10 mA•cm⁻² in 0.5 M H₂SO₄ electrolyte. [17] Recently, it is found that NiCoP bimetallic phosphate derived from the phosphorization of metal-organic frameworks (MOFs) for HER had overpotentials of 105 mV [18] in 0.5 M H₂SO₄ electrolyte and 124 mV in 1.0 M KOH solution [19] at the current density of 10 mA•cm⁻², respectively. The performance of such bimetallic phosphates could be also improved by combining with carbon. [16, 17, 20, 21]

Herein, binder-free NiCoP-carbon nanocomposite (denoted as NiCoP-C(TPA)) film with unique nanostructure was fabricated on Nickel foam (NF) by deposition of a terephthalic acid derived NiCo bimetallic compound precursor film on NF with a hydrothermal synthesis process, followed by carbonization in Ar atmosphere and phosphorization treatment with NaH₂PO₄. The obtained electrocatalysts were characterized by X-ray diffraction (XRD), scanning electron microscope (SEM) with an energy dispersive X-ray (EDX) detector, high-resolution transmission electron microscope (TEM), high-resolution Raman spectroscopy, Fourier transform infrared spectrometer (FT-IR), and X-ray photoelectron spectroscopy (XPS). The HER activity was evaluated by using linear sweep voltammetry (LSV) in acidic, alkaline, and neutral electrolytes. Moreover, the

long-term stability was tested at current densities of both 10 and 100 mA cm⁻², and a cyclic voltammetry test was also conducted for 1000 cycles. For comparison, monometallic phosphides of NiP-C(TPA) and CoP-C(TPA) coated NF electrodes were also fabricated. The effects of the molar ratio of Ni/Co and carbonization temperatures were also investigated. It is expected to provide novel bimetallic phosphide based electrocatalysts with high activity and stability for HER in the water splitting process.

3.2 EXPERIMENT

3.2.1 Chemicals and materials

Nickel (II) nitrate hexahydrate (Ni(NO₃)₂•6H₂O, 98%), cobalt (II) nitrate hexahydrate (Co(NO₃)₂•6H₂O, 99.9%), sodium dihydrogen phosphate dihydrate (NaH₂PO₄•2H₂O, 99%), disodium hydrogen phosphate (NaH₂PO₄, 99%), sulfuric acid (H₂SO₄, 97%), hydrochloric acid (HCl) and ethanol (C₂H₅OH, 99.5%) were purchased from Wako, Japan. Terephthalic acid (99%), malonic acid (99%), adipic acid (99%), and N, N-dimethyl acetamide (99%) were purchased from Tokyo Chemical Industry Co., Ltd. Sodium monophosphate (NaH₂PO₂) for phosphorization was purchased from Sigma-Aldrich, Japan. De-ionized water (18.2 MΩ cm) was used in all experiments. Nickel foam (NF, thickness: 1.5 mm, bulk density: 0.23 g/cm³ number of pores per inch: 110) was purchased from MTI, Japan.

3.2.2 Synthesis of organic acid derived NiCo bimetallic compound film on NF

The nickel foam (size: 2 x 2 cm²) was pretreated by HCl (1.0 M) to remove the native surface oxide layer and then ultrasonically washed in de-ionized water and ethanol for several times and dried. In a typical synthesis process, 0.6 mmol of nickel nitrate, 0.4 mmol of cobalt nitrate, and 0.2 mmol of terephthalic acid (TPA) were dissolved in 25 mL of the mixture of N, N-dimethyl acetamide (DMAc), and ethanol with a molar ratio of 5/3 and then stirred for 30 min. The solution was then transferred into a Teflon-lined autoclave to immerse the pre-treat nickel foam. Thereafter, the hydrothermal synthesis was performed at 150 °C for 20 h. After cooled down to room temperature, the nickel foam was taken out from the Teflon-lined autoclave and washed by water and ethanol successively. After dried in a vacuum oven at 60 °C for 12 h, the TPA derived NiCo bimetallic compound film-coated NF electrode was obtained. This material is denoted as

NiCo(TPA)/NF. For comparison, monometallic Ni(TPA)/NF and Co(TPA)/NF were also prepared. Before phosphorization treatment, the obtained NiCo(TPA)/NF electrode was carbonized in a tube furnace at 500 °C for 3 h in Ar atmosphere with a heating rate of 2°C/min to increase the crystallinity of materials and simultaneously to form conductive carbon species in the NiCo bimetallic compound. The obtained electrode at this stage is denoted as NiCo-C(TPA)/NF. Similarly, For comparison, monometallic Ni(TPA)/NF and Co(TPA)/NF electrodes were also carbonized in Ar atmosphere with the same conditions to obtain Ni-C(TPA)/NF and Co-C(TPA)/NF electrodes. For comparison, the calcination in air at the same conditions was also performed and the obtained electrode is denoted as NiCoO(TPA)/NF.

In addition, to investigate the effect of carbonization temperature in Ar atmosphere on the final electrocatalytic performance, the obtained NiCo(TPA)/NF electrodes were also carbonized in a tube furnace at different temperatures. As shown in Figure 3.4, the NiCo-C(TPA) obtained at the carbonization temperature of 500 °C exhibited the best performance. Thus, the NiCo-C(TPA) obtained by the carbonization temperature was used for further study.

3.2.3 Phosphorization for the preparation of NiCoP-C(TPA)/NF electrode

The phosphorization was performed in a tube furnace with an Ar gas flow rate of 60 cm³/min. Before the phosphorization, the above obtained NiCo-C(TPA)/NF electrode was cut into a size of 2 x 1 cm² at first and then put in a porcelain combustion boat at the downflow side of the tube furnace. Meanwhile, 1.0 g of NaH₂PO₂ was put in the up-flow side of the tube furnace. The phosphorization time was 3 h at a temperature of 300 °C with a heating rate of 2 °C/min.



Figure 3.1 Schematic illustration of NiCoP-C(TPA)/NF electrode fabrication.

3.2.4 Characterizations

The morphologies of various samples were characterized by a scanning electron microscope (SEM, SU8010, HITACHI, JAPAN) with an energy dispersive X-ray detector (EDS, Horiba Scientific) and the nanostructures were observed by a transmission electron microscope (TEM, JEM-2100F, JEOL). Before the TEM observation, the sample was well dispersed on a Cu grid mesh (Japan, Nisshin EM Co., Ltd. Tokyo). The powder X-ray diffraction (XRD) analysis was performed on a Rigaku Smartlab diffractometer (Japan) with Cu-K α as the radiation source ($\lambda=0.15406$ nm) in a range of 20 $^{\circ}$ -80 $^{\circ}$ to determine the crystalline structure. X-ray photoelectron spectroscopy (XPS) spectrum was measured at room temperature using a VG Scientific ESCALab250i-XL instrument with an Al-K α X-ray source. Fourier transformed infrared (FT-IR) spectrum was obtained in transmission mode on a Jasco FT-IR-4200 spectrometer (Japan) with a wavenumber range of 4000-400 cm $^{-1}$. The carbon states in the electrocatalysts were measured by using a Raman spectrophotometer (NRS 5100, Jasco, Japan) equipping a laser source of 532 nm.

3.2.5 Electrochemical measurements

Electrochemical measurements were conducted on an electrochemical workstation (potentiostat) with a three-electrode system at room temperature in 1.0 M KOH (pH=14), 0.5 M H $_2$ SO $_4$ (pH=1), and 1.0 M phosphate-buffered saline (PBS, pH=7) solutions, respectively. Carbon rod and Hg/HgO electrode (for alkaline electrolyte) or and Ag/AgCl electrode (for acidic and neutral electrolytes) and the obtained electrode (1 x 1 cm 2) were

used as the counter electrode, the reference electrode and the working electrode, respectively. Herein, HER performance was evaluated by using linear sweep voltammetry (LSV) with a scan rate of 1 mV s^{-1} at a potential range of 0 to -0.6 V (vs RHE). Electrochemical impedance spectroscopy (EIS) measurement was carried out with a frequency range from 100 kHz to 0.01 Hz at an overpotential of 200 mV. The potential in the alkaline electrolyte with respect to the reversible hydrogen electrode (RHE) was calculated by: $E (\text{V vs RHE}) = E (\text{Hg/HgO}) + (0.059 \times \text{pH}) + 0.098\text{V}$ whereas those in acidic and neutral electrolytes were calculated by: $E (\text{V vs RHE}) = E(\text{Ag/AgCl}) + (0.059 \times \text{pH}) + 0.197$. The electrochemical active surface area (ECSA) of various electrocatalysts at non-faradaic overpotentials was measured by cyclic voltammetry (CV) at a potential range of 0.1-0.3 V vs. RHE. The C_{dl} was estimated by plotting current density at different scan rate ($\Delta J = J_a - J_c$) at a potential of 0.2 V. The stability tests were performed in three ways: (i) chronoamperometry measurement at a fixed overpotential of 78 mV for 20 h; (ii) chronopotentiometry measurement at a fixed current density of -100 mA cm^{-2} for 20 h; and (iii) cyclic voltammetry test at a potential range from 0.1 to -0.3 V (vs RHE) for 1000 cycles.

3.3 RESULTS AND DISCUSSION

3.3.1 Influence of preparation parameters on HER catalytic performance

HER Performance

To investigate the effect of the kinds of organic dicarboxylic acids on the formation of NiCo bimetallic compound film on the NF, terephthalic acid, and other two organic acids without benzene ring in their molecule structures, i.e., malonic acid and adipic acid, were used. The obtained electrodes are denoted as NiCo(Malonic)/NF and NiCo(Adipic)/NF respectively. However, as shown in Fig. 3.2 and Table 3.1, NiCo(TPA)/NF electrode showed an overpotential of $232 \text{ mV}@10 \text{ mA cm}^{-2}$ and a Tafel slope of 130 mV dec^{-1} , which was lower than the other two. Thus, TPA derived NiCo bimetallic compound films were selected for further study.

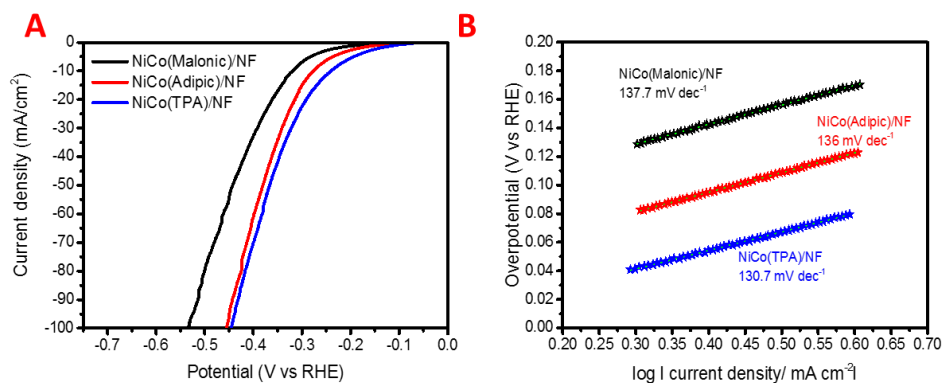


Figure 3.2 Electrochemical evaluation of three organic acid derived NiCo(organic compound) films on nickel foam electrode before calcination: (A) LSV polarization curves for HER; (B) Tafel slopes in 1.0 M KOH electrolyte at a scan rate of 1 mV s⁻¹.

To investigate the effects of the molar ratio of Ni/Co in the initial synthesis solution, three Ni/Co initial molar ratios of 1/1, 2/3, and 3/2 were used. The obtained NiCo(TPA)/NF electrodes were calcined in a tube furnace at 500 °C for 3 h in Ar atmosphere with a heating rate of 2°C/min. As shown in Figure 3.3 and Table 3.2, NiCo-C(TPA) based on the Ni/Co initial molar ratio of 3/2, i.e., Ni_{0.6}Co_{0.4}-C(TPA), exhibited the best electrocatalytic performance. Thus, the NiCoP-C(TPA) obtained by this Ni/Co initial molar ratio was used for further study.

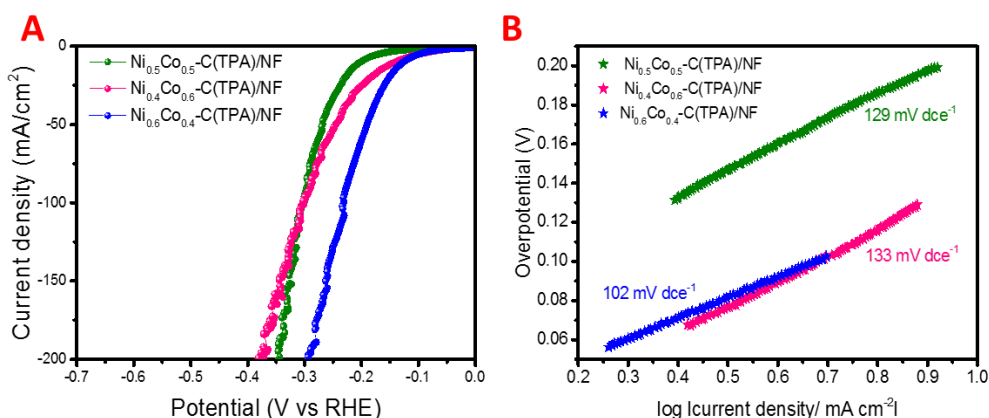


Figure 3.3 Electrochemical evaluation of NiCo-C(TPA)/NF electrodes with different mole ratios of Ni/Co: (A) LSV polarization curves for HER; (B) Tafel slopes in 1.0 M KOH electrolyte at a scan rate of 1 mV s⁻¹.

Table 3.1 Summary of the overpotentials @ 10 mA cm⁻² current density and the corresponding Tafel slope of the three organic acid derived NiCo(organic compound) films on nickel foam electrodes in Figure 6.

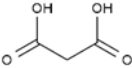
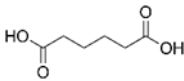
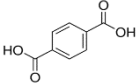
Electrode	Organic acid	Overpotential (mV @10mA/cm ²)	Tafel slope (mVdec ⁻¹)
NiCo(Malonic)/NF		320	137.7
NiCo(Adipic)/NF		277.4	136
NiCo(TPA)/NF		232	130.7

Table 3.2 Summary of the overpotentials @ 10 mA cm⁻² current density and the corresponding Tafel slopes of NiCo-C(TPA)/NF electrodes with different Ni/Co molar ratios in Figure S2.

Electrode	Overpotential (mV@10mA/cm ²)	Tafel slope (mVdec ⁻¹)
Ni _{0.5} Co _{0.5} -C(TPA)/NF	208	129
Ni _{0.4} Co _{0.6} -C(TPA)/NF	147	133
Ni _{0.6} Co _{0.4} -C(TPA)/NF	133	102

3.3.2 Microstructure and composition analysis of NiCoP-C(TPA)/NF catalyst.

Scheme 3.1 illustrates the NiCoP-C(TPA)/NF fabrication process. In the first step, DMAc is used to dissolve TPA powder with EtOH, and serves for the deprotonation of TPA. Meanwhile, the two carboxylate groups on TPA could preferentially coordinate to Ni²⁺ and Co²⁺ during the deprotonation process. [22] As such, with the assistance of TPA, NiCo bimetallic compound film was densely and uniformly formed on the surface of NF (Figure 3.4) via the hydrothermal synthesis firstly, which is called NiCo(TPA) film. Then, it was carbonized at 500 °C in the Ar gas flow, and carbon species contained bimetallic compound (NiCo-C(TPA)) with porous structure was achieved (Figure 3.6A). Finally, after the phosphorization in the tube furnace at 300 °C, a NiCoP-C(TPA)/NF electrode with nanorod structure (Figure 3.6B) was obtained. Figure 3.4 shows the Raman spectrum of NiCo-(TPA) film after the hydrothermal synthesis. Four typical peaks at 1606 cm⁻¹, 1431 cm⁻¹, 1163 cm⁻¹, and 858 cm⁻¹ correspondings to the C-H group in benzene dicarboxylate (BDC²⁻) [23] indicated that TPA was combined in the NiCo(TPA)film. In addition, when comparing FT-IR spectra of pure TPA and NiCo(TPA) film (Figure S6), a weak absorption peak 1500 cm⁻¹ attributed to the $\nu(\text{C}=\text{C})$ stretch of the benzene ring in TPA also maintained in the NiCo(TPA) film. Moreover, the strong characteristic peak of C=O at 1690 cm⁻¹ in pure TPA did not appear in the NiCo(TPA) film, but two peaks at 1580 cm⁻¹ and 1357 cm⁻¹ assigned to the asymmetric and symmetric stretching modes of the coordinated COO group, respectively, were observed, which indicated the coordination between the carboxyl groups of benzene dicarboxylate with Ni and Co. It also corresponded to the FT-IR spectrum of pure TPA. [24] Figure 3.6C shows EDS mapping of the surface of NiCoP-C(TPA)/NF electrode.

One can see that Ni, Co, and P species were homogeneously distributed on the surface, indicating that terephthalic acid served as the good linker to Ni and Co elements. In the HRTEM image (left figure in Figure 3.6D), a carbon layer with a graphite structure was found in NiCoP-C(TPA), which should be derived from the thermal decomposition of terephthalic acid. As shown in Figure 3.5, SEM and TEM images of NiP-C(TPA) and CoP-C(TPA) were different from those of NiCoP-C(TPA), but NiP and CoP particles were found in the carbon matrixes. Thus, the combination of Ni and Co resulted in different morphology of NiCoP-C(TPA), which could also affect the electrocatalytic performance. Obviously, the Ni-Co bimetallic phosphide composite had a higher activity

for HER due to the special nanostructure with the possible synergistic effect. [25, 26] Moreover, Figure 3.6E shows the Raman spectra of NiCo-C(TPA) and NiCoP-C(TPA), in which the two broad peaks are located at around 1350 cm^{-1} and 1585 cm^{-1} were observed, corresponding to the D-band and G-band of graphitic carbon, respectively. One can see that the I_D/I_G ratio increased from 0.93 to 0.955 after the phosphorization, indicating that the crystalline structure was slightly enhanced. The formation of graphitic carbon on the surface of bimetallic phosphide nanoparticles and the high degree of graphitization should improve the electroconductivity and enhance the electrocatalytic activity. [27, 28] Moreover, the intensity ratio of I_D/I_G is often used to evaluate the fraction of the defects in the graphitic materials, and the higher value of I_D/I_G , the more defective carbon structures there are. It is a benefit for the activity enhancement. Meanwhile, as shown in the right HRTEM image of Figure 3.6D, the well-resolved lattice fringe with the inter-planar spacing of 0.22 nm corresponded to the (111) lattice plans of hexagonal NiCoP, [29] which was in agreement with the XRD analysis result as shown in Fig. 3.8A in the following. The crystal structure of NiCoP-C(TPA) was characterized by XRD. As shown in Figure 3.8A, the wide peak in the range of $20\text{-}30^\circ$ corresponded to the carbon, and the characteristic diffraction of (111), (201), (210), (300), (211) and (222) corresponding to the hexagonal NiCoP (JCDP no. 71-2336) were observed. Meanwhile, as shown in Figure 3.7, as NiCo(TPA) was carbonized at $500\text{ }^\circ\text{C}$ in the Ar gas flow, the typical diffraction peaks at 44.8° , 51.83° , and 76.35° were well indexed to the (111), (200)

and (220) planes of NiCo alloy [30, 31] indicating that the bimetallic NiCo alloy was formed in the carbonization process.

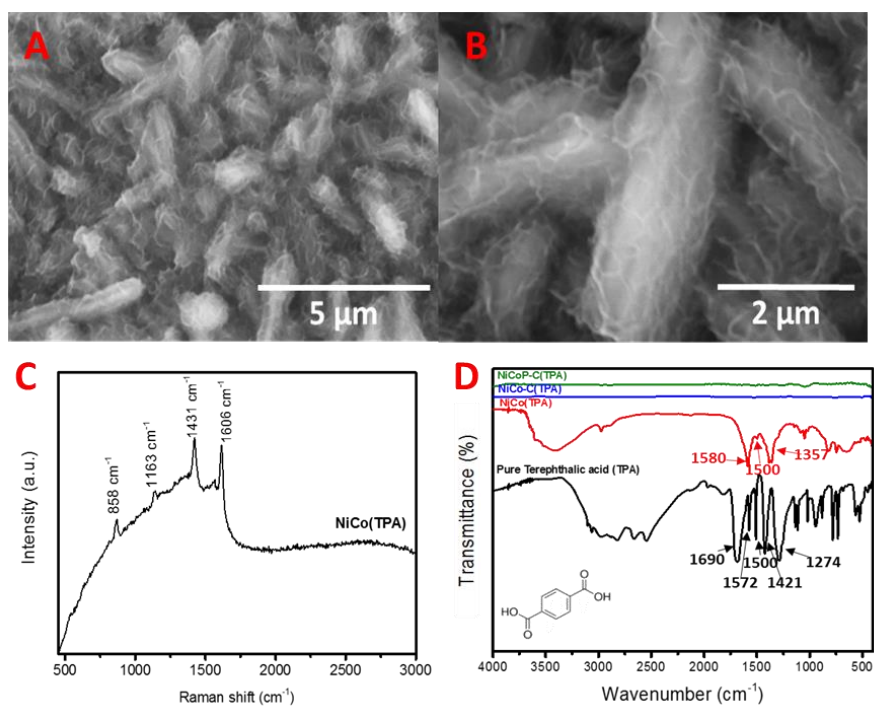


Figure 3.4 (A and B) SEM image of NiCo-(TPA) film after the hydrothermal synthesis but without calcination process at (A) 5 μ m and (B) 2 μ m. (c) Raman spectra of NiCo(TPA) before calcination. (D) FT-IR spectra of pure terephthalic acid (TPA), NiCo(TPA) before calcination, NiCo-C(TPA) and NiCoP-C(TPA).

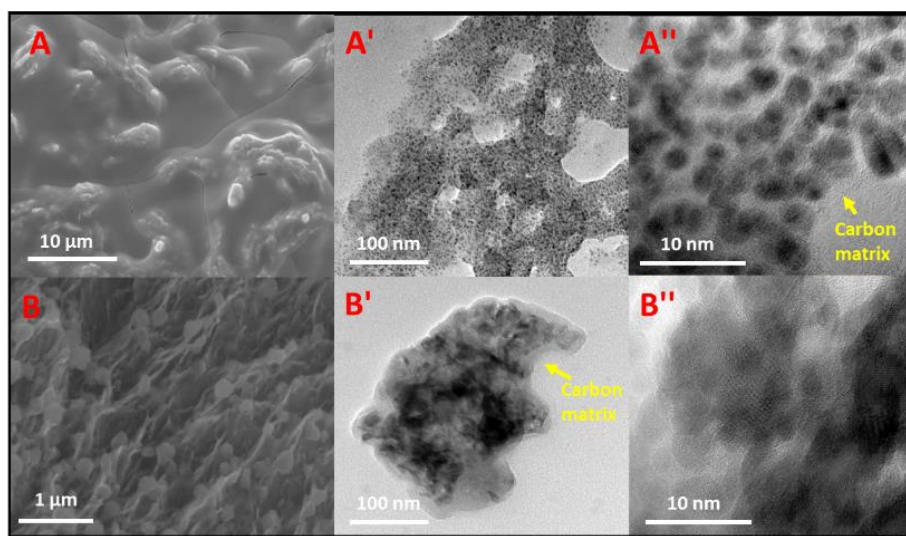


Figure 3.5 SEM images of (A) NiP-C(TPA) (B) CoP-C(TPA). TEM images of (A', A'') NiP-C(TPA) and (B', B'') CoP-C(TPA).

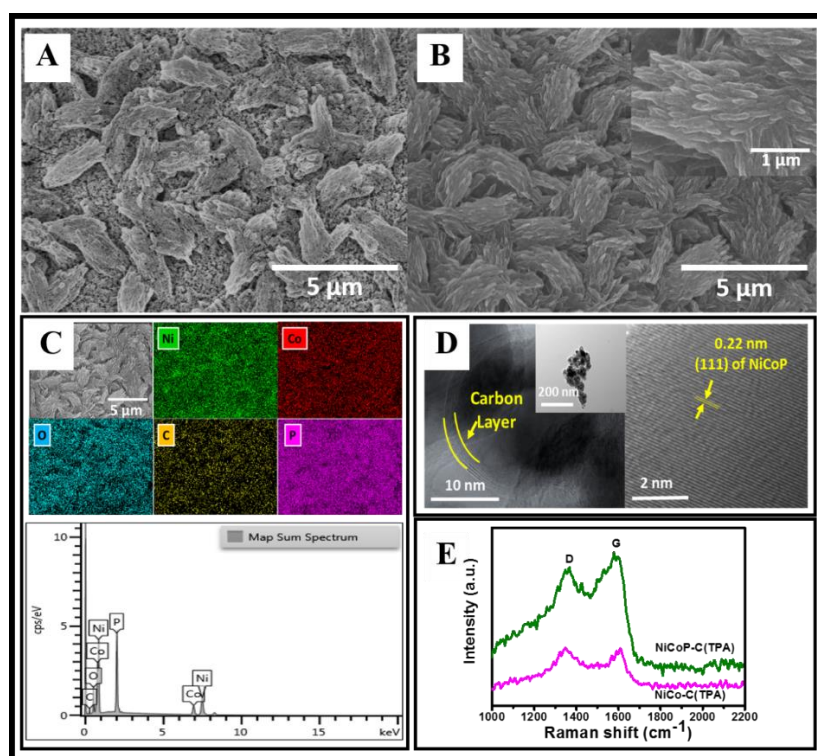


Figure 3.6 (A, B) SEM images of (A) NiCo-C(TPA)/NF and (B) NiCoP-C(TPA)/NF; (C) EDS mapping of NiCoP-C(TPA)/NF; (D) TEM and HRTEM images of NiCoP-C(TPA)/NF; (E) Raman spectra of NiCo-C(TPA)/NF and NiCoP-C(TPA)/NF.

The surface states of NiCo-C(TPA) and NiCoP-C(TPA) films were further investigated by XPS. As shown in Figure 3.8B, the XPS survey spectrum NiCo-C(TPA) had main peaks at 286, 532, 780, and 856 eV, which assigned to C 1s, O 1s, Co 2p, and Ni 2p transitions. Besides, for the NiCoP-C(TPA) film, a peak at 134.6 eV related to the P 2p transition was additionally observed. In the high-resolution Ni 2p spectra (Figure 2C), two main peaks at a binding energy of 856.9 eV and 874 eV in the NiCo-C(TPA) film shifted to 857.2 eV and 875 eV after the phosphorization, which is assigned to the Ni 2p_{3/2} and Ni 2p_{1/2} transitions, for Ni²⁺ species, respectively. [32] Similarly, in the high-resolution Co 2p spectra (Figure 2D), two typical peaks at a binding energy of 781.5 eV and 796 eV in the NiCo-C(TPA)film also shifted to 782.4 eV and 798.5 eV in the NiCoP-C(TPA), which are assigned to the Co 2p_{3/2} and Co 2p_{1/2} transitions, for Co²⁺ species, respectively. [19, 32] The shifting could have resulted from the change of electronic states due to the interaction between P and metal during the phosphorization. Meanwhile, the two satellites were observed in Figures 3.8C and 3.8D, which should be related to the surface oxidation with the formation of Ni-O and Co-O species due to the exposure of sample in air. Moreover, metallic states of Ni (Ni⁰) and Co (Co⁰) were also confirmed, which could enhance the electron transfer from NiCo alloy to P and this is favorable for the adsorption and desorption of reactant and product molecules during the electrolysis. [33] The P 2p spectrum (Figure 3.8E) shows one peak at a low binding energy of 129.2

eV and 131 eV associated with metal phosphides and the other peak at a high binding energy of 134.2 eV associated with the oxidation of P species. [34]

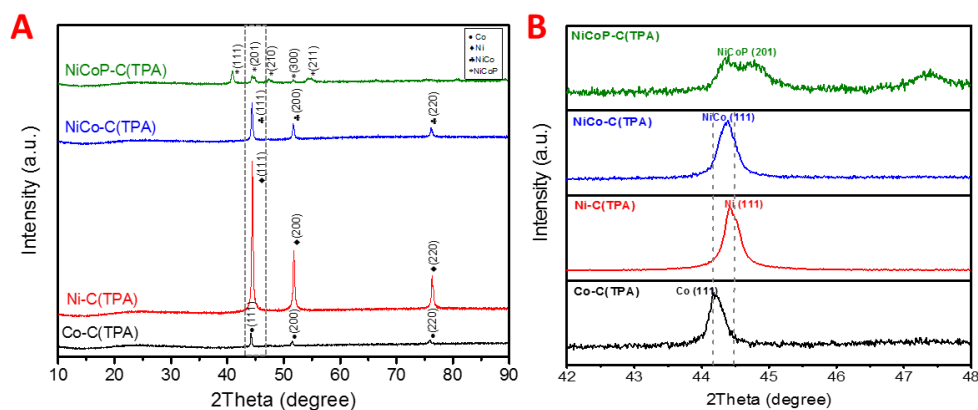


Figure 3.7 (A) XRD patterns of Co-C(TPA), Ni-C(TPA), NiCo-C(TPA) and NiCoP-C(TPA). (B) The corresponding magnification region with 2θ ranging from 42° to 48° .

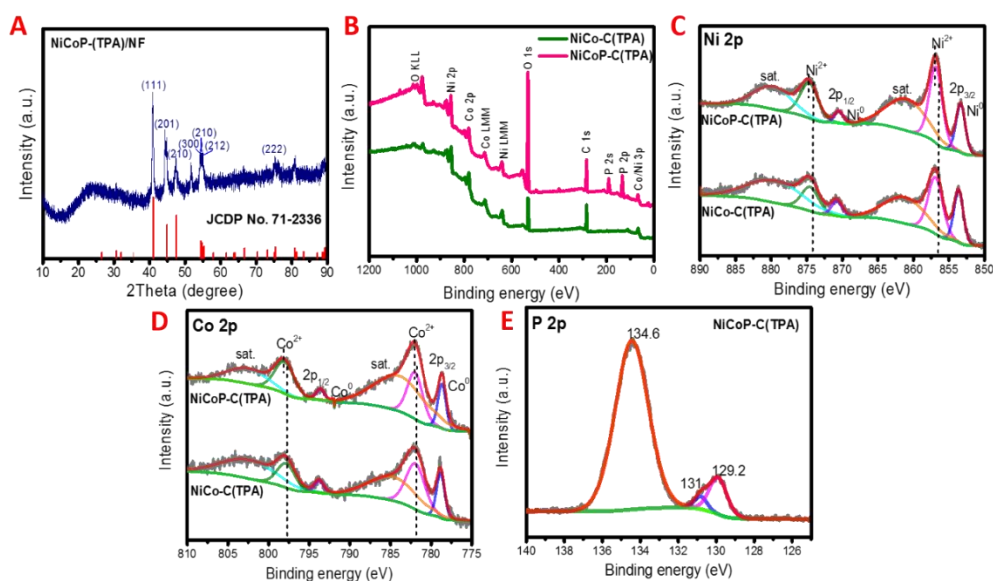


Figure 3.8 (A) XRD pattern of NiCoP-C(TPA); (B) Survey XPS spectra of NiCo-C(TPA) and NiCoP-C(TPA); and the related XPS spectra of (C) Ni 2p, (D) Co 2p, (E) P 2p in NiCoP-C(TPA).

3.3.3 Catalytic activity, conductivity and stability analysis of electrodes.

HER activities of NiCoP-C(TPA)/NF and other related samples were evaluated in 1 M KOH electrolyte, and the LSV polarization curves are shown in Figure 3.9A. A 20% wt Pt/C coated on NF electrode exhibited high HER performance with very low onset potential. However, as the current density was increased over 200 mA/cm², since a large amount of H₂ was generated, the coated 20 wt% Pt/C catalysts began to fall off from the substrate. In comparison, the in-situ grown NiCoP-C(TPA)/NF electrodes can work at the higher current density and no catalyst fall-off phenomenon was observed. Herein, the NiCoP-C(TPA)/NF electrode exhibited an overpotential as low as 78 mV at the 10 mA cm⁻² current density, which was much lower than those of NF (267 mV), Co-C(TPA)/NF (247 mV), Ni-C(TPA)/NF (193 mV), CoP-C(TPA)/NF (200 mV), NiP-C(TPA)/NF (137 mV) and NiCo-C(TPA)/NF (133 mV). Moreover, its overpotential was lower than most of the reported transition metal phosphides (Table 3.5). Meanwhile, the HER kinetics were investigated by the Tafel plots based on the corresponding LSV polarization curves. As shown in Figure 3.9B, the linear fitting resulted in a small Tafel slope of 73.4 mV dec⁻¹, which was also much smaller than NF (255.2 mV dec⁻¹), Co-C(TPA)/NF (173.9 mV dec⁻¹), CoP-C(TPA)/NF (162.8 mV dec⁻¹), Ni-C(TPA)/NF (170.5 mV dec⁻¹), NiP-C(TPA)/NF (113 mV dec⁻¹), and NiCo-C(TPA)/NF (107.4 mV dec⁻¹). This much smaller Tafel slope indicates that the NiCoP-C(TPA) had more rapid reaction kinetics, which was better than or comparable to those reported transition metal phosphides (Table 3.5). Tafel slope can be also directly measured by an electrochemical workstation (Potentiostat) with a three-electrode system in 1 M KOH electrolyte, in which Pt wire, Hg/HgO electrode, and the prepared electrode were used as the counter electrode, reference electrode, and working electrode, respectively. In this case, the Tafel slope was estimated by remaining the potential range as that in the LSV test with a step height of 0.5 mV, a step time of 3 s, and an ultra-low scan rate of 0.1 mV/s. As shown in Figure 3.10, the Tafel slopes for NiCoP-C(TPA)/NF and 20%wt Pt/C/NF directly measured from the potentiostat workstation were 69 mV/dec and 30.2 mV/dec (which is close to the theoretical Tafel slope Pt/C, i.e., 30 mV/dec), respectively. From Figure 3.10 and Table 3.3, one can see that the difference of the Tafel slopes obtained by using the two methods was not so significant. More discussion on this can be found in the supporting information.

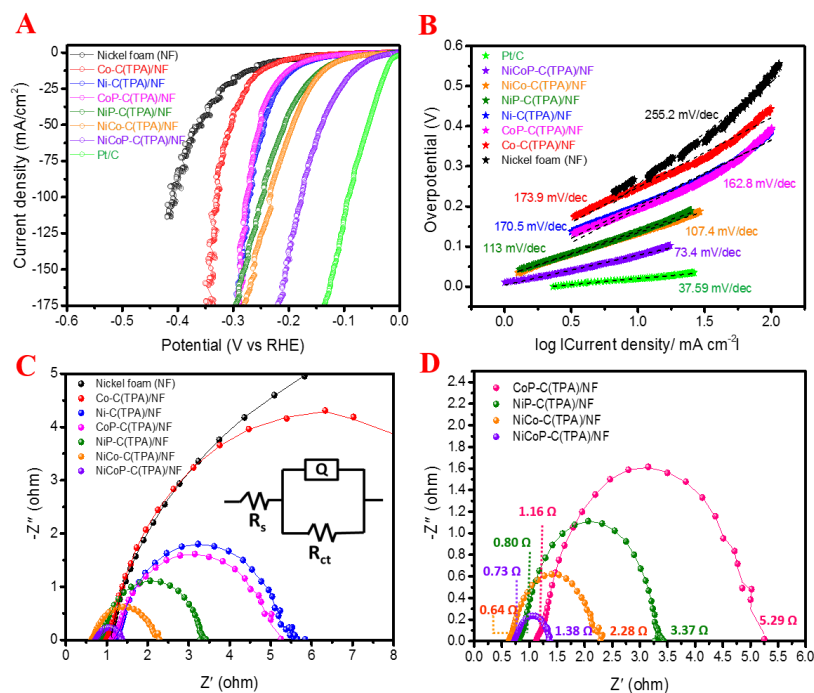


Figure 3.9 Electrochemical performances of various samples in HER. (A) LSV polarization curves at a scan rate of 1 mV s⁻¹ collected in 1 M KOH electrolyte. (B) Corresponding Tafel plots are derived from the LSV curves in (A). (C) EIS Nyquist plots of various electrodes at an overpotential of 200 mV in 1 M KOH electrolyte. (D) Enlarged Nyquist plots of CoP-C(TPA)/NF, NiP-C(TPA)/NF, NiCo-C(TPA)/NF and NiCoP-C(TPA)/NF in (C).

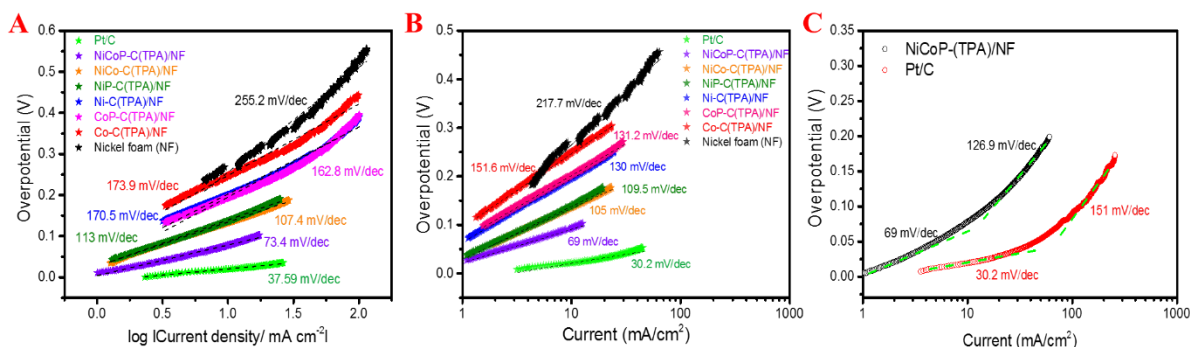


Figure 3.10 (A) Tafel curves converted from voltammogram. (B) Tafel curves were obtained by directly measuring the Tafel characteristics using the electrochemical workstation. (C) Estimated Tafel data for evaluation of the reaction rate-determining step (selection of NiCoP-(TPA)/NF and 20% wt Pt/C coated NF as the examples).

Table 3.3 Comparison Tafel slopes from two different techniques-based Figure 3.10.

Catalyst	Tafel slope from voltammogram	Tafel slope directly from electrochemical station
20%wt Pt/C	37.59	30.2
NiCoP-C(TPA)/NF	73.4	69
NiCo-C(TPA)/NF	107.4	105
NiP-C(TPA)/NF	113	109.5
CoP-C(TPA)/NF	162.8	130
Ni-C(TPA)/NF	170.5	131.2
Co-C(TPA)/NF	173.9	151.6
Nickel foam (NF)	255.2	217.7

The interfacial resistance between electrode-electrolyte and the electrode kinetics during HER were evaluated by EIS. In general, the reaction rate on the electrode is controlled by the charge transfer resistance (R_{ct}), and the lower R_{ct} means the faster reaction rate. As shown in Figure 3.9(C), R_{ct} of the electrochemical reaction corresponded to the semicircle in high frequency and the slope line in the low frequency of the Nyquist plot related to the electrode surface kinetics. One can see that the NiCoP-C(TPA)/NF electrode possessed a much smaller charge transfer resistance (R_{ct}) of $\sim 1.38 \Omega$ than the NiCo-C(TPA)/NF (2.28Ω), NiP-C(TPA)/NF (3.37Ω), and CoP-C(TPA)/NF (5.29Ω). The lower R_{ct} value for NiCoP-C(TPA)/NF electrode implied it had better charge transferability and higher catalytic activity for HER when compared with others, which should be mainly resulted from the unique nanostructure of NiCoP-C and proper synergistic contribution of Ni, Co, P and C species. [35] Especially, the incorporation of graphitic carbon with the NiCoP and the synergistic effect formed between them led to the excellent electrical conductivity, further resulting in a smaller Tafel slope. In addition, Figure 3.9D shows the enlarged EIS curves from CoP-C(TPA)/NF, NiP-C(TPA)/NF, NiCo-C(TPA)/NF and NiCoP-C(TPA)/NF electrodes, in which a smaller series resistance (R_s) of the NiCoP-C(TPA)/NF electrode was observed. It confirmed that the NiCoP-

C(TPA) electrocatalyst layer is electrically contacted with the substrate very well, ensuring good electrical contacts and mechanical stability, which should be also beneficial for the superior stability as shown in the following. Thus, the bimetallic phosphide catalysts covered by carbon layer can improve charge conductivity and electron transfer kinetics in the interface.

The electrochemical double-layer capacitance (C_{dl}) is proportional to the electrochemically active surface area (ECSA) and the roughness, which can be measured using the cyclic voltammetry (CV) method by recording the cyclic voltammetry at different scan rates. Based on the results measured in a potential window between 0.1-0.3 V (vs RHE) at the current density ranged from 5 to 100 mV s^{-1} (Figures 3.11A, B, C), the NiCoP-C(TPA)/NF electrode exhibited the highest C_{dl} of 60 mF cm^{-2} , which was nearly 5 and 30 times higher than those of the NiCo-C(TPA)/NF (12.8 mF cm^{-2}) and NF (1.9 mF cm^{-2}), respectively, indicating that the phosphorization is an important way to improve the ECSA of bimetallic materials. Herein, the higher ECSA indicates exposure of more numbers of active sites in NiCoP-C(TPA). The ECSA normalized electrocatalytic performance was evaluated by setting the ECSA of NF as 1, and as such, the ECSAs of NiCo-C(TPA)/NF and NiCoP-C(TPA)/NF were 6.74 and 31.6, respectively. The obtained HER polarization curves based on the normalized LSV current density of the electrodes based on the ESCA corresponding to Figure 3.6(A) are shown in Figure 3.11 (E). Before ECSA normalization, the apparent overpotentials are $133 \text{ mV}@10 \text{ mA cm}^{-2}$ and $78 \text{ mV}@10 \text{ mA cm}^{-2}$ for the NiCo-C(TPA)/NF and NiCoP-C(TPA)/NF, respectively. However, after ECSA normalization, these values became $178 \text{ mV}@10 \text{ mA cm}^{-2}$ and $120.3 \text{ mV}@10 \text{ mA cm}^{-2}$. It should be noted that after the ECSA normalization, the real overpotential difference of the NiCo-C(TPA)/NF and NiCoP-C(TPA)/NF was still large, indicating that ECSA of the coated electrocatalysts on the NF plays the main role in the performance. In addition, the roughness factor (R_f) of NF, NiCo-C(TPA)/NF and NiCoP-C(TPA)/NF was calculated to be 0.0475×10^3 , 0.32×10^3 and 1.5×10^3 , respectively (Table 3.4), also indicated that NiCoP-C(TPA) had the highest roughness, which could provide more active sites. [36, 37]

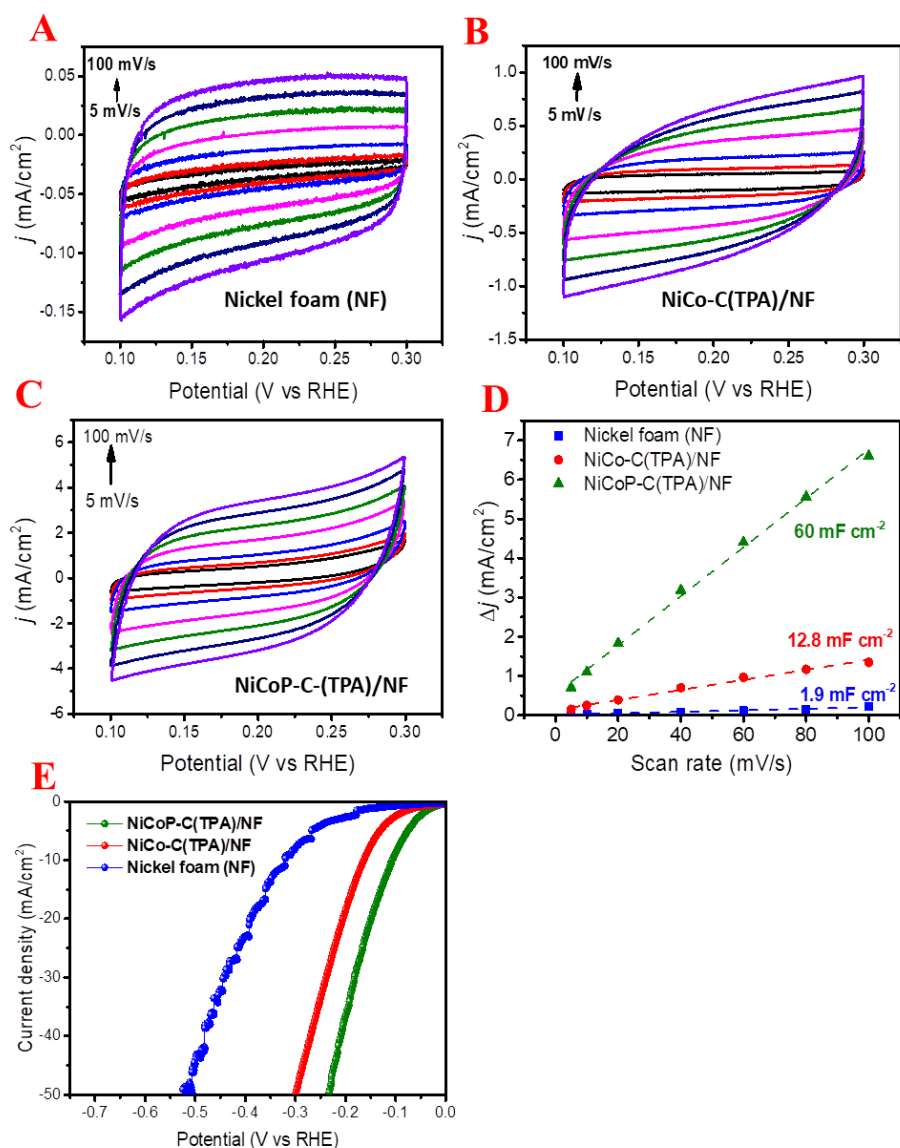


Figure 3.11 Cyclic voltammograms of (A) nickel foam (NF), (B) NiCo-C(TPA)/NF, (C) NiCoP-C(TPA)/NF collected between a potential range of 0.1-0.3V (vs RHE) with scan rates of 5, 10, 20, 40, 60, 80, 100 mV/s, respectively in 1 M KOH electrolyte. (D) Dependence of current on the scan rate at different double layer capacitances for the estimation of the electrochemical surface area. (E) LSV polarization curve normalized based on ECSA.

Table 3.4 Calculated ECSA and roughness of surface (R_f) of the samples in Figure S8.

Electrode	Cdl (mF cm^{-2})	Cs (mF cm^{-2})	ECSA ($\times 10^3$)	GSA (cm^2)	Rf ($\times 10^3$)
Nickel foam (NF)	1.9	0.04	0.0475	1.00	0.0475
NiCo-C(TPA)/NF	12.8	0.04	0.320	1.00	0.320
NiCoP-C(TPA)/NF	60	0.04	1.500	1.00	1.500

Figure 3.12(A) shows a multi-step chronopotentiometry curve for the NiCoP-(TPA)/NF electrode, in which the current density started at -20 mA cm^{-2} with an increment of 20 mA cm^{-2} for every 500 s until gradually reaching -200 mA cm^{-2} . The potential maintained at a constant value at each current density until up to -220 mA cm^{-2} , demonstrating that the NiCoP-(TPA)/NF electrode had outstanding mass transportation property and mechanical robustness. Nice contact of NiCoP (bimetallic phosphide) particles with graphite carbon derived from terephthalic acid are supposedly contributed to the nice durability performance of this electrode as indicated by the TEM images shown in Figures 3.4. [38, 39] As shown in Figure 3.12(C), the stability tests for NiCoP-C(TPA)/NF electrode were performed in three ways: (i) chronoamperometry measurement at a fixed overpotential of 78 mV for 20 h, (ii) chronopotentiometry measurement at a fixed current density of -100 mA cm^{-2} for 20 h; and (iii) cyclic voltammetry test at a potential range from 0.1 to -0.3 V (vs RHE) for 1000 cycles. One can see that the chronoamperometry measured at a constant overpotential of 78 mV for 20 h maintained a constant current density of -10 mA cm^{-2} . Moreover, the electrode kept stable when worked at a high current density of -100 mA cm^{-2} for 20 h. Meanwhile, the LSV polarization curve remained almost unchanged even after 1000 cycles. Therefore, the NiCoP-C(TPA)/NF electrode had excellent long-term stability even at a high current density in an alkaline electrolyte. After a long-term durability test (20 h), it is found that the NiCoP-C(TPA) catalysts remained uniformly coating on the NF substrate and showed almost the same image as the fresh one. Additionally, from the EDS mappings of Ni, Co, C, and P species, they

were also almost the same as the fresh ones after the long-term stability test. (Figure 3.13) Moreover, as shown in the XPS spectra in the following Figure 3.14, after the stability test, the binding energy peaks at 871 eV and 853.6 eV, corresponding to the Ni 2p_{1/2} and Ni 2p_{3/2} peaks, respectively, disappeared, indicating that Ni species had been oxidized. Meanwhile, the binding energy peaks at 739.9 eV and 778.7 eV, corresponding to Co 2p_{1/2} and Co 2p_{3/2}, respectively, also disappeared, indicating that Co species had also been oxidized. In addition, the intensity of the P spectrum decreased to some extent and the board peaks at 134.6 eV and 129.2 eV shifted a little due to the oxidation of P species. As for O species, the spectrum of O 1s can be deconvoluted into three peaks, which correspond to oxy metal or hydroxy metal (531.4 eV, 532.5 eV) and phosphorus oxygen (533.5 eV). After the stability test, the intensity of O spectrum changed only a little, indicating that the main active species for the HER should be NiCoP in the alkaline electrolyte although part of P was oxidized. As indicated by the HER activity stability test, the performance was not obviously affected by the slight oxidation of the electrocatalyst. [40] In addition, hydrogen gas production during the electrolysis at 10 mA cm⁻² was experimentally quantified. As shown in Figure 3.12D, the fitted curve of theoretical H₂ production amount is $y_1 = 0.00308X_1$, whereas the fitted curve of the measured H₂ production amount is $y_2 = 0.00289X_2$, thus the faradic efficiency is $y_2/y_1 = 0.00289/0.00308 \sim 94\%$ in this study.

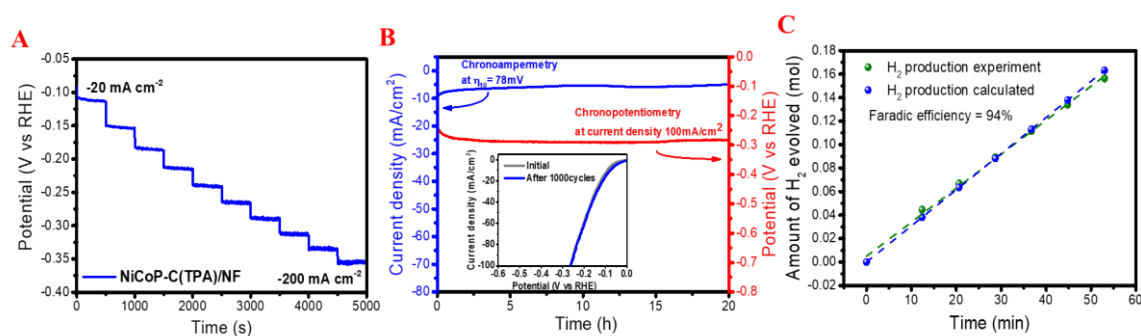


Figure 3.12 (A) HER multi-step chronopotentiometry curve of NiCoP-(TPA)/NF electrode with the current density started at current density -20 mA cm^{-2} and ended at -200 mA cm^{-2} with an increment of 20 mA cm^{-2} every 500s. (B) Chronopotentiometry curves of NiCoP-(TPA)/NF electrode at a current density of 100 mA cm^{-2} (red line) and at the constant overpotential of 78 mV (Blue line) collected at a duration time of 20 h in

1 M KOH electrolyte (Inset figure: LSV curves before and after 1000 cycles). (C) Faradaic efficiency of H₂ production for NiCoP-C(TPA)/NF at a current density of -10 mA cm⁻².

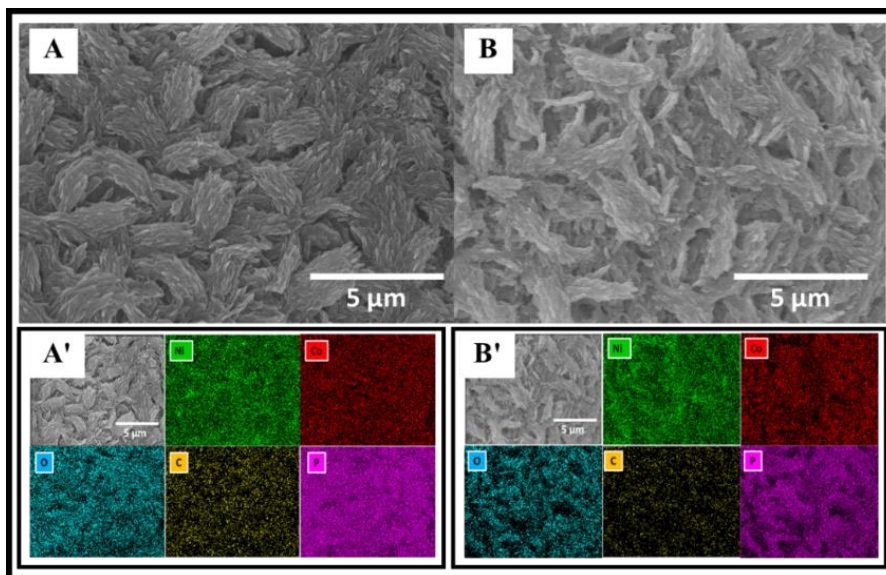


Figure 3.13 SEM image of NiCoP-C(TPA)/NF (A) fresh catalyst (B) after stability test 20h EDS mapping of NiCoP-C(TPA)/NF (A') before a test and (B') after test stability test in 1M KOH electrolyte.

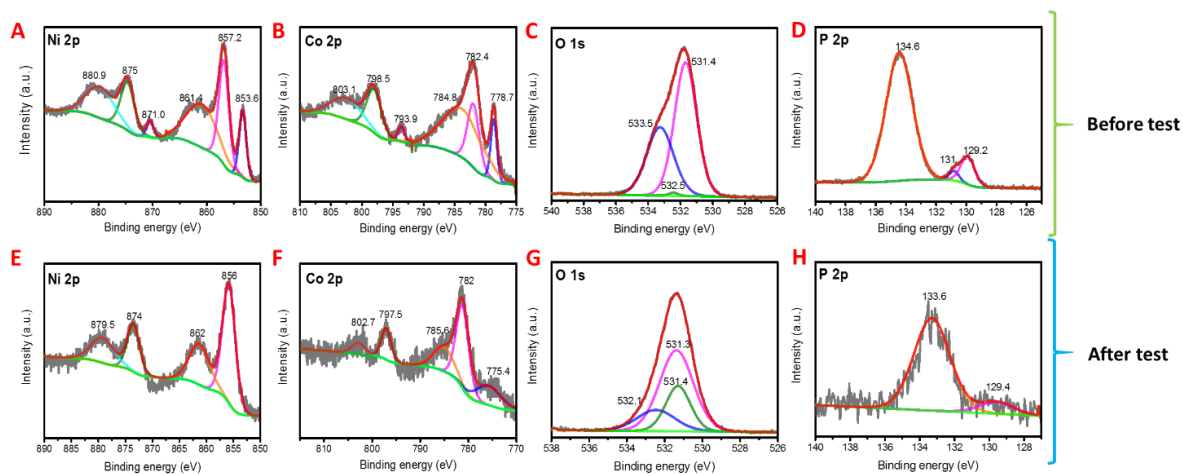


Figure 3.14 High-resolution XPS spectra of NiCoP-C(TPA) of (A-D) before HER test and (E-H) after HER test in the alkaline media solution.

3.3.4 Catalytic activity, conductivity and stability analysis of electrodes compare wide pH range electrolyte.

Furthermore, the HER activity of NiCoP-(TPA)/NF in acidic and neutral electrolytes were also investigated. As shown in Figure 3.15, the NiCoP-C(TPA)/NF electrode also exhibited superior HER performance in the acidic electrolyte with an overpotential of 94 mV@10 mA cm⁻², a Tafel slope of 81.1 mV dec⁻¹, and long-term stability. However, in the neutral electrolyte, a relatively high overpotential of 248 mV@10 mA cm⁻² with a high Tafel slope of 112.5 mV dec⁻¹ was obtained. Meanwhile, the LSV polarization curve also changed to some extent after 1000 cycles, indicating that it is not so suitable for working in neutral electrolyte. Thus, NiCoP-C(TPA)/NF electrode should be more suitable for water splitting in the alkaline electrolyte as other phosphide materials. [41]

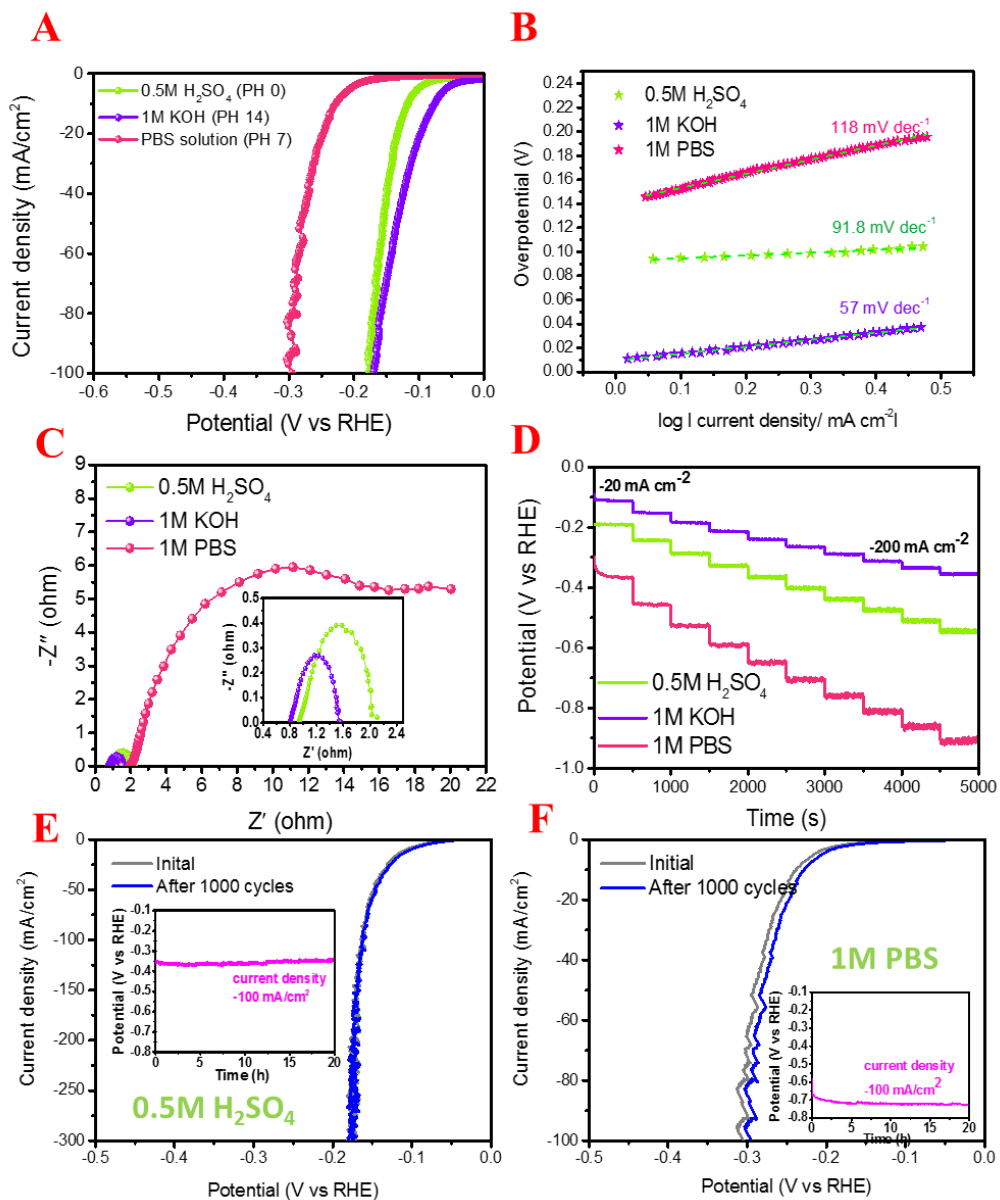


Figure 3.15 HER performances of NiCoP-C(TPA)/NF in acidic, neutral and alkaline electrolytes. (A) LSV curves. (B) Tafel plots. (C) Nyquist plots at an overpotential of 200 mV and (D) Multi-current step started at a current density of -20 mA cm^{-2} and ended at -200 mA cm^{-2} with an increment of 20 mA cm^{-2} every 500 sec. (E,F) Chronopotentiometry of NiCoP-C(TPA)/NF at a current density of -100 mA cm^{-2} duration a period of 20 h in (E) $0.5 \text{ M H}_2\text{SO}_4$ (pH=0). (F) 1 M PBS (pH=7).

Table 3.5 Comparison of this work with other related electrocatalysts working in an alkaline electrolyte in the works of literature.

Electrocatalyst	Overpotential (mV) @10mA/cm ²	Tafel slope (mVdec ⁻¹)	Electrolyte	Electrode	Ref.
NiCoP-C(TPA)/NF	78	58	1 M KOH	Nickel foam	This work
NiCo-MOF	180	168	0.1 M KOH	Nickel foam	[42]
NiCoFe-MOF	110	114	0.1 M KOH	Nickel foam	[42]
Ni ₂ P-CoP	105	64	1 M KOH	Glassy carbon	[18]
Ni ₂ P	137	67	1 M KOH	Glassy carbon	[18]
CoP	184	66	1 M KOH	Glassy carbon	[18]
C@Ni ₈ P ₃	114	59	1 M KOH	Nickel foam	[16]
Ni-Co-P	150	60.6	1 M KOH	Nickel foam	[43]
NiCoP/CC(Nest-like)	62	68.2	1 M KOH	Carbon cloth	[44]
CoP/CC	290	115.9	1 M KOH	Carbon cloth	[44]
NiP ₂ NS/CC	102	64	1 M KOH	Carbon cloth	[45]
CoP/rGO	150	38	1 M KOH	Glassy carbon	[46]
Ni ₂ P/Ni/NF	98	72	1 M KOH	Nickel foam	[47]
Cu _{0.3} Co _{0.2} P	220	122	1 M KOH	Glassy carbon	[48]
Mn-CoP	95	53	1 M KOH	Carbon rod	[41]
Pt/C	32	33	1 M KOH	Pt foil	[19]

3.4 CONCLUSION

In summary, binder-free graphite carbon combined NiCo alloy phosphide nanocomposite, i.e., NiCoP-C(TPA), film with unique nanostructure was successfully fabricated on NF for the first time. In the fabrication process, terephthalic acid was used as the template to derive NiCo bimetallic precursor film on NF in a hydrothermal synthesis process, followed by calcination in an Ar atmosphere and phosphorization treatment with NaH_2PO_2 . As such, the bimetallic NiCo phosphide nanoparticles were well combined with the graphite carbon in the final NiCoP-C(TPA) electrocatalyst. The obtained NiCoP-C(TPA) electrocatalyst exhibited much higher activity than monometallic phosphides of NiP-C(TPA) and CoP-C(TPA). It showed an overpotential as low as $78 \text{ mV}@ 10 \text{ mA cm}^{-2}$ with a small Tafel slope of 58 mV dec^{-1} , a faradic efficiency of $\sim 94\%$, and long-term stability at high current density in the alkaline electrolyte. Meanwhile, it also exhibited superior HER performance in the acidic electrolyte with an overpotential of $94 \text{ mV}@ 10 \text{ mA cm}^{-2}$, a Tafel slope of 91.8 mV dec^{-1} and long-term stability although in the neutral electrolyte a relatively high overpotential of $248 \text{ mV}@ 10 \text{ mA cm}^{-2}$ with a high Tafel slope of 118 mV dec^{-1} were obtained. It indicates that using polycarboxylic acids as templates is an effective way to produce high-performance bimetallic phosphide based electrocatalysts with special nanostructure for HER in water splitting.

REFERENCES

- [1] X. Li, X. Hao, A. Abudula, G. Guan, Nanostructured Catalysts for Electrochemical Water Splitting: Current State and Prospects, *J. Mater. Chem. A*, 2016, 4, 11973-12000.
- [2] J. Chen, B. Lim, E. P. Lee, Y. Xia, Shape-Controlled Synthesis of Platinum Nanocrystals for Catalytic and Electrocatalytic Applications, *Nano Today*, 2009, 4, 81-95.
- [3] R. Gómez, J. M. Orts, B. Álvarez-Ruiz, J. M. Feliu, Effect of Temperature on Hydrogen Adsorption on Pt(111), Pt(110), and Pt(100) Electrodes in 0.1 M HClO_4 , *J. Phys. Chem. B*, 2004, 108, 228-238.

- [4] Y. Chen, R. Ren, Z. Wen, S. Ci, J. Chang, S. Mao, J. Chen, Superior Electrocatalysis for Hydrogen Evolution with Crumpled Graphene/Tungsten Disulfide/Tungsten Trioxide Ternary Nanohybrids, *Nano Energy*, 2018, 47, 66-73.
- [5] B. Ma, Z. Yang, Z. Yuan, Y. Chen, Effective Surface Roughening of Three-Dimensional Copper Foam via Sulfurization Treatment as a Bifunctional Electrocatalyst for Water Splitting, *Int. J. Hydrog. Energy*, 2019, 44(3), 1620-1626.
- [6] B. You, N. Jiang, M. Sheng, M. W. Bhushan, Y. Sun, Hierarchically Porous Urchin-Like Ni₂P Superstructures Supported on Nickel Foam as Efficient Bifunctional Electrocatalysts for Overall Water Splitting, *ACS Catal.*, 2016, 6, 714-721.
- [7] Q. Li, Z. Xing, A. M. Asiri, P. Jiang, X. Sun, Cobalt Phosphide Nanoparticles Film Growth on Carbon Cloth: A High-Performance Cathode for Electrochemical Hydrogen Evolution, *Int. J. Hydrog. Energy*, 2014, 39, 16806-16811.
- [8] Q. Qin, H. Jang, P. Li, B. Yuan, X. Liu, J. Cho, A Tannic Acid-Derived N-, P-Codoped Carbon-Supported Iron-Based Nanocomposite as an Advanced Trifunctional Electrocatalyst for the Overall Water Splitting Cells and Zinc-Air Batteries, *Adv. Energy Mater.*, 2019, 9, 1803312.
- [9] C. Tang, N. Cheng, Z. Pu, W. Xing, X. Sun, NiSe Nanowire Film Supported on Nickel Foam: An Efficient and Stable 3D Bifunctional Electrode for Full Water Splitting, *Angew. Chem.*, 2015, 54, 9351-9355.
- [10] J. Tian, Q. Liu, A. M. Asiri, X. Sun, Self-Supported Nanoporous Cobalt Phosphide Nanowire Arrays: An Efficient 3D Hydrogen-Evolving Cathode over the Wide Range of pH 0–14, *J. Am. Chem. Soc.*, 2014, 136, 7587-7590.
- [11] Y. Lv and X. Wang, Nonprecious Metal Phosphides as Catalysts for Hydrogen Evolution, Oxygen Reduction and Evolution Reactions, *Catal. Sci. Technol.*, 2017, 7, 3676-3691.
- [12] C. G. Read, J. F. Callejas, C. F. Holder, R. E. Schaak, General Strategy for the Synthesis of Transition Metal Phosphide Films for Electrocatalytic Hydrogen and Oxygen Evolution, *ACS Appl. Mater. Interfaces*, 2016, 8, 12798-12803.
- [13] Y. Yan, L. Thia, B. Y. Xia, X. Ge, Z. Liu, A. Fisher, X. Wang, Construction of Efficient 3D Gas Evolution Electrocatalyst for Hydrogen Evolution: Porous FeP Nanowire Arrays on Graphene Sheets, *Adv. Sci.*, 2015, 2, 1500120.

- [14] Y. Liang, Q. Liu, A. M. Asiri, X. Sun, Y. Luo, Self-Supported FeP Nanorod Arrays: A Cost-Effective 3D Hydrogen Evolution Cathode with High Catalytic Activity, *ACS Catal.*, 2014, 4, 4065-4069.
- [15] B. Ma, Z. Yang, Y. Chen, Z. Yuan, Nickel Cobalt Phosphide with Three-Dimensional Nanostructure as a Highly Efficient Electrocatalyst for Hydrogen Evolution Reaction in Both Acidic and Alkaline Electrolytes, *Nano Research*, 2019, 12(2), 375-380.
- [16] J. Yu, Q. Li, N. Chen, C-Y. Xu, L. Zhen, J. Wu, V. P. Dravid, Carbon-Coated Nickel Phosphide Nanosheets as Efficient Dual-Electrocatalyst for Overall Water Splitting, *ACS Appl. Mater. Interfaces*, 2016, 8, 27850–27858.
- [17] Q. Liu, J. Tian, W. Cui, P. Jiang, N. Cheng, A. M. Asiri, X. Sun, Carbon Nanotubes Decorated with CoP Nanocrystals: A Highly Active Non-Noble-Metal Nanohybrid Electrocatalyst for Hydrogen Evolution, *Angew. Chem.*, 2014, 126, 6828-6832.
- [18] X. Liang, B. Zheng, L. Chen, J. Zhang, Z. Zhuang, B. Chen, MOF-Derived Formation of Ni₂P–CoP Bimetallic Phosphides with Strong Interfacial Effect toward Electrocatalytic Water Splitting, *ACS Appl. Mater. Interfaces*, 2017, 9, 23222-23229.
- [19] Y. Li, J. Liu, C. Chen, X. Zhang, J. Chen, Preparation of NiCoP Hollow Quasi-Polyhedra and Their Electrocatalytic Properties for Hydrogen Evolution in Alkaline Solution, *ACS Appl. Mater. Interfaces*, 2017, 9, 5982-5991.
- [20] B. Y. Guan, L. Yu, X. W. Lou, A Dual-Metal–Organic-Framework Derived Electrocatalyst for Oxygen Reduction, *Energy Environ. Sci.*, 2016, 9, 3092-3096.
- [21] J. Tang, R. R. Salunkhe, J. Liu, N. L. Torad, M. Imura, S. Furukawa, Y. Yamauchi, Thermal Conversion of Core–Shell Metal–Organic Frameworks: A New Method for Selectively Functionalized Nanoporous Hybrid Carbon, *J. Am. Chem. Soc.*, 2015, 137, 1572-1580.
- [22] Z. Zhang, Y. Chen, S. He, J. Zhang, X. Xu, Y. Yang, F. Nosheen, F. Saleem, W. He, X. Wang, Hierarchical Zn/Ni-MOF-2 Nanosheet-Assembled Hollow Nanocubes for Multicomponent Catalytic Reactions, *Angew. Chem.*, 2014, 126, 12725-12729.
- [23] S. He, Z. Li, J. Wang, P. Wen, J. Gao, L. Ma, Z. Yang, S. Yang, MOF-Derived Ni_xCo_{1-x}(OH)₂ Composite Microspheres for High-Performance Supercapacitors, *RSC Adv.*, 2016, 6, 49478-49486.

- [24] F. Zhang, L. Hao, L. Zhang, X. Zhang, Solid-State Thermolysis Preparation of Co_3O_4 Nano/Micro Superstructures from Metal-Organic Framework for Supercapacitors, *Int. J. Electrochem. Sci.*, 2011, 6, 2943-2954.
- [25] A. L. Wang, J. Lin, H. Xu, Y. X. Tonga, G. R. Li, Ni_2P - CoP hybrid nanosheet arrays supported on carbon cloth as an efficient flexible cathode for hydrogen evolution, *Mater. Chem. A*, 2016, 4, 16992-16999.
- [26] S. Fu, C. Zhu, J. Song, M. H. Engelhard, X. Li, D. Du, Y. Lin, Highly Ordered Mesoporous Bimetallic Phosphides as Efficient Oxygen Evolution Electrocatalysts, *ACS Energy Letter*, 2016, 1, 792-796.
- [27] Z. Yu, Y. Bai, Y. Wang, Y. Liu, Y. Zhao, Y. Liu, K. Sun, One-step Synthesis of Three-Dimensional Nitrogen and Sulfur Co-Doped Graphene Networks as Low Cost Metal-Free Counter Electrodes for Dye-Sensitized Solar Cells, *Chem. Eng. J.*, 2017, 311, 302-309.
- [28] Q. Li, Z. Li, Z. Zhang, C. Li, J. Ma, C. Wang, X. Ge, S. Dong, L. Yin, Low-Temperature Solution-Based Phosphorization Reaction Route to Sn_4P_3 /Reduced Graphene Oxide Nanohybrids as Anodes for Sodium Ion Batteries, *Adv. Energy Mater.*, 2016, 6, 1600376.
- [29] M. Tong, L. Wang, P. Yu, X. Liu, H. Fu, 3D Network Nanostructured NiCoP Nanosheets Supported on N-doped Carbon Coated Ni Foam as a Highly Active Bifunctional Electrocatalyst for Hydrogen and Oxygen Evolution Reactions, *Front Chem Sci Eng.*, 2018, 12, 417-424.
- [30] M. Motlak, N. A. M. Barakat, M. S. Akhtar, A. M. Hamza, B.-S. Kim, C. S. Kim, K. A. Khalil, A. A. Almajid, High Performance of NiCo Nanoparticles-Doped Carbon Nanofibers as Counter Electrode for Dye-Sensitized Solar Cells, *Electrochim. Acta.*, 2015, 160, 1-6.
- [31] X. Jiang, H. Li, S. Li, S. Huang, C. Zhu, L. Hou, Metal-Organic Framework-Derived Ni-Co Alloy@Carbon Microspheres as High-Performance Counter Electrode Catalysts for Dye-Sensitized Solar Cells, *Chem. Eng. J.*, 2018, 334, 419-431.
- [32] J. Li, G. Wei, Y. Zhu, Y. Xi, X. Pan, Y. Ji, I. V. Zatovsky, W. Han, Hierarchical NiCoP Nanocone Arrays Supported on Ni Foam as an Efficient and Stable Bifunctional Electrocatalyst for Overall Water Splitting, *J. Mater. Chem. A*, 2017, 5, 14828-14837.

- [33] E. J. Popczun, J. R. McKone, C. G. Read, A. J. Biacchi, A. M. Wiltrout, N. S. Lewis, R. E. Schaak, Nanostructured Nickel Phosphide as an Electrocatalyst for the Hydrogen Evolution Reaction, *J. Am. Chem. Soc.*, 2013, 135, 9267-9270.
- [34] X. Zhang, A. Wu, X. Wang, C. Tian, R. An, H. Fu, Porous NiCoP Nanosheets as Efficient and Stable Positive Electrodes for Advanced Asymmetric Supercapacitors, *J. Mater. Chem. A*, 2018, 6, 17905-17914.
- [35] H. Wang, B. Hou, Y. Yang, Q. Chen, M. Zhu, A. Thomas, Y. Liao, Cobalt Nanocrystals Encapsulated in Heteroatom-Rich Porous Carbons Derived from Conjugated Microporous Polymers for Efficient Electrocatalytic Hydrogen Evolution, *Small*, 2018, 14, 1803232.
- [36] J. Bao, X. Zhang, B. Fan, J. Zhang, M. Zhou, W. Yang, X. Hu, H. Wang, B. Pan, Y. Xie, Ultrathin Spinel-Structured Nanosheets Rich in Oxygen Deficiencies for Enhanced Electrocatalytic Water Oxidation, *Angew. Chem.*, 2015, 25, 7399-7404.
- [37] X. Shang, K.-L. Yan, Y. Rao, B. Dong, J.-Q. Chi, Y.-R. Liu, X. Li, Y.-M. Chai, C.-G. Liu, In Situ Cathodic Activation of V-Incorporated Ni_xS_y Nanowires for Enhanced Hydrogen Evolution, *Nanoscale* 2017, 9, 12353-12363.
- [38] S. Hao and Y. Yang, Water Splitting in Near-Neutral Media: Using an Mn–Co-based Nanowire Array as a Complementary Electrocatalyst, *J. Mater. Chem. A*, 2017, 5, 12091-12095.
- [39] X. Lu and C. Zhao, Electrodeposition of Hierarchically Structured Three-Dimensional Nickel–Iron Electrodes for Efficient Oxygen Evolution at High Current Densities, *Nat. Commun.*, 2015, 6, 6616.
- [40] X. Wang, W. Li, D. Xiong, D. Y. Petrovykh, L. Liu, Bifunctional Nickel Phosphide Nanocatalysts Supported on Carbon Fiber Paper for Highly Efficient and Stable Overall Water Splitting, *Adv. Funct. Mater.*, 2016, 26, 4067-4077.
- [41] X. Li, S. Li, A. Yoshida, S. Sirisomboonchai, K. Tang, Z. Zuo, X. Hao, A. Abudula, G. Guan, Mn Doped CoP Nanoparticle Clusters: An Efficient Electrocatalyst for Hydrogen Evolution Reaction, *Catal. Sci. Technol.*, 2018, 8, 4407-4412.
- [42] W. Ahn, M. G. Park, D. U. Lee, M. H. Seo, G. Jiang, Z. P. Cano, F. M. Hassan, Z. Chen, Hollow Multivoid Nanocuboids Derived from Ternary Ni-Co-Fe Prussian

- Blue Analog for Dual - Electrocatalysis of Oxygen and Hydrogen Evolution Reactions, *Adv. Funct. Mater.*, 2018, 28, 1802129.
- [43] Y. Feng, X.-Y. Yu, U. Paik, Nickel cobalt phosphides quasi-hollow nanocubes as an efficient electrocatalyst for hydrogen evolution in alkaline solution, *ChemComm.*, 2016, 52, 1633-1636.
- [44] C. Du, L. Yang, F. Yang, G. Cheng, W. Luo, Nest-like NiCoP for Highly Efficient Overall Water Splitting, *ACS Catalysis*, 2017, 7, 4131-4137.
- [45] P. Jiang, Q. Liu, X. Sun, NiP₂ nanosheet arrays supported on carbon cloth: an efficient 3D hydrogen evolution cathode in both acidic and alkaline solutions, *Nanoscale*, 2014, 6, 13440-13445.
- [46] D. Liu, Q. Lu, Y. Luo, X. Sun, A. M. Asiri, NiCo₂S₄ nanowires array as an efficient bifunctional electrocatalyst for full water splitting with superior activity, *Nanoscale* 2015, 7, 15122-15126.
- [47] C. Tang, L. Gan, R. Zhang, W. Lu, X. Jiang, A. M. Asiri, X. Sun, J. Wang, L. Chen, Ternary Fe_xCo_{1-x}P Nanowire Array as a Robust Hydrogen Evolution Reaction Electrocatalyst with Pt-like Activity: Experimental and Theoretical Insight, *Nano Letters*, 2016, 16, 6617-6621.
- [48] J. Song, C. Zhu, B. Z. Xu, S. Fu, M. H. Engelhard, R. Ye, D. Du, S. P. Beckman, Y. Lin, Water Splitting: Bimetallic Cobalt - Based Phosphide Zeolitic Imidazolate Framework: CoP_x Phase - Dependent Electrical Conductivity and Hydrogen Atom Adsorption Energy for Efficient Overall Water Splitting, *Adv. Energy Mater.*, 2017, 7, 1601555.

CHAPTER 4 Fabrication of CuO_xnanowires@NiMnO_x nanosheets core@shell-type electrocatalysts: crucial roles of defect modification and valence state for overall water electrolysis

4.1 INTRODUCTION

Water electrolysis is regarded as one of the useful and green routes for energy storage and conversion, which can utilize unstable renewable energy and surplus electricity to split water into clean hydrogen fuel. The electrocatalytic water splitting process includes two half-reactions, i.e., hydrogen evolution reaction (HER) and oxygen evolution reaction (OER), [5, 6] in which hydronium (H⁺) and hydroxyl (OH⁻) ions are the key reactants in acidic and alkaline electrolytes, respectively. [5, 6] However, it is difficult to perform water electrolysis in a neutral medium (pH=7) without any supporting electrolyte due to the poor conductivity. Some studies have been dedicated to achieving higher electrocatalytic performances under neutral pH conditions using buffered solutions including some salt electrolytes such as phosphates, borates, and carbonates, and the onset potentials were found to be comparable to those in acidic and alkaline media. [11, 12] Comparing to the acidic and alkaline electrolytes, the neutral one in the water electrolysis has many intrinsic benefits such as minimizing the adverse environmental impacts and prolonging the lifetime of devices. However, the development of efficient electrocatalysts working in the neutral electrolytes is full of a challenge owing to the relatively sluggish reaction kinetics. In general, to attain substantial reaction rates in water electrolysis at the neutral medium, the water molecule must act as the reactant. Meanwhile, in the neutral buffered solution, the buffering ionization ($BA = A^- + B^+$) is rapid in both directions to reach equilibrium between BA and ($B^+ + A^-$) on the surface of an electrode, which will maintain the neutral pH level at least in the bulk of the solution. [14-16]

The benchmarking noble-metal-based electrocatalysts such as Pt/C for HER and IrO₂, Ir/C or RuO₂ for OER always own extraordinary electrocatalytic activity with great stability even in the neutral media due to their inert behaviors. However, they also have disadvantages such as high prices and scarcity. [18, 19] Thus, the development of efficient

bifunctional electrocatalysts with low cost, high stability, and environmental benignity, particularly based on non-noble metal materials for the water electrolysis is highly challenging and desiring. Especially, as the alternatives of electrocatalysts, earth-abundance transition-metal-based ones with high performance should be crucial to pave the way for the hydrogen economy era. To improve the catalytic activity, creating three-dimensional (3D) nanostructures of transition metals/metal (hydr)oxides on the electrode without the binders is considered a promising way in electrode preparations, and various transition metal-based materials with ideal atomic arrangements have been developed as active electrocatalysts to improve electronic transportation as well as electrochemical stability for water electrolysis. [23-25] In particular, for the electrocatalysts working in neutral pH solutions, a combination of the metal with carbon materials, fabrication of metal alloys, and doping of foreign metal on metal oxides have been applied to realize electronic structure modification, and thereby improving the catalytic performance. [28, 29]

Mn-containing materials, especially various manganese oxides (MnOx) such as MnO₂, Mn₂O₃, Mn₅O₈, and complex oxides such as MnFe₂O₄ and metal-doped MnO₂ have been considered as potential electrocatalysts for water electrolysis due to their earth-abundant, inexpensive, and special electronic structure. [30-37] Mn-based oxides always have Mn³⁺/Mn⁴⁺ redox couple, which has flexible electronic configurations with high conductivity and catalytic activity. It is found that MnOx has low activity in acidic medium since Mn³⁺ on the surface is easily converted to Mn²⁺ and Mn⁴⁺ at pH<9 due to the disproportionation reaction whereas Mn³⁺ can be effectively stabilized by the comproportionation of Mn²⁺ and Mn⁴⁺ in alkaline medium. [35, 36] Thus, how to control the disproportionation and comproportionation of Mn³⁺ is essential for the development of Mn-based electrocatalyst working in neutral pH solutions. Kuo et al. [37] synthesized a mesoporous MnOx with a crystalline structure of Mn³⁺-rich Mn₂O₃ using a one-step inverse micelle templating method. Meng et al. [30] found that electrocatalytic activity is strongly dependent on the crystallographic structures of MnOx, which followed an order of α -MnO₂ > AMO > β -MnO₂ > δ -MnO₂. Jeong et al. [50] investigated Mn₅O₈ with mixed Mn valences, and also found that Mn³⁺ played an important role in the catalysis of OER under the neutral pH solution.

Currently, it becomes a rising hot topic by designing of the bimetallic compound to controllably modify and engineer the electronic distribution for achieving the synergistic regulation of activity, conductivity, and stability of electrocatalysts. For the transition metal-based catalysts, the introduction of a second element into the host lattices could also cause obvious regulation of the electronic structure of the compound host and change the H adsorption free energy, leading to good catalytic properties. [53] Especially, many studies exhibited that the bimetallic oxides have better intrinsic OER property than the single metal oxide. [54-61] For instance, Wang et al. [66] prepared bimetallic phosphide embedded carbonaceous matrix (FeNiP/C) electrocatalyst, which presented 3D hollow barrel shape with a high specific surface area and exhibited excellent OER catalytic performance, reaching a current density of 10 mA cm^{-2} at a low overpotential of 229 mV with a low Tafel slope. Jia et al. [71] combined the bimetallic nanoplate with the multi-wall carbon nanotubes (CoMn-LDH/MWCNT), which also exhibited excellent OER activity (a low overpotential of 300 mV@ 10 mA cm^{-2}) with outstanding long-term electrocatalytic stability.

Various morphologies of copper oxide (CuOx) such as CuOx leaf and CuOx nanowires can be fabricated and used as catalysts and catalyst supports. [73, 74] Moreover, the combination of CuOx with other transition metal oxides could further improve the conductivity of electrocatalysts, thereby enhancing the catalytic performance. For instance, Rong et al. [76] fabricated paintbrush-like Cu-Cu₃P on Cu foam, which exhibited excellent performance for overall water electrolysis with a low cell voltage of 1.55 V to deliver the standard current density of 10 mA cm^{-2} . Zhou et al. [78] prepared hierarchical CuOx@Co₃O₄ NRs on a Cu foam, which also showed a bifunctional activity towards water splitting with a small overpotential of 240 mV for the OER and 242 mV for the HER at a current density of 50 mA cm^{-2} , along with low Tafel slopes of 46 and 61 mV dec⁻¹, respectively, and ultrahigh faradaic efficiencies.

Various defects endow the ability to affect the adsorption energy of reactants or intermediates as well as the dissociation energy of the produced gas, which can promote the conversion and generation of reactants and intermediates. [19] In addition, theoretical studies proved that the materials with rich defects close to the Fermi level could regulate the electronic structure and improve the electrical conductivity, and thereby enhancing

the catalytic activity and stability.[19] Thus, defect engineering should be an efficient route to improve the HER catalysis performance of metal oxide, As demonstrated by Wang et al., [81] the dehydration and reduction process for the preparation of 3D hierarchical Co nanoparticles modified $\text{Co}_2\text{Mo}_3\text{O}_8$ nanosheets by thermal reduction of $\text{CoMoO}_4 \cdot n\text{H}_2\text{O}$ precursor induced the formation of nanoporous morphology and Co vacancy defective structure so that the HER catalytic activity was greatly improved. Especially, the defects with the edge dislocations can enhance the electrochemical performance of metal oxides by accelerating ion conduction. [33-37] To date, many researchers mainly focused on the studies of point defects (such as doping and vacancy). However, the influences of one-dimensional line defects (such as edge dislocation, screw dislocation, etc.) and two-dimensional planar defects on the catalytic activity of bimetallic oxides have not been investigated in depth. While one-dimensional and two-dimensional defects, such as edge dislocation were built by lattice mismatch engineering at the interface of catalyst or between neighboring layers in multilayer composites, it could effectively tune the crystalline structure and intrinsic activity of catalysts. [82]

Herein, NiMn oxide nanosheets (NiMnOx NSs) were electrodeposited on the CuOx nanowires (NWs) grown on the copper foam (CF) using a unipolar pulse electrodeposition (UPED) method to fabricate 3D hierarchical core-shell structure electrocatalysts for both HER and OER in the water electrolysis under either neutral pH or alkaline medium. The obtained CuOx NWs @NiMnOx NSs core@shell-type bifunctional electrocatalysts were characterized by SEM (scanning electron microscope) with EDS (energy dispersive X-ray detector), TEM (transmission electron microscope), XRD (powder X-ray diffraction), and XPS (X-ray photoelectron spectroscopy) to understand its micro- and nano-structures, the crystalline structure, and elemental compositions and valence states on the surface. The electrochemical characteristics and HER and OER performances in the neutral pH solutions were examined and compared with those in alkaline solutions. In addition, the two-electrode system with CuOx NWs @NiMnOx NSs/CF || CuOx NWs @NiMnOx NSs/CF as a cathode (-) and anode (+) was applied for the testing of overall water electrolysis performance in both neutral pH and alkaline media.

4.2 EXPERIMENTAL

4.2.1 Chemicals and Materials

Nickel (II) nitrate hexahydrate ($\text{Ni}(\text{NO}_3)_2 \cdot 6\text{H}_2\text{O}$, purity 98%), potassium hydroxide (KOH, 85%), sodium dihydrogen phosphate dihydrate ($\text{NaH}_2\text{PO}_4 \cdot 2\text{H}_2\text{O}$, purity 99%), disodium hydrogen phosphate (NaH_2PO_4 , purity 99%), hydrochloric acid (HCl, Conc. 36%) and ethanol ($\text{C}_2\text{H}_5\text{OH}$, Conc. 99.5%) were purchased from Wako, Japan. Manganese (II) nitrate tetrahydrate ($\text{Mn}(\text{NO}_3)_2 \cdot 4\text{H}_2\text{O}$, purity $\geq 97\%$) was purchased from Sigma-Aldrich, Japan. De-ionized (DI) water (18.2 M Ω cm) was used for the preparations of solutions and electrolytes. Copper foam (CF, thickness: 1.6 mm, bulk density: 350 g/m²) was purchased from Xiamen TOB New Energy Technology Co. Ltd.

4.2.2 Generation of $\text{Cu}(\text{OH})_2$ nanowires on Cu foam.

Firstly, the CF sheet (size: 2 x 2 cm²) was pre-treated by 1.0 M HCl in an ultrasonic bath for 10 min to remove the oxidized layer on the surface, and then washed successively by ethanol and DI water several times. Thereafter, $\text{Cu}(\text{OH})_2$ nanowires ($\text{Cu}(\text{OH})_2$ NWs) were directly grown on the surface of CF substrate by an electro-oxidation process, in which CF, Pt wire, and Ag/AgCl standard reference electrode were used as the working, counter and reference electrodes in a three-electrode electrochemical system with 3.0 M KOH electrolyte at a constant current of 80 mA for 1200 s. As such, the $\text{Cu}(\text{OH})_2$ NWs were generated on the surface of CF with a color-changing to light blue, then the electrode was washed with DI water several times and dried at room temperature overnight.

4.2.3 Synthesis CuO_x NWs@ NiMnO_x NSs on CF substrate.

NiMn oxide nanosheets (NiMnO_x NSs) were electrodeposited on the above prepared $\text{Cu}(\text{OH})_2$ NWs/CF using a unipolar pulse electro-deposition (UPED) method in a three-electrode system. In brief, the electrolyte with $\text{Ni}(\text{NO}_3)_2 \cdot 6\text{H}_2\text{O}$ and $\text{Mn}(\text{NO}_3)_2 \cdot 4\text{H}_2\text{O}$ was prepared by using 100 ml of DI water with a stirring time of 15 min. Herein, different Ni/Mn ratios of 1/4, 1/1, and 4/1 with a total metal ion concentration of 0.1 M were used for the preparation of different electrolytes to investigate the effect of Ni/Mn ratio on the catalytic performance. The $\text{Cu}(\text{OH})_2$ NWs/CF was used as the working electrode, and Pt wire and standard Ag/AgCl

reference electrode were served as the counter and reference electrodes, respectively. The pulse potential was set at -1 V with an on/off time of 1 s based on the preliminary experimental results. The cycle numbers were set as 500, 1000, 1500, and 2000 respectively to investigate the effect of cycle number on the performance of the final electrocatalyst. After the electrodeposition process, the obtained Cu(OH)₂ NWs@NiMn NSs/CF was washed by DI-water several times and dried in a vacuum oven at 80 °C for 12 h. Finally, the electrode was calcinated in the air at 350 °C for 2 h with a heating rate of 2 °C/min. As such, the CuO_x NWs@NiMnO_x NSs/CF electrode was obtained.

4.2.4 Characterizations

The morphologies of various samples were characterized by a scanning electron microscope (SEM, SU8010, HITACHI, JAPAN) with an energy dispersive X-ray detector (EDS, Horiba Scientific) and the nanostructures were observed by a transmission electron microscope (TEM, JEM-2100F, JEOL). Before the TEM observation, the sample was well dispersed on a Cu grid mesh (Japan, Nisshin EM Co., Ltd. Tokyo). The powder X-ray diffraction (XRD) analysis was performed on a Rigaku Smartlab diffractometer (Japan) with Cu-K α as the radiation source ($\lambda=0.15406$ nm) in a range of 20°-80° to determine the crystalline structure. X-ray photoelectron spectroscopy (XPS) spectrum was measured at room temperature using a VG Scientific ESCALab250i-XL instrument with an Al-K α X-ray source.

4.2.4 Electrochemical measurements

Electrochemical measurement was conducted on an electrochemical workstation (VersaSTAT 4, Princeton, USA) with a three-electrode system at room temperature in a 1.0 M phosphate-buffered (PB) solution (pH 6.8-7). The obtained electrode (1 x 1 cm²), Ag/AgCl (in KCl saturated) reference electrode, and carbon rod were used as the working, reference, and counter electrodes, respectively. For comparison, 1.0 M KOH (pH =14) was also used as the electrolyte, and in this case, carbon rod and Hg/HgO (in 1M NaOH) were used as counter and reference electrodes, respectively. HER and OER performances were evaluated by using linear sweep voltammetry (LSV) with a scan rate of 2 mV s⁻¹ at a potential range of 0 to -0.6 V (for HER) and 1.3 to 2.0 V (for OER). Electrochemical impedance spectroscopy (EIS) measurement was carried out with

a frequency range from 100 kHz to 0.01 Hz at an overpotential of 200 mV. The potential in the neutral pH electrolyte was calculated by: $E \text{ (V vs RHE)} = E(\text{Ag/AgCl}) + (0.059 \times \text{pH}) + 0.197$, Whereas that in the alkaline electrolyte with respect to the reversible hydrogen electrode (RHE) was calculated by: $E \text{ (V vs RHE)} = E(\text{Hg/HgO}) + (0.059 \times \text{pH}) + 0.098$. The electrochemical active surface areas (ECSAs) of various electrocatalysts at non-faradaic overpotentials were measured by cyclic voltammetry (CV) at a potential range of 0.1-0.3 V (vs RHE). The Cdl was estimated by plotting current densities at different scan rates at a potential of 0.2 V. The stability tests were performed in two ways: (i) chronopotentiometry measurement at a fixed current density of -10 mA cm^{-2} for 40 h; and (ii) cyclic voltammetry test in a potential range from 0.1 to -0.3 V (vs RHE) for 1000 cycles. Finally, the two-electrode system using CuOx NWs@NiMnOx NSs/CF || CuOx NWs @NiMnOx NSs/CF as the cathode (-) and anode (+) was used for the testing of overall water electrolysis performance, in which the linear sweep curve (LSV) was measured with a potential range of 1.3-2.0 V at a scan rate of 2 mV/s.

4.3 RESULTS AND DISCUSSION

4.3.1 Microstructure and composition analysis of CuOx NWs@NiMnOx/CF catalyst.

Figure 4.1 illustrates the fabrication process for CuOx NWs @NiMnOx NSs/CF electrode. As stated above, firstly, Cu(OH)₂ NWs were grown directly on the CF substrate by anodization of CF in 3.0 M KOH solution. Then, bimetallic NiMn hydroxide NSs were electrodeposited on these Cu NWs via the UPED method, finally, the electrode was calcined at 350 °C in air, and as such, CuOx NWs @NiMnOx NSs/CF electrode was obtained.

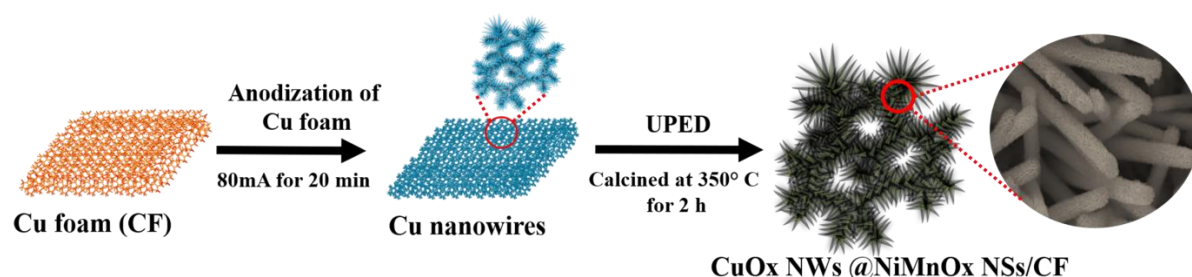


Figure 4.1 Schematic illustration for the fabrication of CuOx NWs @NiMnOx NSs/CF electrode.

Figure 4.2 shows SEM images of the obtained Cu(OH)₂ NWs (Fig. 2A), CuOx NWs@MnOx (Fig. 2B), CuOx NWs@NiO (Fig. 4.2C) and CuOx NWs@NiMnOx NSs (Fig. 4.2D) on CF, and elemental distributions on the surface of CuOx NWs@NiMnOx NSs/CF electrode (Fig. 4.2E). As shown in Fig. 4.2B and 4.3A', the MnOx was well grown on the CuOx NWs as a core-shell structure in the absence of Ni species, where the legible lattice of 0.205 nm is related to the (211) plane of MnO₂. However, NiO particles were not uniformly distributed on the CuOx NWs in the absence of Mn species and some large bulk NiO particles were formed on the surface of the electrode (Fig. 4.2C). In contrast, the NiMnOx NSs were homogeneously and fully covered on the CuOx NW cores (Figs. 4.2D) with uniformly elemental distributions (Fig. 4.2E). The nanosheet formation probably followed the mechanism in the formation of layered double hydroxide (LDH) (e.g., as indicated in *Adv. Funct. Mater.* 24, 934-942 (2014)). [83] Firstly, Ni²⁺ and Mn²⁺ reacted with hydroxide (OH)⁻ ions generated on the electrode to form nuclei and grew into the primary particles. In this process, some Mn²⁺ would change to Mn³⁺ and/or Mn⁴⁺ by the applied potential, which should play an important role in the gradual formation of Ni(OH)₂/Mn(OH)₂ composite like Ni-Mn LDH with a nanosheet structure on the surface of Cu nanowire due to the continuous aggregation of the nickel and manganese hydroxide composite to chain state with the assistance of applied pulse potential. In addition, due to the random dispersion of the nickel and manganese hydroxide primary particles, the nanosheets distributed on the surface of Cu nanowire along with different directions, the obtained Ni(OH)₂/Mn(OH)₂ composite nanosheet were intersected, and after calcination, the NiMnOx nanosheets were also intersected as shown in Fig. 4.2D. In contrast, the MnOx or NiO particles rather than nanosheets were

generated on Cu nanowire since the LDH nanosheet is impossible to be formed with the single metal precursor. Meanwhile, TEM measurement (Fig. 4.2F) shows that the obtained catalysts had a core@shell structure. As revealed in Fig 4.3B', the NiO endowed a large crystallite size and intact crystal structure and the lattice distance of 0.247 nm reflected the (111) crystal plans. In contrast, rich defects were observed in the HRTEM image of CuO_x NWs@NiMnO_x NSs, in which the lattice fringe spacing of 0.256 nm approached the (311) plane of NiMn₂O₄ (Figure 4.3C').

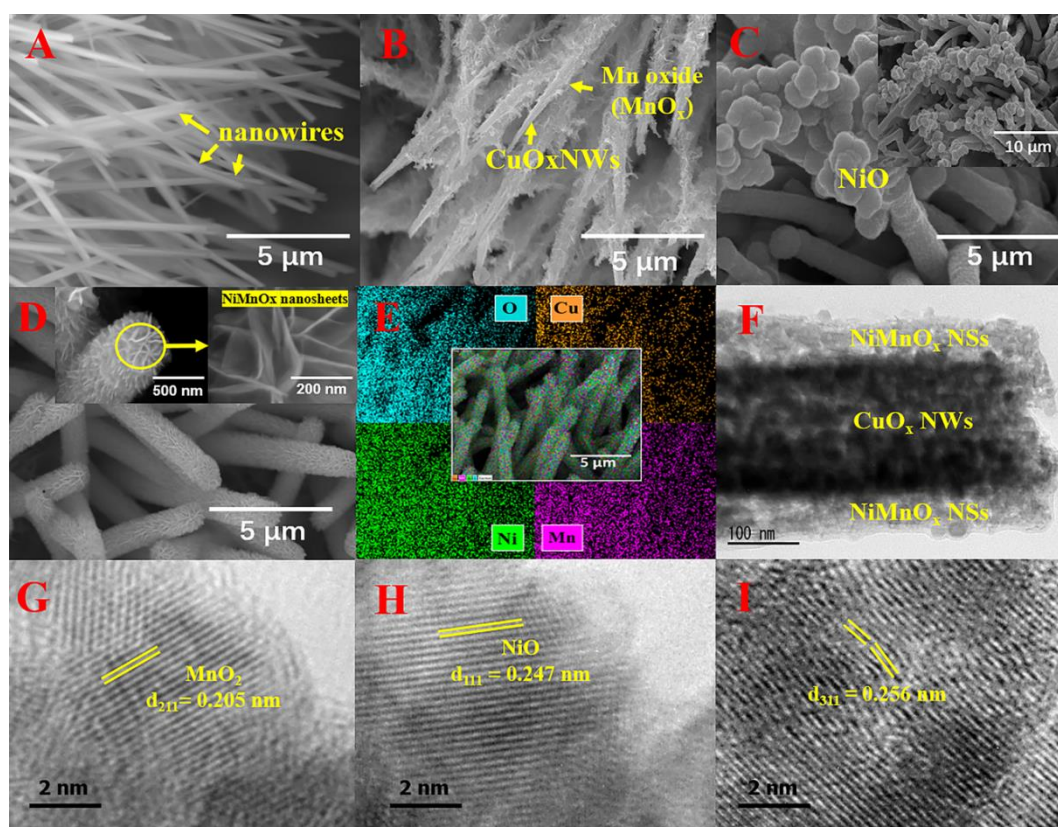


Figure 4.2 SEM images of the obtained Cu(OH)₂ NWs (A), CuO_x NWs@MnO_x (B), CuO_x NWs@NiO (C) and CuO_x NWs@NiMnO_x NSs (D) on CF; elemental distributions on CuO_x NWs@NiMnO_x NSs/CF electrode (inset: enlarged SEM image at scales of 500 nm and 200 nm) (E); and TEM image of CuO_x NWs@NiMnO_x NSs (F). TEM image with an enlargement scale of 2 nm for MnO₂ crystal in CuO_x NWs@MnO_x (G), NiO of CuO_x@NiO (H) and defect structure of NiMn₂O₄ in the obtained CuO_x NWs@NiMnO_x NSs.

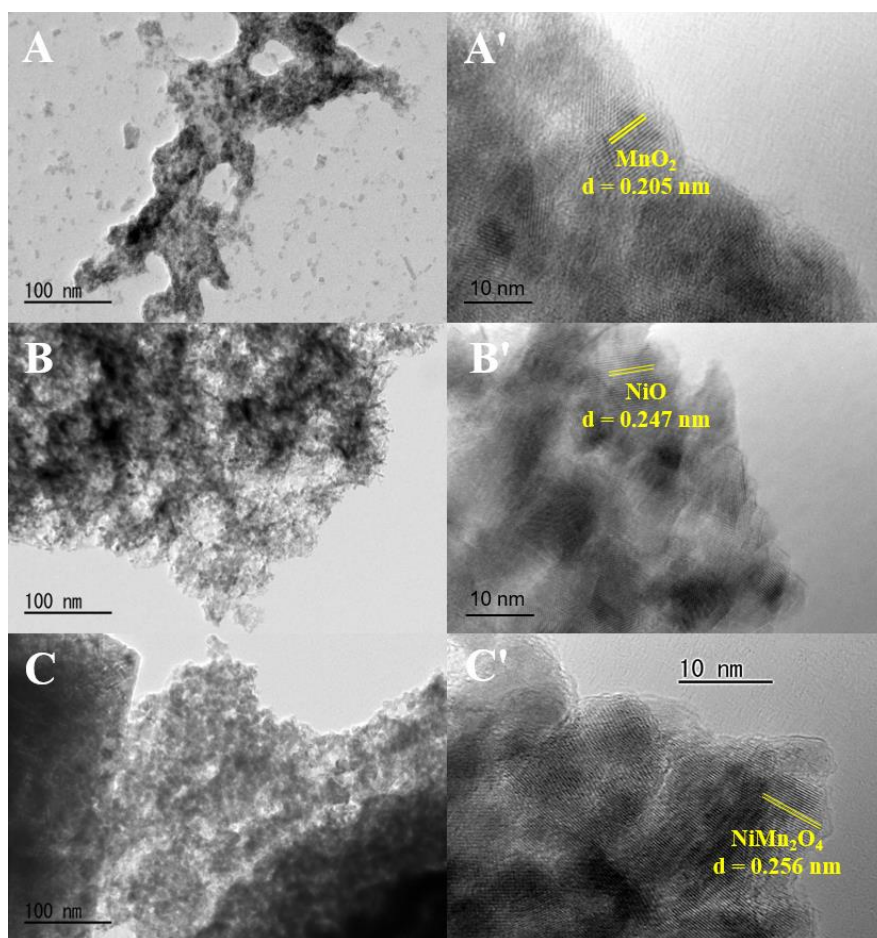


Figure 4.3 TEM images of (A, A') MnOx, (B, B') NiO, and (C, C') NiMnOx NSs.

In addition, comparing with the prepared MnOx and NiO, it is obvious that the prepared NiMnOx exposed abundant defect structure in HRTEM (Fig. 4.2 G-I). To explore the reasons for defect formation of NiMnOx, the crystal structures of the electrodeposited Ni and Mn-based hydroxides were measured. Unexpectedly, as shown in Fig. 4.4 and Fig. 4.5, the obtained material consisted of Ni(OH)₂/Mn(OH)₂ composite, in which Ni and Mn-based hydroxide particles with 1-4 nm diameter mixed. It is found that there were obvious edge sites among different particles. After the calcination treatment, the Ni(OH)₂/Mn(OH)₂ composite was converted to NiMnOx (Fig. 4.6), in which nanodots built nanosheet arrays and rich crystalline defects of lattice distortion, vacancy, amorphous-like structure, edge dislocation, screw dislocation, and additional active edge sites were observed. the adsorption energy of reactant and/or intermediates, as well as the dissociation energy of the produced gas, thereby promoting the conversion and generation of reactants and intermediates. [84] These defect structures could be

formed during the reaction between $\text{Ni}(\text{OH})_2$ and $\text{Mn}(\text{OH})_2$, where the edge sites among different crystalline grains and the discrepancy of atomic radii led to the distortion of host lattices. Herein, various defects could endow the ability to affect Moreover, theoretical studies proved that the materials with rich defects close to the Fermi level could regulate the electronic structure and improve the electrical conductivity, and subsequently enhance the catalytic activity and stability. [84] In addition, the crystalline fringes along the crooked edge were discontinuous, which could provide abundant defects. Moreover, it should be noted that the defect-rich structure resulted from the partial cracking of the regions along the basal planes (Fig. 4.4G and L). These additional active edge sites should lead to higher electrocatalytic activity and internal conductivity than those amorphous or polycrystalline catalysts. [85-88]

Moreover, the lattice distortion resulted in numerous vacancies, which led to coordination-unsaturated spinel crystal and unstable valence states of Ni and Mn elements (Fig. 4.4F). Besides, typical one-dimensional edges, e.g., the edge dislocation and screw dislocation, were observed in the exposed planes of NiMnOx material. Herein, the screw dislocation in the lattice structure of a crystal could lead to the atoms rearranged in a helical pattern (Fig. 4.4K), by which the crystal along with a plane slip one half across the other by a lattice vector. Meanwhile, the crystal deformation due to the screw dislocation could regulate the electronic structure and subsequently affect the catalytic activity and stability of NiMnOx. Furthermore, the edge dislocation can be considered as a kind of defect where an extra half-plane of atoms is introduced midway through the crystal, distorting nearby planes of atoms. When enough force is applied from one side of the crystal structure, this extra plane passes through planes of atoms breaking and joining bonds with them until it reaches the grain boundary (Fig. 4.4G). In addition, the deformation of crystalline results in a special strain field around the dislocation defect area, and the strain field leads to the formation of vacancies and charge aggregation. Recently, many works indicated that the optimal control of oxygen vacancies of oxides could improve the electronic conductivity as well as OH^- adsorption, [89] and the metal vacancy defect was also considered to promote the water absorption. [90] In addition, Sun et al. believed that the abundant edge dislocations in Co_3O_4 materials with tensile stress could attract foreign solute Li^+ , facilitating Li^+ diffusion and transport. [91]

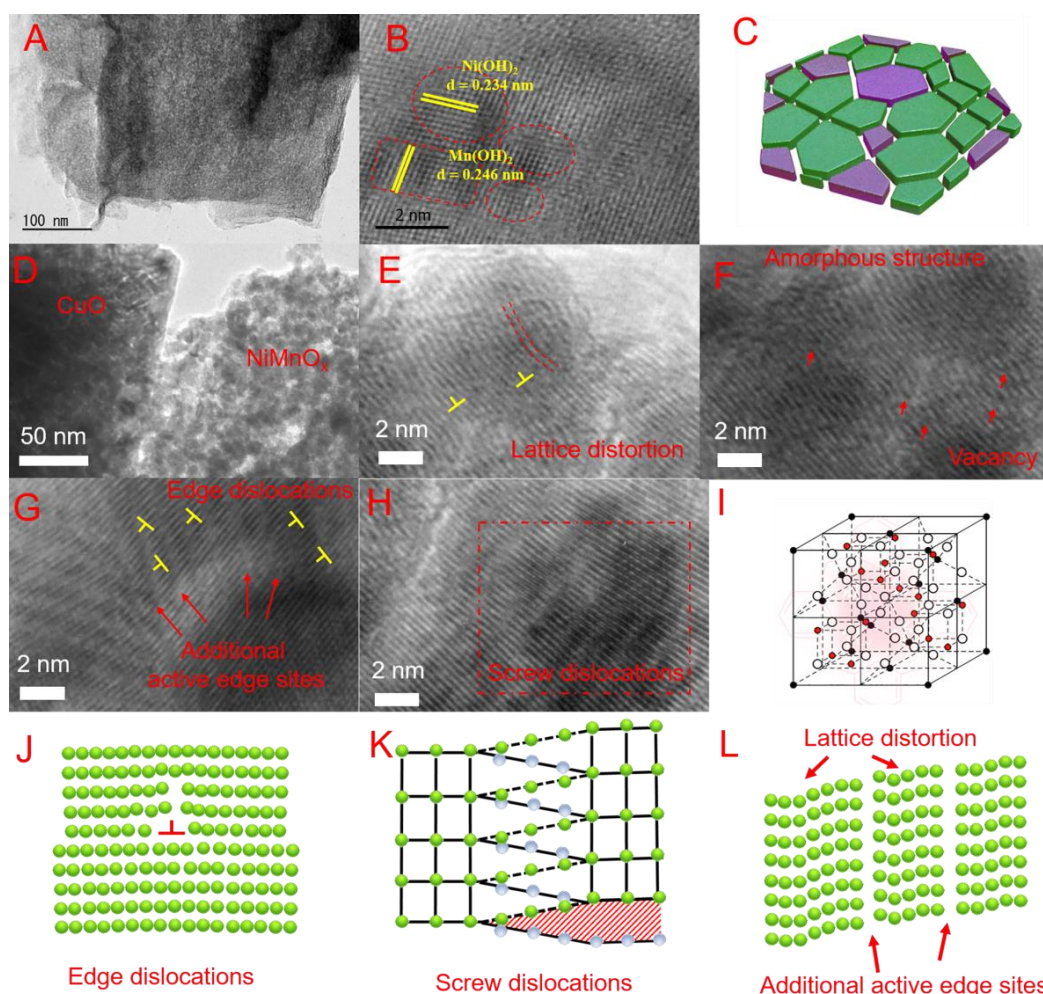


Figure 4.4 TEM images of the obtained Ni(OH)₂/Mn(OH)₂ NSs (A, B); TEM images of the obtained CuO_x NWs@NiMnO_x NSs (D) on CF; and corresponding partial enlarged views (D, E, F); Schematic diagram of edge dislocation (G), screw dislocation (H), lattice distortion and additional active edge sites (I).

Stimulated by the unique defect-rich crystal structure of NiMnO_x nanosheets, the structure, and composition of the obtained composite were further analyzed by XRD and XPS. As shown in Fig. 4.6A, the diffraction peaks at 37.38° and 43.27° related to Cu₂O (JCPDS 78-2076) and those at 36.50°, 43.27° corresponding to CuO (JCPDS 45-0937) were observed, indicating that CuO and Cu₂O coexisted in the present catalysts. Meanwhile, the diffraction peaks of MnO_x, NiO, and NiMnO_x NSs were too weak to clearly observed due to the strong peaks corresponding to Cu species. Herein, we also prepared MnO_x, NiO, and NiMnO_x NSs on carbon paper substrate at the same conditions in the absence of CuO_x NWs, and their corresponding XRD patterns are shown in Figures

4.6B-C. One can see that the diffraction peaks at 37.44° , 43.43° , and 63° were from NiO (JCPDS 47-1049) (Fig. 4.6B), and those at 18.38° , 38.44° , and 43.84° indicated the formation of α -MnO₂ (JCPDS 42-1348) in the catalysts (Fig. 4.6C), which should be a benefit for the OER. [30] In addition, it is found that the crystal of NiMnOx composite was close to the spinel structure of NiMn₂O₄ (Fig. 4.6D), which had an obvious right shift at the location of (311) peak.

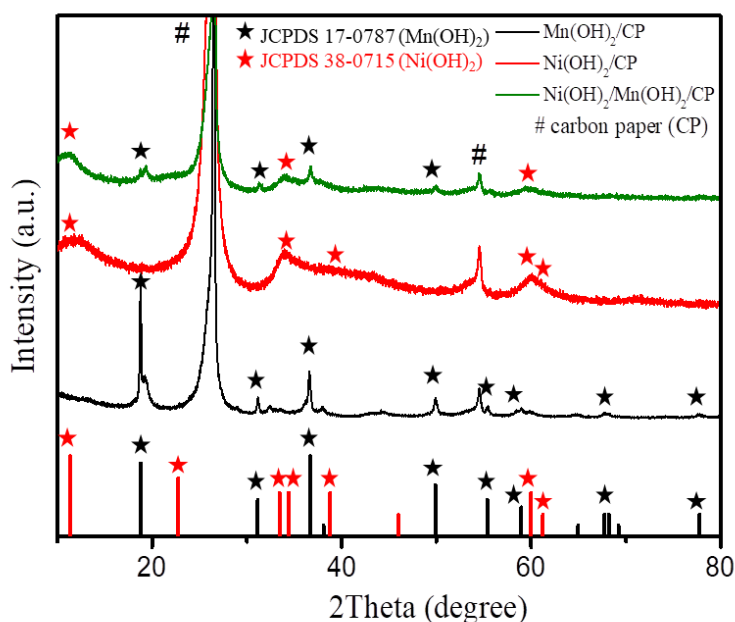


Figure 4.5 (A) XRD patterns of Mn(OH)₂/CP, Ni(OH)₂/CP and Mn(OH)₂/Ni(OH)₂/CP composite.

In addition, the exceptional peak broadening of the NiMnOx also indicated the existence of rich crystalline defects. As shown in Figs. 4.7 and 4.8, the composite was mainly consisted of Ni, Mn, O, Cu elements. In the Cu 2p spectrum (Fig. 4.7B), two peaks at 933.72 and 953.00 eV corresponding to the Cu 2p_{3/2} and Cu 2p_{1/2} peaks of Cu⁺ (Cu₂O), respectively. Meanwhile, the binding energies at 934.74 and 954.7 eV with two satellites assigned to the Cu 2p_{3/2} and Cu 2p_{1/2} peaks of Cu²⁺ (CuO) respectively were also observed, [92] which are in agreement with the XRD analysis results. Moreover, in the Mn 2p spectrum, the two fitting peaks at 641.42 and 642.78 eV related to Mn 2p_{3/2} assigned to Mn³⁺ and Mn⁴⁺ respectively, whereas the binding energy peaks at 652.66 and

653.94 eV related to Mn 2p_{1/2} corresponded to Mn³⁺ and Mn⁴⁺. [21] As such, the percentage ratio of Mn³⁺/Mn⁴⁺ was calculated to be 39.07/60.93 based on the peak areas of the valence states of elements (Table 4.1).

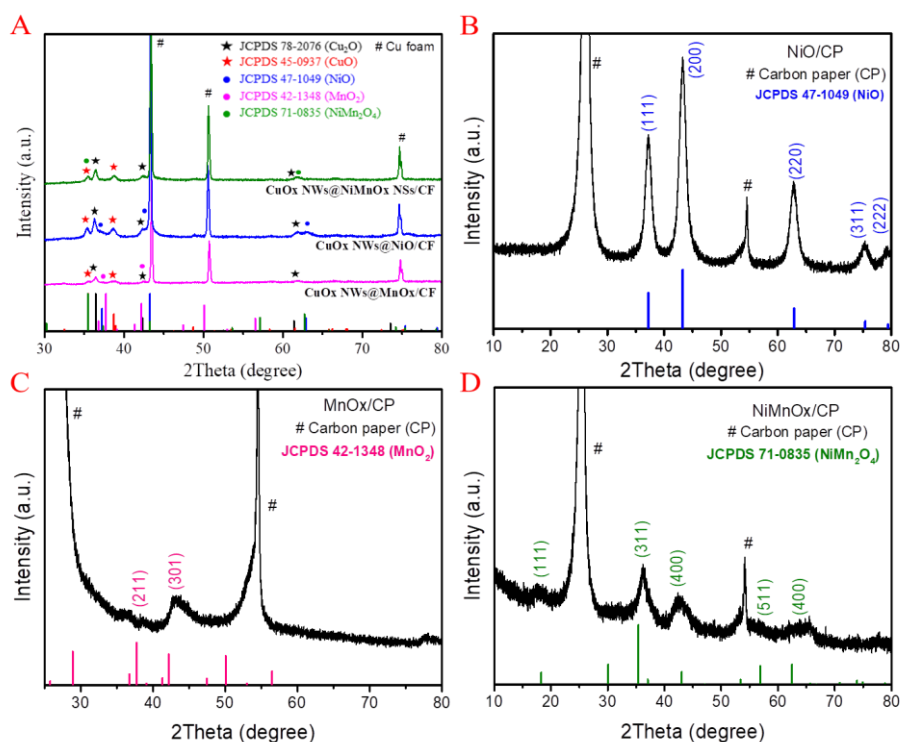


Figure 4.6 (A) XRD patterns of CuOx NWs@MnOx/CF, CuOx NWs@NiO/CF, CuOx NWs@NiMnOx NSs/CF. (B-D) XRD pattern of catalysts deposited on carbon paper (CP) substrate (D) NiO/CP (C) MnOx/CP (D) NiMnOx NSs/CP.

Besides, the chemical valence states of Ni 2p XPS spectra of CuOx NWs@NiMnOx are shown in Fig. 4.7D, in which the deconvolution of Ni 2p_{3/2} (854.8 ~ 855.87 eV of Ni³⁺ and Ni²⁺) and 2p_{1/2} at 872.82~871.5 eV peaks with two satellites (861.49 and 879.47 eV) also indicated the existence of Ni³⁺/ Ni²⁺ couple in the catalyst. [93] Moreover, the spin-orbit splitting values of the Ni 2p_{1/2} and Ni 2p_{3/2} were over 15 eV, also indicating the presence of Ni²⁺ and Ni³⁺ species [94]. Here, the relative atomic ratio of Ni²⁺/Ni³⁺ in the CuOx NWs@NiMnOx composite was compared with that of the published normal NiMn₂O₄ material by estimating the covered area of the fitted curve [95]. It is found that the atomic molar ratio of Ni²⁺/Ni³⁺ in NiMnOx of CuOx NWs@NiMnOx was higher than that of normal NiMn₂O₄, proving that more Ni²⁺ species

appeared in CuOx NWs@NiMnOx than Ni³⁺. In other words, more coordination-unsaturated spinel structure was achieved during Mn introduction and defect formation process. [96, 97] For the O 1s spectra (Fig. 4.7C), the peak at 528.9 eV corresponded to the typical metal-oxygen (Ni-O or Mn-O) bond, and the peak appeared at the higher binding energy of 531.1 eV was attributed to the defect sites with low oxygen coordination, [98] which corresponded to the HRTEM results. It should be noted that the oxygen vacancy defects could reduce the barrier for the OH⁻ adsorption because of the low oxygen-coordination sites in the MO₆ structure. Hence, a lower overpotential was achieved in this study. [92, 99, 100]

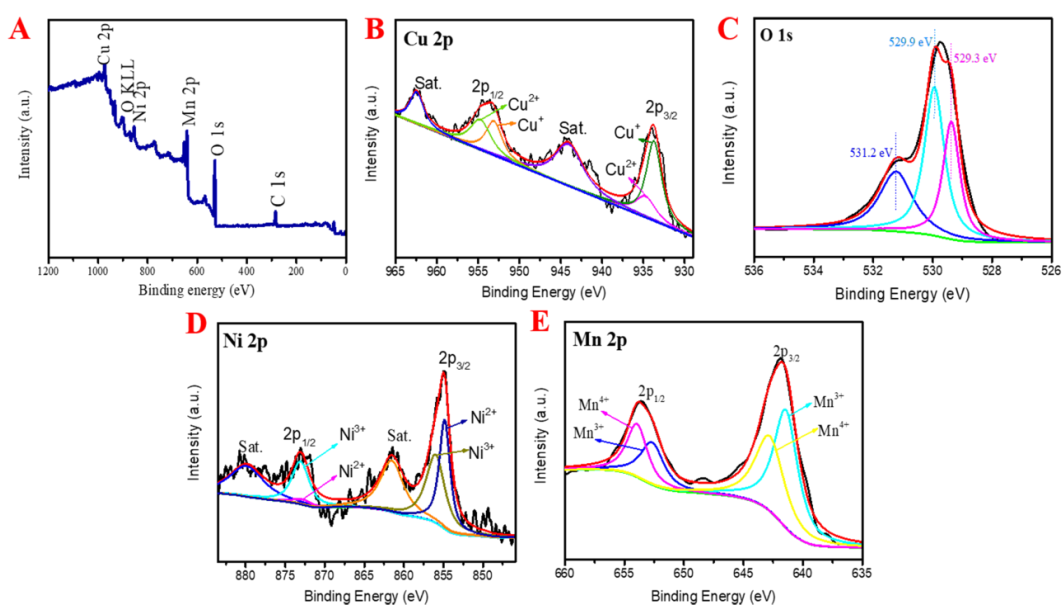


Figure 4.7 High-resolution XPS spectra of CuOx NWs@NiMnOx NSs: (A) survey peak, (B) Cu 2p, (C) O 1s, (D) Ni 2p, and (E) Mn 2p spectra.

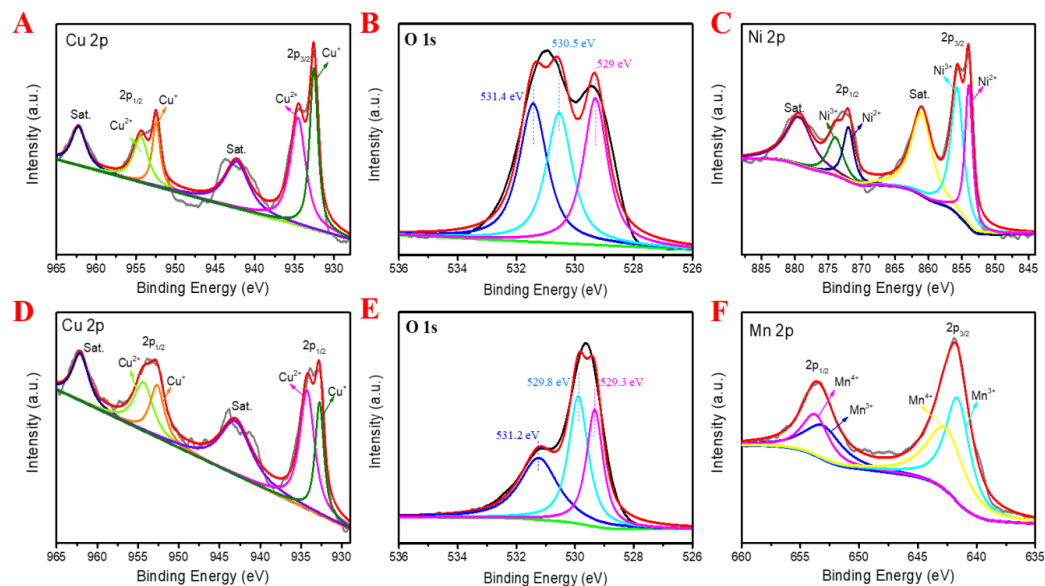


Figure 4.8 High-resolution XPS spectra of (A-C) CuOx NWs@NiO: (A) Cu 2p, (B) O 1s, (C) Ni 2p, and (D-F) CuOx NWs@MnOx: (D) Cu 2p, (E) O 1s, (F) Mn 2p.

4.3.2 HER and OER in alkaline medium

4.3.2.1 Influence of preparation parameters of CuOx NWs@NiMnOx NSs/CF catalyst.

As stated above, Mn-containing electrocatalysts always show stable performance in the alkaline medium. Herein, to select the best bifunctional CuOx NWs@NiMnOx NSs/CF electrode, the performances of the obtained electrocatalysts were evaluated in the alkaline medium at first. To find the optimum Ni/Mn molar ratio in the CuOx NWs@NiMnOx NSs/CF electrode and the optimum cycle number during the electrodeposition of NiMn hydroxide on Cu(OH)₂ NWs core during the preparation of electrode by the UPED method, the electrodes fabricated with different Ni/Mn initial ratios in the precursors and different UPED cycles were firstly tested in alkaline solutions.

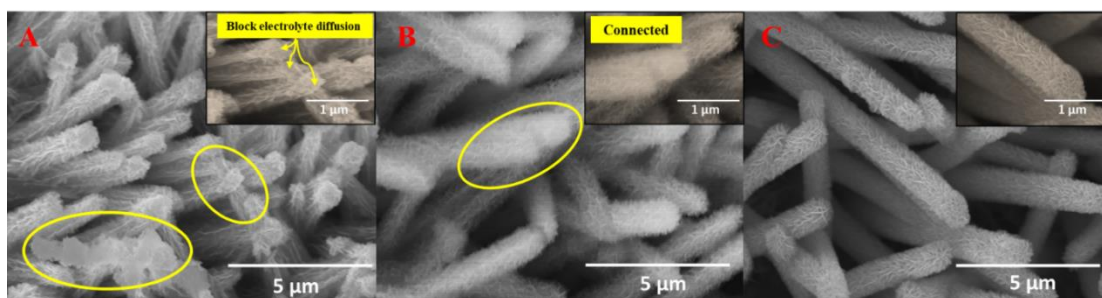


Figure 4.9 SEM images of CuOx NWs@NiMnOx NSs prepared with different ratios of Ni:Mn in the initial precursors: (A) 4:1 (B) 1:1 (C) 1:4.

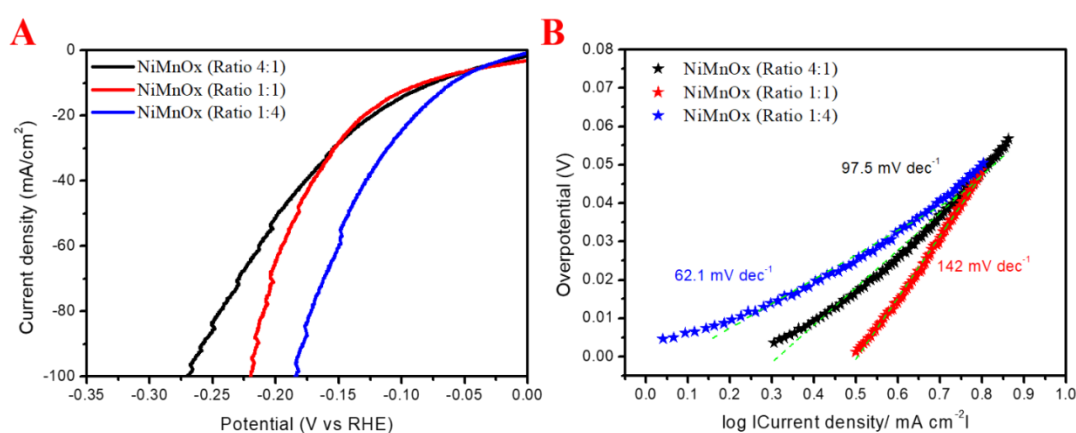


Figure 4.10 LSV polarization curves in 1.0 M KOH solution for HER over CuOx NWs@NiMnOx NSs/CF electrodes prepared at different Ni/Mn ratios (4:1, 1:1 and 1:4) in the initial precursor (A) and related Tafel plots (B).

As shown in Figures 4.9-4.10, the catalyst with the initial Ni/Mn molar ratio of 1/4 exhibited the lowest overpotential with the smallest Tafel slope among all the prepared catalyst with the initial Ni/Mn molar ratio from 1/4 to 4/1. It is found that fluffy NiMnOx nanosheets were formed on CuOx nanowires in the case with less amount of Mn species in the initial solution (e.g., Ni/Mn molar ratio of 4/1), and with the increasing of the Mn species in the initial solution, NiMnOx nanosheets were uniformly formed on the CuOx nanowire, thereby leading to better catalytic performance. Meanwhile, for the fabricated CuOx NWs@NiMnOx NSs/CF electrodes with the initial Ni/Mn molar ratio of 1/4. As shown in Figure 4.11, the catalytic performance was improved with the increase in the deposition cycle until 1500 cycles but decreased as the deposition cycle time was further increased to 2000 cycles. In addition, as shown in Figure 4.12, as too many

deposition cycles (e.g., 2000 cycles) were used, some large bulk particles of NiMnOx were formed on the CuOx NWs, and the electrochemical performance (as shown in the following sections) was decreased.

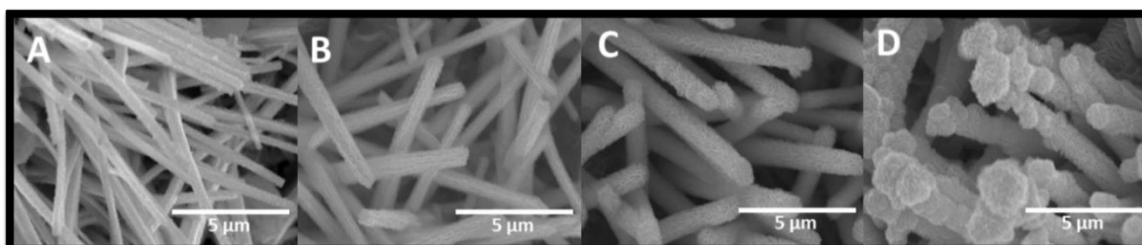


Figure 4.11 SEM images of CuOx NWs@NiMnOx NSs prepared with different UPED deposition cycles: (A) 500 cycles (B) 1000 cycles (C) 1500 cycles and (D) 2000 cycles.

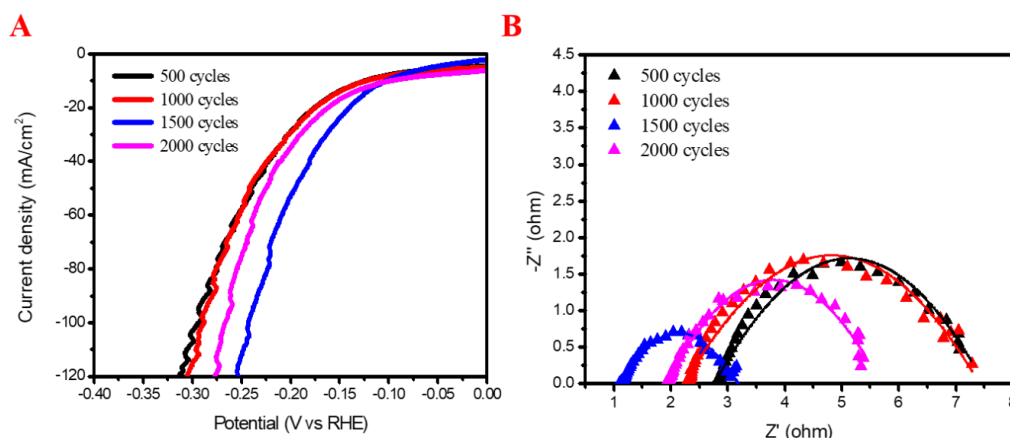


Figure 4.12 LSV polarization curves in the 1.0 M KOH solution for HER over CuOx NWs@NiMnOx NSs/CF electrodes prepared with different UPED deposition cycles (500, 1000, 1500, and 2000 cycles) (A) and the related Nyquist plots at a potential of 0.2 V (B).

4.3.2.2 Catalytic activity, conductivity and stability analysis of HER and OER in alkaline solution.

The obtained NiMnOx NSs with a dense structure could block the electrolyte diffusion and electron transfer. [101] Thus, in this study, the CuOx NWs@NiMnOx NSs/CF electrode prepared at 1500 cycles with the precursor containing the initial Ni/Mn molar ratio of 1/4 during UPED process was selected for further investigations. MnO/CF, NiO/CF, CuOx NWs@MnO/CF, and CuOx NWs@NiO/CF electrodes were also fabricated and their HER and OER performances at a scan rate of 2 mV/s in 1.0 M KOH

were tested. As shown in Figure 4.14 in the supporting materials, the CuOx NWs@NiO/CF exhibited a lower overpotential than the NiO/CF one and meanwhile, the CuOx NWs@MnO/CF electrode also showed a lower overpotential than the MnO/CF one, indicating that the synergistic interaction between two metal oxides enhanced the electrocatalytic activity. Moreover, as shown in Figure 4.13A, the CuOx NWs@NiMnOx/CF exhibited more excellent electrocatalytic activity than those of CuOx NWs@MnO/CF and CuOx NWs@NiO/CF electrodes, further confirmed that the synergistic interaction of different oxides can enhance the electrochemical activity. Besides, as shown in Figure 4.14, the CuOx NWs@NiMnOx NSs/CF with a core-shell structure exhibited higher activity than the NiMnOx/CF electrode. Herein, a uniform distribution of NiMnOx nanosheets on the surface of CuOx nanowires could generate a massive number of active sites, and provide more channels for electrolyte diffusion and reduce the charge transfer resistance since no binder was used in the electrode.

One can see that the CuOx NWs@NiMnOx NSs/CF electrode exhibited an overpotential as low as 71.6 mV at the standard current density of 10 mA cm⁻², which was much lower than the bare CF (496 mV), CuOx NWs/CF (295 mV), MnO/CF(180 mV), NiO/CF(95 mV), CuOx NWs@MnOx/CF (196.4 mV), CuOx NWs@NiO/CF (105 mV). Moreover, its performance was near 20% wt Pt/C (57.2 mV) coated CF electrode. Herein, since the 20% wt Pt/C was coated on CF by using binders, it easily fell from the CF at high current densities due to the large amount of H₂ generated. Thus, the obtained CuOx NWs@NiMnOx NSs/CF electrode should be more stable at a high current density operation. Meanwhile, in the linear region of overpotential vs log *J* (as shown in Fig. 4.13B), the Tafel slope of the CuOx NWs@NiMnOx NSs/CF electrode was also as low as 62.7 mV dec⁻¹, which was much lower than those of bare CF (293 mV dec⁻¹), CuOx NWs/CF (134.9 mV dec⁻¹), MnO/CF(212.6 mV dce⁻¹), NiO/CF(131 mV dec⁻¹), CuOx NWs@MnOx/CF (159 mV dec⁻¹), CuOx NWs@NiO/CF (156.9 mV dec⁻¹), and much closer to that of commercial 20% wt Pt/C coated CF electrode (36.3 mV dec⁻¹). Herein, since the Tafel slope can determine the overpotential required to reach the working current density on the electrode, a low Tafel slope is generally desirable, especially for a high operating current density. For HER, it could follow the Volmer, Hyrovsky, and Tafel pathways, i.e., Volmer (H₂O + e⁻ → H_{ads} + OH⁻), Heyrovsky (H_{ads} + H₂O + e⁻ → H₂ +

OH⁻), and Tafel ($H_{ads} + H_{ads} \rightarrow H_2$). In the Volmer reaction, the slow H^+ adsorption rate should be the determining step. Meanwhile, the Heyrovsky and Tafel reactions are the electrochemical desorption process. However, based on the small Tafel slope result of the CuOx NWs@NiMnOx NSs/CF electrode, it can propose that the HER over it should follow the Volmer-Heyrovsky mechanism, in which the adsorption of water molecule could be accelerated by the formation of H_{ads} (Volmer step), thereby promoting the charge transfer between catalyst and water molecules and enhance the catalytic activity. [100, 102]

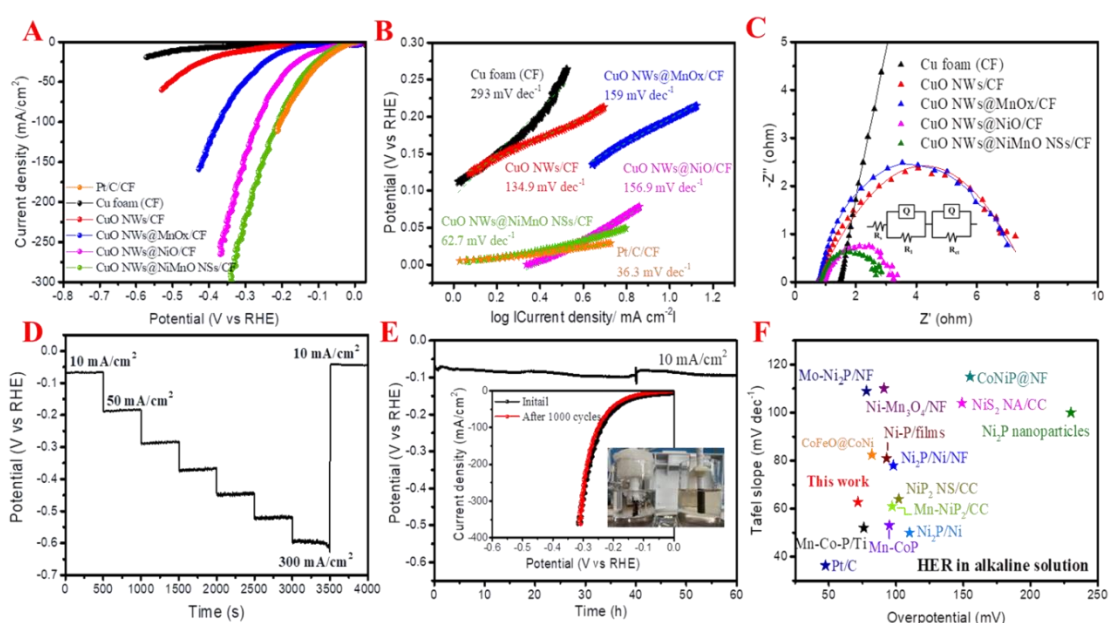


Figure 4.13 (A) LSV polarization curves for HER over various prepared electrodes at a scan rate of 2 mV/s; (B) Tafel plots; (C) Nyquist plots of various electrodes at an overpotential of 200 mV. (D) Multi-current step test for the CuOx NWs@NiMnOx NSs/CF electrode started from the current density of 10 until 300 mA cm⁻² with an increment of 50 mA cm⁻² every 500 s and returned to 10 mA cm⁻² after tested at 300 mA cm⁻²; (E) Chronopotentiometric curve obtained with the CuOx NWs@NiMnOx NSs/CF electrode in 1.0 M KOH solution with the standard current density of 10 mA cm⁻² for continuous 60 h test (inset: HER polarization curves before and after the 1000 cycles). (F) Comparison with the reported results on the Ni- and Mn-based electrodes at the standard current density 10 mA cm⁻² in the alkaline media: 20wt% Pt/C (this work), Mn-CoP [3], Mn-NiP₂/CC [10], Mn-Co-P/Ti [21], NiP₂ NS/CC [27], Ni₂P/Ni/NF [39], Ni-

P/film [43], CoFe@CoNi [46], Ni₂P nanoparticles [48], NiS₂ NA/CC [41], Ni-Mn₃O₄/NF [31] and Mo-Ni₂P/NF [65]. (CC: carbon cloth; NF: nickel foam)

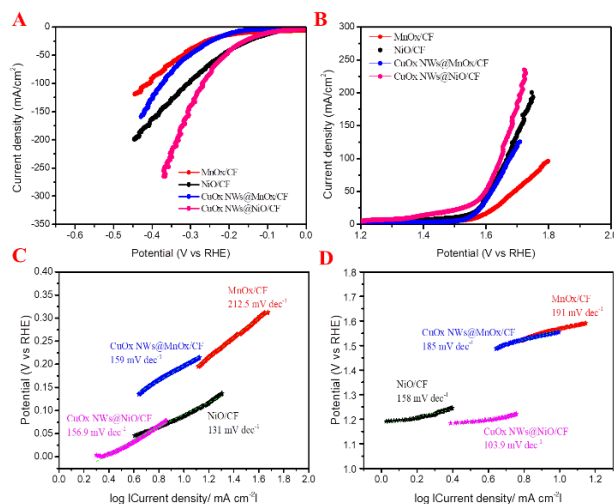


Figure 4.14 Water electrolysis performance of MnOx/CF, NiO/CF, CuOx NWs@MnOx/CF, CuOx NWs@NiO/CF, NiMnOx/CF, and CuOx NWs@NiMnOx NSs/CF electrodes (A-B) LSV polarization curves at a scan rate of 2 mV/s in 1.0 M KOH solution: (A) HER and (B) OER. (C-D) Tafel plots (C) HER and (D) OER.

Moreover, as shown in Figure 4.13C, the CuOx NWs@NiMnOx NSs/CF electrode presented a very low resistance, indicating the good connection between the electrocatalyst and the CF substrate, which could improve the electron conductivity, and provide an ideal pathway for the electron transportation without high kinetic limitation. [100, 102, 103] In addition, the apparent electrochemical surface area (ECSA) of the electrocatalyst was determined by measuring the double-layer capacitance (C_{dl}) with the cyclic voltammetry (CV) in a potential window of 0.1-0.3 (V vs RHE) with a scan rate range of 5-30 mV/s (Figure 4.15A-E). As shown in Figure 4.15F, the CuOx NWs@NiMnOx NSs/CF electrode exhibited an extremely high capacitance (C_{dl}) of 106 mF cm⁻¹, which was much higher than those of CuOx NWs@NiO/CF (78.85 mF cm⁻¹), CuOx NWs@MnOx/CF (65.56 mF cm⁻¹) and CuOx NWs/CF (37.85 mF cm⁻¹), indicating that it had much more surface-active sites due to the special structure and synergistic function of Ni and Mn species. [8] Furthermore, the multi-current step test for the CuOx NWs@NiMnOx NSs/CF electrode started from the current density of 10 until 300 mA

cm^{-2} with an increment of 50 mA cm^{-2} every 500 s and returned to 10 mA cm^{-2} after the test at 300 mA cm^{-2} was also performed. As shown in Fig 4.13D, the potential kept constant at each step and it was completely recovered after the high current density operation, indicating that the $\text{CuOx NWs@NiMnOx NSs/CF}$ electrode had good electroconductivity and mechanical robustness. Meanwhile, as shown in Fig. 4.13E, the $\text{CuOx NWs@NiMnOx NSs/CF}$ electrode maintained stable at the standard current density of 10 mA cm^{-1} for at least 60 h continuous test whereas its polarization kept almost unchanged after the cyclic voltammetric test for 1000 cycles, indicating that this electrocatalyst had excellent long-term stability in the alkaline medium, which is similar as other Mn-containing ones. [28, 30-37, 79, 104] In addition, comparing with other reported excellent Ni- and Mn-based electrocatalysts for HER, as shown in Fig. 4.13F, the HER performance of $\text{CuOx NWs@NiMnOx NSs}$ was also on the top level.

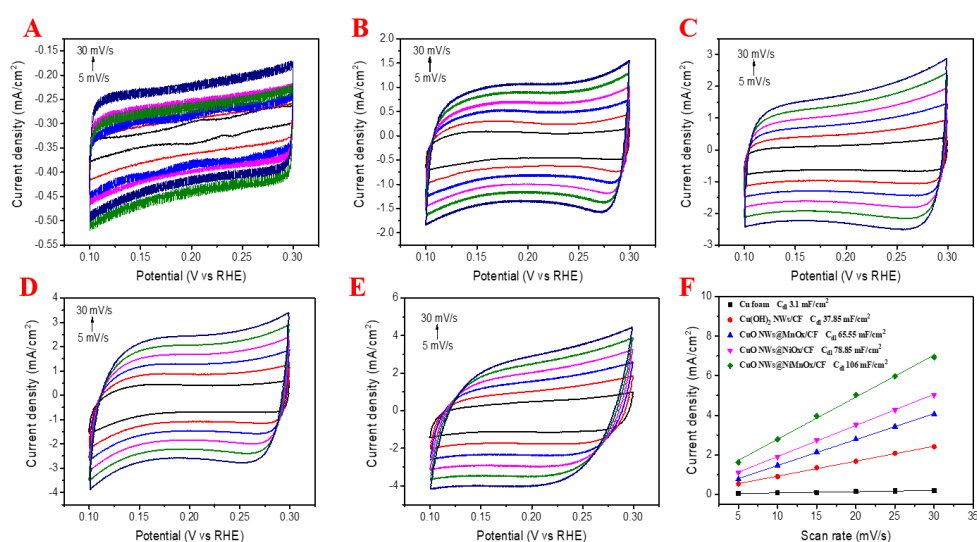


Figure 4.15 Cyclic voltammetry curves of (A) bare CF (CF), (B) CuOx NWs/CF , (C) CuOx NWs@MnOx/CF , (D) CuOx NWs@NiO/CF , (E) $\text{CuOx NWs@NiMnOx NSs/CF}$ collected between a potential range of 0.1-0.3 V (vs RHE) with scan rates of 5, 10, 15, 20, 25, 30 mV/s, respectively, in 1.0 M KOH solution. (F) Dependence of current on the scan rate at different double layer capacitances for the estimation of the electrochemical active surface area.

Figure 4.16A shows LSV polarization curves for OER over various prepared electrodes in 1.0 M KOH solution with a scan rate of 2 mV/s. One can see that the CuOx

NWs@NiMnOx NSs/CF electrode exhibited low overpotentials of 225 and 370 mV at the current densities of 10 and 100 mA cm⁻², respectively, which were much lower than those of CuOx NWs@NiO/CF (150 mV @10 mA cm⁻² and 520 mV @100 mA cm⁻²), CuOx NWs@MnOx/CF (326 mV @10 mA cm⁻² and 547 mV @100 mA cm⁻²), CuOx NWs/CF (386 mV @10 mA cm⁻² and 685 mV @100 mA cm⁻²) and the bare CF (496 mV @10 mA cm⁻²). Especially, it showed higher catalytic performance for OER even than that of the benchmark RuO₂ coated CF electrode (301 mV@10 mA cm⁻²). Meanwhile, as shown in Fig. 6B, it exhibited a Tafel slope as low as 80 mV dec⁻¹, which was also lower than that of RuO₂ coated CF electrode (86.8 mV dec⁻¹). Herein, the oxidation states of metal elements could involve in the formation of intermediates during OER followed the following process: $M + OH^- \leftrightarrow M(OH)_{ad}^- \leftrightarrow M(OH)_{ad} \leftrightarrow M(OH)_{ad} + e^-$ or $M + OH^- \leftrightarrow M(OH)_{ad} + e^-$, in which the charge transfer could lead to O₂ evolution by $M(OH)_{ad} + OH^- \rightarrow Ms + 1/2O_2 + H_2O + e^-$. [105] Fig. 4.16C shows the Nyquist plots and the corresponding equivalent circuits. It revealed that the charge-transfer resistance (R_{ct}) of the CuOx NWs@NiMnOx NSs/CF electrode was much lower than others, implying the fast electron transfer in it. Meanwhile, the CuOx NWs@NiMnOx NSs/CF also had a small series resistance (R_s), indicating the highly electrical integration and the intimate contact of the electrocatalysts with the substrate. Fig. 4.16D shows the multi-current step test for the OER over CuOx NWs@NiMnOx NSs/CF electrode started from the current density of 10 until 300 mA cm⁻² with an increment of 50 mA cm⁻² every 500 s and returned back to 10 mA cm⁻² after performed at 300 mA cm⁻², in which the potential kept constant at each step and it was completely recovered after the high current density operation, also indicating that the CuOx NWs@NiMnOx NSs/CF electrode had good electroconductivity and mechanical robustness in OER process. Moreover, as shown in Fig. 4.16E, the CuOx NWs@NiMnOx NSs/CF electrode also had excellent long-term stability at the standard current density of 10 mA cm⁻² for at least 60 h continuous test whereas its LSV polarization kept almost unchanged after the cyclic voltammetric test for 1000 cycles. In addition, comparing with other reported excellent Ni- and Mn-based electrocatalysts for OER, as shown in Fig. 4.16F, the OER performance of CuOx NWs@NiMnOx NSs was also ranked in the top level.

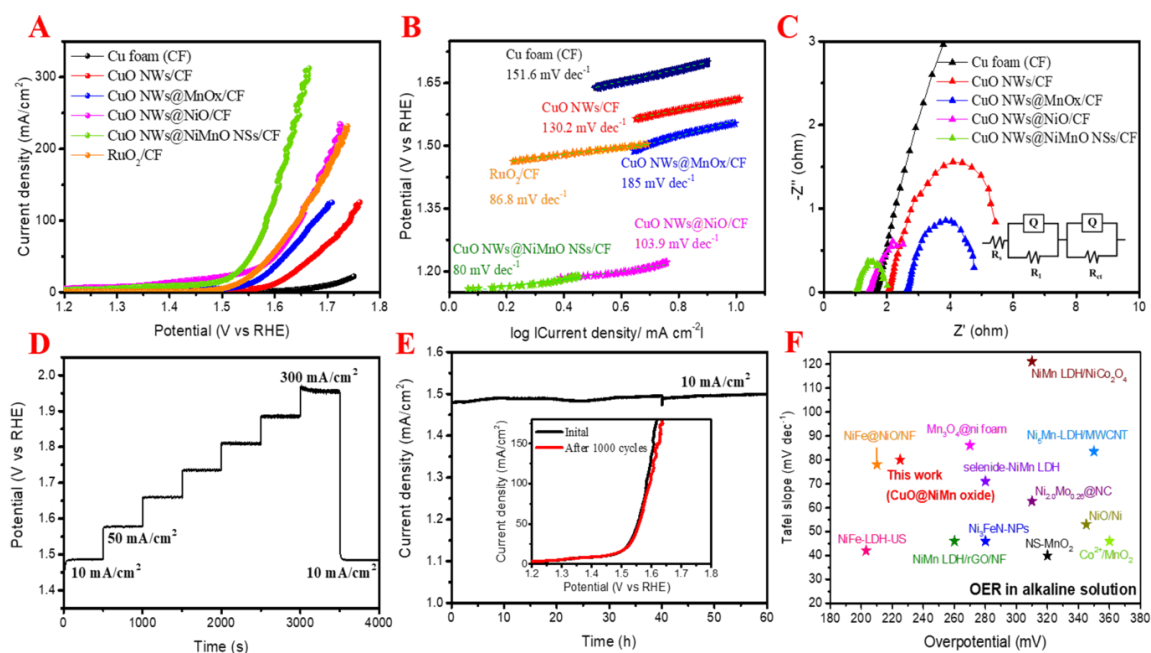


Figure 4.16 (A) LSV polarization curves for OER over various prepared electrodes at a scan rate of 2 mV/s; (B) Tafel plots; (C) Nyquist plots of various electrodes at an overpotential of 200 mV. (D) Multi-current step test for the CuOx NWs@NiMnOx NSs/CF electrode started from the current density of 10 until 300 mA cm⁻² with an increment of 50 mA cm⁻² every 500 s and returned to 10 mA cm⁻² after tested at 300 mA cm⁻²; (E) Chronopotentiometric curve obtained with the CuOx NWs@NiMnOx NSs/CF electrode in 1.0 M KOH solution with the standard current density of 10 mA cm⁻² for continuous 60 h test (inset: OER polarization curves before and after the 1000 cycles). (F) Comparison with the reported results on the Ni- and Mn-based electrodes at the standard current density 10 mA cm⁻² in the alkaline media: NiFe-LDH-US [4], Ni₃FeN-NPs [9], Co²⁺/MnO₂ [20], Ni_{2.0}Mo_{0.26}@NC [26], , Mn₃O₄@NF [40], NiFe@NiO/NF [44], NiO/Ni [44], NS-MnO₂ [49], NiMn LDH/NiCo₂O₄ [52], selenide- NiMn LDH/GC [63], NiMn LDH/RGO/NF [68], NiMn-LDH/GC [68], Ni₅Mn-LDH/MWCNT [71] (US: ultrasonic treatment; NPs: nanoparticles; NC: nitrogen-doped carbon; NF: nickel foam; LDH: layer double hydroxide; RGO: reduce graphene oxide; GC: glassy carbon; MWCNT: Multi-walled carbon nanotubes).

4.3.3 HER and OER in neutral pH medium.

The catalytic performances of the CuOx NWs@NiMnOx NSs/CF electrode for HER and OER in the neutral pH medium (1.0 M PB solution) were further investigated. As shown in Figures 4.17A and 4.17B, for the HER, the CuOx NWs@NiMnOx NSs/CF electrode presented a much lower overpotential of 80.7 mV at the standard current density of 10 mA cm⁻², which was near that of the commercial 20% wt Pt/C/CF electrode. Moreover, the overpotentials at high current densities of 50 mA cm⁻² and 100 mA cm⁻² (498 mV and 556 mV) were even lower than those of commercial 20% wt Pt/C/CF electrode. Meanwhile, the Tafel slope of CuOx NWs@NiMnOx NSs/CF electrode was also as low as 77.6 mV dec⁻¹, which was close to that of the commercial 20% wt Pt/C coated CF electrode (Tafel slop: 63 mV dec⁻¹), indicating the favorable catalytic kinetics. The electrochemical reaction in the neutral pH solution could occur via the Volmer-Tafel reaction pathway or Volmer-Heyrosky reaction pathway ($\text{H}_2\text{O} + \text{e}^- \rightarrow \text{H}_{\text{ads}} + \text{OH}^-$), Heyrovsky pathway ($\text{H}_{\text{ads}} + \text{H}_2\text{O} + \text{e}^- \rightarrow \text{H}_2 + \text{OH}^-$), and Tafel pathway ($2\text{H}_{\text{ads}} \rightarrow \text{H}_2$). As such, the adsorbed water molecule on the electrocatalyst could be reduced to a hydrogen atom (H) and hydroxide ion (OH⁻) via either Volmer Tafel or Volmer-Heyrovsky pathways. Based on the Tafel slope value of CuOx NWs@NiMnOx NSs/CF in neutral pH medium, the HER over it should be via the Volmer-Heyrovsky pathway. [106, 107] Meanwhile, for the OER, the CuOx NWs@NiMnOx NSs/CF electrode exhibited an overpotential of 390 mV at the standard current density of 10 mA cm⁻² with a small Tafel slope of 101.6 mV dec⁻¹. Meanwhile, the CuOx NWs@NiMnOx NSs/CF electrode also showed higher OER performance than the commercial RuO₂ on Cu foam. In the neutral pH media, the intermediates most commonly generated in the catalytic process of OER over the transition metal oxides could be M-OH₂, M-OH, and M-O species, which should be also formed on the CuOx NWs@NiMnOx NSs with various elemental valence states in the PB neutral pH solution.

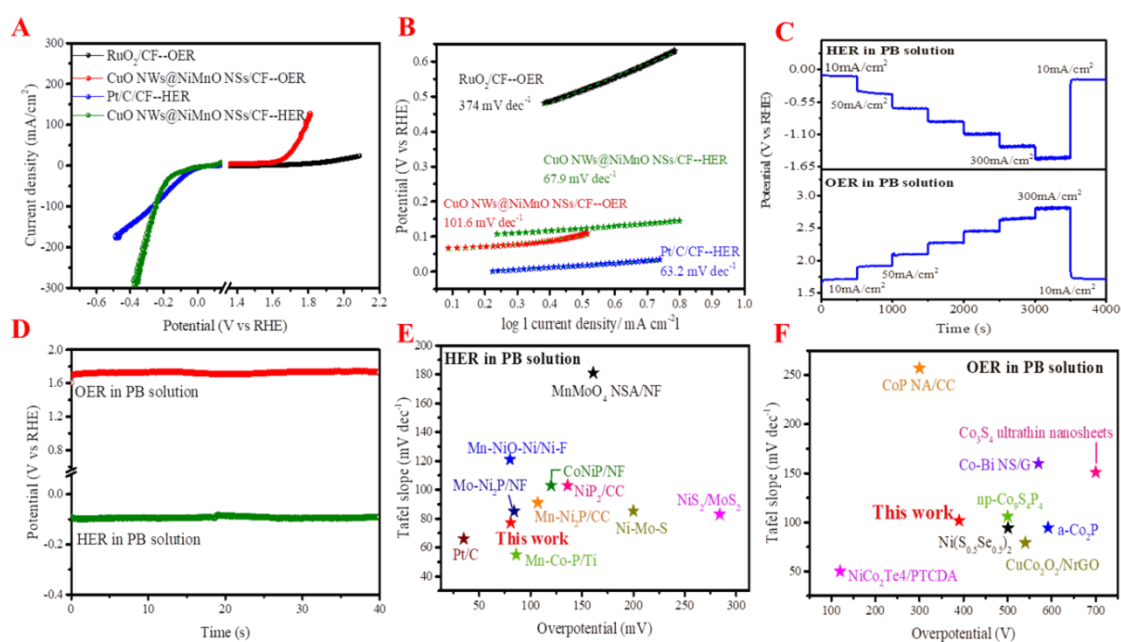


Figure 4.17 LSV polarization curves for HER and OER over the CuOx NWs@NiMnOx NSs/CF electrode at a scan rate of 2 mV/s and compared with the noble-metal-based catalysts of Pt/C and RuO₂ in the neutral pH media; (B) Tafel plots corresponding to Fig. 6 (A); (C) Multi-current step test for the CuOx NWs@NiMnOx NSs/CF electrode started from the current density of 10 until 300 mA cm⁻² with an increment of 50 mA cm⁻² every 500 s and returned to 10 mA cm⁻² after tested at 300 mA cm⁻². (D) Chronopotentiometric curves obtained with the CuOx NWs@NiMnOx NSs/CF electrode in 1.0 M PB solution with the standard current density of 10 mA cm⁻² for continuous 40 h HER and OER tests; (E) Comparison with the reported results on the Ni- and Mn-based electrodes at the standard current density 10 mA cm⁻² for HER in the neutral pH solution: MnMoO₄ NSA/NF [2], Mn-NiO-Ni/Ni-F [8], CoNiP/NF [17], NiP₂/CC [10], Mo-Ni₂P/NF [41], Mn-Ni₂P/CC [10], Ni-Mo-S [47], NiS₂/MoS₂ [51], Mn-Co-P/Ti [21]. (Herein, NF: nickel foam; Ni-F: nickel foam; CC: carbon cloth) (F) Comparison with the reported results on the Ni- and Mn-based electrodes at the standard current density 10 mA cm⁻² for OER in neutral pH solutions: CoP NA/CC [64], Co₂S₄ ultrathin nanosheet [69], Co-Bi NS/G [70], np-Co₉S₄P₄ [67], a-Co₂P [77], Ni(S_{0.5}Se_{0.5}) [79], CuCo₂O₂/NrGO [80], NiCo₂Te₄/PTCDA [72]. (Herein, CC: carbon cloth; G: graphene; PTCDA: perylene-3, 4, 9, 10-tetracarboxylic dianhydride).

As such, the OER that occurred on it could involve a turnover-limiting chemical step preceded by a proton-coupled electron transfer (PCET) equilibrium step where the HPO_4^{2-} ions in the solution served as the proton acceptor for the proton generated on the surface of $\text{CuOx NWs@NiMnOx NSs}$ as reported in the literature. [108] Fig. 4.17C shows the multi-current step tests for the HER and OER over $\text{CuOx NWs@NiMnOx NSs/CF}$ electrode started from the current density of 10 until 300 mA cm^{-2} with an increment of 50 mA cm^{-2} every 500 s and returned to 10 mA cm^{-2} after the operation at 300 mA cm^{-2} , in which both potentials also kept constant at each step and both were completely recovered after the high current density operation, also indicating that the $\text{CuOx NWs@NiMnOx NSs/CF}$ electrode had good electro-conductivity and mechanical robustness in the neutral pH medium. Moreover, as shown in Fig. 4.17D, the $\text{CuOx NWs@NiMnOx NSs/CF}$ electrode also had excellent long-term stability at the standard current density of 10 mA cm^{-2} for either HER or OER in 40 h continuous tests. In addition, comparing with other reported excellent Ni- and Mn-based electrocatalysts for HER and OER as shown in Figs. 4.17E and 4.17F, respectively, the $\text{CuOx NWs@NiMnOx NSs}$ was also on the top level.

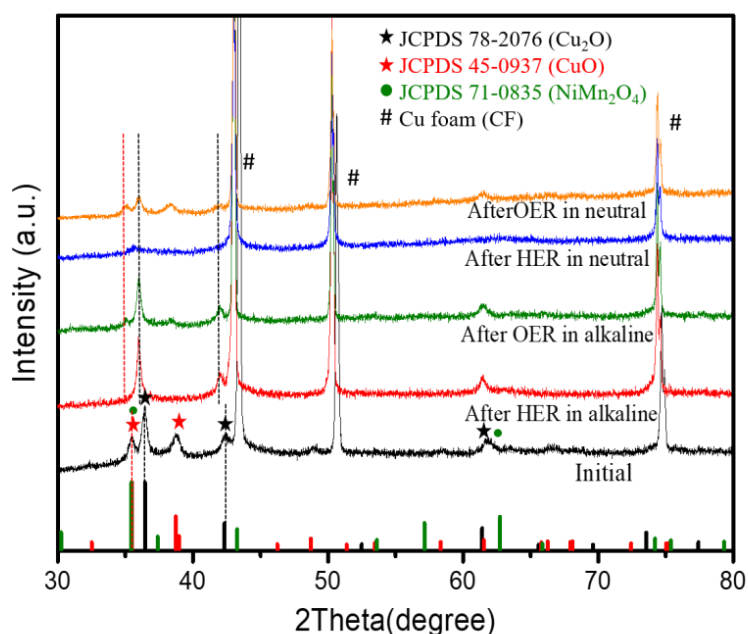


Figure 4.18 XRD pattern of $\text{CuOx NWs@ NiMnOx NSs/CF}$ after HER and OER stability test in alkaline and neutral media solution.

As shown in Figure 4.18, after HER stability test in alkaline and neutral electrolytes, the Cu₂O phase remained on the electrode but CuO phase disappeared due to the reduction environment. Meanwhile, after OER stability test in the alkaline and neutral pH electrolytes, both Cu₂O and CuO phases remained. However, due to the strong peaks corresponding to the Cu substrate on the XRD patterns, the NiMnOx composite phase was difficult to be detected by the XRD analysis. Instead, in this study, XPS analysis was used to study the elemental valence states in the CuOx NWs@NiMnOx after the stability test. As shown in Figures 4.19-4.20 and Tables S4.1-S4.2, the relative ratio of Ni²⁺ increased after the HER stability test, indicating that the Ni³⁺ species was reduced to Ni²⁺ during the HER process. [109] In contrast, the Ni²⁺ species on the surface was oxidized to Ni³⁺ after the OER stability test. It should be noted that the high valence is a benefit for the OER. [110] Meanwhile, for Mn species, due to the disproportionation reaction of $2\text{Mn}^{3+} \rightarrow \text{Mn}^{2+} + \text{Mn}^{4+}$, the Mn 2p_{3/2} peak can be deconvoluted into three peaks at the binding energies of 638.02 ~ 640.93 eV, 641.51 ~ 642.02 eV, and 643.29 ~ 644.23 eV, corresponding to Mn²⁺, Mn³⁺, and Mn⁴⁺, respectively.

Herein, although some Mn³⁺ species were changed to Mn²⁺, the relative amount of Mn³⁺ was still higher than those of Mn²⁺ and Mn⁴⁺. These results indicated the Mn³⁺ in the present catalysts was also effectively stabilized by the proportion reaction in either neutral pH or alkaline solutions. From the Cu 2p XPS spectrum after the HER stability test, the characteristic peaks corresponding to Cu⁺ and Cu²⁺ species were observed. Meanwhile, from the Cu 2p XPS spectrum after the OER stability test, the characteristic peak of Cu⁺ species was decreased while that of Cu²⁺ species increased, indicating that the Cu⁺ (Cu₂O) on the Cu nanowires was oxidized to Cu²⁺ (CuO), but these Cu²⁺ species could act as OER active sites. [111] In addition, as shown in Figure 4.21, the morphology of the catalysts after the stability test maintained almost the same as the initial one.

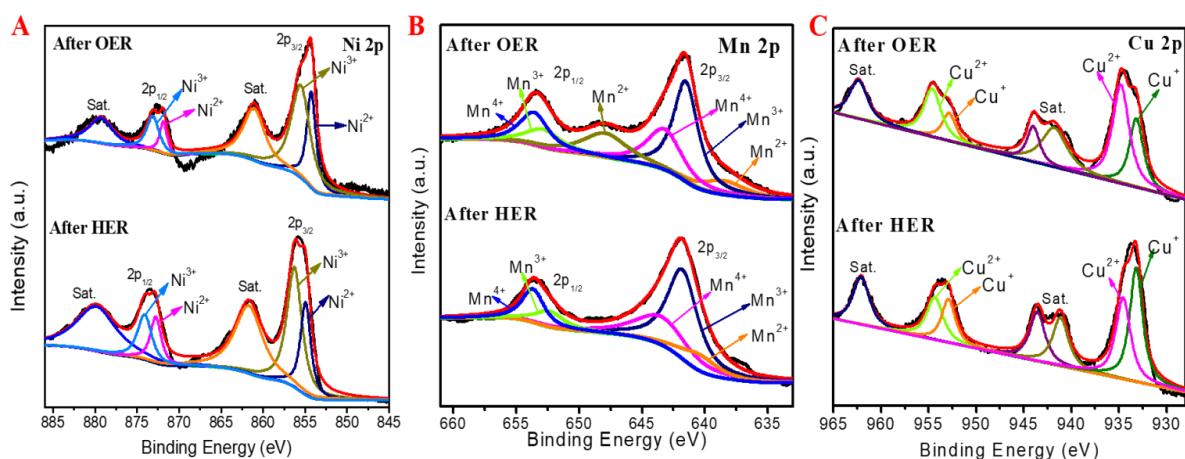


Figure 4.19 High-resolution XPS spectra of the CuOx NWs@NiMnOx NSs after the stability test in the alkaline pH solutions for HER and OER: (A) Ni 2p, (B) Mn 2p and (C) Cu 2p.

Table 4.1 Element valence states of Ni, Mn and Cu species in the CuOx NWs@NiMnOx NSs and their relative percentage ratio based on the deconvolution of peak areas.

Catalysts	Peak area ratio of Metal species (%)		
	Mn ²⁺ /Mn ³⁺ /Mn ⁴⁺	Ni ²⁺ /Ni ³⁺	Cu ⁺ /Cu ²⁺
After HER stability test	10.22/52.84/36.94	59.00/41.00	52.17 / 47.83
After OER stability test	23.60/43.32/33.08	48.63/51.37	35.37 / 64.63
Fresh	- / 57.16 / 42.84	39.07/ 60.93	62.78 / 37.22

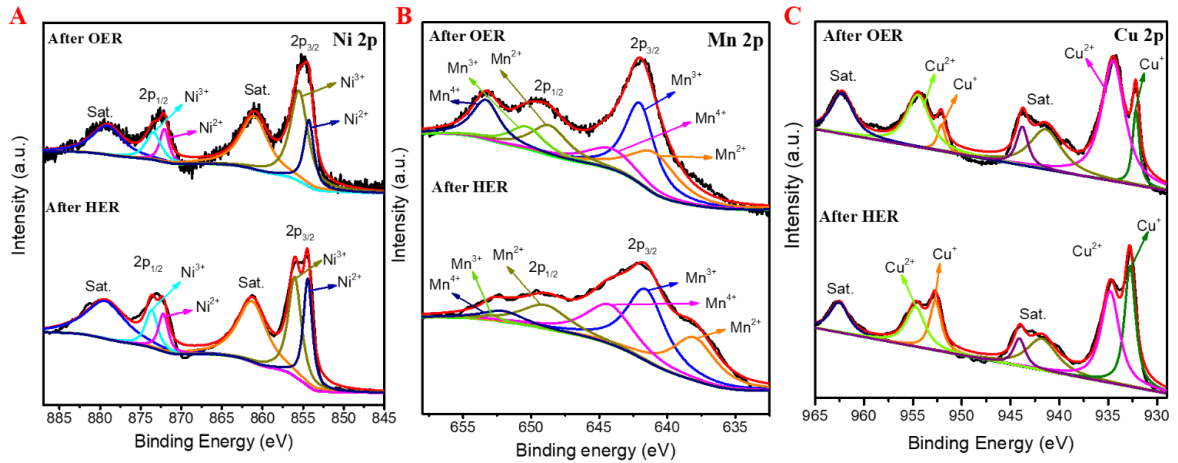


Figure 4.20 High-resolution XPS spectra of the CuOx NWs@NiMnOx NSs after the stability test in the neutral pH solution for HER and OER: (A) Ni 2p, (B) Mn 2p and (C) Cu 2p.

Table 4.2 Element valence states of Ni, Mn and Cu species in the CuOx NWs@NiMnOx NSs and their relative percentage ratio based on the deconvolution of peak areas.

Catalysts	Peak area ratio of metal species (%)		
	Mn ²⁺ /Mn ³⁺ /Mn ⁴⁺	Ni ²⁺ /Ni ³⁺	Cu ⁺ /Cu ²⁺
After HER stability test	34.95 / 36.74 / 28.31	42.97 / 57.03	55.9 / 44.1
After OER stability test	36.02 / 38.28 / 25.70	32.39/67.61	15.32 / 84.68
Fresh	- / 57.16 / 42.84	39.07/ 60.93	62.78 / 37.22

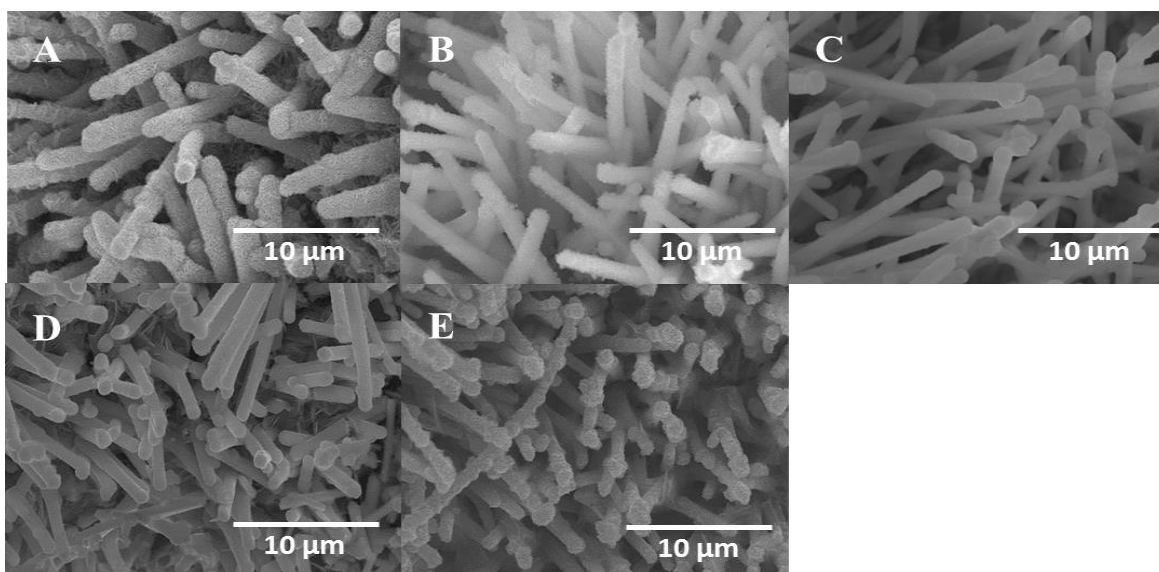


Figure 4.21 SEM images of CuO_x NWs@NiMnO_x NSs catalysts: (A) before the test; (B) after HER stability test in 1.0 M KOH solution; (C) after HER stability test in neutral PB solution; (D) after OER stability test in 1.0 M KOH solutions; and (E) after OER stability test in neutral PB solution.

In this work, the CuO_x NWs@NiMnO_x NSs catalyst exhibited excellent activity in either HER or OER. As stated above, it should result from the following factors: (i) hierarchical CuO_x NWs@NiMnO_x NSs core@shell nanostructure increased the surface-active area with good charge transferability; (ii) abundant Mn³⁺ species existed on the surface of the NiMnO_x NSs, which provided more active sites for either HER or OER; (iii) the combining of Mn with Ni effectively decreased the impedance and enhanced the kinetic transfer during the reactions; (iv) the direct grown of catalyst on the CuO_x NWs covering CF substrate reduced the resistance between catalysts and substrate; and (v) more importantly, the defect modification and valence state played the crucial roles. Especially, the formed additional edge defects should increase to the catalytic active sites, thereby leading to higher electrocatalytic activity and internal conductivity. [112, 113]

4.3.4 Overall-Water Splitting in alkaline and neutral solution.

Inspired by the superior HER and OER performances of the CuO_x NWs@NiMnO_x NSs/CF electrode, it was used as both cathode and anode to make a two-electrode system for the overall water electrolysis. As shown in Figure 4.22A, a low cell voltage of 1.62 V at the standard current density of 10 mA cm⁻² was obtained in the 1.0 M KOH solution,

which is close to the performance of the system composed of noble-metal-based electrocatalysts coated electrodes (Pt/C || RuO₂). Meanwhile, this two-electrode system also had a low cell voltage of ~1.75 V at the current density 10 mA cm⁻² in the 1.0 M neutral PB solution, which is even lower than that of the system composed by the noble-metal-based electrocatalysts coated electrodes. Moreover, this two-electrode system also exhibited long-term stability in the 1.0 M KOH solution (Fig. 4.22B) as well as in the 1.0 M neutral PB solution (Fig. 4.22C). In addition, comparing with other recent reported Ni- and/or Mn-based bifunctional catalysts in both alkaline and neutral media, it also showed more excellent performance (Fig. 4.22B and 4.22C).

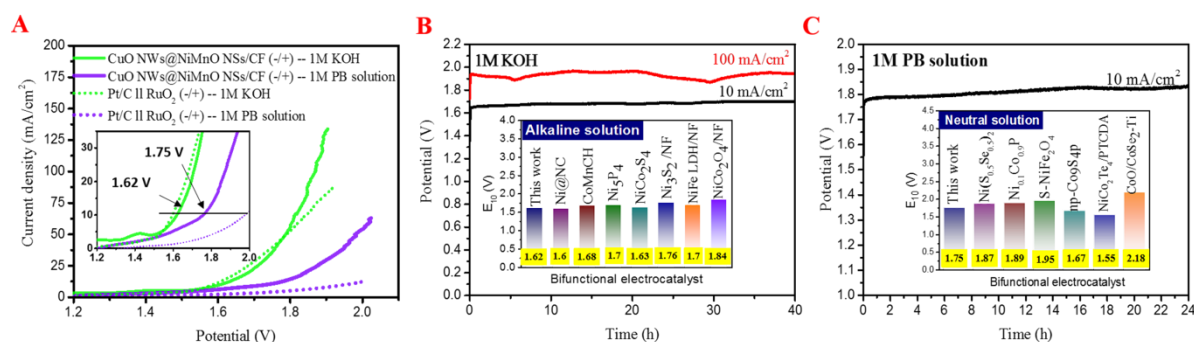


Figure 4.22 Overall water electrolysis in neutral and alkaline solutions. (A) LSV curves obtained during the overall water electrolysis in the two-electrode cell consisting of CuOx NWs@NiMnOx NSs/CF || CuOx NWs@NiMnOx NSs/CF (-/+) and compared with the Pt/C||RuO₂ (-/+) cell; (B) Chronopotentiometric curves at current density of 10 mA cm⁻² for 40 h continuous test in the alkaline solution (inset: Comparison with the recent reported ones: Ni@NC [1], CoMnCH [7], Ni₅P₄ [13], NiCo₂S₅ [22], Ni₃S₂/NF [38], NiFe LDH/NF [42] and NiCo₂O₄/NF [45]. Herein, NC: nitrogen-doped carbon, CH: carbonate hydroxide, NF: nickel foam). (C) Chronopotentiometric curve at the current density of 10 mA cm⁻² for 24 h continuous test in neutral pH solution (inset: Comparison with the recent reported ones: Ni(S_{0.5}Se_{0.5}) [11], Ni_{0.5}Co_{0.5}P [45], S-NiFe₂O₄ [62], np-Co₃S₄P [67], NiCo₂Te₄/PTCDA [72], and CoO/CoSe₂-Ti [75]. Herein, PTCDA: perylene-3, 4, 9, 10-tetracarboxylic dianhydride).

To assess the Faradic efficiency (FE), the generated H₂ and O₂ in the two-electrode system were collected, and the obtained moles were compared with the theoretical amounts of H₂ and O₂ calculated based on the I-t curves by applying the Faraday law. As

shown in Figure 4.23, it is found that the FEs of hydrogen/oxygen productions reached nearly 96/95% and 93/94% in the alkaline and neutral pH media, respectively. All these results indicated that the obtained CuOx NWs@NiMnOx NSs should be a promising bifunctional electrocatalyst for the water electrolysis.

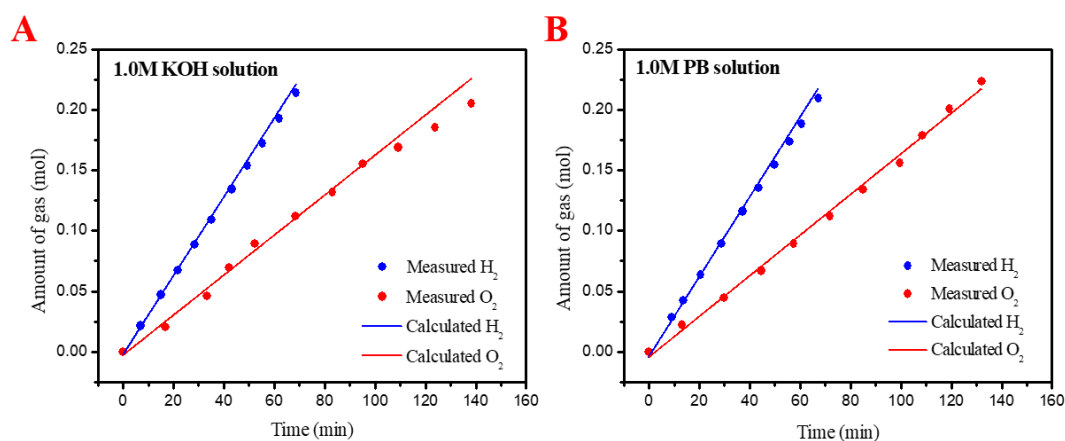


Figure 4.23 Theoretical hydrogen and oxygen evolution amounts vs. measured gas evolutions in 1.0 M KOH and 1.0 M PB solutions during the course of electrolysis using CuOx NWs@NiMnOx NSs/CF electrodes in the two-electrode system for overall water electrolysis.

4.4 CONCLUSIONS

In summary, the CuOx NWs@NiMnOx NSs electrocatalyst with a core@shell structure was successfully coated on the CF substrate by a three-step process including an oxidation step for the construction of nanowire structure on the surface of CF substrate, a UPED process to deposit NiMn bimetal hydroxide composite layer on the nanowire and a calcination step to obtain the final CuOx NWs@NiMnOx NSs/CF electrode. NiMnOx NSs endowed numerous vacancies, scattered defects, and dislocations, which led to the partial crack of the inert basal planes, resulting in extra active edge sites and enhanced catalytic activity. Besides, the valence states of Ni and Mn elements were unstable in the defect-modified NiMnOx, which could change during the electrolysis process. Especially, comparing with initial NiMnOx, more Ni³⁺ and Mn⁴⁺ were formed during the OER process, which can be simultaneously converted to Ni²⁺ and Mn³⁺ during the HER process. As a result, the CuOx NWs@NiMnOx NSs electrocatalyst coated electrode showed the overpotentials as low as 71.6 and 80.7 mV at the standard current density of

10 mA cm⁻² with Tafel slopes of 62.7 and 77.6 mV dec⁻¹ for HER and 225 and 390 mV with Tafel slopes of 80 and 101.6 mV dce⁻¹ for OER in the alkaline and neutral pH electrolytes, respectively, with long-term stability, which are close to or even better than the performances of those benchmarking Pt/C and RuO₂ electrocatalysts. Moreover, a two-electrode system using it as the bifunctional electrocatalyst for the overall water electrolysis represented cell voltages of 1.62 and 1.75 V with the FEs of nearly 96/95% and 93/94% for hydrogen/oxygen productions in the alkaline and neutral pH electrolytes, respectively.

REFERENCES

- [1] Y. Xu, W. Tu, B. Zhang, S. Yin, Y. Huang, M. Kraft and R. Xu, Nickel Nanoparticles Encapsulated in Few-Layer Nitrogen-Doped Graphene Derived from Metal–Organic Frameworks as Efficient Bifunctional Electrocatalysts for Overall Water Splitting, *Adv. Mater.*, 2017, 29, 1605957.
- [2] L. Wen, Y. Sun, T. Zhang, Y. Bai, X. Li, X. Lyu, W. Cai and Y. Li, MnMoO₄ Nanosheet Array: An Efficient Electrocatalyst for Hydrogen Evolution Reaction with Enhanced Activity Over a Wide pH Range, *Nanotechnology*, 2018, 29, 335403.
- [3] X. Li, S. Li, A. Yoshida, S. Sirisomboonchai, K. Tang, Z. Zuo, X. Hao, A. Abudula and G. Guan, Mn Doped CoP Nanoparticle Clusters: An Efficient Electrocatalyst for Hydrogen Evolution Reaction, *Catalysis Science & Technology*, 2018, 8, 4407-4412.
- [4] X. Li, X. Hao, Z. Wang, A. Abudula and G. Guan, In-situ Intercalation of NiFe LDH Materials: An Efficient Approach to Improve Electrocatalytic Activity and Stability for Water Splitting, *Journal of Power Sources*, 2017, 347, 193-200.
- [5] Y. Jiao, Y. Zheng, M. Jaroniec and S. Z. Qiao, Design of Electrocatalysts for Oxygen-and Hydrogen-Involving Energy Conversion Reactions, *Chemical Society Reviews*, 2015, 44, 2060-2086.
- [6] J. Li, Y. Wang, T. Zhou, H. Zhang, X. Sun, J. Tang, L. Zhang, A. M. Al-Enizi, Z. Yang and G. Zheng, Nanoparticle Superlattices as Efficient Bifunctional Electrocatalysts for Water Splitting, *Journal of the American Chemical Society*, 2015, 137, 14305-14312.

- [7] T. Tang, W.-J. Jiang, S. Niu, N. Liu, H. Luo, Y.-Y. Chen, S.-F. Jin, F. Gao, L.-J. Wan and J.-S. Hu, Electronic and Morphological Dual Modulation of Cobalt Carbonate Hydroxides by Mn Doping toward Highly Efficient and Stable Bifunctional Electrocatalysts for Overall Water Splitting, *Journal of the American Chemical Society*, 2017, 139, 8320-8328.
- [8] X. Lu, J. Pan, E. Lovell, T. H. Tan, Y. H. Ng and R. Amal, A Sea-change: Manganese doped Nickel/Nickel Oxide Electrocatalysts for Hydrogen Generation from Seawater, *Energy & Environmental Science*, 2018, 11, 1898-1910.
- [9] X. Jia, Y. Zhao, G. Chen, L. Shang, R. Shi, X. Kang, G. I. N. Waterhouse, L.-Z. Wu, C.-H. Tung and T. Zhang, Water Splitting: Ni₃FeN Nanoparticles Derived from Ultrathin NiFe-Layered Double Hydroxide Nanosheets: An Efficient Overall Water Splitting Electrocatalyst, *Adv. Energy Mater.*, 2016, 6, 1502585.
- [10] X. Wang, H. Zhou, D. Zhang, M. Pi, J. Feng and S. Chen, Mn-Doped NiP₂ Nanosheets as An Efficient Electrocatalyst for Enhanced Hydrogen Evolution Reaction at All pH Values, *Journal of Power Sources*, 2018, 387, 1-8.
- [11] L. Zeng, K. Sun, Y. Chen, Z. Liu, Y. Chen, Y. Pan, R. Zhao, Y. Liu and C. Liu, Neutral-pH Overall Water Splitting Catalyzed Efficiently by A Hollow and Porous Structured Ternary Nickel Sulfoselenide Electrocatalyst, *Journal of Materials Chemistry A*, 2019, 7, 16793-16802.
- [12] Y.-Y. Ma, C.-X. Wu, X.-J. Feng, H.-Q. Tan, L.-K. Yan, Y. Liu, Z.-H. Kang, E.-B. Wang and Y.-G. Li, Highly Efficient Hydrogen Evolution from Seawater by a Low-cost and Stable CoMoP@C Electrocatalyst Superior to Pt/C, *Energy & Environmental Science*, 2017, 10, 788-798.
- [13] M. Ledendecker, S. Krick Calderón, C. Papp, H.-P. Steinrück, M. Antonietti and M. Shalom, The Synthesis of Nanostructured Ni₅P₄ Films and their Use as a Non-Noble Bifunctional Electrocatalyst for Full Water Splitting, *Angew. Chem., Int. Ed.*, 2015, 54, 12361-12365.

- [14] R. Wu, B. Xiao, Q. Gao, Y.-R. Zheng, X.-S. Zheng, J.-F. Zhu, M.-R. Gao and S.-H. Yu, A Janus Nickel Cobalt Phosphide Catalyst for High-Efficiency Neutral-pH Water Splitting, *Angew. Chem., Int. Ed.*, 2018, 57, 15445-15449.
- [15] T. Shinagawa, M. T.-K. Ng and K. Takanebe, Electrolyte Engineering toward Efficient Water Splitting at Mild pH, *ChemSusChem*, 2017, 10, 4155-4162.
- [16] T. Shinagawa and K. Takanebe, Electrocatalytic Hydrogen Evolution under Densely Buffered Neutral pH Conditions, *The Journal of Physical Chemistry C*, 2015, 119, 20453-20458.
- [17] A. Han, H. Chen, H. Zhang, Z. Sun and P. Du, Ternary Metal Phosphide Nanosheets as a Highly Efficient Electrocatalyst for Water Reduction to Hydrogen over a Wide pH Range from 0 to 14, *Journal of Materials Chemistry A*, 2016, 4, 10195-10202.
- [18] J. Chen, B. Lim, E. P. Lee and Y. Xia, Shape-Controlled Synthesis of Platinum Nanocrystals for Catalytic and Electrocatalytic Applications, *Nano Today*, 2009, 4, 81-95.
- [19] E. Fabbri, A. Habereder, K. Waltar, R. Kötz and T. J. Schmidt, Developments and Perspectives of Oxide-based Catalysts for The Oxygen Evolution Reaction, *Catalysis Science & Technology*, 2014, 4, 3800-3821.
- [20] A. C. Thenuwara, S. L. Shumlas, N. H. Attanayake, Y. V. Aulin, I. G. McKendry, Q. Qiao, Y. Zhu, E. Borguet, M. J. Zdilla and D. R. Strongin, Intercalation of Cobalt into the Interlayer of Birnessite Improves Oxygen Evolution Catalysis, *ACS Catalysis*, 2016, 6, 7739-7743.
- [21] T. Liu, X. Ma, D. Liu, S. Hao, G. Du, Y. Ma, A. M. Asiri, X. Sun and L. Chen, Mn Doping of CoP Nanosheets Array: An Efficient Electrocatalyst for Hydrogen Evolution Reaction with Enhanced Activity at All pH Values, *ACS Catalysis*, 2017, 7, 98-102.
- [22] A. Sivanantham, P. Ganesan and S. Shanmugam, Hierarchical NiCo₂S₄ Nanowire Arrays Supported on Ni Foam: An Efficient and Durable Bifunctional Electrocatalyst

- for Oxygen and Hydrogen Evolution Reactions, *Adv. Funct. Mater.*, 2016, 26, 4661-4672.
- [23] Y. Shi, Recent Advances in Transition Metal Phosphide Nanomaterials: Synthesis and Applications in Hydrogen Evolution Reaction, *Chemical Society reviews*, 2016, 45, 1529-1541.
- [24] E. J. Popczun, J. R. McKone, C. G. Read, A. J. Biacchi, A. M. Wiltrout, N. S. Lewis and R. E. Schaak, Nanostructured Nickel Phosphide as an Electrocatalyst for the Hydrogen Evolution Reaction, *Journal of the American Chemical Society*, 2013, 135, 9267-9270.
- [25] S. Sirisomboonchai, S. Li, A. Yoshida, S. Kongparakul, C. Samart, Y. Kansha, X. Hao, A. Abudula and G. Guan, Terephthalic Acid Induced Binder-free NiCoP–Carbon Nanocomposite for Highly Efficient Electrocatalysis of Hydrogen Evolution Reaction, *Catalysis Science & Technology*, 2019, 9, 4651-4658.
- [26] X. Zhang, L. Huang, Y. Han, M. Xu and S. Dong, Nitrogen-doped Carbon Encapsulating γ -MoC/Ni Heterostructures for Efficient Oxygen Evolution Electrocatalysts, *Nanoscale*, 2017, 9, 5583-5588.
- [27] P. Jiang, Q. Liu and X. Sun, NiP₂ Nanosheet Arrays Supported on Carbon cloth: An Efficient 3D Hydrogen Evolution Cathode in Both Acidic and Alkaline Solutions, *Nanoscale*, 2014, 6, 13440-13445.
- [28] S. Hao and Y. Yang, Water Splitting in Near-neutral Media: Using an Mn–Co-Based Nanowire Array as a Complementary Electrocatalyst, *Journal of Materials Chemistry A*, 2017, 5, 12091-12095.
- [29] J. Wu, D. Wang, S. Wan, H. Liu, C. Wang and X. Wang, An Efficient Cobalt Phosphide Electrocatalyst Derived from Cobalt Phosphonate Complex for All-pH Hydrogen Evolution Reaction and Overall Water Splitting in Alkaline Solution, *Small*, 2020, 16, 1900550.
- [30] Y. Meng, W. Song, H. Huang, Z. Ren, S.-Y. Chen and S. L. Suib, Structure–Property Relationship of Bifunctional MnO₂ Nanostructures: Highly Efficient, Ultra-Stable

- Electrochemical Water Oxidation and Oxygen Reduction Reaction Catalysts Identified in Alkaline Media, *Journal of the American Chemical Society*, 2014, 136, 11452-11464.
- [31] X. Li, P. F. Liu, L. Zhang, M. Y. Zu, Y. X. Yang and H. G. Yang, Enhancing Alkaline Hydrogen Evolution Reaction Activity Through Ni–Mn₃O₄ Nanocomposites, *Chemical Communications*, 2016, 52, 10566-10569.
- [32] J. Du, G. Zhou, H. Zhang, C. Cheng, J. Ma, W. Wei, L. Chen and T. Wang, Ultrathin Porous NiCo₂O₄ Nanosheet Arrays on Flexible Carbon Fabric for High-Performance Supercapacitors, *ACS Applied Materials & Interfaces*, 2013, 5, 7405-7409.
- [33] X. Wang, W. Li, D. Xiong, D. Y. Petrovykh and L. Liu, Bifunctional Catalysts: Bifunctional Nickel Phosphide Nanocatalysts Supported on Carbon Fiber Paper for Highly Efficient and Stable Overall Water Splitting, *Adv. Funct. Mater.*, 2016, 26, 4066-4066.
- [34] T. Takashima, K. Hashimoto and R. Nakamura, Inhibition of Charge Disproportionation of MnO₂ Electrocatalysts for Efficient Water Oxidation under Neutral Conditions, *Journal of the American Chemical Society*, 2012, 134, 18153-18156.
- [35] T. Takashima, K. Hashimoto and R. Nakamura, Mechanisms of pH-Dependent Activity for Water Oxidation to Molecular Oxygen by MnO₂ Electrocatalysts, *Journal of the American Chemical Society*, 2012, 134, 1519-1527.
- [36] M. Huynh, C. Shi, S. J. L. Billinge and D. G. Nocera, Nature of Activated Manganese Oxide for Oxygen Evolution, *Journal of the American Chemical Society*, 2015, 137, 14887-14904.
- [37] C.-H. Kuo, I. M. Mosa, A. S. Poyraz, S. Biswas, A. M. El-Sawy, W. Song, Z. Luo, S.-Y. Chen, J. F. Rusling, J. He and S. L. Suib, Robust Mesoporous Manganese Oxide Catalysts for Water Oxidation, *ACS Catalysis*, 2015, 5, 1693-1699.
- [38] L.-L. Feng, G. Yu, Y. Wu, G.-D. Li, H. Li, Y. Sun, T. Asefa, W. Chen and X. Zou, High-Index Faceted Ni₃S₂ Nanosheet Arrays as Highly Active and Ultrastable

- Electrocatalysts for Water Splitting, *Journal of the American Chemical Society*, 2015, 137, 14023-14026.
- [39] B. You, N. Jiang, M. Sheng, M. W. Bhushan and Y. Sun, Hierarchically Porous Urchin-Like Ni₂P Superstructures Supported on Nickel Foam as Efficient Bifunctional Electrocatalysts for Overall Water Splitting, *ACS Catalysis*, 2016, 6, 714-721.
- [40] M. Q. Yu, Y. H. Li, S. Yang, P. F. Liu, L. F. Pan, L. Zhang and H. G. Yang, Mn₃O₄ Nano-Octahedrons on Ni foam as an Efficient Three-Dimensional Oxygen Evolution Electrocatalyst, *Journal of Materials Chemistry A*, 2015, 3, 14101-14104.
- [41] C. Tang, Z. Pu, Q. Liu, A. M. Asiri and X. Sun, NiS₂ Nanosheets Array Grown on Carbon Cloth as an Efficient 3D Hydrogen Evolution Cathode, *Electrochimica Acta*, 2015, 153, 508-514.
- [42] J. Luo, J.-H. Im, M. T. Mayer, M. Schreier, M. K. Nazeeruddin, N.-G. Park, S. D. Tilley, H. J. Fan and M. Grätzel, Water photolysis at 12.3% Efficiency via Perovskite Photovoltaics and Earth-abundant Catalysts, *Science*, 2014, 345, 1593.
- [43] N. Jiang, B. You, M. Sheng and Y. Sun, Bifunctionality and Mechanism of Electrodeposited Nickel–Phosphorous Films for Efficient Overall Water Splitting, *ChemCatChem*, 2016, 8, 106-112.
- [44] S. Sirisomboonchai, S. Li, A. Yoshida, X. Li, C. Samart, A. Abudula and G. Guan, Fabrication of NiO Microflake@NiFe-LDH Nanosheet Heterostructure Electrocatalysts for Oxygen Evolution Reaction, *ACS Sustainable Chemistry & Engineering*, 2019, 7, 2327-2334.
- [45] L. Ma, W. Zhang, P. Zhao, J. Liang, Y. Hu, G. Zhu, R. Chen, Z. Tie, J. Liu and Z. Jin, Highly Efficient Overall Water Splitting Driven by All-Inorganic Perovskite Solar Cells and Promoted by Bifunctional Bimetallic Phosphide Nanowire Arrays, *Journal of Materials Chemistry A*, 2018, 6, 20076-20082.
- [46] S. Li, S. Sirisomboonchai, A. Yoshida, X. An, X. Hao, A. Abudula and G. Guan, Bifunctional CoNi/CoFe₂O₄ /Ni Foam Electrodes for Efficient Overall Water

- Splitting at a High Current Density, *Journal of Materials Chemistry A*, 2018, 6, 19221-19230.
- [47] J. Miao, F.-X. Xiao, H. B. Yang, S. Y. Khoo, J. Chen, Z. Fan, Y.-Y. Hsu, H. M. Chen, H. Zhang and B. Liu, Hierarchical Ni-Mo-S Nanosheets on Carbon Fiber Cloth: A Flexible Electrode for Efficient Hydrogen Generation in Neutral Electrolyte, *Science Advances*, 2015, 1, e1500259.
- [48] L. Feng, H. Vrubel, M. Bensimon and X. Hu, Easily-Prepared Dinickel Phosphide (Ni₂P) Nanoparticles as an Efficient and Robust Electrocatalyst for Hydrogen Evolution, *Physical Chemistry Chemical Physics*, 2014, 16, 5917-5921.
- [49] Y. Zhao, C. Chang, F. Teng, Y. Zhao, G. Chen, R. Shi, G. I. N. Waterhouse, W. Huang and T. Zhang, Defect-Engineered Ultrathin δ -MnO₂ Nanosheet Arrays as Bifunctional Electrodes for Efficient Overall Water Splitting, *Adv. Energy Mater.*, 2017, 7, 1700005.
- [50] D. Jeong, K. Jin, S. E. Jerng, H. Seo, D. Kim, S. H. Nahm, S. H. Kim and K. T. Nam, Mn₅O₈ Nanoparticles as Efficient Water Oxidation Catalysts at Neutral pH, *ACS Catalysis*, 2015, 5, 4624-4628.
- [51] P. Kuang, T. Tong, K. Fan and J. Yu, In Situ Fabrication of Ni-Mo Bimetal Sulfide Hybrid as an Efficient Electrocatalyst for Hydrogen Evolution over a Wide pH Range, *ACS Catalysis*, 2017, 7, 6179-6187.
- [52] L. Yang, L. Chen, D. Yang, X. Yu, H. Xue and L. Feng, NiMn Layered Double Hydroxide Nanosheets/NiCo₂O₄ Nanowires with Surface Rich High Valence State Metal Oxide as an Efficient Electrocatalyst for Oxygen Evolution Reaction, *Journal of Power Sources*, 2018, 392, 23-32.
- [53] Y. Yan, B. Y. Xia, B. Zhao and X. Wang, A Review on Noble-Metal-Free Bifunctional Heterogeneous Catalysts for Overall Electrochemical Water Splitting, *Journal of Materials Chemistry A*, 2016, 4, 17587-17603.

- [54] Y. Li, L. Hu, W. Zheng, X. Peng, M. Liu, P. K. Chu and L. Y. S. Lee, Ni/Co-Based Nanosheet Arrays for Efficient Oxygen Evolution Reaction, *Nano Energy*, 2018, 52, 360-368.
- [55] H.-Y. Wang, Y.-Y. Hsu, R. Chen, T.-S. Chan, H. M. Chen and B. Liu, Ni³⁺-Induced Formation of Active NiOOH on the Spinel Ni–Co Oxide Surface for Efficient Oxygen Evolution Reaction, *Advanced Energy Materials*, 2015, 5.
- [56] G. Wu, W. Chen, X. Zheng, D. He, Y. Luo, X. Wang, J. Yang, Y. Wu, W. Yan, Z. Zhuang, X. Hong and Y. Li, Hierarchical Fe-doped NiO_x Nanotubes Assembled from Ultrathin Nanosheets Containing Trivalent Nickel for Oxygen Evolution Reaction, *Nano Energy*, 2017, 38, 167-174.
- [57] R. P. Antony, A. K. Satpati, K. Bhattacharyya and B. N. Jagatap, MOF Derived Nonstoichiometric Ni_xCo_{3-x}O_{4-y} Nanocage for Superior Electrocatalytic Oxygen Evolution, *Advanced Materials Interfaces*, 2016, 3, 1600632.
- [58] M. Tahir, L. Pan, R. Zhang, Y.-C. Wang, G. Shen, I. Aslam, M. A. Qadeer, N. Mahmood, W. Xu, L. Wang, X. Zhang and J.-J. Zou, High-Valence-State NiO/Co₃O₄ Nanoparticles on Nitrogen-Doped Carbon for Oxygen Evolution at Low Overpotential, *ACS Energy Letters*, 2017, 2, 2177-2182.
- [59] J. Duan, S. Chen, A. Vasileff and S. Z. Qiao, Anion and Cation Modulation in Metal Compounds for Bifunctional Overall Water Splitting, *ACS Nano*, 2016, 10, 8738-8745.
- [60] B. Zhang, X. Zheng, O. Voznyy, R. Comin, M. Bajdich, M. García-Melchor, L. Han, J. Xu, M. Liu, L. Zheng, F. P. García de Arquer, C. T. Dinh, F. Fan, M. Yuan, E. Yassitepe, N. Chen, T. Regier, P. Liu, Y. Li, P. De Luna, A. Janmohamed, H. L. Xin, H. Yang, A. Vojvodic and E. H. Sargent, Homogeneously Dispersed Multimetal Oxygen-Evolving Catalysts, *Science*, 2016, 352, 333.
- [61] C. Zhu, D. Wen, S. Leubner, M. Oschatz, W. Liu, M. Holzschuh, F. Simon, S. Kaskel and A. Eychmüller, Nickel Cobalt Oxide Hollow Nanosponges as Advanced

- Electrocatalysts for The Oxygen Evolution Reaction, *Chemical Communications*, 2015, 51, 7851-7854.
- [62] J. Liu, D. Zhu, T. Ling, A. Vasileff and S.-Z. Qiao, S-NiFe₂O₄ Ultra-small Nanoparticle Built Nanosheets for Efficient Water Splitting in Alkaline and Neutral pH, *Nano Energy*, 2017, 40, 264-273.
- [63] J. Du, Z. Zou, A. Yu and C. Xu, Selenization of NiMn-Layered Double Hydroxide with Enhanced Electrocatalytic Activity for Oxygen Evolution, *Dalton Transactions*, 2018, 47, 7492-7497.
- [64] T. Liu, L. Xie, J. Yang, R. Kong, G. Du, A. M. Asiri, X. Sun and L. Chen, Self-Standing CoP Nanosheets Array: A Three-Dimensional Bifunctional Catalyst Electrode for Overall Water Splitting in both Neutral and Alkaline Media, *ChemElectroChem*, 2017, 4, 1840-1845.
- [65] Y. Sun, L. Hang, Q. Shen, T. Zhang, H. Li, X. Zhang, X. Lyu and Y. Li, Mo Doped Ni₂P Nanowire Arrays: An Efficient Electrocatalyst for The Hydrogen Evolution Reaction with Enhanced Activity at All pH Values, *Nanoscale*, 2017, 9, 16674-16679.
- [66] X. Wang, L. Chai, J. Ding, L. Zhong, Y. Du, T.-T. Li, Y. Hu, J. Qian and S. Huang, Chemical and Morphological Transformation of MOF-derived Bimetallic Phosphide for Efficient Oxygen Evolution, *Nano Energy*, 2019, 62, 745-753.
- [67] Y. Tan, M. Luo, P. Liu, C. Cheng, J. Han, K. Watanabe and M. Chen, Three-Dimensional Nanoporous Co₉S₄P₄ Pentlandite as a Bifunctional Electrocatalyst for Overall Neutral Water Splitting, *ACS Applied Materials & Interfaces*, 2019, 11, 3880-3888.
- [68] W. Ma, R. Ma, J. Wu, P. Sun, X. Liu, K. Zhou and T. Sasaki, Development of Efficient Electrocatalysts via Molecular Hybridization of NiMn Layered Double Hydroxide Nanosheets and Graphene, *Nanoscale*, 2016, 8, 10425-10432.
- [69] Y. Liu, C. Xiao, M. Lyu, Y. Lin, W. Cai, P. Huang, W. Tong, Y. Zou and Y. Xie, Ultrathin Co₃S₄ Nanosheets that Synergistically Engineer Spin States and Exposed

- Polyhedra that Promote Water Oxidation under Neutral Conditions, *Angew. Chem., Int. Ed.*, 2015, 54, 11231-11235.
- [70] P. Chen, K. Xu, T. Zhou, Y. Tong, J. Wu, H. Cheng, X. Lu, H. Ding, C. Wu and Y. Xie, Strong-Coupled Cobalt Borate Nanosheets/Graphene Hybrid as Electrocatalyst for Water Oxidation Under Both Alkaline and Neutral Conditions, *Angew. Chem., Int. Ed.*, 2016, 55, 2488-2492.
- [71] G. Jia, Y. Hu, Q. Qian, Y. Yao, S. Zhang, Z. Li and Z. Zou, Formation of Hierarchical Structure Composed of (Co/Ni)Mn-LDH Nanosheets on MWCNT Backbones for Efficient Electrocatalytic Water Oxidation, *ACS Applied Materials & Interfaces*, 2016, 8, 14527-14534.
- [72] L. Tao, M. Huang, S. Guo, Q. Wang, M. Li, X. Xiao, G. Cao, Y. Shao, Y. Shen, Y. Fu and M. Wang, Surface Modification of NiCo₂Te₄ Nanoclusters: a Highly Efficient Electrocatalyst for Overall Water-splitting in Neutral Solution, *Applied Catalysis B: Environmental*, 2019, 254, 424-431.
- [73] Q. Zhou, T.-T. Li, J. Wang, F. Guo and Y.-Q. Zheng, Hierarchical Cu₂S NRs@CoS Core-Shell Structure and Its Derivative Towards Synergistic Electrocatalytic Water Splitting, *Electrochimica Acta*, 2019, 296, 1035-1041.
- [74] Q. Zhou, T.-T. Li, F. Guo and Y.-Q. Zheng, Construction of Hierarchically Structured CuO@CoP Anode for Efficient Oxygen Evolution Reaction, *ACS Sustainable Chemistry & Engineering*, 2018, 6, 11303-11312.
- [75] K. Li, J. Zhang, R. Wu, Y. Yu and B. Zhang, Anchoring CoO Domains on CoSe₂ Nanobelts as Bifunctional Electrocatalysts for Overall Water Splitting in Neutral Media, *Adv. Sci.*, 2016, 3, 1500426.
- [76] Y. Rong, Y. Ma, F. Guo, J. Qian, H. Li, M. Zhou, Z. Xu, Y.-Q. Zheng and T.-T. Li, Paintbrush-like Co doped Cu₃P Grown on Cu foam as An Efficient Janus Electrode for Overall Water Splitting, *International Journal of Hydrogen Energy*, 2019, 44, 28833-28840.

- [77] L. Q. Zhou, C. Ling, H. Zhou, X. Wang, J. Liao, G. K. Reddy, L. Deng, T. C. Peck, R. Zhang, M. S. Whittingham, C. Wang, C.-W. Chu, Y. Yao and H. Jia, A High-Performance Oxygen Evolution Catalyst in Neutral-pH for Sunlight-Driven CO₂ Reduction, *Nat. Communications*, 2019, 10, 4081.
- [78] Q. Zhou, T.-T. Li, J. Qian, Y. Hu, F. Guo and Y.-Q. Zheng, Self-supported Hierarchical CuO_x@Co₃O₄ Heterostructures as Efficient Bifunctional Electrocatalysts for Water Splitting, *Journal of Materials Chemistry A*, 2018, 6, 14431-14439.
- [79] Y. Gorlin, B. Lassalle-Kaiser, J. D. Benck, S. Gul, S. M. Webb, V. K. Yachandra, J. Yano and T. F. Jaramillo, In Situ X-ray Absorption Spectroscopy Investigation of a Bifunctional Manganese Oxide Catalyst with High Activity for Electrochemical Water Oxidation and Oxygen Reduction, *Journal of the American Chemical Society*, 2013, 135, 8525-8534.
- [80] L. Xie, R. Zhang, L. Cui, D. Liu, S. Hao, Y. Ma, G. Du, A. M. Asiri and X. Sun, High-Performance Electrolytic Oxygen Evolution in Neutral Media Catalyzed by a Cobalt Phosphate Nanoarray, *Angew. Chem., Int. Ed.*, 2017, 56, 1064-1068.
- [81] M. Zang, N. Xu, G. Cao, Z. Chen, J. Cui, L. Gan, H. Dai, X. Yang and P. Wang, Cobalt Molybdenum Oxide Derived High-Performance Electrocatalyst for the Hydrogen Evolution Reaction, *ACS Catalysis*, 2018, 8, 5062-5069.
- [82] X. Li, X. Su, Y. Pei, J. Liu, X. Zheng, K. Tang, G. Guan and X. Hao, Generation of Edge Dislocation Defects in Co₃O₄ Catalysts: An Efficient Tactic to Improve Catalytic Activity for Oxygen Evolution, *Journal of Materials Chemistry A*, 2019, 7, 10745-10750.
- [83] H. Chen, L. Hu, M. Chen, Y. Yan and L. Wu, Nickel–Cobalt Layered Double Hydroxide Nanosheets for High-performance Supercapacitor Electrode Materials, *Adv. Funct. Mater.*, 2014, 24, 934-942.

- [84] G. Huang, Z. Xiao, R. Chen and S. Wang, Defect Engineering of Cobalt-Based Materials for Electrocatalytic Water Splitting, *ACS Sustainable Chemistry & Engineering*, 2018, 6, 15954-15969.
- [85] J. Xie, H. Zhang, S. Li, R. Wang, X. Sun, M. Zhou, J. Zhou, X. W. Lou and Y. Xie, Defect-Rich MoS₂ Ultrathin Nanosheets with Additional Active Edge Sites for Enhanced Electrocatalytic Hydrogen Evolution, *Advanced Materials*, 2013, 25, 5807-5813.
- [86] F. Liang, Y. Yu, W. Zhou, X. Xu and Z. Zhu, Highly Defective CeO₂ as A Promoter for Efficient and Stable Water Oxidation, *Journal of Materials Chemistry A*, 2015, 3, 634-640.
- [87] N. Zhang, X. Li, H. Ye, S. Chen, H. Ju, D. Liu, Y. Lin, W. Ye, C. Wang, Q. Xu, J. Zhu, L. Song, J. Jiang and Y. Xiong, Oxide Defect Engineering Enables to Couple Solar Energy into Oxygen Activation, *Journal of the American Chemical Society*, 2016, 138, 8928-8935.
- [88] S. Hu, M. R. Shaner, J. A. Beardslee, M. Lichterman, B. S. Brunshwig and N. S. Lewis, Amorphous TiO₂ Coatings Stabilize Si, GaAs, and GaP Photoanodes for Efficient Water Oxidation, *Science*, 2014, 344, 1005.
- [89] L. Zhuang, Y. Jia, T. He, A. Du, X. Yan, L. Ge, Z. Zhu and X. Yao, Tuning Oxygen Vacancies in Two-dimensional Iron-cobalt Oxide Nanosheets Through Hydrogenation for Enhanced Oxygen Evolution Activity, *Nano Research*, 2018, 11, 3509-3518.
- [90] R. Zhang, Y.-C. Zhang, L. Pan, G.-Q. Shen, N. Mahmood, Y.-H. Ma, Y. Shi, W. Jia, L. Wang, X. Zhang, W. Xu and J.-J. Zou, Engineering Cobalt Defects in Cobalt Oxide for Highly Efficient Electrocatalytic Oxygen Evolution, *ACS Catalysis*, 2018, 8, 3803-3811.
- [91] C. Yan, G. Chen, J. Sun, C. Lv and J. Pei, Edge Dislocation Surface Modification: A New and Efficient Strategy for Realizing Outstanding Lithium Storage Performance, *Nano Energy*, 2015, 15, 558-566.

- [92] J. Sun, W. Li, B. Zhang, G. Li, L. Jiang, Z. Chen, R. Zou and J. Hu, 3D Core/Shell Hierarchies of MnOOH Ultrathin Nanosheets Grown on NiO Nanosheet Arrays for High-performance Supercapacitors, *Nano Energy*, 2014, 4, 56-64.
- [93] J. Kan, L. Deng, B. Li, Q. Huang, S. Zhu, S. Shen and Y. Chen, Performance of co-doped Mn-Ce Catalysts Supported on Cordierite for Low Concentration Chlorobenzene Oxidation, *Applied Catalysis A: General*, 2017, 530, 21-29.
- [94] P. W. Menezes, A. Indra, O. Levy, K. Kailasam, V. Gutkin, J. Pfrommer and M. Driess, Using Nickel Manganese Oxide Catalysts for Efficient Water Oxidation, *Chemical Communications*, 2015, 51, 5005-5008.
- [95] X. He, F. Yin, Y. Li, H. Wang, J. Chen, Y. Wang and B. Chen, NiMnO₃/NiMn₂O₄ Oxides Synthesized via the Aid of Pollen: Ilmenite/Spinel Hybrid Nanoparticles for Highly Efficient Bifunctional Oxygen Electrocatalysis, *ACS Applied Materials & Interfaces*, 2016, 8, 26740-26757.
- [96] J. Huang, J. Chen, T. Yao, J. He, S. Jiang, Z. Sun, Q. Liu, W. Cheng, F. Hu, Y. Jiang, Z. Pan and S. Wei, CoOOH Nanosheets with High Mass Activity for Water Oxidation, *Angewandte Chemie International Edition*, 2015, 127, 8846-8851.
- [97] J. Huang, Q. Shang, Y. Huang, F. Tang, Q. Zhang, Q. Liu, S. Jiang, F. Hu, W. Liu, Y. Luo, T. Yao, Y. Jiang, Z. Pan, Z. Sun and S. Wei, Oxyhydroxide Nanosheets with Highly Efficient Electron-Hole Pair Separation for Hydrogen Evolution, *Angewandte Chemie International Edition*, 2016, 55, 2137-2141.
- [98] J. Bao, X. Zhang, B. Fan, J. Zhang, M. Zhou, W. Yang, X. Hu, H. Wang, B. Pan and Y. Xie, Ultrathin Spinel-Structured Nanosheets Rich in Oxygen Deficiencies for Enhanced Electrocatalytic Water Oxidation, *Angewandte Chemie International Edition*, 2015, 127, 7507-7512.
- [99] Y. Feng, X.-Y. Yu and U. Paik, Nickel Cobalt Phosphides Quasi-hollow Nanocubes as An Efficient Electrocatalyst for Hydrogen Evolution in Alkaline Solution, *Chemical Communications*, 2016, 52, 1633-1636.

- [100] B. E. Conway and B. V. Tilak, Interfacial Processes Involving Electrocatalytic Evolution and Oxidation of H₂, and The Role of Chemisorbed H, *Electrochimica Acta*, 2002, 47, 3571-3594.
- [101] Q. Lu, G. S. Hutchings, W. Yu, Y. Zhou, R. V. Forest, R. Tao, J. Rosen, B. T. Yonemoto, Z. Cao, H. Zheng, J. Q. Xiao, F. Jiao and J. G. Chen, Highly Porous Non-Precious Bimetallic Electrocatalysts for Efficient Hydrogen Evolution, *Nature Communications*, 2015, 6, 6567.
- [102] C. Hu, L. Zhang and J. Gong, Recent Progress Made in The Mechanism Comprehension and Design of Electrocatalysts for Alkaline Water Splitting, *Energy & Environmental Science*, 2019, 12, 2620-2645.
- [103] L. Yu, H. Zhou, J. Sun, F. Qin, F. Yu, J. Bao, Y. Yu, S. Chen and Z. Ren, Cu Nanowires Shelled with NiFe Layered Double Hydroxide Nanosheets as Bifunctional Electrocatalysts for Overall Water Splitting, *Energy & Environmental Science*, 2017, 10, 1820-1827.
- [104] I. Zaharieva, P. Chernev, M. Risch, K. Klingan, M. Kohlhoff, A. Fischer and H. Dau, Electrosynthesis, Functional, and Structural Characterization of A Water-oxidizing Manganese Oxide, *Energy & Environmental Science*, 2012, 5, 7081-7089.
- [105] E. B. Castro and C. A. Gervasi, Electrodeposited Ni-Co-oxide Electrodes: Characterization and Kinetics of The Oxygen Evolution Reaction, *International Journal of Hydrogen Energy*, 2000, 25, 1163-1170.
- [106] M. K. Bates, Q. Jia, N. Ramaswamy, R. J. Allen and S. Mukerjee, Composite Ni/NiO-Cr₂O₃ Catalyst for Alkaline Hydrogen Evolution Reaction, *The Journal of Physical Chemistry C*, 2015, 119, 5467-5477.
- [107] T. Shinagawa, A. T. Garcia-Esparza and K. Takanabe, Insight on Tafel Slopes from A Microkinetic Analysis of Aqueous Electrocatalysis for Energy Conversion, *Scientific Reports*, 2015, 5, 13801.

- [108] Y. Surendranath, M. W. Kanan and D. G. Nocera, Mechanistic Studies of the Oxygen Evolution Reaction by a Cobalt-Phosphate Catalyst at Neutral pH, *Journal of the American Chemical Society*, 2010, 132, 16501-16509.
- [109] M. Cabán-Acevedo, M. L. Stone, J. R. Schmidt, J. G. Thomas, Q. Ding, H.-C. Chang, M.-L. Tsai, J.-H. He and S. Jin, Efficient Hydrogen Evolution Catalysis using Ternary Pyrite-type Cobalt Phosphosulphide, *Nature Materials*, 2015, 14, 1245-1251.
- [110] D. Zhong, L. Zhang, C. Li, D. Li, C. Wei, Q. Zhao, J. Li and J. Gong, Nanostructured NiFe (oxy)hydroxide with Easily Oxidized Ni Towards Efficient Oxygen Evolution Reactions, *Journal of Materials Chemistry A*, 2018, 6, 16810-16817.
- [111] X.-X. Ma, L. Chen, Z. Zhang and J.-L. Tang, Electrochemical Performance Evaluation of CuO@Cu₂O Nanowires Array on Cu Foam as Bifunctional Electrocatalyst for Efficient Water Splitting, *Chinese Journal of Analytical Chemistry*, 2020, 48, e20001-e20012.
- [112] S. M. Alley and E. L. Thomas, *The Structure of Materials*, Wiley, New York, 1988.
- [113] C.-H. Chen, E. C. Njagi, S.-Y. Chen, D. T. Horvath, L. Xu, A. Morey, C. Mackin, R. Joesten and S. L. Suib, Structural Distortion of Molybdenum-Doped Manganese Oxide Octahedral Molecular Sieves for Enhanced Catalytic Performance, *Inorganic Chemistry*, 2015, 54, 10163-10171.

CHAPTER 5 Conclusions and Prospect

5.1 Conclusions

Water splitting is an attractive technology for the production of pure oxygen and hydrogen gas via an electrochemical way, which can be also transferred from unstable renewable energy to stable chemical energy. The main factor to drive efficient water splitting over the electrocatalysts is the overpotential, which is different in acidic, alkaline, and neutral electrolytes. In this study, a novel Ni-based nanostructured electrocatalyst for OER, a new-type nickel-cobalt phosphide electrocatalyst for HER with long-term stability in a wide pH condition, and core-shell nanostructured bifunctional electrocatalysts for overall water splitting were developed, and the following conclusions were obtained:

- To decrease the overpotential in the OER process, a NiO microflake@NiFe-LDH nanosheet with core@shell heterostructure was grown on a 3D Ni foam substrate by using a two-step hydrothermal synthesis followed by a calcination process, which exhibited high efficiency with an overpotential of 265 mV@10 mA cm⁻². Furthermore, after treated in organic solution via an ultrasonic method, the overpotential was decreased to 210 mV with a small Tafel slope of 72 mV dec⁻¹ in the alkaline solution. Additionally, the NiO@NiFe-LDH/NF-US showed the synergistic interactions between NiO micro flakes and NiFe-LDH nanosheets with a special 3D nanostructure, which contributed to the enhanced activity performance and excellent long-term stability in at least 50 h even at high current densities of 50 and 100 mA cm⁻², with high faradic efficiency of O₂ production.
- Binder-free graphite carbon combined NiCo alloy phosphide nanocomposite, i.e., NiCoP-C(TPA), with unique nanostructure was successfully prepared by using terephthalic acid as the soft template to derive NiCo bimetallic precursor film on NF in a hydrothermal synthesis process, followed by calcination in an Ar atmosphere and phosphorization treatment with P source (NaH₂PO₂). The bimetallic NiCo phosphide nanoparticles were well combined with the graphite carbon, which exhibited much higher activity than the monometallic phosphides with an overpotential as low as 78 mV@10 mA cm⁻², a small Tafel slope of 73.4 mV dec⁻¹, a faradic efficiency of ~94% and long-term stability at the high current density in the alkaline electrolyte. Meanwhile, it also exhibited superior HER performance in the acidic electrolyte with

an overpotential of 94 mV@10 mA cm⁻², a Tafel slope of 81.1 mV dec⁻¹, and long-term stability although, in the neutral electrolyte, a relatively high overpotential of 248 mV@10 mA cm⁻² with a high Tafel slope of 112.5 mV dec⁻¹ was obtained. It indicated that using polycarboxylic acids (organic solution) as templates is an effective way to produce high-performance bimetallic phosphide-based electrocatalysts with a special nanostructure for HER.

- To fabricate a bifunctional catalyst for the overall water splitting, a core@shell structure electrocatalyst of CuO_x NWs@NiMnO_x NSs was successfully coated on the CF substrate by a three-step process including an oxidation step for the construction of nanowire structure on the surface of CF substrate, a UPED process to deposit NiMn bimetal hydroxide composite layer on the nanowire and a calcination step. Herein, nickel-manganese oxide endowed numerous vacancies, scattered defects, and dislocations for the enhancement of catalytic activity. Moreover, combining oxides with bimetallic elements was considered as an efficient route to modify the electronic distribution for improving the intrinsic activity of electrocatalysts, and further engineering the defect structure and adjusting the valence state could provide more adsorption sites as well as active sites for the decomposition of the reactants and/or intermediates. NiMnO_x nanosheets with rich defects were electrochemically deposited on the surface of Cu(OH)₂ nanowires followed by a thermal treatment process to form a CuO_x nanowires @NiMnO_x nanosheets (CuO_x NWs@NiMnO_x NSs) electrocatalyst with core-shell configuration. Structure characterizations indicated that NiMnO_x nanosheet had numerous vacancies with scattered defects and dislocations with partial cracking of the inert basal planes, resulting in extra active edge sites and coordination-unsaturated spinel crystal. As such, the valence states of Ni and Mn elements became unstable in the defect modified NiMnO_x materials under the applied potential. Comparing with the initial NiMnO_x, more Ni³⁺ and Mn⁴⁺ were formed during the oxygen evolution reaction (OER) whereas they were converted to Ni²⁺ and Mn³⁺ during the hydrogen evolution reaction (HER). These controllable valence state changes of metal elements endowed the NiMnO_x to have a high ability for catalyzing overall water electrolysis. As a result, the CuO_x NWs@NiMnO_x NSs bifunctional electrocatalysts exhibited high performances in both HER and OER in alkaline electrolyte. Meanwhile, by using the same electrocatalysts in the neutral

electrolyte, the overpotentials@10 mA cm⁻² was also as low as 80.7 and 390 mV with Tafel slopes of 77.6 and 101.6 mV dce⁻¹ for HER and OER, respectively. A two-electrode overall water electrolysis system using this bifunctional electrocatalyst exhibited low cell voltages of 1.62 and 1.75V in the alkaline and neutral electrolytes respectively at the standard current density of 10 mA cm⁻² with long-term stability, indicating that this CuO_x NWs@NiMnO_x NSs core@shell-type material should be effective bifunctional electrocatalysts in both alkaline and neutral pH media.

5.2 Prospects

Although some excellent electrocatalysts have been developed in the work and by other researchers, for the large-scale application, various researches and developments are still necessary for future works:

- **Electrocatalysts support:** To date, various 3D electrocatalyst supports such as nickel foam (NF) and Cu foam (CF) have been widely applied as the electrode substrates and the obtained electrodes always exhibited highly active for the OER, HER, and both. However, these metal foams are unstable in the acid electrolyte. It is suggested to develop non-metal 3D supports based on carbon materials for the loading of electrocatalysts for the water splitting in a wide pH environment.
- **Higher performance electrocatalysts:** To date, various electrocatalysts with excellent performances have been developed in the lab. However, for practical applications, those electrocatalysts which can work as the bifunctional electrocatalysts for the overall water splitting in a wide pH range are still necessary. Especially, how to coat them in a large-area electrode and how to make them stable in extreme conditions are expected. Among various electrocatalyst materials, some transition metals such as Mn and W should be promising candidates for water splitting in all pH ranges. It is suggested to develop Mn and/or W-based electrocatalysts for water splitting.
- **Electrolyte environments:** Various electrocatalysts have shown excellent performances for HER and OER in the environments of strong acid or alkaline electrolytes. However, the strong pH condition always results in a corrosive issue. In future studies, more attention should be paid to the developments of electrocatalysts which can work in neutral electrolytes and even in seawater.

CURRICULUM VITAE

Personal details

Name: SUCHADA SIRISOMBOONCHAI
Nationality: THAI
Date of birth: 19 March 1993
Email: suchada.ssc@gmail.com

Educations

2018,4-2021,3: D.Eng. (Safety Science and Technology), Hirosaki University, Japan
2015,8-2017,8: M.Sc. (Chemistry Science and Technology), Thammasat University, Thailand
2010,6-2015,5: B.Sc. (Chemistry Science and Technology), Thammasat University, Thailand

Experiences

- Research student, Huazhong University of Science and Technology, China (April-May 2017).
- Research student (Topic: Synthesis of bio-oil by using solid catalyst), Energy conversion engineering group, Institute of Regional Innovation (IRI), Japan (May-July 2014).

Scholarships and Awards

- **Excellent Student Recognition Award**, Doctoral course, of Hirosaki University, (2020).
- **Japan Government (Monbukagakusho) Scholarship**, Doctoral. course, Hirosaki University, Japan (2017-2021).

List of Publications and Presentations

Publications

- 1) **Suchada Sirisomboonchai**, Xiumin Li, Nutthaphak Kitiphapiboon, Rinrada Channoo, Shasha Li, Yufei Ma, Suwadee Kongparakul, Chanatip Samart, Abuliti Abudula, Guoqing Guan, "Fabrication of CuOx nanowires@NiMnOx nanosheets core@shell-type electrocatalysts: crucial roles of defect modification and valence state for overall water electrolysis", *Journal of Materials Chemistry A*, Vol. 8, pp. 16463-16476, 2020.
- 2) **Suchada Sirisomboonchai**, Shasha Li, Akihiro Yoshida, Suwadee Kongparakul, Chanatip Samart, Yasuki Kansha, Xiaogang Hao, Abuliti Abudula, Guoqing Guan, "Terephthalic Acid Induced Binder-free NiCoP-carbon Nanocomposite for Highly Efficient Electrocatalysis of Hydrogen Evolution Reaction," *Catalysis Science & Technology*, Vol. 9, pp. 4651-4658, 7, 2019.
- 3) **Suchada Sirisomboonchai**, Shasha Li, Akihiro Yoshida, Xiumin Li, Chanatip Samart, Abuliti Abudula, Guoqing Guan, "Fabrication of NiO microflake @ NiFe-LDH nanosheet heterostructure electrocatalysts for oxygen evolution reaction," *ACS Sustainable Chemistry & Engineering*, Vol. 7, 2, pp. 2327–2334, 1, 2019.
- 4) Shasha Li, **Suchada Sirisomboonchai**, Xiaowei An, Xuli Ma, Peng Li, Lixia Ling, Xiaogang Hao, Abuliti Abudula, and Guoqing Guan, "Engineering Interfacial Structures to Accelerate Hydrogen Evolution Efficiency of MoS₂ over a Wide pH Range," *Nanoscale*, Vol 12, pp. 6810-6820, 2020.
- 5) Jiajia Wang, Xiyan Yue, Yanyan Yang, **Suchada Sirisomboonchai**, Peifen Wang, Xuli Ma, Abuliti Abudula, Guoqing Guan, "Earth-abundant transition-metal-based bifunctional catalysts for overall electrochemical water splitting: A review," *Journal of Alloys and Compounds*, Vol. 819, pp. 153346, 2020.
- 6) Shasha Li, **Suchada Sirisomboonchai**, Akihiro Yoshida, Xiaowei An, Xiaogang Hao, Abuliti Abudula, and Guoqing Guan, "Bifunctional CoNi/CoFe₂O₄ /Ni Foam Electrodes for Efficient Overall Water Splitting at a High Current Density," *Journal of Materials Chemistry A*, Vol. 6, pp. 9221-19230, 2018.
- 7) Xiumin Li, Shasha Li, Akihiro Yoshida, **Suchada Sirisomboonchai**, Keyong Tang, Zhijun Zuo, Xiaogang Hao, Abuliti Abudula, Guoqing Guan, "Mn doped CoP

nanoparticle clusters: an efficient electrocatalyst for hydrogen evolution reaction," Catalysis Science & Technology, Vol. 8, pp. 4407-4412, 2018

International presentations

- 1) **Suchada Sirisomboonchai**, Shasha Li, Akihiro Yoshida, Suwadee Kongparakul, Chanatip Samart, Katsuki Kusakabe, Xiaogang Hao, Abuliti Abudula, Guoqing Guan, "Hierarchical Ni-Co composites for electrocatalytic hydrogen evolution reaction," The 31st International Symposium on Chemical Engineering, Chiang Mai, Thailand, November 30-December 2, 2018.
- 2) **Suchada Sirisomboonchai**, Akihiro Yoshida, Abuliti Abudula, Guoqing Guan, "Cu nanowire@MnNiP Electrocatalysts for Water Splitting in Neutral Solution," 18th Asian Pacific Confederation of Chemical Engineering Congress (APCChE 2019), Sapporo, Hokkaido, Japan, September 23-27, 2019.
- 3) **Suchada Sirisomboonchai**, Rinrada Channoo, Nutthaphak Kitiphapiboon, Akihiro Yoshida, Suwadee Kongparakul, Chanatip Samart, Abuliti Abudula, Guoqing Guan, "In-situ construction of 3D core-shell structure on Cu foam electrode for driven hydrogen production via overall water splitting," The Pure and Applied Chemistry International Conference 2020 (PACCON 2020), Bangkok, Thailand. February 13th – 14th, 2020.

Domestic presentations

- 1) **Suchada Sirisomboonchai**、吉田 曉弘、阿布里提、官国清、"Nanostructured nickel-cobalt bimetallic phosphide for hydrogen evolution reduction、" 化学工学会 第 84 年会、芝浦工業大学、2019 年 3 月 13-15 日.
- 2) **Suchada Sirisomboonchai**, Shasha Li, Akihiro Yoshida, Abuliti Abudula, Guoqing Guan, "Fabrication of NiO nanoflake @ NiFe-LDH nanosheet heterostructured electrocatalyst for oxygen evolution reaction," 4 校學術交流会, 岩手大学、2018 年 10 月 30 日.
- 3) Shasha Li, **Suchada Sirisomboonchai**, Akihiro Yoshida, Abuliti Abudula, Xiaogang Hao, Guoqing Guan, "Bifunctional CoNi/CoFe₂O₄ /Ni Foam Electrodes for Efficient Water Splitting, "Joint Meeting of the Tohoku Area Chemistry Societies of 2018,

Akita University, September 15-16, 2018.

- 4) **Suchada Sirisomboonchai**, 李莎莎、吉田曉弘、阿布里提、官国清、“牡丹状のモルフォロジーを有する水分解用 NiFe-LDH/NiO 触媒電極の作製、”第 27 回日本エネルギー学会大会, 日大理工学部駿河台キャンパス, 2018 年 8 月 8-9 日。
- 5) 李莎莎, 吉田曉弘, **Suchada Sirisomboonchai**, 阿布里提, Hao Xiaogang, 官国清, “高活性・高安定性のコバルトホスホスルフィド水素発生触媒、” 化学工学会第 83 年会, 関西大学千里山キャンパス, 大阪, 2018 年 3 月 13-15 日。
- 6) 安小偉, **Suchada Sirisomboonchai**, 楊言言, ショケイテイパイルザ, 吉田曉弘, 于涛, 阿布里提, 官国清, “二酸化炭素電解還元のためのビスマス系触媒の in-situ モルフォロジー変換、” 2019 電気化学会秋季大会、山梨大学、甲府、2019 年 9 月 5 日~9 月 6 日。
- 7) パティルアマル, **Suchada Sirisomboonchai**, 岳喜岩, 吉田曉弘, 阿布里提, 官国清, “スーパーキャパシタ用の酸化グラフェンベースのナノ構造 NiCo₂O₄@MnO₂ ハイブリッド正極を簡単に合成、” 2019 電気化学会秋季大会、山梨大学、甲府、2019 年 9 月 5 日~9 月 6 日。
- 8) PATIL AMAR, 岳喜岩, 安小偉, **Suchada Sirisomboonchai**, 于涛, 吉田曉弘, 阿布里提, 官国清, “Graphene oxide based nanostructured V₂O₅@RuO₂ hybrid positive electrode for high performance pseudocapacitor、” 電気化学会第 87 回大会, 名古屋工業大学, 2020 年 3 月 17 日 (火) ~19 日 (木)

List of Patents

- 1) **Suchada Sirisomboonchai**, 官国清, 吉田曉弘, 阿布里提, 関和治, “電極触媒及びその製造方法、並びに水素の製造方法,” 出願番号：特願 2019-200148, 出願日：2019年11月1日。
- 2) **Suchada Sirisomboonchai**, 官国清, 吉田曉弘, 関和治, 阿布里提, “新規水電解触媒”, 特願 2018-248275, 出願日：2018年12月28日。
- 3) **Suchada Sirisomboonchai**, 吉田曉弘, 官国清, 関和治, 阿布里提, “電極の製造方法、電極及び水素の製造方法,”特願 2018-136044,出願日：2018年7月19日。
- 4) 李莎莎, **Suchada Sirisomboonchai**, 吉田曉弘, 官国清, 関和治, 阿布里提, “電極触媒及びその製造方法,”特願 2018-202781,出願日：2018年10月29日。
- 5) ナッタパック ギティパットピブーン, 官国清, **Suchada Sirisomboonchai**, 関和治, 阿布里提, “電極触媒及びその製造方法、並びに水素の製造方法”, 出願番号：特願 2020-172736, 出願日：2020年10月13日。